The Dissertation Committee for Jingwen Wu
certifies that this is the approved version of the following dissertation:

Massive Star Formation, From the Milky Way to Distant Galaxies

Committee:

Neal J. Evans II, Supervisor

Paul A. Vanden Bout

Daniel T. Jaffe

Paul M. Harvey

Karl Gebhardt

Gary J. Hill

Massive Star Formation, From the Milky Way to Distant Galaxies

by

Jingwen Wu, B.S., M.S.

DISSERTATION

Presented to the Faculty of the Graduate School of

The University of Texas at Austin

in Partial Fulfillment

of the Requirements

for the Degree of

DOCTOR OF PHILOSOPHY

THE UNIVERSITY OF TEXAS AT AUSTIN

August 2006

To my parents, and to all I love.

Acknowledgments

I have been in Austin for 5 years. During these years, there are so many people I want to thank. They have made my study in Austin a wonderful experience.

Firstly I want to thank my advisor, Neal Evans. It is my biggest pleasure to have Neal as my advisor. He is great in research; he is strict in instruction; and he is so nice in personality. I really enjoy the nights to observe with him in the summit of Mauna Kea, the weekly meeting to discuss with him in the office, and the home parties to chat with him and his wife Leslie in their house. I learned a lot from him, both in science and in the attitude to science; he gave me an good example of my future career. I want to thank Paul Vanden Bout, my outside committee member. He is very nice and patient; he has helped a lot on my study in the field of high-z star formation. I want to give thanks to Dan Jaffe, a great professor that shows lot of interests on my research and is glad to give advices; he can always bring up some insight and constructive suggestions on my study. I want to thank other members in my committee, Paul Harvey, Karl Gebhardt, Gary Hill, and John Lacy who has been in my 2nd year defense committee. They are good committee members to guide my research.

I am grateful to other graduate students in my group. Yancy, Claudia,

Katelyn, Jeong-Eun, Chad and Kaisa, they had been there before I came to the group, and I did get their sincere help during the years. I also want to thank Andrea, Mike and Jo-Hsin, they came after me, but have helped a lot on observations, data management, and many other group works; I feel so lucky to be in such a nice group.

I want to express my appreciation to people in the department. There is Stephanie, the graduate coordinator; she has been so nice and helpful to every student, especially for foreign students like me. I should also say thanks to Elizabeth Korves, the previous coordinator, and Craig and Volker, the previous and current student advisor. And yes, thanks to my great officemates, Julia, Diana, Fergal, Anges, and Jarrett, you have made 16.220 one of the best office in the department. There are other friends in the department, Zhu, Zhaohui, Juntai, Marty, and so many of them; also there are many friends in my life; we play volleyball, badminton together, share happiness and sadness together. I want to thank them all, since they have made these 5 years one of the best time in my life.

Massive Star Formation, From the Milky Way to Distant Galaxies

Publication No. _____

Jingwen Wu, Ph.D.
The University of Texas at Austin, 2006

Supervisor: Neal J. Evans II

Studying massive star formation is hard, both observationally and theoretically. Many basic questions concerning the formation and early evolution of massive stars remain unclear. Based on a series of spectral lines and mapping surveys on a large sample of massive star-forming cores, we have been able to study the dynamics and physical properties of massive star-forming regions. The HCN 3-2 survey has revealed a large fraction of line asymmetry that indicates the global existence of infall in massive cores. Using the spectra and maps of multiple HCN and CS transitions, as well as of their isotopes, we have started to model the massive star-forming cores with a 1D Monte Carlo simulation. The surveys of dense gas tracers in Galactic cores revealed a linear correlation between the star formation rate, as indicated by the infrared luminosity, and the amount of the dense gas, as traced by the line luminosity

of dense gas tracer like HCN 1-0. The linear L_{IR}-L'$_{HCN1-0}$ correlation was found to extend over 8 orders of magnitude, from distant starburst and normal galaxies to Galactic massive cores, with a lower cutoff in luminosity. It suggests that star formation may follow a simple relationship when the appropriate tracers are used, and we may understand distant star formation in terms of the known properties of local star-forming regions. To explain this linear correlation, we propose the existence of a basic unit for the clustered star formation in galaxies, with the basic units similar to the massive dense cores studied in the Galaxy.

Table of Contents

List of Tables

List of Figures

Chapter 1

Introduction

Stars form in molecular clouds. In the current theoretical frame work, there is a dichotomy in the mode of star formation (Shu et al. 1987): a relatively isolated mode of star formation, and a mode in which stars form in clusters. Low-mass stars (a few solar mass) can form either in isolation or in clusters, while massive stars form almost exclusively in clustered environments. The study of low-mass star formation has seen great progress in the last several decades. Theoretical and observational works have revealed a scheme of how a low mass star form, which is commonly accepted by astronomers to explain star formation of sun-like stars and the formation of planet systems: it starts from the cloud fragmentation, and some clumps become condensed by gravity to form dense cores; the core collapses from inside-out, central object forms via accretion from a surrounding disk; a stellar wind breaks out of the envelope along the rotational axis to create a outflow; the surrounding envelope gets dispersed by the wind; and finally a new star shows up (e.g., Shu et al. 1987).

Clustered star formation is the dominant mode of star formation in the Galaxy, since most of stars (70-90%) form in this mode (Lada & Lada 2003), and massive star formation almost always occurs in clustered mode.

However, the mechanism of massive star formation remains unclear. One of the major difficulties for this study is the lack of observational data on massive star forming regions, since these regions are usually very distant. The other difficulty comes from the extreme complexity of the environment where high-mass stars form and evolve. Even more observations are needed to allow statistical studies amid this complexity

The goal of the study of massive star formation is to establish how a Giant Molecular Cloud (GMC) evolves into a stellar cluster, and how do individual massive stars form during that process. A natural thought is that massive star formation goes through a similar process to the formation of low mass stars. For example, are fragmentation, core collapse, accretion through disks, and outflows also necessary in the formation of massive stars or star clusters? Recent works indeed have discovered indications of fragmentation (Beuther & Schilke 2004), accretion disks (e.g. Patel et al. 2005, Thi & Bik, 2005), outflows (e.g. Zhang et al. 2005), and infall (e.g. Sollins et al. 2005) in some individual massive star forming regions; these are valuable pieces to make up the picture of massive star formation. However, these results provide only some hints to the answer, and we are still far from understanding how massive star formation proceeds. More general observational and theoretical studies are needed to describe the true picture.

An interesting period of massive star formation is the period when massive dense cores collapse to form internal proto-stars, during which the dynamics of the core changes from a relatively static state to a very active state.

Large mass motions like infall, outflow, and turbulence, give more observable features than other evolutionary phases. Different dynamical models predict different physical conditions for the cloud, such as density profiles, velocity field, and so on. Observations towards massive dense cores will provide good constraints to those models.

For the formation of an individual high-mass star in such a massive core, a theoretical difficulty exists. For stars with mass greater than 20 $M_{\odot}$, the radiation pressure generated by the new internal source will stop the further accretion, and thus a higher mass star can not form. Two major theories have been brought up to solve this problem. One suggests that the massive star can be formed by direct collisions between lower mass stars, or via competitive accretion (e.g. Bonnell et al. 2004). The other approach keeps the low-mass-like accretion system, but uses improved treatment of the accretion process to see if the radiation barrier can be overcome. (e.g. McKee & Tan 2002, 2003). Both models have some observational support; Further observations are needed to tell which model is correct.

Massive star formation occurs at the center of GMC cores. These regions are opaque, dense, and turbulent, and they can only be well traced by molecular dense gas tracers like CS, HCN, and by optically thin dust continuum emission. Some systematic surveys have been carried out to probe the physical conditions of massive star forming regions. For example, a large sample of massive star-forming cores that are associated with water masers has been surveyed with multiple CS transitions (Plume et al. 1992, 1997), a

subsample of which have been mapped with the CS 5-4 transition (Shirley et al. 2002) and dust continuum (Mueller et al. 2003). Rich information about the physical conditions of these massive cores, such as mean density, density profile, the size, mass, and bolometric luminosity of the cores, were obtained. For the purpose of understanding how massive star formation proceeds from a dense core to stars, the next step is to establish the dynamical models for the observed cores, and test the models to explain the observations, with the goal to reveal the dynamical process and create a detailed model of massive star formation. This requires more observations and modeling. For instance, HCN is another dense gas tracer that is worth surveying and modeling. It is a better tracer to trace infall in massive star forming regions (Wu & Evans 2003, Chap. 2).

A model including the chemical evolution and dynamical evolution has been successfully applied to fit observations of some low-mass star forming regions (e.g. Lee at al. 2003, Evans et al. 2005). Similar attempts can be tried on massive regions. Because the chemical model for the massive star forming region is still not very clear, and the models between gas and dust in massive regions are not fully self-consistent yet, we will start with a simple model based on the models from low-mass regions.

Finally, let's put the massive star formation in the context of galaxies besides the Milky Way. Indications of extreme star formation have been found in distant starburst galaxies, even at large redshifts (e.g. Isaak et al. 2002, Solomon & Vanden Bout 2005). Is the star formation there the same as seen

in the Galaxy? Massive star forming cores are the potential links to connect star formation from the Milky Way to other galaxies. Massive star formation is likely the dominant star-forming mode in other galaxies as it is in the Milky Way; also only massive star forming regions or groups of them (e.g. super star clusters), are bright enough to be seen from nearby, or even distant galaxies. If we can correlate the properties of Galactic massive star forming cores to some variable that is observable in remote galaxies, the connection of Galactic and extragalactic star formation can be made.

A promising such correlation might have been found recently. A survey with HCN 1-0 towards a large sample of galaxies (Gao & Solomon 2004a,b) discovered that the luminosity of HCN 1-0 has a tighter correlation than the luminosity of CO with the infrared luminosity (L_{IR}). L_{IR} indicates the star formation rate, while L_{HCN1-0} is an indicator of the amount of dense gas. The L_{HCN1-0}-L_{IR} correlation was found to be linear for both nearby normal galaxies and distant starburst galaxies, suggesting the star formation efficiency is constant in these different systems in terms of the dense gas. A similar trend has been found in the study of Galactic massive core with CS and dust emission (Shirley et al. 2003, Mueller et al. 2002). A better test for this correlation is to map the massive cores with HCN directly.

My work for this thesis is largely based on a series of surveys of spectral lines and a mapping survey with HCN and CS toward a large sample of massive star-forming cores, as well as a mapping survey on low-mass cores with 350 μm continuum emission. We already have 350 μm maps of the massive cores

and had modeled them with continuum model (Mueller et al. 2002), but no models with molecular lines had been made. The molecular line and mapping surveys will help to model molecular emission in massive cores. For low-mass cores, we have modeled them with many molecular lines (e.g. Young et al. 2004, Evans et al. 2005), but no 350 μm data have been taken. So I made a mapping survey in 350 μm towards a sample of low-mass dense cores to constrain the continuum model. These works, especially the works on massive cores, can not directly answer many questions raised above for massive star formation, but they do make progress on the right way to solve some of them.

The chapters of the thesis include five individual papers; two have been published (Chap. 2, Wu & Evans 2003, and Chap. 6, Wu et al. 2005), and three (Chap. 3, Chap. 4 and chap. 5) are in preparation. The first paper (Chap. 2) introduces a line survey with HCN 3-2 towards 28 massive star forming cores. In the survey we discovered that a large fraction of cores show characteristic blue asymmetric line profile that indicates infall, showing that HCN 3-2 is a good infall tracer in massive dense cores. The survey provides the first strong indication of global collapse in high-mass star-forming regions by a systematic survey. In the second paper (Chap. 3), we present the results of our mapping survey on more than 50 massive cores with multiple HCN and CS transitions. The core properties were obtained, and the difference between different tracers are discussed. In the third paper (Chap. 4), we attempt to model the massive cores with collapse or static models using an 1D Monte Carlo simulation, and an empirical chemical model. Chapter 5 describes the

survey of 53 low-mass dense cores with a submillimeter continuum bolometer (SHARCII). The survey is a follow-up project to the Spitzer Legacy Program "From Molecular Cores to Planet-Forming Disks", with the purpose being to create a complete data set of nearby low-mass dense cores from the infrared to the submillimeter. This is the only work in which I deal with low-mass star formation in my PhD studies, which gives me experience in the low-mass field. In Chapter 6, we report the discovery of a linear L_{HCN1-0}-L_{IR} correlation that extends from galaxies scale to Galactic scale, with nearly the same ratio of infrared luminosity to HCN luminosity found over 7-8 orders of magnitude in L_{IR}, with a lower cutoff around $10^{4.5}$ $L_{\odot}$ of infrared luminosity. The linear correlation suggests that we may understand distant star formation in terms of the known properties of local star-forming regions. A summary of the thesis is given in Chapter 7.

Chapter 2

Indications of Inflow Motions in Regions Forming Massive Stars

2.1 Abstract

Observational evidence for inflowing motions in massive star forming regions has been extremely rare. We have made a spectroscopic survey of a sample of 28 massive star forming cores associated with water masers. An optically thick line of HCN 3−2 was used in combination with optically thin lines ($H^{13}CN$ 3−2 or $C^{34}S$ 5−4, 3−2, and 2−1), to identify "blue" line profiles that can indicate inflow. Comparing intensities for 18 double-peaked line profiles yields 11 blue and 3 red profiles that are statistically significant. In the full sample of 28 sources, 12 show blue profiles and 6 show red profiles that are statistically significant based on the velocity offsets of lines that are optically thick from those that are optically thin. These results indicate that HCN $3-2$ emission may trace inflow in regions forming high-mass stars.

2.2 Introduction

Gravitational collapse is a widely accepted theoretical explanation of star formation, but the observational evidence for collapse has long been con-

troversial (e.g., Evans 1991, Myers et al. 2000). The major difficulty is that collapse proceeds at a relatively low velocity and is easily masked by other motions (e.g., outflows, rotation and turbulence) in the cloud cores. A general prediction of collapse models is a "blue profile," a line asymmetry with the peak skewed to the blue side in optically thick lines, while an optically thin line must peak at the absorption part (usually a dip) of the optically thick line to rule out the possibility of two velocity components.

For an individual source, one must exclude rotation or outflow blobs as the source of the blue profile by mapping the source. However, the predominance of blue profiles in a survey, based on some objective criteria, can be an indication that inflow is a statistically likely explanation. We use the term "inflow" to distinguish evidence of inflowing motions from a claim of gravitational collapse or infall. A profile that survives these tests provides a strong indication of inflow, and the source can be seen as a collapse candidate. To become a credible example of gravitational collapse, gravity must be a plausible source of the motions, and the line profiles should agree with some detailed model (Evans 2003).

Progress has been made in the last decade in studying low mass star forming regions, triggered by the observation of blue profiles toward B335 in lines of H_2CO and CS and later the fitting (Zhou 1993, 1994, Choi et al. 1995) of these lines with an inside-out collapse model (Shu 1977). Systematic surveys have been made and predominantly blue profiles have been found toward Class 0 (Gregersen et al. 1997, Mardones et al. 1997), Class I (Gregersen et al.

2000), and Class −1 (also known as pre-protostellar cores) sources (Gregersen & Evans 2000, Lee, Myers, & Tafalla 1999, 2001). Evidence of collapse has been increasingly accepted in low mass star forming regions.

Evidence of inflow has been elusive in massive star forming regions, partly because of the extremely complex and turbulent environment in massive clouds. Spectral inflow signatures have been reported in a few sources including NGC 2264 IRS (Wolf-Chase & Gregersen 1997), W49 (Welch et al. 1988, Dickel & Auer 1994), G10.6-0.4 (Keto et al. 1988) and W51 (Zhang & Ho 1997, Zhang et al. 1998). However, surveys have not revealed statistical evidence of inflow (e.g., Williams & Myers 1999).

The characteristic blue profile will appear only if the molecular tracer has a suitable optical depth and critical density. For example, using moderately opaque tracers H_2CO and CS, which are good tracers of blue profiles in Class 0 sources, Mardones et al. (1997) found a low fraction of blue profiles in a sample of Class I sources. With a more opaque line of HCO^+ 3−2, Gregersen et al. (2000) detected a blue fraction in Class I sources comparable to that in Class 0 sources. The inflow tracers used in low mass cores may no longer be suitable to probe inflow motion in high mass cores, which are typically 100 times denser at a given radius than low mass cores (Mueller et al. 2002). In a recent survey for blue profiles in high mass star forming regions, Williams & Myers (1999) used CS 2−1 (critical density n_c is $3.9\times\ 10^5$ cm^{-3} at $T_K = 100$ K) as the optically thick line. Three out of 19 sources showed self-absorption features, 1 of which had a blue profile. We have used the HCN 3−2 line, which

may be more opaque in denser regions ($n_c = 6.8 \times 10^7$ cm^{-3} at $T_K = 100$ K) than CS $2-1$.

2.3 Observations

The sample is a subset of a larger sample of dense cores associated with H_2O masers that have been surveyed with several CS transitions (Plume et al. 1992, 1997) and mapped in CS and dust emission (Shirley et al. 2003, Mueller et al. 2002). The sources mapped in CS 5-4 (Shirley et al. 2003) have virial masses within the nominal core radius (R_{CS}) ranging from 30 $M_\odot$ to 2750 $M_\odot$, with a mean of 920 $M_\odot$. That sample was selected to have CS $7-6$ emission with $T_R^* \geq 1$ K. The sample for HCN observations was selected randomly from the sample in Shirley et al. (2003), trying to cover all the range of mass in that sample. This sample has a mean virial mass of 800 $M_\odot$. We used HCN $3-2$ lines as the optically thick lines. $H^{13}CN$ $3-2$, or $C^{34}S$ $5-4$, $3-2$, and $2-1$ lines were used as optically thin lines. For comparison, CS $5-4$ lines were also taken from our previous observations (Shirley et al. 2003).

All observations except the $C^{34}S$ $2-1$ and $3-2$ lines were made at the 10.4 m telescope at the Caltech Submillimeter Observatory [1] (CSO). The $C^{34}S$ $2-1$ and $3-2$ data were taken from observations (Plume et al. 1997) at the IRAM 30-m telescope at Pico Veleta, Spain. The observing date, line frequency, beam size, main beam efficiency and velocity resolution of each line

[1]The CSO is operated by the California Institute of Technology under funding from the National Science Foundation, contract AST 90-15755.

Table 2.1 Observing Parameters for observed lines

Line	Date (UT)	ν^a (GHz)	θ_{mb} ($''$)	η_{mb}	v_{res} (kms^{-1})
HCN 3−2	2002 Jun	265.886434	28.1	0.64	0.11
HCN 3−2	2002 Dec	265.886434	28.1	0.60	0.11
$H^{13}CN$ 3−2	2002 Dec	259.011814	28.9	0.60	0.11
$H^{13}CN$ 3−2	2003 May	259.011814	28.9	0.58	0.17
$C^{34}S$ 5−4	2001 Jul	241.016089	31.0	0.73	0.12
$C^{34}S$ 2−1	1991 Apr,Oct	96.4129495	25.0	0.60	0.31
$C^{34}S$ 3−2	1990 Jun	144.617101	17.0	0.60	0.21
CS 5−4	1997 Apr	244.935557	24.5	0.56	0.12

Note. — ^{a}:The rest frequencies of HCN 3-2 and $H^{13}CN$ 3−2 have been updated according to Ahrens et al. (2002). Those of CS and $C^{34}S$ have been updated according to Gottlieb et al. (2003).

are listed in Table 2.1. The rest frequencies of HCN $3-2$, $H^{13}CN$ $3-2$, and $C^{34}S$ lines have been updated (Ahrens et al. 2002, Gottlieb et al. 2003) after our observations. We have corrected our data to the new frequencies listed in Table 2.1. The position switching mode was used; offset positions were checked for HCN emission and found to be clear ($T_A^* < 0.5$ K). Pointing was checked periodically using planets and CO-bright stars. The pointing accuracy was better than $6''$.

2.4 Results

Table 2.2 lists our sources with their observed and derived parameters. Self-absorption features appeared in many sources. We characterize the line profiles by v_{thick}, the velocity at the peak of the HCN $3-2$ line, v_{thin}, the velocity at the peak of the optically thin tracer, and Δv_{thin}, the linewidth of the thin tracer. Values were measured with a cursor or from a Gaussian fit, as appropriate. Moving clockwise from the lower left, Figure 2.1 illustrates the sample's range from a clearly blue profile (a) to a red profile (d).

A blue profile is a rather general feature of inflowing motion, but it only arises for the right combination of critical density and opacity of the line. It is predicted for velocity fields that decrease with radius, as in inside-out collapse models (Zhou & Evans 1994), but also for more general velocity fields (e.g., Myers et al. 1996). In a simple model with two uniform layers approaching each other (Myers et al. 1996), the shape of the profile is affected by both the optical depth of the line and the inflow velocity of the front layer (Myers et al. 2000). In the most opaque sources, as shown in Figure 2.1(a), both HCN 3−2 and CS 5−4 lines show a blue profile, but the HCN 3−2 line presents deeper absorption. As opacity drops, only HCN shows an absorption dip, as seen in Fig 2.1(b), and the less opaque CS 5−4 line becomes a single peak with a red shoulder. If the inflow velocity is high enough, the red peak disappears, leaving only a flat wing as seen in Fig 2.1(c).

The ratio of the blue peak to red peak $[T_R^*(B)/T_R^*(R)]$ is one measure of the line asymmetry. A "blue profile" should have a stronger blue peak

Table 2.2. Observed and derived parameters [a] for HCN 3-2 survey

Source	R.A. (1950.0)	Decl. (1950.0)	dist (kpc)	v_{thick} [b] (km s^{-1})	v_{thin} [c] (km s^{-1})	Δv_{thin} [d] (km s^{-1})	δv	Prof[e]	$T_R^*(B)/T_R^*(R)$
RCW142	17 47 04.5	−28 53 42	2.0	14.27(05)	17.24(05)[2]	5.60(12)	−0.53(02)	B	4.18(69)
W28A2(1)	17 57 26.8	−24 03 54	2.6	10.55(05)	9.17(08)[1]	6.68(21)	0.21(01)		...
M8E	18 01 49.1	−24 26 57	1.8	12.26(05)	10.65(10)[1]	3.34(27)	0.48(05)	R	0.95(08)
9.62+0.10	18 03 16.0	−20 32 01	7.0	7.11(06)	5.29(09)[1]	5.89(26)	0.31(02)	R	0.26(04)
10.60−0.40	18 07 30.7	−19 56 28	6.5	−6.51(05)	−4.51(08)[1]	6.93(18)	−0.29(01)	B	2.28(13)
19.61-0.23	18 24 50.1	−11 58 22	4.0	40.52(05)	42.16(15)[3]	7.18(29)	−0.23(02)		1.61(42)
23.95+0.16	18 31 40.8	−07 57 17	5.8	78.75(17)	80.15(09)[2]	2.39(22)	−0.59(11)	B	1.17(25)
W43S	18 43 26.7	−02 42 40	8.5	96.83(05)	98.17(08)[1]	6.00(23)	−0.22(02)		1.68(15)
W44	18 50 46.1	+01 11 11	3.7	54.46(05)	57.20(08)[1]	5.78(10)	−0.47(01)	B	3.31(31)
35.58-0.03	18 53 51.4	+02 16 29	10.2	53.79(06)	54.04(15)[3]	5.16(27)	−0.05(03)		...
48.61+0.02	19 18 13.1	+13 49 44	11.8	17.87(05)	18.03(11)[2]	2.34(21)	−0.07(05)		...
59.78+0.06	19 41 04.2	+23 36 42	2.2	21.89(05)	22.63(07)[2]	2.21(23)	−0.33(05)	B	...
S88B	19 44 42.0	+25 05 30	2.1	22.30(11)	21.42(05)[2]	2.36(13)	0.37(05)	R	...
ON2S	20 19 48.9	+37 15 52	5.5	−0.05(05)	−0.90(06)[2]	3.65(14)	0.23(02)		...
W75N	20 36 50.5	+42 27 01	3.0	11.70(10)	9.26(08)[1]	5.47(07)	0.45(02)	R	0.71(04)
DR21S	20 37 13.8	+42 08 52	3.0	−5.68(05)	−2.18(10)[4]	4.38(13)	−0.80(03)	B	1.99(11)
W75(OH)	20 37 14.0	+42 12 12	3.0	−6.01(05)	−3.32(08)[1]	5.95(17)	−0.45(04)	B	1.29(06)
CEPA	22 54 19.2	+61 45 44	0.7	−12.42(13)	−10.39(09)[2]	3.68(19)	−0.55(05)	B	1.06(07)
S158	23 11 36.1	+61 10 30	2.8	−59.46(11)	−56.23(12)[1]	6.15(29)	−0.53(03)	B	1.78(20)
S157	23 13 53.1	+59 45 18	2.5	−45.05(11)	−43.82(10)[4]	2.56(20)	−0.48(07)	B	1.39(33)
121.30+0.66	00 33 53.3	+63 12 32	1.2	−18.55(05)	−17.77(09)[1]	3.09(23)	−0.25(04)		1.33(14)
123.07−6.31	00 49 29.2	+56 17 36	2.2	−32.67(05)	−30.84(11)[1]	4.68(28)	−0.39(04)	B	1.27(28)
W3(OH)	02 23 17.3	+61 38 58	2.4	−49.39(05)	−46.85(08)[1]	5.18(20)	−0.49(03)	B	1.44(15)
136.38+2.27	02 46 11.7	+61 47 34	4.5	−42.18(18)	−42.35(10)[4]	2.03(16)	0.08(10)		...
S231	05 35 51.3	+35 44 16	2.3	−14.22(05)	−16.41(05)[1]	3.72(14)	0.59(03)	R	0.34(07)
S235	05 37 31.8	+35 40 18	1.6	−17.26(05)	−17.44(04)[1]	2.73(10)	0.07(02)		...
S252A	06 05 36.5	+20 39 34	1.5	9.90(05)	9.10(06)[1]	2.57(14)	0.31(04)	R	....
S255/7	06 09 58.2	+18 00 17	1.3	6.80(10)	6.98(10)[4]	2.57(10)	-0.07(06)		...

Note. — [a]: Distances are taken from Shirley et al. (2003) and Mueller er al. (2002).
[b]:v_{thick} is the velocity of the peak of the optically thick line, in this case HCN 3−2. [c]: v_{thin} is the velocity of the peak of the optically thin line, whether $H^{13}CN$ 3−2 or $C^{34}S$ 5−4, 2−1, and 3−2, indicated by 1, 2, 3 and 4 respectively. [d]: FWHM of the optically thin line. [e]: Profile of the line judged from δv. B denotes blue profile and R denotes red profile.

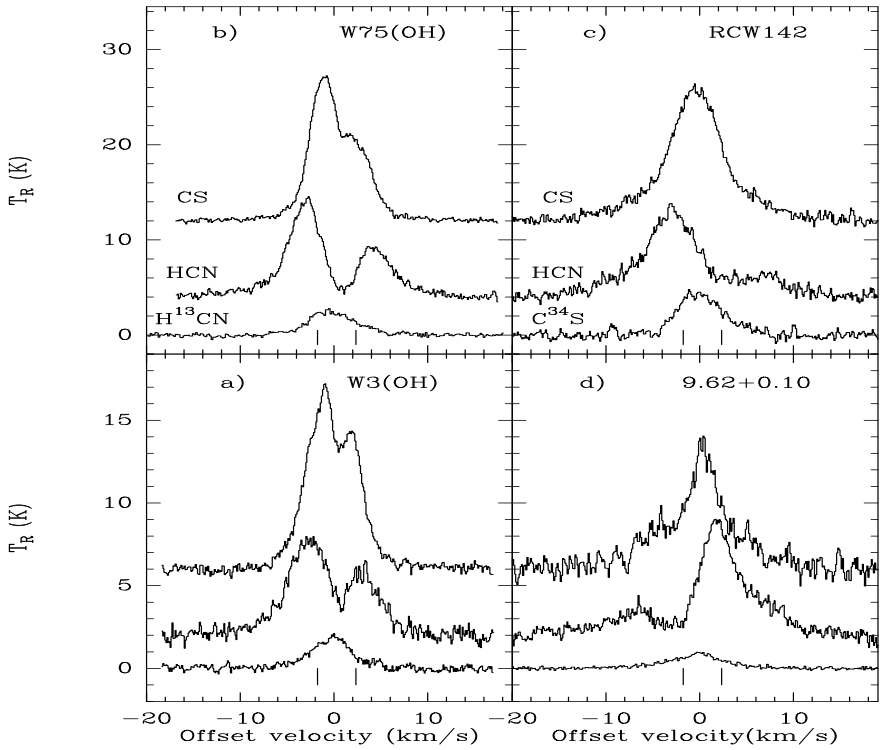

Figure 2.1 Line profiles of HCN $3-2$ (middle lines), CS $5-4$ (upper lines) and optically thin lines (lower lines, $H^{13}CN$ $3-2$ for a), b), d) and $C^{34}S$ $5-4$ for c). HCN $3-2$ and CS $5-4$ lines have been displaced upward for clarity. All lines are plotted with the velocity relative to the optically thin line's central velocity. The two vertical lines below the spectra indicate the location of the outermost hyperfine components of the HCN $3-2$ line. The radiation temperature T_R has been corrected for main beam efficiency.

than red peak: $T_R^*(B)/T_R^*(R) > 1$ by a statistically significant amount. We calculated these ratios for the 18 sources with double-peaked spectra, as listed in Table 2.2. Eleven sources have a ratio of blue to red significantly greater than unity, and 3 have a ratio significantly less than unity; the other four cases

do not differ from unity by more than 1σ. The overall trend is a sign of the blue predominance in the sample.

Not all line profiles from collapsing cores will show 2 peaks; some will appear as lines skewed to the blue or lines with red shoulders. An alternative definition (Mardones et al. 1997) is useful for these cases as well. A line can be identified as a blue profile if the peak of the optically thick line is shifted blueward, with the velocity difference between the peaks of the optically thick line and the optically thin line greater than a quarter of the linewidth of the optically thin line: $\delta v = (v_{thick} - v_{thin})/\Delta v_{thin} < -0.25$. A red profile would have $\delta v > 0.25$. The calculated δv for our sample are listed in 2.2. Twelve blue profiles and 6 red profiles were identified by this method, with statistically significant ($\geq 1\sigma$) values of δv. The distributions of $T_R^*(B)/T_R^*(R)$ and δv are presented in Figure 2.2, which clearly shows the blue profile predominance.

The concept of the "excess" was introduced by Mardones et al. (1997) to quantify the statistics of the line asymmetry in a survey: $E = (N_{blue} - N_{red})/N_{total}$, where N_{blue} and N_{red} are the numbers of blue and red profiles in the total sample of N_{total} sources (28 in the present case). Using the line ratios or the δv measure, the excesses in our sample are $E = 0.29$ and 0.21, respectively. For comparison, surveys of low mass star forming regions with HCO^+ $3-2$ found $E = 0.30$, 0.31 and 0.31 for Class -1, Class 0 and Class I samples, respectively (Evans 2003). Although a single line with a blue profile may be explained by outflow or rotation, a large sample with a random distribution of angles between the outflow or rotation axis and the line of sight

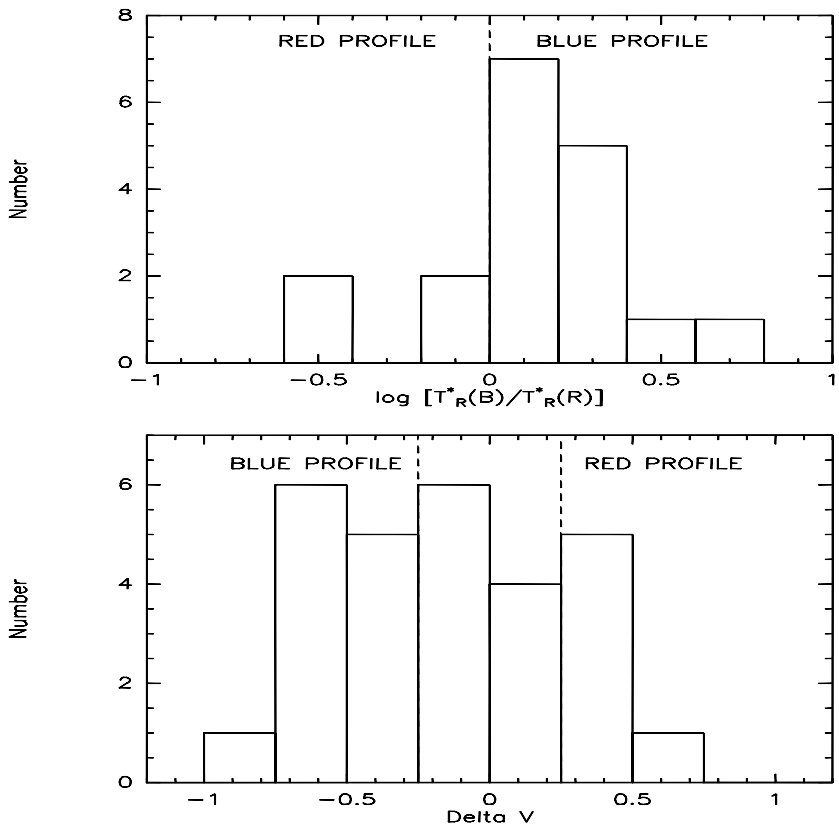

Figure 2.2 Distribution of $\log[T_R^*(B)/T_R^*(R)]$ for the 18 double-peaked sources (top plot) and distribution of δv for all the 28 sources in the sample (bottom plot). Note that only 11 of the 14 blue and 3 of the 4 red sources in the top plot have ratios greater or less than unity by more than 1 σ.

should result in a zero excess. A significant excess in a sample is statistical evidence of inflow. The probability that the observed number of blue and red sources could result from random sampling of a distribution that actually has equal numbers in blue and red bins, with the total equal to the actual total, is 0.03 for the intensity criterion and 0.16 for the δv criterion. The statistical sig-

nificance is similar to that found for studies of low-mass regions by Gregersen et al. (2000).

2.5 Discussion

Before accepting the inflow interpretation, we should examine other possible explanations for the line profiles. One possibility is that another molecular line contributes to the blue peak. The mean shift of the peak for the 12 blue profiles, $\langle v_{thick} - v_{thin} \rangle = -2.18 \pm 0.86$ km s^{-1}. Examination of transition catalogs revealed only two lines within ± 5 km s^{-1} of the HCN line that have energies above ground corresponding to less than 300 K: a line of glycolaldehyde shifted by -0.4 km s^{-1}; and a line of c-SiC_3 shifted by $+1.45$ km s^{-1}. Neither of these is likely to contribute significantly to the observed line profile. Accurate information on the hyperfine structure of the HCN $3-2$ transition has been reported recently (Ahrens et al. 2002). The stronger components are all within 0.3 km s^{-1} of the line center; the two outer hyperfine components ($F = 2-2$ and $3-3$) lie at -2.35 and 1.75 km s^{-1}, respectively. These outer components could affect the line profiles, but they have the same intrinsic line strengths, at 0.037 of the total line strength. Ahrens et al. (2002) found the blue-shifted component ($F = 2-2$) to be anomalously *weak* in their observations of TMC-1. Thus, it seems unlikely that this component is contributing strongly to the blue peak, but it remains a remote possibility.

For 13 sources where $H^{13}CN$ is not available we used $C^{34}S$ as the optically thin line. Based on the 9 sources for which we have both $H^{13}CN$ 3-2

and $C^{34}S$ 5-4 lines, the center velocity of $H^{13}CN$ 3-2 has a mean shift of -0.30 km s^{-1} relative to the center of the $C^{34}S$ 5-4 line, but the linewidth of the $H^{13}CN$ line is 1.24 times that of the $C^{34}S$ line. These facts suggest that the $H^{13}CN$ 3-2 is not optically thin, and using it might make it harder to detect blue profiles. Indeed, using the $C^{34}S$ lines instead added two blue sources in the δv statistic, yielding an excess of 0.29, identical to that for the line ratio method. We conclude that the choice of optically thin line does not have a major effect on our statistics, but we have made a conservative choice by using $H^{13}CN$ lines where possible.

The self-absorption feature appears as long as the column density is high enough (log N(CS)$\geq$ 14.3 for this sample). While HCN $3-2$ works well for such dense, opaque cores, a different tracer may be needed for regions of lower column density. The two-layer model predicts that $|\delta v|$ should increase with optical depth (see Fig. 2 of Myers et al. 1996). We observe that $|\delta v|$ increases with log N(CS), though the correlation is weak. The relation between $|\delta v|$ and column density supports the idea that the blue profile only appears when the line has a suitable optical depth and critical density. The excesses based on the δv test for the CS $5-4$ and $2-1$ lines in this sample are $E = -0.04$ and 0.05, respectively. These negligible excesses are expected if the CS lines are less opaque in the inflow region.

The current work is only a promising indication that inflow in regions forming massive stars may be studied using HCN $3-2$ lines. The sources in this sample span a wide range of distances; even if inflow motions are present,

they may be related to formation of individual stars in nearby regions and formation of a cluster in more distant regions. In future work, we will extend the sample to sources with smaller column density. Maps will be made to test whether the blue profile peaks toward the center or whether it is associated with outflows. Sources that pass that test will become collapse candidates. Using the models of density and temperature established by observations of dust emission on the same sources (Mueller et al. 2002), we could then test some models of collapse to learn whether we are finally seeing gravitational infall in massive cores.

Chapter 3

Mapping Surveys of High-Mass Star-Forming Cores with HCN and CS

3.1 Introduction

Most of stars in our Galaxy form in regions where high-mass stars are forming (Elmegreen 1985, Carpenter 2000, Lada & Lada 2003). Despite its importance, the study of massive star formation remains a less developed field, in contrast to the progress made in the study of low mass star-formation in both theoretical and observational aspects. The major difficulties for studying the massive star formation are that these regions are usually quite distant, and their environment is more complex than the low mass case. Although many methods commonly used in analyzing low mass star forming regions fail to apply to the high mass case, masers and some chemical signatures may prove to be possible ways to trace the early stages of massive star formation (Evans 2003). Studies of a large sample of such massive cores that are associated with masers may be a good start to study the statistical properties of massive star forming regions.

The UT star formation group has been studying the early stages of massive star formation by exploring a big sample of massive dense cores associated

with water masers, which has been observed with multiple CS transitions (CS 2-1, 3-2, 5-4, and $C^{34}S$ lines, Plume et al. 1992, 1997). Using the LVG code, the mean densities of these cores were obtained; the density in these massive cores is very high ($\sim 10^6 cm^{-2}$). A subsample of these sources have been further studied with the maps of CS 5-4 transitions and 350 μm dust continuum (Shirley et al. 2003, Mueller et al. 2002); both are good tracers for dense molecular cores. Based on the dust continuum data, a 1D model has been built to explore the mass and density distribution of those massive cores (Mueller et al. 2003).

The next step is to set up physical models for these cores, constrained by both continuum and molecular line emission, to fully understand the physical and dynamical properties of massive star forming regions. More molecular lines that can trace dense cores, as well as their maps, are needed for this purpose. We decided to use HCN, which is another dense gas tracer like CS, to probe these massive cores. HCN may be a even better tracer than CS to reveal the dynamical information in massive cores, since our initial survey with HCN 3-2 found a larger fraction of sources showing spectral infall signatures (Wu & Evans 2003).

Both HCN and CS have been used to study star formation in other galaxies. Recent work (Gao & Solomon 2004a,b) shows that the luminosity of HCN (1-0) has a tight and linear correlation with infrared luminosity, for both nearby normal galaxies and distant starburst galaxies, suggesting that star formation efficiency may be constant in these different systems measured

against tracers of the dense gas. Massive star-forming regions are the potential link to connect star formation from the Galaxy to distant galaxies, since they are the only regions that are bright enough to be seen in remote galaxies, and we can study them in detail in the local Universe. We can test this L_{HCN}-L_{IR} correlation on the Galactic scale, by mapping HCN in massive cores to get the total HCN luminosity. By comparing HCN observations and the derived properties of Galactic massive cores derived from CS, we may be able to apply our knowledge of Galactic star formation to star formation in distant galaxies.

In order to set up a complete database to study the physical conditions of massive star forming regions, to constrain the simulation to model individual massive cores, and to connect star formation to extragalactic scales, we have carried out a mapping survey on a large sample of massive star forming cores, with multiple HCN and CS transitions. In this Chapter we report the results of these surveys.

3.2 Observations

The sample in the survey is a subset of a larger sample of dense cores associated with H_2O masers that have been surveyed with several CS transitions (Plume et al. 1992, 1997), most of which have been mapped with CS and dust emission (Shirley et al. 2003, Mueller et al. 2002). Table 3.1 lists the information on sources that have been mapped in this survey. The sources mapped in CS 5-4 (Shirley et al. 2003) have virial masses within the nominal core radius (R_{CS}) ranging from 30 $M_\odot$ to 2750 $M_\odot$, with a mean of 920 $M_\odot$.

The sources in this category have infrared luminosities ranging from 10^3 - 10^7 $L_\odot$ and most contain compact or ultracompact H II (UCHII) regions. These cores are massive, and they have been well explored by our group; we will focus on these sources for statistical studies of the properties of massive cores. To extend the sample towards lower luminosities for the study of L_{HCN}-L_{IR} correlation, we selected 14 IRAS sources from outflow surveys (Zhang et al. 2005; Wu et al. 2004) and a few lower mass cores from other publications. These sources are listed in part 2 of Table 3.1, separated by a line from the well studied massive cores in Table 3.1. These cores have various luminosities; in this paper they are not included in our statistics of the properties of massive cores.

Table 3.1. Mapping surveys towards massive cores [a]

Source	α (1950.0)	δ (1950.0)	dist kpc	ref. [b]	CS $2 \rightarrow 1$	CS[c] $5 \rightarrow 4$	CS $7 \rightarrow 6$	HCN $1 \rightarrow 0$	HCN $3 \rightarrow 2$	350 μm [d] SHARC
G121.30+0.66	00 33 53.3	63 12 32	1.2	1	M	M	M	M	M	M
G123.07-6.31	00 49 29.2	56 17 36	2.2	2	M	M	M	M	M	M
W3(2)	02 21 53.1	61 52 20	2.4	18						M
W3(OH)	02 23 17.3	61 38 58	2.4	3	M	M	M	M	M	M
GL490	03 23 38.9	58 36 33	0.9	17					M	M
S231	05 35 51.3	35 44 16	2.3	2	M	M	M	M	M	M
S235	05 37 31.8	35 40 18	1.6	2	M	M	M	M	M	M
S241	06 00 40.9	30 14 54	4.7	2	M	M		M	M	M
MonR2	06 05 21.6	−06 22 28	0.9	1					M	M
S252A	06 05 36.5	20 39 34	1.5	2	M	M	M	M	M	M
S255	06 09 58.3	18 00 12	1.3	2	M	M	M	M	M	
RCW142	17 47 04.1	−28 53 42	2.0	5	M	M	M	M	M	M
W28A2(1)	17 57 26.8	−24 03 54	2.6	5,6	M	M	M	M		M
M8E	18 01 49.1	−24 26 57	1.8	2	M	M	M	M	M	M
G9.62+0.10	18 03 16.0	−20 32 01	7.0	7	M	M	M	M	M	M
G8.67−0.36	18 03 18.6	−21 37 59	4.5	8	M	M	M	M	M	M
W31 (1)	18 05 40.4	−19 52 21	12.0	4		M	M			
G10.60−0.40	18 07 30.7	−19 56 28	6.5	9	M	M	M	M	M	M
G12.42+0.50	18 07 56.4	−17 56 37	2.1	10	M	M		M		M
G12.89+0.49	18 08 56.3	−17 32 16	3.5	8	M	M	M		M	M
G12.21−0.10	18 09 43.7	−18 25 09	13.7	11	M	M	M	M		M
W33cont	18 11 18.3	−17 56 21	4.1	9		M	M			
G13.87+0.28	18 11 41.5	−16 46 34	4.4	12	M	M	M	M		M
W33A	18 11 44.0	−17 53 09	4.5	5		M	M			M
G14.33−0.64	18 16 00.8	−16 49 06	2.6	8		M	M		M	M
G19.61−0.23	18 24 50.1	−11 58 22	4.0	4	M	M	M	M	M	M
G20.08−0.13	18 25 22.6	−11 30 45	3.4	7		M	M			
G23.95+0.16	18 31 40.8	−07 57 17	5.8	9	M	M	M	M		M
G24.49−0.04	18 33 22.8	−07 33 54	3.5	1		M	M			M
W42	18 33 30.3	−07 14 42	9.1	13		M	M			
G28.86+0.07	18 41 07.9	−03 38 41	8.5	5		M				
W43S	18 43 26.7	−02 42 40	8.5	4,14	M	M	M	M	M	M
G31.41+0.31	18 44 59.5	−01 16 07	7.9	12		M	M			M

Table 3.1 (cont'd)

Source	α (1950.0)	δ (1950.0)	dist kpc	ref. [b]	CS $2 \rightarrow 1$	CS[c] $5 \rightarrow 4$	CS $7 \rightarrow 6$	HCN $1 \rightarrow 0$	HCN $3 \rightarrow 2$	350 μm [d] SHARC
W43 Main3	18 45 11.2	−01 57 57	6.8	4		M	M			
G31.44−0.26	18 46 57.5	−01 32 33	10.7	9		M	M			
G32.05+0.06	18 47 02.0	−00 49 19	8.5	9		M	M			
G32.80+0.20	18 47 57.3	−00 05 28	15.6	13		M	M			
W44	18 50 46.1	01 11 11	3.7	9	M	M	M	M	M	
S76E	18 53 45.6	07 49 16	2.1	1		M				M
G35.58−0.03	18 53 51.4	02 16 29	3.5	13	M	M	M	M		M
G35.20−0.74	18 55 40.8	01 36 30	3.3	9		M	M			
W49N	19 07 49.8	09 01 17	14.0	4	M	M	M	M		
W49S	19 09 58.2	09 00 03	14.0	4		M	M			
OH43.80−0.13	19 09 31.2	09 30 51	2.7	13		M				
G45.07+0.13	19 11 00.3	10 45 42	9.7	13	M	M	M	M	M	M
G48.61+0.02	19 18 13.1	13 49 44	11.8	1	M	M	M	M	M	M
W51W	19 20 53.3	14 20 47	7.0	17		M	M			
W51M	19 21 26.2	14 24 36	7.0	17	M	M	M	M	M	
G59.78+0.06	19 41 04.2	23 36 42	2.2	1	M	M		M		
S87	19 44 14.0	24 28 10	1.9	15	M	M		M		M
S88B	19 44 42.0	25 05 30	2.1	2	M	M	M	M	M	M
K3-50	19 59 50.1	33 24 17	9.0	4	M	M		M		
ON 1	20 08 09.9	31 22 42	6.0	1	M	M	M	M		M
ON 2S	20 19 48.9	37 15 52	5.5	1	M	M	M	M	M	M
ON 2N	20 19 51.8	37 17 01	5.5	1		M	M			
S106	20 25 32.8	37 12 54	4.1	16	M	M	M	M		M
W75N	20 36 50.5	42 27 01	3.0	4	M	M	M	M		
DR21 S	20 37 13.8	42 08 52	3.0	4	M	M	M	M	M	
W75(OH)	20 37 14.1	42 12 12	3.0	4	M	M	M	M	M	
G97.53+3.19	21 30 37.0	55 40 36	7.9	1		M			M	M
BFS 11-B	21 41 57.6	65 53 17	2.0	5		M	M			M
CepA	22 54 19.2	61 45 44	0.73	17	M	M		M	M	M
S158	23 11 36.1	61 10 30	2.8	2	M	M		M	M	M
S158A	23 11 36.7	61 11 51	2.8	2	M	M		M	M	M
NGC7538-IRS9	23 11 52.8	61 10 59	2.8	2	M			M	M	M
S157	23 13 53.1	59 45 18	2.5	2	M	M	M	M	M	M

We mapped massive cores with HCN 3-2, HCN 1-0, CS 7-6, and CS 2-1 transitions. Maps of each transition usually didn't cover all sources in our sample, but we have attempted to map as many sources as possible in all the tracers. Beside maps, we also observed the optically thin isotopes of HCN and CS ($H^{13}CN$ 3-2 and $C^{34}S$ 5-4) at the center position of most of these massive cores to constrain models and to study infall in massive cores.

Observations were taken between 1996 to 2006, with information presented in Table 3.2. Maps of HCN 1-0 and CS 2-1 were made with the 14-m telescope of the Five College Radio Astronomy Observatory (FCRAO). The 16-element focal plane array (SEQUOIA) was used, with typical system temperatures 100-200K. A velocity resolution of 0.1 km/s was achieved with the 25 MHz bandwidth on the dual channel correlator (DCC). We convert the measured T_A^* to T_R via $T_R = T_A^*/(\eta_{FSS}\eta_c)$, with $\eta_{FSS} = 0.7$. The value of η_c depends on source size; for the typical map in this study ($\sim 10'$), $\eta_C = 0.7$. The map size was extended until the edge of the HCN $J = 1 \rightarrow 0$ and CS $J = 2 \rightarrow 1$ emission was reached, typically at the 2σ level (mean $\sigma \sim 0.3$ K km/s), so we could get the total line luminosity.

All the other observations were made at the 10.4 m telescope at the Caltech Submillimeter Observatory [1] (CSO). The observing date, line frequency, beam size, main beam efficiency of each line are listed in Table 3.2. The rest frequencies of HCN $3-2$, $H^{13}CN$ $3-2$, and $C^{34}S$ 5-4 lines have been updated

[1]The CSO is operated by the California Institute of Technology under funding from the National Science Foundation, contract AST 90-15755.

Table 3.1 (cont'd)

Source	α (1950.0)	δ (1950.0)	dist kpc	ref. [b]	CS $2 \rightarrow 1$	CS[c] $5 \rightarrow 4$	CS $7 \rightarrow 6$	HCN $1 \rightarrow 0$	HCN $3 \rightarrow 2$	350 μm [d] SHARC
IRAS19094+0944	19 09 29.2	09 44 42	6.11	19	M			M		
IRAS20050+2720	20 05 02.5	27 20 09	0.73	19	M			M	M	
IRAS20106+3545	20 10 38.0	35 45 42	1.64	19	M			M		
IRAS20126+4104	20 12 40.1	41 04 21	4.18	19	M			M		
IRAS20188+3928	20 18 50.8	39 28 18	0.31	19	M			M		
IRAS20216+4107	20 21 38.0	41 07 56	1.70	20	M			M	M	
IRAS20220+3728	20 22 03.6	37 28 25	4.49	19	M			M		
IRAS20333+4102	20 33 21.4	41 02 53	1.6	19	M			M		
IRAS21391+5802	21 39 10.3	58 02 29	0.75	19	M			M		
IRAS22172+5549	22 17 17.7	55 49 40	2.87	19	M			M		
IRAS22198+6336	22 19 50.7	63 36 33	1.28	19	M			M		
IRAS23011+6126	23 01 10.0	61 26 16	0.73	20	M			M	M	
IRAS23385+6053	23 38 30.1	60 53 43	6.94	19	M			M		
IRAS03282+3035	03 28 15.2	30 35 14	0.22	21	M			M		
L483	18 14 50.6	-04 40 49	0.20	22					M	
L1251B	22 37 40.8	74 55 50	0.30	23	M			M		

[a] "M" in the table indicates that the source has been mapped in this transition

[b] 1. R_N Plume et al. 1992, 2. Blitz et al. 1982, 3. Harris & Wynn-Williams 1976, 4.Genzel & Downes 1977, 5. Braz & Epchtein 1983, 6. Chini et al. 1986, 7. Hofner et al. 1996, 8. Val'tts et al. 2000, 9. Solomon et al. 1987, 10. Zinchecnko et al. 1994, 11. Hunter et al. 2000, 12. Churchwell et al. 1990, 13. Downes et al. 1980, 14. Wood & Churchwell 1989, 15. Brand & Blitz 1993, 16. Wink et al. 1982, 17. Zhou et al. 1996, 18. Plume et al. 1997, 19. Zhang et al. 2005, 20. Wu et al. 2004, 21. Cernis 1990, 22. Dame & Thaddeus 1985, 23. Kun & Prusti 1993.

[c] Done by Shirley et al. (2003).

[d] Done by Mueller et al. (2002).

(Ahrens et al. 2002, Gottlieb et al. 2003) after some of our observations. We have corrected our data to the new frequencies listed in Table 3.2. The position switching mode was used; offset positions were checked when necessary. This is important for tracers that may show absorption features in the spectra (for example, HCN 3-2). We checked all the offset positions for HCN 3-2 emission and found them to be clear ($T_A^* < 0.5$ K). Pointing was checked periodically using planets and CO-bright stars. The pointing accuracy was usually better than $6''$ for all the runs. Map sizes of HCN 3-2 and CS 7-6 were extended to at least the point where the emission was one third of the peak strength, but usually go to as low as one tenth of the peak strength (typically the 3σ level, and the mean $\sigma \sim 1$ K km/s).

3.3 Observational Results

The spectral line information at the central position of each map is listed in Table 3.3 to Table 3.5. Table 3.3 presents the peak temperature of the line (T_R^*), integrated intensity ($\int T_R^* d\nu$), LSR velocity, and FWHM linewidth of CS 2-1, CS 7-6, and $C^{34}S$ 5-4 transitions for massive cores. Comparing to old CS 2-1 and CS 7-6 data in Plume et al. (1992, 1997) that was observed with the IRAM 30m telescope at Pico Veleta, the derived T_R^* and $\int T_R^* d\nu$, as well as the FWHM linewidth from FCRAO and CSO are slightly different from Plume's result, due to the different beam size of these telescopes. But the V_{LSR}s agree well between different telescopes.

Table 3.2 Observing Information

Transitions	Dates	Telescope	freguency (GHz)	θ_{mb} (arcsec)	η_{mb}
HCN 3-2	Jun 2002	CSO	265886.188	28.1	0.64
	Dec 2002	CSO	265886.188	28.1	0.60
	Jul 2003	CSO	265886.434	28.1	0.76
	Jan 2004	CSO	265886.434	28.1	0.66
	Jun 2004	CSO	265886.434	28.1	0.64
CS 5-4	Sep 1996	CSO	244935.610	24.5	0.56
	Dec 1996	CSO	244935.610	24.5	0.54
	Apr 1997	CSO	244935.610	24.5	0.56
	Jun 1997	CSO	244935.610	24.5	0.58
	Dec 1997	CSO	244935.610	24.5	0.56
	Jul 1998	CSO	244935.610	24.5	0.56
	Jul 1999	CSO	244935.610	24.5	0.60
CS 7-6	Jul 1998	CSO	342882.900	16.9	0.59
	Dec 1998	CSO	342882.900	20.5	0.61
	Jun 2000	CSO	342882.900	24.7	0.77
	Dec 2000	CSO	342882.900	24.7	0.63
	Jun 2002	CSO	342882.900	24.7	0.53
HCN 1-0	Apr 2004	FCRAO	88631.847	58.0	0.50
	Dec 2004	FCRAO	88631.847	58.0	0.50
	Feb 2005	FCRAO	88631.847	58.0	0.50
CS 2-1	Apr 2004	FCRAO	97980.968	50.0	0.50
	Dec 2004	FCRAO	97980.968	50.0	0.50
	Feb 2005	FCRAO	97980.968	50.0	0.50
$C^{34}S$ 5-4	Dec 1998	CSO	241016.176	31.0	0.66
	Jul 2001	CSO	241016.176	31.0	0.73
	Jan 2002	CSO	241016.176	31.0	0.53
	Jun 2002	CSO	241016.176	31.0	0.59
	Nov 2005	CSO	241016.089	31.0	0.80
$H^{13}CN$ 3-2	Dec 2002	CSO	259011.814	28.9	0.60
	May 2003	CSO	259011.814	28.9	0.58
	Jun 2004	CSO	259011.814	28.9	0.64
	Jun 2006	CSO	259011.814	28.9	0.80

Table 3.3. Observational Results of CS and C^{34} Transitions

SOURCE	CS 2 → 1				CS 7 → 6				$C^{34}S$ 5 → 4			
	T_R^* (K)	$\int T_R^* d\nu$ ($Kkms^{-1}$)	V_{LSR} (kms^{-1})	FWHM (kms^{-1})	T_R^* (K)	$\int T_R^* d\nu$ ($Kkms^{-1}$)	V_{LSR} (kms^{-1})	FWHM (kms^{-1})	T_R^* (K)	$\int T_R^* d\nu$ ($Kkms^{-1}$)	V_{LSR} (kms^{-1})	FWHM (kms^{-1})
G121.30+0.66	4.2	18.9	-17.87(03)	3.82(09)	3.1	9.0	-17.44(05)	2.58(13)	0.2	0.6	-17.64(17)*	2.87(37)
G123.07-6.31	3.6	13.9	-30.56(04)	3.56(10)	2.6	14.3	-30.97(09)	5.33(21)	0.2	1.3	-30.29(37)*	5.35(108)
G135.28+2.80	...	...	...	...	0.9	2.8	-71.49(09)	2.47(26)	...	...	...	...
W3(OH)	6.7	36.0	-46.80(01)	5.02(03)	8.1	50.9	-47.65(04)	6.05(10)	1.0	5.9	-47.49(08)	5.50(20)
S231	3.6	18.4	-16.74(06)	4.76(16)	3.5	17.3	-15.82(04)	4.38(11)	0.5	1.2	-15.77(07)	2.48(15)
S235	4.1	10.9	-16.78(02)	2.33(06)	5.0	19.5	-17.09(02)	3.38(04)	0.8	2.0	-16.93(09)	2.35(24)
S241	2.5	7.3	-8.74(02)	2.63(05)	0.6	1.9	-8.79(11)	2.98(24)	...	...	...	...
S252A	3.8	12.8	9.05(03)	3.09(07)	2.7	10.5	9.63(05)	3.57(11)	...	...	...	...
S255					7.2	32.6	7.52(02)	4.03(05)	1.1	3.9	7.34(09)	3.03(25)
RCW142	7.3	44.2	17.08(03)	5.23(08)	10.6*	83.0	16.63(03)	6.81(07)	4.3	26.5	17.35(05)	5.60(12)
W28A2(1)	5.4	30.1	9.38(03)	4.77(09)	12.5*	131.5	10.40(03)	9.29(09	3.4	23.4	9.77(03)	5.91(09)
M8 E	4.3	10.4	10.58(03)	2.15(08)	5.3	18.4	10.91(03)	3.29(07)	1.9	4.6	10.81(03)	2.23(08)
G9.62+0.10	2.3	17.9	4.72(17)	7.27(43)	5.9	48.9	5.42(04)	7.42(11)	1.8	15.7	4.28(06)	6.73(17)
G8.67−0.36	1.7	14.3	35.23(13)	8.12(32)	4.6	30.1	34.97(04)	5.74(10)	1.0	5.7	34.84(08)	5.08(23)
W31 (1)	...	...	...	...	3.0	19.9	65.00(18)	5.84(43)	0.9	8.0	66.27(12)	8.56(29)
G10.60−0.40	4.2	31.3	-3.24(06)	6.67(14)	13.0*	131.3	-3.56(03)	9.17(07)	4.1	29.8	-2.86(03)	6.72(08)
G12.42+0.50	2.4	11.4	18.18(07)	4.32(18)	...	...	...	...	...	...	...	...
G12.89+0.49	1.5	8.1	33.77(16)	4.39(44)	3.9	21.1	33.18(04)	5.09(09)	1.3	5.2	33.22(03)	3.78(08)
G12.21−0.10	1.0	7.3	24.92(12)	7.16(28)	2.4	18.8	23.72(08)	7.63(19)	0.6	4.1	24.44(08)	7.06(18)
W33cont	...	...	...	...	8.4	69.5	35.45(02)	7.79(06)	3.8	21.2	35.25(02)	5.13(05)
G13.87+0.28	11.2	76.3	...	6.38(06)	4.6	14.4	48.32(03)	2.57(07)	0.9	2.5	48.57(07)	2.50(17)
W33A	0.7	3.6	35.58(16)	5.63(36)	1.6	10.3	37.59(14)	5.78(41)	0.7	2.4	37.89(08)	3.22(24)
G14.33−0.64	0.8	5.3	22.66(12)	5.60(34)	6.6	34.7	22.16(04)	4.78(11)	1.5	4.4	22.19(03)	2.74(08)
G19.61−0.23	0.6	4.0	42.67(24)	6.08(68)	3.1	31.1	42.63(17)	9.72(39)	...	...	...	...
G20.08−0.13	...	...	...	...	3.0	29.1	41.74(06)	8.83(17)	...	...	...	...
G23.95+0.16	3.4	10.4	79.54(03)	2.65(09)	2.9	8.5	80.57(05)	2.74(11)	1.2	2.9	80.26(09)	2.39(22)
G24.49−0.04	1.3	7.3	110.17(08)	4.57(23)	1.3	4.4	109.60(15)	6.14(38)	...	...	...	...
W42	...	...	...	...	4.3	36.5	110.90(07)	7.65(18)	...	...	...	...
W43S	5.5	28.2	97.51(02)	4.38(05)	7.2	41.0	97.76(05)	5.13(11)	1.4	5.9	98.00(02)	3.97(04)
G31.41+0.31	...	...	...	...	4.6	37.4	96.22(04)	7.27(11)	1.2	7.8	96.97(06)	5.86(15)
W43 Main3	...	...	...	...	2.3	18.8	98.36(10)	7.53(25)	...	...	...	...
G31.44−0.26	...	...	...	...	2.6	12.9	86.75(04)	4.68(09)	0.6	2.2	87.07(16)	3.80(36)

Table 3.3 (cont'd)

SOURCE	CS 2 → 1				CS 7 → 6				$C^{34}S$ 5 → 4			
	T_R^* (K)	$\int T_R^* d\nu$ ($Kkms^{-1}$)	V_{LSR} (kms^{-1})	FWHM (kms^{-1})	T_R^* (K)	$\int T_R^* d\nu$ ($Kkms^{-1}$)	V_{LSR} (kms^{-1})	FWHM (kms^{-1})	T_R^* (K)	$\int T_R^* d\nu$ ($Kkms^{-1}$)	V_{LSR} (kms^{-1})	FWHM (kms^{-1})
G32.05+0.06	...	...	...	...	1.5	11.7	95.50(10)	7.26(22)	0.3	1.2	95.71(22)	6.10(66)
G32.80+0.20	...	...	...	...	4.4	38.8	14.22(08)	8.40(18)	...	...	...	...
W44	7.0	32.8	57.62(02)	4.12(04)	11.8	74.9	57.49(02)	5.68(06)	4.3	22.1	58.24(02)	4.03(08)*
G35.58−0.03	0.8	4.5	53.22(12)	5.11(29)	3.0	19.7	53.22(08)	5.72(23)	0.3	2.0	53.95(31)	5.88(82)
G35.20−0.74	...	...	...	...	3.6	28.1	34.69(13)	7.12(30)	0.5	2.4	33.71(10)	4.70(26)
W49N	2.1	40.2	2.54(11)	7.51(23)	8.9*	130.7	6.81(05)	13.88(11)	0.5	3.6	3.18(18)	6.41(39)
	2.8	...	12.00(08)	7.78(19)	...	...	...	...	0.6	4.7	12.36(19)	7.86(43)
W49S	...	...	...	...	2.8	23.2	15.42(08)	7.78(18)	0.2	1.9	14.82(23)	7.56(54)
G45.07+0.13	2.0	12.2	59.05(07)	5.13(21)	5.7	43.1	59.28(06)	7.00(15)	1.2	8.7	59.27(08)	6.33(23)
G48.61+0.02	2.0	9.3	18.45(04)	4.08(11)	1.8	12.0	18.00(08)	6.00(24)	0.2	0.5	18.13(11)	2.34(21)
W51W	6.3	71.8	56.82(03)	10.57(06)	5.2	23.6	51.04(05)	4.12(12)	0.9	3.5	51.01(08)	3.39(25)
W51M	...	...	...	...	13.1	149.6	56.29(02)1	0.69(06)	2.8	27.4	56.99(07)	8.96(17)
G59.78+0.06	2.6	7.2	22.78(04)	2.36(10)	...	...	...	...	0.5	1.2	22.74(10)	2.22(31)
S87	4.1	13.9	23.21(02)	3.17(06)	...	...	...	...	0.4	1.1	23.33(09)	2.38(20)
S88B	5.0	15.6	21.60(03)	2.81(07)	1.7	4.7	21.88(05)	2.23(12)	0.5	1.3	21.53(05)	2.36(13)
K3-50	1.3	10.6	-24.75(09)	7.24(25)	...	...	...	...	0.1	0.9	-25.09(31)	7.61(70)
ON 1	2.5	15.2	11.56(03)	5.44(08)	3.1	12.7	11.44(08)	4.18(18)	0.5	2.1	11.70(13)	4.21(28)
ON 2S	4.1	24.2	-1.13(05)	5.22(12)	4.5	22.1	-1.58(06)	4.54(15)	0.5	2.0	-1.29(06)	3.65(14)
ON 2N	...	...	...	...	3.8	21.4	0.28(09)	5.23(20)	0.8	3.2	0.34(05)	3.72(11)
S106	2.8	10.2	-1.28(02)	2.92(07)	1.8	9.4	-2.37(11)	4.91(24)	...	...	...	...
W75N	6.5	29.0	9.41(02)	4.14(04)	11.3	65.4	9.48(02)	5.02(06)	1.5	7.0	9.64(04)	4.22(11)
DR21 S	...	...	...	...	...	...	...	...	1.4	8.1	-2.29(06)	4.94(19)
W75(OH)	6.7*	37.4	-3.57(02)	5.31(04)	15.6*	92.3	-3.64(01)	5.47(03)	1.3	7.4	-2.73(08)	5.45(17)
BFS 11-B	...	...	...	...	1.5	5.8	-9.79(12)	3.73(31)	...	...	...	...
CepA	5.1	25.5	-11.05(03)	4.58(08)	...	...	...	...	0.8	3.0	-10.39(09)	3.68(19)
S158	7.8	45.7	-56.56(03)	5.25(06)	...	...	...	...	1.2	5.2	-55.74(05)	4.30(13)
S158A	...	...	...	...	...	...	...	...	1.1	4.1	-57.21(11)	3.64(27)
NGC7538-IRS9	...	...	...	...	...	...	...	...	...	...	...	...
S157	2.9	11.5	-43.57(04)	3.50(10)	1.9	7.1	-44.70(07)	3.53(18)	...	...	...	...
IRAS18586+010	0.9	3.8	38.42(10)	3.60(29)	...	...	...	...	...	...	...	...
IRAS19094+0944	0.8	2.1	65.47(08)	2.72(20)	...	...	...	...	...	...	...	...
IRAS20050+2720	1.5	5.5	6.48(09)	3.19(22)	...	...	...	...	...	...	...	...

Table 3.4 presents the line information for HCN 3-2 and its isotope $H^{13}CN$ 3-2. The mean integrated intensity ratio of HCN 3-2 to $H^{13}CN$ 3-2 is 9.7±6.8. This ratio is smaller than the usual HCN isotope ratio, partly due to the large fraction of self-absorption features presented in HCN 3-2 lines. About half of the sources in the massive core sample show double peaks. The description of line profiles has been given in Table 3.4. Since more sources have been observed with the HCN 3-2 line and an optically thin line since the paper (Wu & Evans 2003) on the statistics of blue profiles of massive cores (48 vs. 28 in last sample), we can estimate the blue excess (E) again via the δv method and the blue to red intensity ratio method (refer to Chap. 2). We find that $H^{13}CN$ 3-2 is already optically thick in some sources that show absorption features, while $C^{34}S$ 5-4 may be a better optically thin tracer for calculating δv (The mean ratio of the FWHM of $H^{13}CN$ $3-2$ to $C^{34}S$ 5-4 for our sample is 1.27±0.32). So we use $C^{34}S$ 5-4 as the optically thin line to calculate δv in this paper, and we only use $H^{13}CN$ $3-2$ when $C^{34}S$ 5-4 line is not available. The δvs are listed in Table 3.4. Using the δv method, we identified 21 blue and 15 red profiles out of 48 sources; this leads to E=0.13. Using the method based on the intensity ratio of blue peak to red peak, we identified 16 blue and 9 red profiles. The gives E=0.15. Comparing with the result of E=0.21 and E=0.29 for δv and peak ratio method in Wu & Evans (2003), this result indicates that collapse signature is not as common in massive cores as it appeared to be with a smaller sample.

Table 3.3 (cont'd)

SOURCE	CS 2 → 1				CS 7 → 6				$C^{34}S$ 5 → 4			
	T_R^* (K)	$\int T_R^* d\nu$ ($Kkms^{-1}$)	V_{LSR} (kms^{-1})	FWHM (kms^{-1})	T_R^* (K)	$\int T_R^* d\nu$ ($Kkms^{-1}$)	V_{LSR} (kms^{-1})	FWHM (kms^{-1})	T_R^* (K)	$\int T_R^* d\nu$ ($Kkms^{-1}$)	V_{LSR} (kms^{-1})	FWHM (kms^{-1})
IRAS20106+3545	1.5	3.4	7.97(03)	2.04(08)	...	...	...	...	...	...	...	...
IRAS20126+4104	2.6	9.3	-3.52(03)	3.09(07)	...	...	...	...	...	...	...	...
IRAS20188+3928	3.6	16.3	2.05(03)	3.70(09)	...	...	...	...	0.2	0.7	1.74(33)	3.75(92)
IRAS20216+4107	1.1	2.7	-1.70(06)	2.12(17)	...	...	...	...	...	...	...	...
IRAS20220+3728	2.0	8.4	-2.16(05)	3.61(13)	...	...	...	...	...	...	...	...
IRAS20333+4102	3.5	6.9	8.55(01)	1.84(03)	...	...	...	...	...	...	...	...
IRAS21391+5802	3.9	13.1	0.71(02)	2.99(05)	...	...	...	...	...	...	...	...
IRAS22172+5549	1.4	4.0	-43.36(07)	2.61(17)	...	...	...	...	...	...	...	...
IRAS22198+6336	2.1	5.1	-11.09(02)	2.05(06)	...	...	...	...	...	...	...	...
IRAS23011+6126	1.4	3.8	-11.22(06)	2.07(18)	...	...	...	...	...	...	...	...
IRAS23385+6053	1.8	7.1	-49.47(07)	3.90(14)	...	...	...	...	...	...	...	...

Table 3.4. Observational Results of HCN 3-2 and $H^{13}CN$ 3-2 Transitions

SOURCE	$H^{13}CN$ 3 → 2				HCN 3 → 2					
	T_R^* (K)	$\int T_R^* d\nu$ ($Kkms^{-1}$)	V_{LSR} (kms^{-1})	FWHM (kms^{-1})	T_R^* (K)	V_{peak} (kms^{-1})	$\int T_R^* d\nu$ ($Kkms^{-1}$)	V_{LSR} (kms^{-1})	Line[a] Profile	$\delta\upsilon$
G121.30+0.66	0.5(.11)	1.8(0.3)	-17.77(10)	3.06(25)	4.1(.30)	-18.42(22)	22.6(1.1)	-17.00(22)	db	-0.37(08)
G123.07-6.31	0.5(.11)	2.8(0.3)	-30.79(13)	4.87(32)	2.5(.23)	-32.75(22)	22.5(1.0)	-28.90(22)	db	-0.46(12)
W3(2)	0.7(.12)	3.3(0.4)	-38.73(10)	4.48(25)	5.9(.29)	-36.97(32)	32.8(1.4)	-39.77(32)	dr	0.39(04)
W3(OH)	1.8(.13)	10.1(0.5)	-47.16(05)	5.30(12)	6.6(.55)	-49.23(22)	51.3(2.3)	-46.15(22)	db	-0.32(03)
G135.28+2.80	...	...	...	...	0.7(.21)	-42.18(16)	3.3(0.7)	-42.18(19)		
GL490	...	...	...	...	2.4(.55)	-13.18(22)	11.5(1.7)	-13.18(11)		
S231	0.8(.10)	3.3(0.4)	-16.41(06)	3.74(17)	3.5(.23)	-14.12(22)	20.2(1.0)	....	rbs	0.67(07)
S235	1.1(.11)	3.4(0.3)	-17.44(05)	2.71(13)	5.0(.31)	-17.36(11)	29.1(1.0)	-17.36(03)		-0.18(06)
S241	...	...	...	...	1.1(.21)	-8.58(22)	5.4(0.7)	-8.58(11)		
MonR2	...	...	...	...	7.8(.23)	10.19(16)	39.0(0.9)	10.31(02)		
S252A	0.6(.09)	1.7(0.3)	9.13(07)	2.61(16)	3.7(.32)	10.04(22)	20.5(1.2)	9.65(06)	rbs	0.35(05)
S255	...	...	...	...	7.9(.68)	7.98(22)	48.1(2.5)	7.65(05)		0.21(05)
RCW142	2.7(.27)	21.6(1.0)	16.16(09)	7.15(23)	17.8(.45)	14.36(11)	164.9(2.6)	20.77(21)	db	-0.53(02)
W28A2(1)	5.1(.21)	47.8(1.3)	9.23(03)	6.93(09)	13.1(.35)	11.18(22)	177.3(2.3)	11.40(03)	ws	0.24(02)
M8 E	0.8(.13)	2.5(0.4)	10.95(06)	2.76(14)	7.1(.32)	9.54(22)	45.6(1.4)	11.07(10)	d	
G9.62+0.10	1.2(.19)	10.9(0.8)	4.77(10)	8.17(26)	6.2(.60)	7.38(22)	52.0(2.9)	2.67(42)	dr	0.46(02)
G8.67−0.36	1.4(.33)	6.9(1.0)	34.32(13)	4.40(30)	2.7(.16)	31.91(16)	22.4(0.8)	36.19(50)	db	-0.58(04)
W31 (1)	1.1(.11)	7.9(2.0)	64.85(08)	6.69(19)	6.9(.22)	62.71(11)	68.2(1.1)	68.70(21)	db	-0.42(02)
G10.60−0.40	3.6(.21)	30.5(0.9)	-4.16(06)	7.74(14)	11.8(.62)	-6.50(11)	132.2(3.4)	-0.43(10)	db	-0.54(02)
G12.42+0.50	0.9(.26)	1.7(0.6)	17.36(12)	1.79(29)	4.2(.25)	16.06(11)	24.1(0.9)	17.49(09)	db	-0.73(15)
G12.89+0.49	0.8(.19)	5.4(0.8)	33.13(18)	6.42(48)	2.6(.15)	...	21.1(0.7)	33.49(30)	d	
W33cont	2.1(.34)	11.6(1.4)	35.43(11)	5.74(24)	10.0(.38)	39.53(22)	94.3(2.1)	33.75(20)	dr	0.83(02)
W33A	0.7(.23)	4.2(0.8)	37.69(22)	5.40(58)	1.8(.21)	40.49(22)	25.8(1.2)	38.14(11)	rbs	0.81(07)
G14.33−0.64	1.8(.30)	8.8(1.2)	22.25(10)	4.59(25)	7.1(.25)	25.47(11)	69.1(1.5)	21.65(10)	dr	1.20(05)
G19.61−0.23	0.4(.11)	6.3(0.7)	42.57(34)	15.50(85)	3.1(.32)	40.40(22)	45.2(1.9)	40.66(14)	brs	-0.14(02)
G20.08−0.13	...	...	...	...	2.1(.30)	38.46(32)	22.3(1.5)	39.85(16)	brs	
G23.95+0.16	0.4(.09)	1.3(0.3)	80.32(10)	3.24(35)	1.9(.28)	78.57(22)	14.5(1.1)	80.52(22)	db	-0.71(09)
W42	0.9(.32)	8.4(1.4)	110.49(28)	8.55(58)	3.9(.35)	114.49(22)	28.1(1.8)	108.59(22)	dr	0.47(05)
W43S	1.3(.16)	7.1(0.7)	98.11(06)	5.25(16)	6.3(.32)	96.61(22)	52.0(1.4)	96.85(03)	brs	-0.35(03)
G31.41+0.31	1.2(.30)	7.7(1.2)	96.23(16)	5.41(46)	3.2(.28)	93.25(16)	21.5(1.5)	98.67(32)	db	-0.63(03)
G31.44−0.26	...	...	...	...	3.1(.19)	87.87(16)	24.8(0.8)	87.27(05)		0.21(06)
G32.05+0.06	0.4(.16)	3.8(0.6)	95.41(28)	7.17(91)	3.1(.29)	92.08(16)	26.2(1.4)	97.25(32)	db	-0.60(08)

Table 3.4 (cont'd)

SOURCE	$H^{13}CN$ 3 → 2				HCN 3 → 2					
	T_R^* (K)	$\int T_R^* d\nu$ (Kkms^{-1})	V_{LSR} (kms^{-1})	FWHM (kms^{-1})	T_R^* (K)	V_{peak} (kms^{-1})	$\int T_R^* d\nu$ (Kkms^{-1})	V_{LSR} (kms^{-1})	Line[a] Profile	δv
G32.80+0.20	...	...	...	...	3.2(.25)	....	40.8(1.3)	13.74(99)	flat	
W44	3.8(.14)	24.4(0.6)	56.82(04)	5.64(10)	11.5(.32)	54.79(16)	84.9(1.8)	61.17(22)	db	-0.86(04)
S76E	...	...	...	...	7.8(.23)	33.63(16)	53.6(1.0)	32.99(02)	rbs	
G35.58−0.03	0.3(.06)	1.8(0.2)	53.68(13)	6.13(34)	2.8(.34)	52.91(22)	30.0(1.7)	52.91(09)		-0.18(06)
G35.20−0.74	0.7(.20)	6.5(0.8)	34.01(24)	8.26(56)	7.9(.26)	37.34(16)	54.3(1.2)	33.93(32)	dr	0.77(06)
W49N	1.2(.39)	...	...	...	8.7(.33)	3.02(22)	142.4(2.0)	12.44(22)	two	
W49S	...	...	...	...	2.8(.16)	15.32(16)	37.3(0.9)	15.32(06)		0.07(04)
OH43.80−0.13	0.5(.21)	4.8(0.9)	44.17(31)	8.47(77)	2.2(.25)	46.80(32)	23.7(1.2)	42.96(32)	dr	0.31(05)
G45.07+0.13	0.6(.16)	4.3(0.7)	59.13(15)	6.49(35)	4.3(.27)	59.52(22)	41.8(1.5)	59.52(04)	rw	0.04(02)
G48.61+0.02	0.2(.09)	1.4(0.3)	18.04(22)	5.35(67)	2.3(.34)	18.09(11)	18.7(1.4)	18.09(09)		-0.02(07)
W51W	...	...	...	...	2.5(.32)	52.18(32)	18.5(1.2)	51.44(09)	sr	0.35(06)
W51M	3.1(.47)	36.3(2.3)	56.60(15)	11.04(37)	14.2(.44)	51.74(32)	153.9(2.3)	55.65(99)	brs	-0.59(02)
G59.78+0.06	0.2(.11)	0.4(0.2)	22.67(18)	1.96(36)	2.5(.27)	21.52(22)	16.0(1.0)	21.79(06)	sb	-0.55(10)
S87	...	...	...	...	4.6(.28)	22.76(22)	25.9(1.0)	22.67(03)	brs	-0.24(06)
S88B	0.4(.07)	1.3(0.2)	21.85(08)	3.11(18)	2.8(.25)	22.06(22)	15.8(0.9)	22.06(05)		0.22(05)
K3-50	...	...	...	...	4.1(.26)	-22.91(22)	40.3(1.3)	-23.78(05)	sr	0.29(05)
ON 1	0.8(.23)	3.9(0.8)	11.66(17)	4.74(42)	3.8(.40)	13.87(22)	27.2(1.8)	10.72(22)	dr	0.52(05)
ON 2S	0.7(.16)	3.1(0.6)	-1.50(11)	4.31(30)	8.6(.33)	-0.07(22)	68.0(1.6)	-1.59(03)	rbs	0.33(04)
ON 2N	...	...	...	...	4.2(.40)	2.58(22)	46.1(2.0)	0.51(09)	rbs	0.60(04)
S106	...	...	...	...	3.0(.35)	-2.38(22)	20.2(1.4)	-3.00(07)	rbs	
W75N	1.9(.22)	11.1(1.0)	9.67(06)	5.12(16)	9.5(.27)	11.74(22)	92.3(1.7)	9.46(11)	dr	0.50(03)
DR21 S	1.7(.19)	15.2(0.9)	-2.16(10)	8.39(26)	15.8(.36)	-6.02(22)	217.7(2.3)	-2.00(11)	db	-0.76(04)
W75(OH)	1.8(.26)	10.3(1.0)	-3.35(13)	5.26(28)	11.1(.43)	-6.27(22)	80.7(2.2)	-2.24(22)	db	-0.65(03)
G97.53+3.19	...	...	...	...	1.0(.32)	-71.88(22)	8.3(1.5)	-71.88(27)		
CepA	...	...	...	...	7.9(.37)	-12.33(22)	71.5(2.0)	-10.41(22)	db	-0.53(05)
S158	0.9(.13)	5.7(0.5)	-56.29(11)	6.09(26)	5.5(.32)	-59.05(22)	52.0(1.8)	-55.28(22)	db	-0.77(04)
S158A					7.0(.82)	-58.43(22)	37.2(3.7)	-58.13(10)	brs	-0.34(05)
NGC7538-IRS9	...	...	...	...	3.0(.33)	-54.75(22)	18.7(1.3)	....	rbs	
S157	...	...	...	...	3.0(.82)	-45.03(22)	17.8(3.0)	-44.53(15)		-0.36(06)
IRAS20050+2720	...	...	...	...	2.3(.25)	5.94(22)	13.1(0.9)	5.94(06)		
IRAS20216+4107	...	...	...	...	2.0(.28)	-1.31(11)	7.9(0.9)	-1.31(06)		
IRAS23011+6126	...	...	...	...	0.9(.29)	-10.94(22)	7.4(1.0)	-10.94(21)		

Table 3.5 lists the observational results for HCN 1-0 for cores in Table 1. HCN 1-0 has three hyperfine components (F=1-0, F=2-1, F=1-1), separated by -7.064 km/s and 4.842 km/s, respectively. We tried to fit the spectra with 3 gaussian components with the same line width. The peak temperatures of every component, the LSR velocity of the main component (F=2-1), the linewidth, and the integrated intensity were presented in the table. Massive cores usually have large linewidth; sometimes the line width is wider than the separation of hyperfine components, so that two or three of these components will be blended. Sometimes one or two hyperfine components will be optically thick enough to show absorption. We have noted these features in Table 3.5. In the LTE assumption, if the HCN 1-0 line is optically thin, the line ratios between the three hyperfine components are I(F=1-0):I(F=2-1):I(F=1-1)=1:5:3. This doesn't agree with observed ratios for most of our cores as seen in Table 3.5.

Table 3.4 (cont'd)

SOURCE	$H^{13}CN\ 3 \rightarrow 2$				HCN $3 \rightarrow 2$					
	T_R^* (K)	$\int T_R^* d\nu$ (Kkms^{-1})	V_{LSR} (kms^{-1})	FWHM (kms^{-1})	T_R^* (K)	V_{peak} (kms^{-1})	$\int T_R^* d\nu$ (Kkms^{-1})	V_{LSR} (kms^{-1})	Line[a] Profile	δv

[a]Code of line profiles: db, double peak with blue strong; dr, double peaks with red strong; d: double peaks with neither one obviously stronger; flat, the line has a flat top; rbs, blue shoulder with peak skewed to red; brs, red shoulder with peak skewed to blue; ws: wings on both sides; rw, red wing; sr, peak skews to red; br, peak skews to blue; two, the line has two known velocity components.

Table 3.5. Observational Result for HCN 1-0 Transition

Source	T_R^* (K) (F=1-0)	T_R^* (K) (F=2-1)	T_R^* (K) (F=1-1))	$\int T_R^* d\nu$ (Kkms^{-1}) (all hpf Fs)	V_{LSR} (kms^{-1}) (F=2-1)	FWHM (kms^{-1} (F=2-1)	Line[a] profile
G121.30+0.66	0.9(0.2)	4.0(0.2)	...	24.9(1.2)	-18.31(33)	...	ab
G123.07-6.31	0.9(0.2)	2.6(0.2)	1.8(0.2)	19.6(1.0)	-31.13(04)	3.63(05)	
W3(OH)	1.9(0.1)	...	...	41.8(0.7)	...	...	ab,bl
S231	0.7(0.2)	2.3(0.2)	1.3(0.2)	20.1(1.2)	-17.26(06)	4.21(07)	bl
S235	1.2(0.2)	4.3(0.2)	1.5(0.2)	19.0(1.0)	-17.17(02)	2.37(03)	
S241	0.3(0.1)	1.5(0.1)	0.7(0.1)	7.1(0.5)	-8.90(03)	2.66(04)	
S252A	1.0(0.2)	3.5(0.2)	1.6(0.2)	21.6(1.1)	9.05(03)	3.28(04)	
RCW142	3.1(0.3)	5.6(0.3)	3.1(0.3)	73.2(1.6)	16.73(06)	5.31(07)	bl
W28A2(1)	1.9(0.2)	4.0(0.2)	1.0(0.5)	28.1(1.2)	8.65(03)	3.66(04)	
M8E	0.8(0.3)	4.0(0.3)	1.8(0.3)	17.6(1.3)	10.46(03)	2.52(04)	
G9.62+0.10	1.2(0.3)	1.0(0.3)	1.1(0.3)	17.3(1.7)	5.50(13)	4.31(20)	
G8.67−0.36	1.0(0.3)	1.0(0.3)	...	11.4(1.3)	33.15(33)	...	
G10.60−0.40	0.9(0.6)	2.3(1.0)	1.3(0.5)	46.0(1.7)	-3.45(01)	...	bf,bl
G12.42+0.50	0.5(0.3)	1.7(0.3)	1.3(0.3)	15.1(1.3)	17.59(11)	3.88(11)	bl
G12.21−0.10	...	0.5(0.2)	...	4.7(0.8)	...	...	bl
G13.87+0.28	2.9(0.4)	4.4(0.4)	2.7(0.4)	55.3(1.9)	...	...	bl
G19.61−0.23	...	0.2(0.1)	...	1.6(0.5)	...	...	
G23.95+0.16	0.6(0.2)	2.4(0.2)	1.1(0.2)	12.4(1.0)	78.90(04)	2.72(06)	
W43S	1.6(0.1)	2.9(0.1)	1.0(0.1)	26.4(0.8)	96.72(03)	4.03(04)	
W44	1.7(0.2)	2.2(0.2)	...	12.7(0.8)	57.07(04)	2.93(05)	
G35.58−0.03	...	0.5(0.1)	...	5.2(0.7)	...	...	bl
W49N	...	...	...	53.1(1.2)	...	...	bl
G45.07+0.13	0.5(0.2)	0.8(0.2)	0.2(0.2)	10.9(1.1)	59.58(03)	5.93(23)	bl
G48.61+0.02	0.5(0.1)	2.1(0.1)	1.1(0.1)	17.9(0.7)	18.36(03)	4.28(04)	bl
W51M	...	...	...	50.4(1.1)	...	...	bl
G59.78+0.06	0.5(0.2)	2.1(0.2)	1.0(0.2)	12.3(0.9)	22.45(05)	3.01(06)	
S87	1.1(0.2)	4.8(0.2)	2.1(0.2)	31.2(0.8)	22.88(02)	3.71(02)	bl2
S88B	0.9(0.2)	3.9(0.2)	2.3(0.2)	25.2(0.9)	21.54(02)	3.22(03)	bl2
K3-50	...	...	...	24.3(0.8)	...	...	bl
ON 1	...	...	...	16.0(0.7)	...	...	bl
ON 2S	...	...	...	2.5(0.8)	...	...	ab,bl
S106	0.5(0.1)	2.0(0.4)	1.0(0.1)	12.7(0.4)	-1.58(02)	3.22(03)	bl2
W75N	0.8(0.1)	1.4(0.1)	1.0(0.1)	19.3(0.5)	9.75(07)	5.54(08)	bl

Contour maps of HCN 1-0, HCN 3-2, CS 2-1, and CS 7-6 are presented in the Appendix A (fig. A.1 to fig. A.20). The size of the core is characterized by the nominal core radius after beam deconvolution; for example, for HCN 1-0, R_{HCN1-0} is the radius of a circle that has the same area as the half peak intensity contour:

$$R_{HCN1-0} = D(\frac{A_{1/2}}{\pi} - \frac{\theta_{beam}^2}{4})^{1/2},$$

where $A_{1/2}$ is the area within the contour of half peak intensity.

The line luminosity of each core, assuming a gaussian brightness distribution for the source and a gaussian beam, is (we use HCN 1-0 for example)

$$L_{HCN1-0} = 23.5 \times 10^{-6} \times D^2 \times (\frac{\pi \times \theta_s^2}{4ln2}) \times (\frac{\theta_s^2 + \theta_{beam}^2}{\theta_s^2}) \times \int T_R dv. \quad (3.1)$$

Here D is the distance in the unit of kpc, θ_s and θ_{beam} are the angular size of the half-peak HCN 1-0 contour and the beam in arcsecond. This method is parallel to that of Gao & Solomon (2004b), but adapted to Galactic cores.

The total infrared luminosity (8-1000 μm) was calculated based on the 4 IRAS bands (Sanders and Mirabel 1996), as was done for the galaxy sample of Gao & Solomon (2004a):

$$L_{IR} = 0.56 \times D^2 \times (13.48 \times f_{12} + 5.16 \times f_{25} + 2.58 \times f_{60} + f_{100}), \quad (3.2)$$

where f_x is the flux in band x from the four IRAS bands in the units of Jy, D in kpc, and L_{IR} in $L_\odot$. Some authors used the bolometric luminosity (L_{bol}), which is calculated from the SED of the source (e.g. Mueller et al. 2002). Our

Table 3.5 (cont'd)

Source	T_R^* (K) (F=1-0)	T_R^* (K) (F=2-1)	T_R^* (K) (F=1-1))	$\int T_R^* d\nu$ ($Kkms^{-1}$) (all hpf Fs)	V_{LSR} (kms^{-1}) (F=2-1)	FWHM (kms^{-1} (F=2-1)	Line[a] profile
DR21 S	1.2(0.2)	3.4(0.2)	1.4(0.2)	19.4(1.1)	-3.49(07)	5.69(09)	ab,bl
W75(OH)	...	...	...	21.7(1.0)	...	...	ab,bl
CepA	1.0(0.2)	...	...	30.6(0.9)	...	...	bl,bf
S158	3.2(0.3)	5.3(0.3)	1.9(0.3)	57.9(1.5)	-57.14(04)	4.76(05)	bl
S157	0.7(0.2)	2.7(0.2)	1.3(0.2)	19.5(0.9)	-43.58(04)	3.79(05)	bl2
IRAS18586+0106	0.3(0.2)	0.7(0.2)	0.2(0.2)	4.1(0.7)	38.34(10)	3.10(15)	
IRAS19094+0944	0.2(0.1)	0.8(0.1)	0.5(0.1)	5.1(0.6)	65.48(07)	3.13(08)	
IRAS20050+2720	0.3(0.2)	0.5(0.2)	0.3(0.2)	5.7(1.1)	6.06(27)	4.72(25)	bl2
IRAS20106+3545	0.3(0.1)	1.3(0.1)	0.6(0.1)	5.2(0.5)	7.80(03)	2.15(05)	
IRAS20126+4104	0.9(0.1)	2.9(0.1)	1.8(0.1)	19.6(0.6)	-3.60(02)	3.14(02)	bl2
IRAS20188+3928	0.7(0.2)	1.9(0.5)	1.3(0.4)	19.8(0.8)	2.49(06)	4.42(07)	ab? bl,bf
IRAS20216+4107	0.2(0.1)	1.3(0.1)	0.5(0.1)	5.4(0.6)	-1.57(04)	2.32(06)	
IRAS20220+3728	0.4(0.2)	1.8(0.2)	0.3(0.2)	8.9(0.8)	-2.30(05)	3.09(06)	
IRAS20333+4102	0.9(0.1)	4.4(0.1)	1.8(0.1)	16.9(0.6)	8.60(01)	2.21(02)	
IRAS21391+5802	0.9(0.1)	1.8(0.5)	1.2(0.2)	15.0(0.6)	0.50(03)	3.30(04)	ab?
IRAS22172+5549	0.2(0.1)	1.2(0.1)	0.5(0.1)	6.2(0.7)	-43.51(06)	3.05(07)	bl2
IRAS22198+6336	0.5(0.1)	1.3(0.1)	0.5(0.1)	6.0(0.6)	-11.14(04)	2.35(05)	
IRAS23011+6126	0.4(0.1)	0.9(0.1)	0.6(0.1)	6.7(0.6)	-11.76(07)	3.25(09)	
IRAS23385+6053	0.5(0.2)	1.9(0.2)	0.8(0.2)	10.0(0.8)	-49.95(04)	2.91(05)	
IRAS03282+3035	0.8(0.1)	1.3(0.1)	0.8(0.1)	3.3(0.4)	6.94(02)	0.92(04)	
L1251B	0.7(0.1)	1.5(0.3)	0.9(0.2)	5.0(0.3)	-4.03(02)	1.56(02)	ab

[a]Code of line profiles: ab, absorption features on the line; bl, three components are blended; bl2: Only F=2-1 and F=1-1 are blended; bf, the line can not be well fitted by 3 gaussian components.

statistics shows that L_{bol}s calculated in Mueller et al. (2002) are very close to the L_{IR}s calculated in this paper for the same cores.

The calculated sizes and luminosities of cores in each transition are listed in Table 3.6 and Table 3.7, with the mean and median values given at the end of the Tables. The statistics on median and mean value only includes the massive sources, but not those sources listed in part 2 of Table 1, which are mostly not very massive and were added to study the lower luminosity end of the star formation law.

Table 3.6. The FWHM sizes of maps

SOURCE	HCN 3 → 2		HCN 1 → 0		CS 7 → 6		CS 2 → 1	
	R(HCN3-2) (pc)	θ_{dec} [a] ($''$)	R(HCN1-0) (pc)	θ_{dec} [a] ($''$)	R(CS7-6) (pc)	θ_{dec} [a] ($''$)	R(CS2-1) (pc)	θ_{dec} [a] ($''$)
G121.30+0.66	0.09(01)	41.3	0.13(01)	62.4	0.06(01)	21.8	0.16(02)	76.0
G123.07-6.31	0.11(02)	20.9	0.41(06)	76.2	0.11(02)	19.8	0.38(05)	70.8
W3(2)								
W3(OH)	0.22(02)	37.1	0.59(04)	101.9	0.14(01)	24.7	0.54(04)	93.3
G135.28+2.80								
GL490	0.05(01)	24.2						
S231	0.19(03)	34.0	0.43(06)	77.8	0.11(02)	20.1	0.44(06)	79.3
S235	0.14(02)	37.3	0.38(04)	96.8	0.10(01)	24.8	0.32(03)	81.7
S241	0.22(05)	19.7	0.66(08)	58.2	0.07(01)	18.2	0.59(12)	52.2
MonR2								
S252A	0.10(01)	27.5	0.35(08)	95.5			0.40(08)	111.3
S255	0.13(10)	41.0			0.10(02)	32.1		
RCW142	0.20(02)	40.5	0.59(06)	121.8	0.11(01)	23.6	0.36(03)	74.3
W28A2(1)			0.37(03)	58.2	0.10(01)	15.1	0.30(02)	48.4
M8E	0.16(01)	35.8	0.48(13)	109.2	0.08(01)	18.5	0.35(06)	80.1
G9.62+0.10	0.45(04)	26.6	1.13(12)	66.4	0.36(06)	21.3	1.06(21)	62.2
G8.67−0.36	0.38(04)	35.0			0.18(03)	16.4	0.94(22)	86.2
W31 (1)	0.70(10)	24.1			0.82(23)	28.2		
G10.60−0.40	0.38(02)	24.4	1.03(07)	65.4	0.43(03)	27.1	0.93(07)	59.0
G12.42+0.50			0.46(07)	90.7			0.51(09)	99.2
G12.89+0.49					0.10(01)	11.3		
G12.21−0.10			5.31(87)	159.8		U	5.70(86)	171.6
W33cont					0.58(04)	58.7		
G13.87+0.28			1.31(16)	122.4	0.27(05)	25.5	1.30(11)	122.2
W33A					0.18(03)	16.3		
G14.33−0.64	0.13(02)	21.3			0.16(02)	25.0		
G19.61−0.23	0.21(04)	21.4			0.16(02)	16.4	1.67(54)	172.4
G20.08−0.13					0.17(02)	20.6		
G23.95+0.16			1.34(45)	95.5	0.37(07)	26.6	1.08(51)	76.8
G24.49−0.04					0.17(07)	19.7		
W42					0.33(02)	15.2		
G28.86+0.07								
W43S	0.55(06)	26.7	1.84(20)	89.3	0.25(03)	12.1	1.42(12)	69.0
G31.41+0.31					0.24(02)	12.7		
W43 Main3					0.23(03)	13.9		
G31.44−0.26					0.56(09)	21.6		
G32.05+0.06					0.53(16)	25.8		
G32.80+0.20					0.59(07)	15.6		
W44	0.39(03)	43.0	1.27(23)	142.1	0.25(02)	28.4	0.81(05)	89.8
S76E								
G35.58−0.03			0.48(19)	57.1	0.14(03)	16.7	0.56(06)	66.1
G35.20−0.74					0.20(03)	24.4		
W49N			2.79(18)	97.4	1.09(11)	32.0	2.10(13)	73.4
W49S					0.62(22)	18.3		
OH43.80−0.13								
G45.07+0.13	0.56(09)	23.7	1.34(20)	57.1	0.41(07)	17.5	0.77(11)	32.6

Table 3.6 (cont'd)

SOURCE	HCN 3 → 2		HCN 1 → 0		CS 7 → 6		CS 2 → 1	
	R(HCN3-2) (pc)	θ_{dec} [a] ($''$)	R(HCN1-0) (pc)	θ_{dec} [a] ($''$)	R(CS7-6) (pc)	θ_{dec} [a] ($''$)	R(CS2-1) (pc)	θ_{dec} [a] ($''$)
G48.61+0.02	0.66(13)	23.2	3.50(32)	122.4	0.25(05)	8.6	3.09(65)	107.9
W51W					0.53(12)	31.1		
W51M	0.80(14)	47.0	2.34(64)	138.0	0.47(03)	27.7	2.32(15)	136.5
G59.78+0.06			0.46(04)	87.1			0.47(06)	88.4
S87			0.48(03)	103.2			0.45(04)	96.6
S88B	0.17(03)	33.6	0.58(08)	114.3	0.14(02)	26.7	0.32(03)	63.2
K3-50			1.53(12)	70.1			1.44(17)	66.1
ON 1			1.31(11)	90.0	0.32(06)	21.8	1.15(11)	79.3
ON 2S	0.59(09)	44.4	1.09(14)	81.8	0.50(06)	37.4	1.09(13)	81.7
ON 2N					0.39(07)	29.3		
S106			1.06(08)	106.2	0.28(09)	28.5	1.27(13)	127.8
W75N	0.27(03)	36.9	0.63(04)	86.4	0.20(02)	27.5	0.56(06)	77.7
DR21 S	0.24(01)	32.4	0.75(05)	102.5	0.25(02)	34.2	0.78(07)	106.7
W75(OH)	0.37(06)	51.0	0.87(08)	120.3	0.21(02)	28.8	0.79(06)	109.0
G97.53+3.19	0.37(04)	18.0						
BFS 11-B					0.09(04)	18.5		
CepA	0.09(01)	48.5	0.23(02)	130.4			0.27(03)	150.3
S158	0.46(05)	68.3	0.85(06)	125.9			0.77(06)	113.6
S158A	0.37(03)	55.2						
NGC7538-IRS9	0.42(10)	62.3						
S157	0.19(04)	30.9	0.45(06)	74.5	0.17(04)	27.9	0.43(08)	71.7
IRAS19094+0944			1.48(45)	100.0			1.24(66)	84.0
IRAS20050+2720	0.08(02)	43.1	0.23(06)	127.5			0.22(11)	123.8
IRAS20106+3545			0.24(06)	60.3			0.27(07)	67.1
IRAS20126+4104			0.48(04)	47.3			0.49(08)	48.4
IRAS20188+3928			0.07(01)	98.1			0.08(01)	105.5
IRAS20216+4107	0.05(02)	11.6	0.26(03)	62.4			0.20(04)	49.7
IRAS20220+3728			1.40(28)	128.4			1.41(50)	129.3
IRAS20333+4102			0.42(03)	108.6			0.40(04)	103.0
IRAS21391+5802			0.14(02)	77.0			0.14(01)	74.3
IRAS22172+5549			0.36(06)	51.2			0.40(10)	56.8
IRAS22198+6336			0.31(07)	100.0			0.33(07)	106.7
IRAS23011+6126	0.03(01)	17.3	0.17(03)	98.7			0.17(04)	94.7
IRAS23385+6053			1.13(17)	67.3			1.06(17)	63.2
IRAS03282+3035			0.10(03)	187.0			0.09(03)	173.8
L483	0.02(01)	32.2						
L1251B			0.07(01)	92.1			0.09(02)	127.3
Mean[b]	0.32(20)	35(13)	1.08(103)	96(27)	0.29(21)	23(8)	1.00(1.0)	90(31)
Median[b]	0.23	33	0.71	96	0.24	22	0.77	81

[a]The angular FWHM size of the core that deconvelved with the beam size

[b]Statitics does not include the the part 2 sources in Table 1

Table 3.7. Luminosities of massive cores

Source	L(HCN3-2) [a] $Kkms^{-1}pc^2$	L(HCN1-0) [a] $Kkms^{-1}pc^2$	L(CS7-6) [a] $Kkms^{-1}pc^2$	L(CS2-1) [a] $Kkms^{-1}pc^2$	L_{IR} 10^4 $L_\odot$	T_{bol} [b] (K)	L_{bol}/M_{vir} [c] $L/M_\odot$
G121.30+0.66	2.7(37)	3.8(27)	0.5(53)	6.6(33)	0.07	46	3
G123.07-6.31	2.3(34)	39.2(35)	1.4(40)	28.8(31)	0.57	51	12
W3(OH)	31.9(19)	279.2(14)	11.7(19)	222.8(20)	12.20	65	93
GL490	0.3(38)				0.23	112	
S231	13.5(38)	54.6(35)	1.9(37)	59.4(34)	1.08	63	73
S235	8.9(30)	62.7(28)	2.0(33)	39.6(23)	0.52	125	98
S241	3.4(55)	31.0(31)	0.4(41)	27.0(47)	1.37	62	91
MonR2					3.69	98	
S252A	2.2(33)	42.4(56)		65.2(49)	3.65	68	45
S255	12.3(25)		5.1(38)		1.59		
RCW142	101.3(27)	715.1(25)	9.4(14)	117.9(20)	6.56	64	153
W28A2(1)		52.5(20)	7.4(12)	42.3(17)	27.92	60	450
M8E	14.6(19)	84.6(71)	1.0(30)	34.1(41)	1.82	93	166
G9.62+0.10	93.4(19)	284.7(25)	74.9(42)	258.7(48)	56.17	68	157
G8.67−0.36			6.9(22)	305.0(59)	13.13	67	152
W31 (1)	275.2(33)		152.2(67)		164.27		
G10.60−0.40	154.0(13)	751.8(15)	265.2(15)	479.1(18)	110.98	52	334
G12.42+0.50		69.3(38)		87.8(45)	1.85	70	
G12.89+0.49			1.2(28)		4.55	56	115
G12.21−0.10		7139.1(95)	0.1(43)	12948.3(89)	94.54	57	114
W33cont			1123.5(15)				
G13.87+0.28		2084.5(32)	12.0(41)	3289.5(20)	19.35	93	419
W33A			4.9(41)		15.37	65	220
G14.33−0.64	8.4(43)		8.7(38)		2.16		621
G19.61−0.23	20.4(42)		10.9(27)	649.2(88)	19.53	55	141
G20.08−0.13			7.2(32)		4.50	74	
G23.95+0.16		372.2(85)	16.2(47)	177.7(20)	22.91	91	443
G24.49−0.04			2.6(92)		5.46	65	164
W42			26.7(16)				
G28.86+0.07					33.52		
W43S	205.6(27)	1790.8(26)	15.6(27)	756.2(20)	172.83	93	1480
G31.41+0.31			14.9(21)		20.82	55	221
W43 Main3			12.3(31)				

Table 3.7 (cont'd)

Source	L(HCN3-2) [a] $Kkms^{-1}pc^2$	L(HCN1-0) [a] $Kkms^{-1}pc^2$	L(CS7-6) [a] $Kkms^{-1}pc^2$	L(CS2-1) [a] $Kkms^{-1}pc^2$	L_{IR} 10^4 $L_\odot$	T_{bol} [b] (K)	L_{bol}/M_{vir} [c] $L/M_\odot$
G31.44−0.26			41.0(38)		59.89		
G32.05+0.06			29.9(76)		10.53		
G32.80+0.20			85.7(27)				
W44	188.1(20)	764.6(47)	53.5(16)	586.8(14)	53.45		214
S76E					2.95	75	118
G35.58−0.03		18.0(92)	2.7(41)	44.5(28)	4.77	66	33
G35.20−0.74			11.4(39)		4.44		
W49N		7630.7(15)	1951.5(24)	3561.7(13)	489.01		
W49S			64.3(82)				
OH43.80−0.13			68.7(38)		3.24		
G45.07+0.13	86.6(37)	251.6(35)		73.7(33)	137.43	79	446
G48.61+0.02	81.0(45)	5562.2(23)	3.7(46)	2296.8(55)	114.70	70	290
W51W			77.3(58)		84.67		
W51M	1727.6(43)	8350.0(72)	337.2(16)	22641.1(15)	380.00	88	472
G59.78+0.06		75.5(20)		66.2(30)	1.26		
S87		173.3(15)		96.5(19)	3.41	80	
S88B	11.1(38)	187.6(35)	3.0(33)	19.1(23)	10.62	75	562
K3-50		688.0(18)		366.0(29)	242.94		343
ON 1		429.2(20)	15.2(44)	343.8(24)	14.37	57	114
ON 2S	404.0(38)	521.3(30)	133.6(29)	569.1(29)	51.72	80	302
ON 2N			53.3(46)				
S106		548.4(17)	17.6(77)	688.2(25)	51.64	94	692
W75N	83.9(29)	279.2(15)	31.6(18)	189.9(25)			
DR21 S	131.5(12)	600.9(15)	64.7(24)	584.6(22)			506
W75(OH)	144.6(42)	1041.6(21)	43.3(23)	822.1(19)			40
G97.53+3.19	8.8(31)						
BFS 11-B			0.4(08)		0.76	64	66
CepA	8.8(23)	42.8(27)		72.9(30)	8.37	84	
S158	307.9(28)	1177.2(16)		915.5(18)	19.69	91	206
S158A	182.2(17)				15.00	74	
NGC7538-IRS9	101.9(59)				3.60	81	
S157	8.5(46)	59.5(30)	4.0(62)	36.5(47)	2.24	86	141
IRAS19094+0944		210.5(77)		68.0(35)	2.97		

3.4 Discussion

A large sample of massive cores have now been mapped with dense gas tracers (HCN and CS), with a range of J levels. Although all these lines trace dense gas, higher J transitions trace even denser parts of the core. This property can be seen from the contour maps and the derived core sizes. Table 3.8 lists the statistics of the size ratios and luminosity ratios between maps of different tracers. The size of the HCN 3-2 map is about one third of HCN 1-0 maps, while the CS 7-6 map is only one quarter of the size of the CS 2-1 map. The mean value of the luminosity ratio has a large dispersion (the listed uncertainty in Table 3.8 is the sigma of the mean), indicating that the mean has been affected by a few very large values. The median value is more reasonable to reflect the statistical luminosity ratio. The median value for the ratio is 5.3 for L_{HCN1-0} to L_{HCN3-2}, and 19 for L_{CS2-1} to L_{CS7-6}, closer to the square of their size ratio, indicating that the extension of emission contributes most to the difference of luminosities of different J levels for the same molecule. From Table 3.8 we can also tell that HCN 1-0 and CS 2-1 trace almost the same dense regions, while HCN 3-2 and CS 5-4 trace similar regions; their luminosities are also close to each other.

The luminosity ratio of high J to low J transitions reflects the fraction of the amount of very dense gas to less dense gas, or to the total gas; it tells how much of the gas in the core is dense gas. This fraction may have some relations to the physical conditions, or the evolutionary states of the core. We tested the correlations between the luminosity ratio of HCN 3-2 to 1-0, and CS

Table 3.7 (cont'd)

Source	L(HCN3-2) [a] $Kkms^{-1}pc^2$	L(HCN1-0) [a] $Kkms^{-1}pc^2$	L(CS7-6) [a] $Kkms^{-1}pc^2$	L(CS2-1) [a] $Kkms^{-1}pc^2$	L_{IR} 10^4 $L_\odot$	T_{bol} [b] (K)	L_{bol}/M_{vir} [c] $L/M_\odot$
IRAS20050+2720	1.3(80)	11.3(72)		10.8(38)	0.03		
IRAS20106+3545		3.2(65)		3.1(64)	0.14		
IRAS20126+4104		35.7(19)		20.9(37)	5.98		
IRAS20188+3928		2.0(23)		2.5(31)	0.03		
IRAS20216+4107	0.11(84)	5.1(32)		1.7(42)	0.29		
IRAS20220+3728		503.4(52)		585.5(95)	6.07		
IRAS20333+4102		58.5(19)		25.1(28)	0.91		
IRAS21391+5802		4.5(31)		4.9(24)	0.03		
IRAS22172+5549		7.5(43)		6.5(60)	0.36		
IRAS22198+6336		12.5(56)		16.6(51)	0.09		
IRAS23011+6126	0.06(57)	3.7(40)		2.8(56)	0.01		
IRAS23385+6053		135.0(37)		95.0(38)	5.41		
L483	0.02(97)				0.0013		
IRAS03282+3035		1.6(84)		1.2(98)	0.00012		
L1251B		0.4(37)		1.2(67)	0.0011		
Mean[d]	138(54)	1173(372)	100(44)	1410(674)			
Median[d]	56	282	112	206			

[a]Uncertainties in percentage (%)

[b]From Mueller et al. (2003)

[c]From Shirley et al. (2002). L_{bol} is the bolometric luminosity that calculated from the SED of the source (Mueller et al. 2002); M_{vir} was calculated based on the FWHM size of CS 5-4 map and the line width of optically thin $C^{34}S$ 5-4 line.

[d]Statitics does not include the part 2 sources in Table 1.

Table 3.8 Ratio of sizes and Luminosities for different tracers[a]

	$\frac{R_{HCN1-0}}{R_{HCN3-2}}$	$\frac{R_{CS2-1}}{R_{CS7-6}}$	$\frac{R_{HCN1-0}}{R_{CS2-1}}$	$\frac{R_{CS5-4}}{R_{CS7-6}}$	$\frac{R_{HCN3-2}}{R_{CS5-4}}$
Mean	3.01±1.00	4.12±2.40	1.09±0.22	1.42±0.64	1.11±0.21
Median	2.88	3.36	1.06	1.31	1.05
	$\frac{L_{HCN1-0}}{L_{HCN3-2}}$	$\frac{L_{CS2-1}}{L_{CS7-6}}$	$\frac{L_{HCN1-0}}{L_{CS2-1}}$		
mean[b]	9.4±2.7	52±22	1.65±0.20		
median	5.3	19	1.25		

[a]Sizes of CS 5-4 maps come from Shirley et al. (2003).

[b]The uncertainty is the sigma of the mean

7-6 to 2-1, with some characteristic parameters that relate to cores' properties, including the infrared luminosity (L_{IR}, an indicator of star formation rate), the bolometric temperature (T_{bol}, the temperature of a blackbody with the same mean frequency of SED, which may relate to the evolutionary states of a core (Chen et al. 1995), and the luminosity per amount of dense gas (L_{bol}/M_{vir}, an indicator of star formation efficiency). We only considered cores in our well-studied massive cores sample; the sources in part 2 of Table 1 were not included in these tests. One source (121.30+0.66) in the sample has a much lower L_{IR} than the rest of sources, and one source (48.61+0.02) has a very low luminosity ratio of high J to low J transitions, which may be due to the fact that the core size for high J transitions of the source is small enough to be comparable to the beam size. So we didn't include these two unusual cores in our tests on these correlations.

The correlations between the luminosity ratios of high J to low J transitions and L_{IR}, T_{bol}, L_{bol}/M_{vir} are plotted in fig. 3.1 to fig. 3.3. We can see

from the plots that weak correlations exist between L_{HCN3-2}/L_{HCN1-0} and L_{IR}, T_{bol}, and L_{bol}/M_{vir}, with positive slopes for the linear least squares fit, and the χ^2s for the fits are about 1.2 to 1.5. There are no obvious correlations between the L_{CS7-6}/L_{CS2-1} and L_{IR}, T_{bol}, L_{bol}/M_{vir}; the χ^2s for the linear least squares fit are 5 to 6. The ratio of L_{HCN3-2}/L_{HCN1-0} seems to have tighter correlation than L_{CS7-6}/L_{CS2-1} with the physical conditions of massive dense cores.

Finally, let's look at the L_{IR}-$L_{molecule}$ correlation for all our tracers. Fig 3.4 presents the L_{IR} versus $L_{molecule}$ distribution for HCN 1-0, HCN 3-2, CS 2-1 and CS 7-6. The squares in figures are HCN 1-0 observations of galaxies (Gao & Solomon 2004a), and 3 detections of high redshift galaxies with HCN 1-0 (Solomon et al. 2003, Vanden Bout et al. 2004, and Carilli et al. 2005). The solid line shows the best fit of L_{IR}-L'_{HCN1-0} correlation for both Galactic and galactic sources with $L_{IR} > 10^{4.5} L_{\odot}$ (The dashed line). Fig 3.5 shows the correlation between the distance independent ratio L_{IR}/L'_{mol}, an indicator of star formation efficiency, and the L_{IR}, for different tracers.

From fig. 3.4 and fig. 3.5, we can see that the L_{IR}-L_{HCN1-0} correlation found in the galaxies extends to the Galactic scale; the star formation rate per mass of dense gas that is traced by HCN 1-0 is constant from distant galaxies to the Galactic cores, until a cutoff at about $10^{4.5} L_{\odot}$. This cutoff is also obvious for CS 2-1, but not very obvious for HCN 3-2 and CS 7-6, partly due to the lack of lower luminosity sources in their sample. The L_{IR}-L_{HCN1-0} correlation is almost the same for the Galactic cores with $L_{IR} > 10^{4.5} L_{\odot}$, with the slope

nearly unity. The linear least squares fit gives $log(L_{IR}) = 1.04(\pm0.06) \times \log(L_{HCN1-0}) + 2.73(\pm0.16)$, closer to the fit of the galaxy sample: $log(L_{IR}) = 1.00 \times \log(L_{HCN1-0}) + 2.9$. The luminosity of other three tracers also show linear correlations with the infrared luminosity. For HCN 3-2 and CS 2-1, the linear least squares fit gives $(L_{IR}) = 1.07(\pm0.08)\times\log(L_{HCN1-0})+3.46(\pm0.16)$, $(L_{IR}) = 0.81(\pm0.04) \times \log(L_{HCN1-0}) + 3.46(\pm0.10)$, for $L_{IR} > 10^{4.5}L_{\odot}$. For CS 7-6, we fit all the sources together since no sources in part 2 of Table 1 have been observed in this tracer, and the L_{IR}/L_{CS7-6} ratio doesn't obviously drop for our sample (fig. 3.5). The linear least squares fit for L_{IR}-L_{CS7-6} correlation is $(L_{IR}) = 0.98(\pm0.03) \times \log(L_{CS76}) + 4.02(\pm0.05)$. The details of the comparasion of this correlation in the galaxy scales and in the Galactic scales, and the physical meaning of this linear correlation will be discussed in Chapter 6.

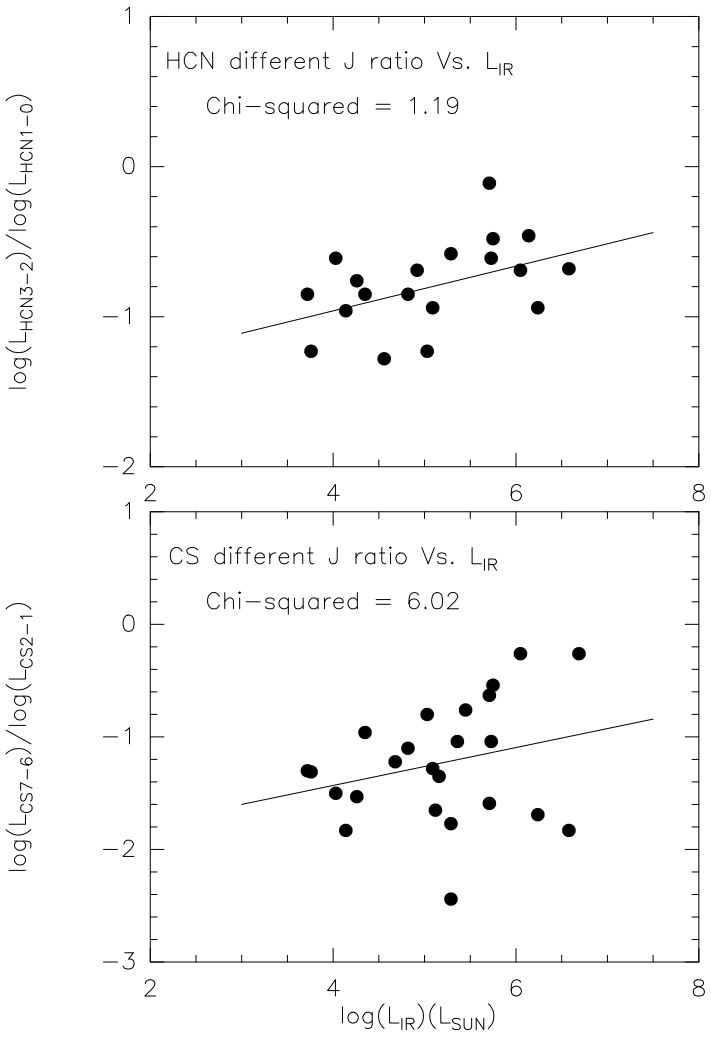

Figure 3.1 Luminosity ratios between different J transitions versus infrared luminosity. The solid line is the linear least squares fit of the sample.

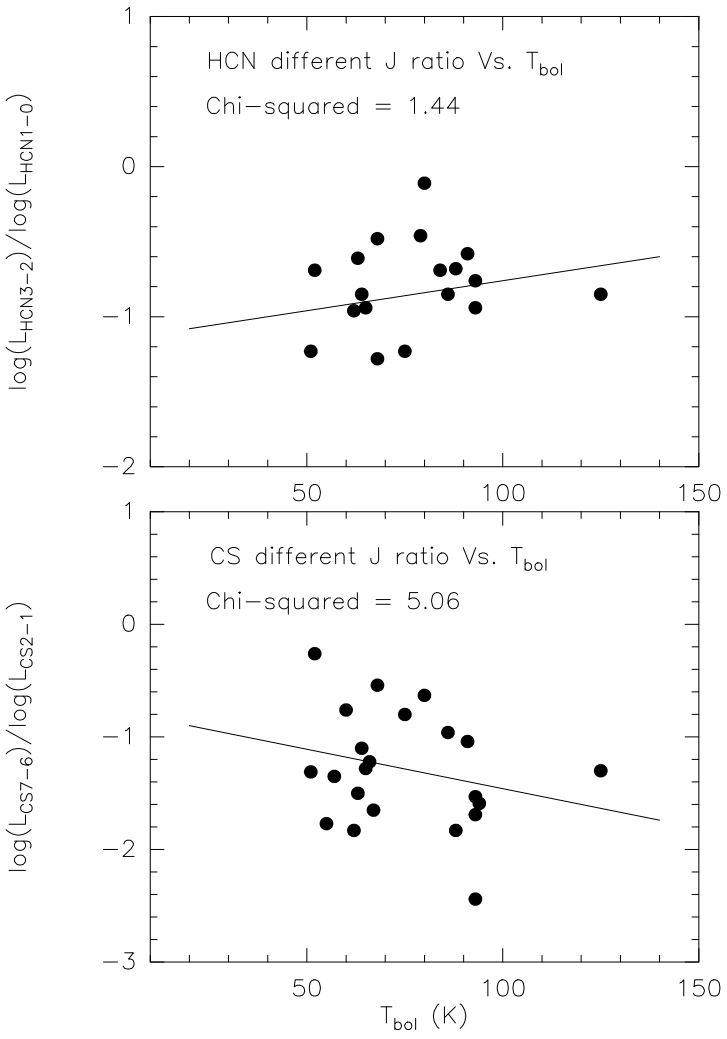

Figure 3.2 Luminosity ratios between different J transitions versus bolometric temperature. The solid line is the linear least squares fit of the sample.

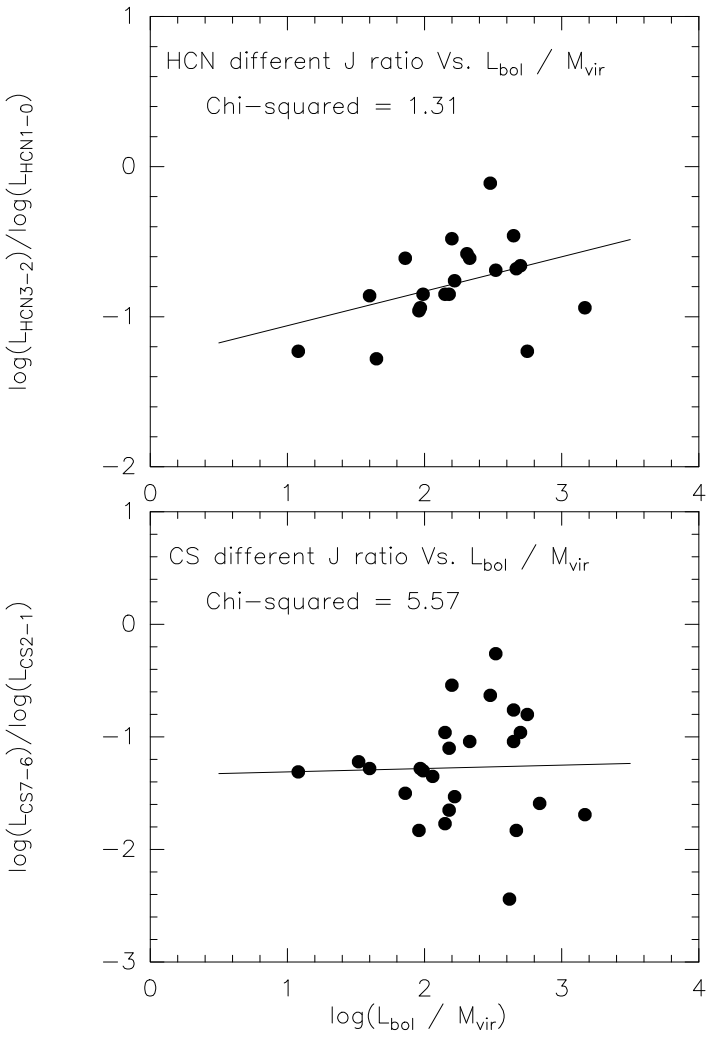

Figure 3.3 Luminosity ratios between different J transitions versus star formation efficiency. The solid line is the linear least squares fit of the sample.

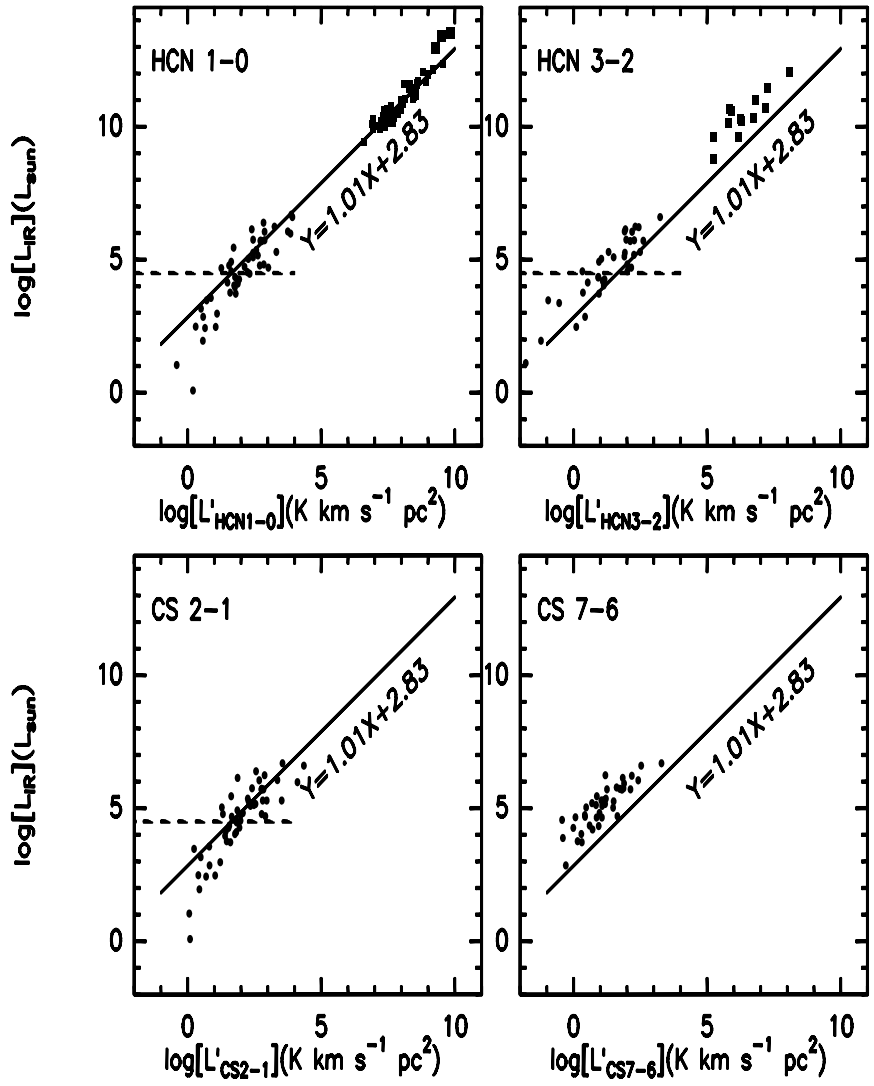

Figure 3.4 L_{IR}-L'$_{mol}$ correlation for HCN 1-0, HCN 3-2, CS 2-1 and CS 7-6 Galactic cores. The squres in the upper left panel are HCN 1-0 observations of galaxies (Gao & Solomon 2004a, Solomon et al. 2003, Vanden Bout et al. 2004, and Carilli et al. 2005). The squares in the upper right panel show the HCN 3-2 observations of galaxies (Paglione et al. 1997). The solid line in the first panel shows the best fit of L_{IR}-L'$_{HCN1-0}$ correlation for both Galactic and galactic sources with $L_{IR} > 10^{4.5} L_{\odot}$ (The dashed line), and is shown in other plots to indicate the correlation shifts between HCN 1-0 and other tracers.

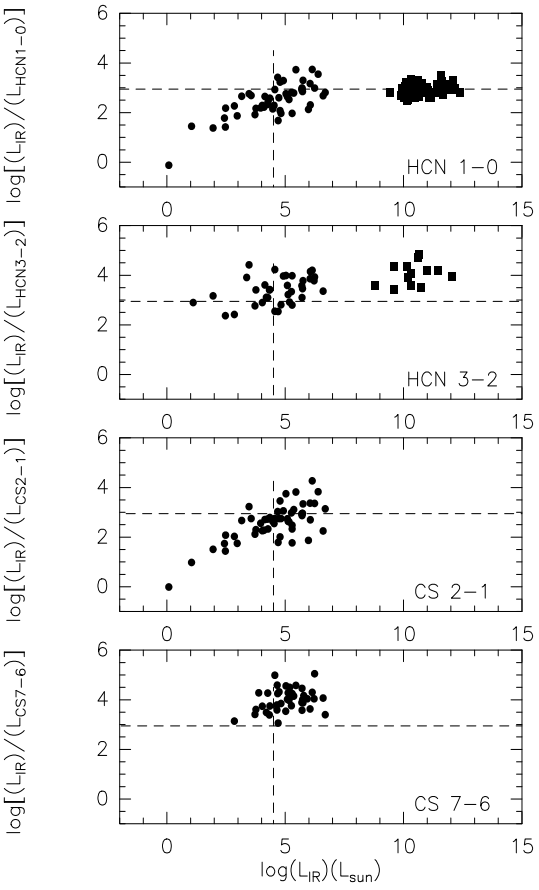

Figure 3.5 Correlations between the distant independent ratio L_{IR}/L'_{mol} vs. L_{IR} for different tracers. The squares in figures are HCN 1-0 observations of galaxies (Gao & Solomon 2004a) in the first panel, and HCN 3-2 observations of galaxies (Paglione et al. 1997) in the second panel. The horizontal dashed line in the top plot indicates the averaged L_{IR}/L'_{HCN1-0} ratio for galaxies; the vertical dashed line in the top plot shows the cutoff at $L_{IR}=10^{4.5}L_{SUN}$. These two lines are also shown in other plots to indicate the relative shifts of L_{IR}/L'_{mol} between HCN 1-0 and other tracers.

Chapter 4

Modeling Massive Star-forming Cores with 1-D Monte Carlo Simulation

4.1 Introduction

Indications of infall in massive star-forming cores have been found recently (e.g. Wu & Evans 2003, Sollins et al. 2005), showing that massive star formation may experience a collapsing phase in the early evolutionary stage, similar to that in low mass star formation. Some papers (e.g. Zhou et al. 1993, Choi et al. 1995, Myers et al. 1996) have modeled the spectral infall signatures in low-mass star-forming regions. More recently, models have included the chemical evolution as well as the dynamical evolution for low mass cores (e.g. Lee, et al. 2003, Evans et al. 2005). But no such attempts have been made for massive star-forming regions.

A large sample of massive star-forming cores has been studied intensively with multiple CS and HCN transitions and their isotopes (Plume et al. 1992, 1997, Shirley et al. 2003, Wu & Evans 2003). These massive cores have been mapped and studied using CS 5-4 transitions (Shirley et al. 2003); Some important physical conditions of these cores have been obtained. Dust continuum emission has been mapped at 350 μm and modeled (Mueller et al.

2002) to derive the density profile of the envelope of these cores.

Recently, we have conducted mapping surveys with other dense gas tracers (CS 2-1, CS 7-6, HCN 1-0, HCN 3-2) towards these massive cores; the results are presented in Chapter 3. Many of these cores were found to have infall signatures in HCN 3-2 spectra (Wu & Evans 2003). HCN and CS are commonly used as dense gas tracers to study star formation in other galaxies. A linear L_{HCN}-L_{IR} correlation has been found to extend from distant starburst galaxies to local Galactic massive star-forming cores (Gao & Solomon, 2004a,b, Wu et al. 2005). Understanding the role of HCN as a tracer of massive star formation in our Galaxy is the key to understanding this L_{HCN}-L_{IR} correlation in the Milky Way and in galaxies, which may be used to connect star formation from near to far.

The goal of this work is to test dynamical models of massive star-forming cores against this rich database, constraining the model with both the continuum emission and the observations of many molecular lines including HCN and CS, in order to understand the mechanism of massive star formation in the Galaxy. In this paper, we have attempted to model the massive star-forming cores with a 1D Monte Carlo simulation code. During the modeling, we considered the dynamical model of an inside-out infall model (Shu 1977), or a power-law infall model; we used an empirical step function for the chemical model of the core; and finally we constrained the modeled molecular spectra with multiple observational transitions. Observational data of HCN 3-2, HCN 1-0, CS 2-1, CS 5-4, CS 7-6, as well as $H^{13}CN$ 3-2, and $C^{34}S$ 5-4 were obtained

at CSO and FCRAO. The details of observations can be found at Chapter 3 of this Thesis.

4.2 Model Description

The routine to model an individual massive core follows a series of steps: create a 1D dynamical model to set the physical conditions of the cloud; use a dust radiative transport code to calculate the dust temperature as a function of radius; calculate gas kinetic temperature using a gas energetic code; vary the molecular abundance as a function of radius, based on likely cloud chemistry; run a Monte Carlo (MC) code to simulate the line radiative transfer; and run a virtual telescope code to model the observations. First we need to set up a physical model for the core. We assume a simple spherical symmetry for the core, in which the core is separated into many parallel shells in structure, with densities and velocities of each layer given by the dynamical model. We consider two types of dynamical models in this paper. One is the inside-out collapse model by Shu (1977). In this model the density profile adopts a power-law form $\rho \propto r^{-p}$, with power index $p = 1.5$ for the freely falling inner envelope and $p = 2.0$ for the static or nearly static outer envelope, with a transition zone in between. Based on the mass continuity equation applied to a spherically symmetric system, if the velocity field also has a power-law distribution $\upsilon \propto r^{-q}$, p and q must satisfy the equation $q = 2 - p$ (e.g. Jorgensen et at 2004). So the velocity field for Shu model is a power-law with a fixed index $q = 0.5$ for the inner infalling part, but $q = 0$ for the outer

envelope. The other model is the power-law model, in which both density and the velocity profile of the entire core can be described by single power-laws, but p and q are flexible, subject to the constraint that $p + q = 2$.

The code to create an inside-out infall model (Shu 1977) is "shu1". Since the "shu1" code was originally written to study infall in low-mass star-forming cores, the density created in this code is not high enough for conditions in high-mass regions. Massive star-formation may be a scaled-up version of low-mass star-formation with increased values of both density and turbulence. For example, the density of massive regions were found to be about 100 times higher than low mass star forming regions, but the density profiles are similar for both high-mass and low-mass star forming cores (Mueller et al. 2002, Shirley et al. 2000, Young et al. 2003). Here we scale up the density profile by a constant scale-up factor ($f_{n,scale}$) for the Shu model. This approach is not rigorously justified, but it is the simplest model to start with. If we start with a general power-law model, we use the code "powerlaw1", and we don't need to scale up density, since the density scaling factor (n_0) is a free parameter in the model now.

After we set up the dynamical model, a dust code (CSDUST3) from Egan et al. (1988) is used to calculate the dust temperature of each grid in the model. This calculation needs some basic information, like the temperature and bolometric luminosity of the central star, and properties of dust, like the type and opacity of dust grain. We used the OH5 dust model (Ossenkopf & Henning 1994) in our calculation. Since most of cores in our sample have been

modeled with their continuum emission as a constraint (Mueller et al. 2002), we just took the stellar properties that successfully fitted the continuum data into our dynamic model.

The next step is to calculate the gas kinetic temperature for each layer of the core. Because of the different grid system of the dust code and the code to calculate molecular emission, we need to set up a slightly different grid for the gas calculation. After this is done, we use the program "gastemp" to calculate gas kinetic temperature from dust temperature.

Then we prepare to simulate the radiative transfer for a specific molecule. The density profile, temperature profile and abundance profile will be set in making a dynamical model for a molecule. These profiles should be the same for the modeling for all the molecules for the same source in one model. A program "tk2mc" is used to insert the kinetic temperature that is calculated from the gas energetics into the grids of the gas model. The last adjustment is to change the abundance profile of the molecule. The molecule will deplete from the gas phase to dust grain surface at low temperature, and evaporate when temperature is high enough. The massive cores have a hot internal source, the abundance of a molecule will be lower at larger radius, and evaporation will start at some radius, inside which the abundance increase. We use the code "varx" to adjust the radius where the evaporation starts and the fraction of molecules that evaporate.

After all these steps, the model goes through a 1D Monte Carlo code "mc1" (Choi et al. 1995) to simulate the radiative transfer. Then a virtual

telescope model "vt1" is applied to the result from MC to simulate the line profile that would be "observed" by a modeled telescope. The modeled line will be compared with the real observations to give feedback to the model. Then the input parameters will be adjusted and the whole process iterated until a good match between modeled lines and observations is achieved.

4.3 Modeling strategy

4.3.1 Modeling strategy for inside-out collapse model

The free parameters to be fitted in a Shu model include infall radius (r_{inf}), inner radius (r_{in}) and outer radius (r_{out}) of the cloud, density scale-up factor ($f_{n,scale}$), microturbulence (b, which is the 1/e halfwidth of the line), molecule's abundance in outer envelope (X_0), depletion or evaporation radius (r_d), depletion or evaporation factor (f_d), and the strength of the Interstellar Radiation Field (G_0).

In the current model, we take a simple step function for the chemical model, in which

$$X(r < r_d) = X_0/f_d, f_d < 1$$

and

$$X(r > r_d) = X_0$$

In massive cores, the central source is the dominant heating source so that the inner envelope is always hotter than the outer part. Then the molecules actually freeze onto dust grain at larger radii, but evaporate towards smaller

radii. In this case, the f_d is always less than 1, and the f_d is actually the evaporation factor. For the current model, we set the r_d to be the radius where the gas temperature drops to the evaporation temperature of HCN (about 40 K), and keep the r_d to be the same for CS, since CS has a similar binding energy as HCN. The abundance will increase by a factor of $1/f_d$ inside this radius. The r_d identified in this way has a strong dependence of the temperature profile, which is mostly decided by the internal source's luminosity and density distribution of the core. So this r_d is not a free parameter in this treatment.

Now we have 8 free parameters to constrain in the model, most of which should be the same for all the molecules for one source except abundance (X) and evaporation factor (f_d). But later we found that sometimes we have to let turbulence (b) vary in order to model some lines, which will be discussed later. Then let's look at how many constraints we have to fit the model. The data of the following transitions at the center position are available for most of cores: HCN 3-2, HCN 1-0, CS 2-1, CS 5-4, CS 7-6, $H^{13}CN$ 3-2, and $C^{34}S$ 5-4. Maps of HCN 3-2, CS 5-4 and CS 7-6 with CSO have smaller beams than CS 2-1 and HCN 1-0 with FCRAO; they can give some constraints on total molecular emission and its variation with radius. So we have 7 single transitions and 3 maps, as well as their internal relations of transitions between different J but same molecule, or between isotopes.

Even with this big database of observations, not all the free parameters can be easily constrained, since there are so many of them and their contributions to some characters of a line profile may be blended. In our modeling work,

we tried to find the indicators that are most sensitive to some parameters, fixing them first, and then we tried to constrain other parameters with physical and chemical background knowledge, experience from previous modeling, and lots of tests. To make a simple start, we have made a few assumptions at this stage. First, since the internal source dominates the heating mechanism, we suppose the interstellar field is less important for these very young massive cores, and we set the G_0=1.0 for all the current testing. Second, we set the evaporation factor f_d=0.01, comparable to those in low-mass examples (e.g. Lee et al. 2003). These assumptions and the method to identify r_d with the evaporation temperature are used to simplify the chemical model in massive cores, because model of such regions are less developed. Once a more complicated chemical model is available, we will revise these parameters or let them be adjustable.

For the rest of the free parameters, the inner and outer radius of the cloud are set as the initial condition of a model and usually do not change during model testing. They are set by either the successful dust model (Mueller et al. 2002), or the experience from other gas models. For example, we usually set the inner radius of the gas model to correspond to $1''$ resolution at the cloud distance, since our tests indicated that using a even smaller inner radius didn't change any observable. We usually set the outer radius to be the one that is used in the dust model, or we estimated it from the extension of emission in contour maps of CS 2-1 or HCN 1-0, which trace relatively less dense envelope and can trace the boundary of the core. We usually set the inner radius for

dust grids to be much less than (about 1/5 of) the inner radius for gas, and the outer radius is set to be larger than gas grids, to make sure the gas grids and dust grids can match in the model. This pattern works well for most of our sources.

The first guess of the infall radius was based on the size of the region showing an infall signature in HCN 3-2 maps. We also found that the intensity ratio of the blue peak to red peak of the optically thick transition HCN 3-2 is very sensitive to the infall radius. This ratio gives a quantitive method to constrain the infall radius, as discussed later in an example.

Then there are three parameters left to be constrained, the abundance of the outer envelope (X), the density scale-up factor ($f_{n,scale}$), and the micro-turbulence (b). These are very important parameters to fit in the model since they directly describe the physical conditions in a cloud. But their effects are blended in line profiles, so they need to be fitted together. For instance, the line width is most sensitive to b, since in massive cores, turbulence dominates the thermal motion in the contribution to line width; but changes in the molecule's abundance can also lead to the broadening of a line when it gets optically thick. Both the density and molecular abundance contribute to the total line strength; you can get an equally strong line by reducing the density but increasing the abundance (see fig. 4.1 a). However, this degeneracy will be broken when the abundance becomes so large that self-absorption becomes important. It will change the line profile, usually showing a absorption dip in the center; this effect can tell the upper limit of abundance and lower limit of

the density scale-up factor (see fig. 4.1 b).

We can see that both X and b have a strong dependence on $f_{n,scale}$; $f_{n,scale}$ is very crucial to set up the model. When $f_{n,scale}$ is set, in principle we can obtain b from the fit of an optically thin line, then X can be constrained by the strength of both optically thin and optically thick lines. What is a good way to constrain $f_{n,scale}$? We took the ratio of two optically thick transitions of the same molecule, CS 7-6 and CS 5-4, as the indicator of density, since the population ratio of the two levels is more sensitive to the change of density than other factors. This method may give a narrow range of $f_{n,scale}$ that can fit. Then we use this density to fit the two groups of isotopes (HCN 3-2 and $H^{13}CN$ 3-2, CS 5-4 and $C^{34}S$ 5-4) together. These transitions should share the same dynamical conditions, but differ in their abundance: X[CS]/X[$C^{34}S$]$\sim$10-20, and X[HCN]/X[$H^{13}CN$]$\sim$70 for ISM (Wilson & Rood 1994). After all these isotopes are fitted, all the parameters should be mostly constrained.

4.3.2 Modeling strategy for power-law model

The major difference for the power-law model compared with Shu model is that we need to set up the density profile and velocity profile with flexible power index p and q. After these physical and dynamical structures of the cloud are set, the following procedures to model a line and to compare to observations are the same as in modeling with Shu model.

In power-law model, we don't need to fit an infall radius (r_{inf}) as in Shu model, but we have to consider some new free parameters: the velocity

scaling factor (V_{r0}) and the density scaling factor (n_0), which are the infall velocity and the density at some specific radius (In our code, these values refer to the velocity and density at r = 1 pc); and the power index of velocity (q) and density (p). So we lose three free parameters in Shu model (r_{inf}, $f_{n,scale}$), but have 3 more (V_{r0}, n_0, p, q, but $p = 2 - q$), with the same numbers of constraints .

Fixing r_{in} and r_{out} to be the same as in Shu model, we need to guess a density distribution (p), and use q = 2-p to get q. Since we have the density distribution from the continuum model (Mueller et al 2002) for most of our sources, we can start the test with a index p that close to the best-fit model from the continuum model. Instead of the density scaled-up factor ($f_{n,scale}$) in Shu model, the density scaling factor (n_0) is the direct parameter to probe gas density in the power-law model, which remains to be the key parameter to constrain abundance (X) and turbulence (b). We use the relative intensity of CS 7-6 and CS 5-4 to constrain the density (n_0), as in modeling with Shu model. The velocity scaling factor (V_0) adds another complexity to the power-law model comparing with Shu model. Now the infall velocity in the envelope may be reflected in the line width, so we need to adjust V_{r0} and b together to constrain the line width and some details (e.g. absorption features) of the line shape. Processes to constrain other free parameters follow the same routines as discussed in modeling with Shu model.

In this section I have outlined the general process that we used to model a massive core. But a real massive core may be more complex than the ideal

case, and sometime the general steps can not give a good fit to all the lines. In that case, we have to consider more complexity in the model, which we will discuss in detail in the modeling on individual cores.

4.4 Two Models in Detail

4.4.1 G10.6-0.4, A Case of a Collapsing Core

G10.6-0.4 is a very massive star-forming core 6.5 kpc away (Solomon et al. 1987), which shows a large-scale infall signature in the HCN 3-2 maps (see Fig 4.2.). The collapse signature of this core has also been seen from an interferometer observation with NH_3 (Sollins et al. 2005). Based on the model of continuum emission (Mueller et al. 2002), the central star luminosity of G10.4-0.6 is $9.2\times10^5 L_\odot$, and the outer cloud radius is 5.7 pc. The latter agrees with the extension of the emission in our HCN 1-0 and CS 2-1 contour maps of G10.6-0.4.

We set the inner radius of the gas in the cloud to be 0.03 pc, roughly corresponding to $1''$ resolution in this distance; we set the thickness of the second grid of gas to be 0.004 pc, and the outer radius of gas layer of the cloud to be 5.7 pc. We set the inner radius of the 1st dust grid to be 0.0063 pc, which is one thousandth of the outer radius of the cloud, and the outer radius of the dust grid to be 6.3 pc. After setting the physical parameters for the model, we started a series of codes to run the model.

4.4.1.1 Model with inside-out collapse model

For collapsing cores, first we want to constrain the infall radius of the core. In the HCN 3-2 map of G10.6-0.4, we noticed that the radius of cloud that shows a blue profile is about 20 to 30 arcseconds, corresponding to 0.6 to 0.9 pc in linear size. Then we varied the infall radius around this size to check the resulting intensity ratio of the blue peak to the red peak of the HCN 3-2 line, as shown in fig. 4.3. By this method, we found that the infall radius of the best fit model for G10.6-0.4 is 0.8 pc.

The next step is to find out the density scale-up factor $f_{n,scale}$. First we used the relative intensity of CS 7-6 to CS 5-4 to constrain this density. We also consider the line shape during the test. When the density is low, the X is so large that the absorption features are too deep. Fig. 4.4 shows the test results. Taking into account both the line shape and the intensity ratio, we conclude that $f_{n,scale}$ is about 45 to 60. We also noticed that CS 2-1 is not well fitted with the parameters that give a good fit for CS 7-6 and CS 5-4, suggesting that CS 2-1 may arise from a different environment than CS 7-6 and CS 5-4.

When we have narrowed down the density range, we model HCN 3-2, $H^{13}CN$ 3-2, CS 7-6, CS 5-4, and $C^{34}S$ 5-4 together, using the observations and the relative abundance between isotopes to constrain X, b, r_d, and further constrain $f_{n,scale}$. The best fit results are shown in fig. 4.5, and the fits to the HCN 3-2 map are presented in fig. 4.6. We can see that most transitions are fitted well, suggesting that the Shu model with an scaled-up density profile

Table 4.1 Best-fit parameters for the inside-out model of G10.6-0.4

Transition	r_{inf}	$f_{n,scale}$	abundance (X_0)	Microturbulence(b)
HCN (3-2)	0.8 pc	45	5×10^{-11}	3.3 km/s
CS (5-4, 7-6)	0.8 pc	45	1.2×10^{-10}	2.7 km/s
H^{13}CN (3-2)	0.8 pc	45	4×10^{-12}	2.7 km/s
C^{34}S (5-4)	0.8 pc	45	1.2×10^{-11}	3.5 km/s

can be applied to this massive star-forming core. The modeled lines are a little weaker than the observed lines in the outer part of fig. 4.6. This may be due to the side-lobe effect of the telescope in real observations, which is not considered in the model. We list the best-fit parameters for the inside-out model of G10.6-0.4 in Table 4.1.

The best-fit microturbulence for G10.6-0.4 is 2.7 kms^{-1}. We didn't include the thermal motion into the calculation because the turbulent motion dominates the line width of massive cores. Since the effective sound speed $a = b/\sqrt{2}$ (Shu et al. 1987), $r_{inf} = 0.8$pc, and the dynamical infall time $t_{inf} = r_{inf}/a$, the mass accretion rate for the inside-out collapse model is $\dot{M}= 0.975 \times a^3/G$. The sound speed in G10.6-0.4 is 1.9 km/s, the dynamical infall time is about 4×10^5 years, and the accretion rate in this collapsing core is about 1.6×10^{-3} $M_\odot$.

The abundance ratios for CS and HCN are X[CS]/X[C^{34}S] $\sim$ 10, and X[HCN]/X[H^{13}CN] $\sim$ 13. The abundance ratio for CS and C^{34}S is within the normal range, but the ratio for HCN to H^{13}CN is somewhat lower than the

usual value (e.g., Wilson & Rood 1994). This low HCN isotope ratio has also been reported in some low mass region (e.g., Jorgensen et at 2004), and it seems to be common in our modeling of massive cores.

4.4.1.2 Some questions and discussions

Although most of these lines are fitted well in this model, there are still problems left: 1). Low J transitions CS 2-1 and HCN 1-0 can not be well fitted with the same conditions as other higher J transitions; 2). All modeled lines have the same microturbulence b except HCN 3-2, which always needs a larger b to fit (fig. 4.5e). 3). The most optically thick lines HCN 3-2 and CS 7-6, CS 5-4 need a slightly different V_{LSR} ($V_{LSR} = -2.8$) than other less opaque lines ($V_{LSR} = -1.5$) to fit. The first two problems are general in our modeling of massive cores; the third is a specific problem for G10.6-0.4. In the following paragraphs we will discuss these problems and try to find the answers.

First, let's see what are the conditions that can fit the observation of CS 2-1 and HCN 1-0 lines. Fig. 4.7 show the best fit for CS 2-1 and HCN 1-0 spectra. We can see that if we keep their abundance to be the same as higher J transitions, then we need to reduce their density scale-up factor to $f_{n,scale} \sim 30$; if we keep the density level to be the same, then we have to reduce their abundance. From our survey we have found that HCN 1-0 lines trace much more extended regions than HCN 3-2 (about 3 times larger in size); the same happens to CS 2-1 comparing to CS 5-4 emission. While HCN 1-0

roughly traces the same size as CS 2-1, the emission areas are similar between HCN 3-2 and CS 5-4. The extended CS 2-1 and HCN 1-0 emission seems to require less molecules than predicted by the model. This may be due to the effect of photodissociation by the interstellar field, which would affect mostly the outer part of the cloud.

Why does HCN 3-2 need a larger line width to fit than the rest of the lines? We first consider the influence from the hyperfine components. HCN 3-2 has 5 hyperfine components with close frequencies, but the main component has more than 70% of the intensity. We have tried to model the HCN 3-2 with a model that considers every hyperfine component as a individual line, and later to combine their contributions together. The result is shown in fig. 4.8. It seems that the line should be much too strong if we keep the best-fit condition and treat each hyperfine component independently. To get the total strength to be correct, we have to decrease the density a lot. As we see in the case when $f_{n,scale}$=10, the total strength is about right, but we can't get the right absorption dip in line profile, and we know from modeling CS transitions that $f_{n,scale}$ can not be so small, otherwise the very high abundance will lead to serious absorption in CS lines, which wasn't shown. The only explanation to this is that we can't treat each hyperfine component individually, since their frequencies are within the linewidth, and they can trap each other's emission. We also can't totally exclude the possibility that the hyperfine components may have something to do with the larger line width for the HCN 3-2 transition.

Another possible explanation for the wider line of HCN 3-2 is that this tracer traces the more turbulent part deep in the core, where infall occurs. HCN 3-2 is the only tracer in our lines that shows obvious infall signature in this and other massive cores.

One puzzle for this model for G10.6-0.4 is that to fit HCN 3-2, CS 7-6, and CS 5-4 lines, we need a different V_{LSR} (V_{LSR}=-2.8) than for the other lines (V_{LSR}=-1.5). There is no obvious reason that the central velocity for an optically thick line is different from what is revealed by optically thin lines. Let's see what happens if we just use V_{LSR}=-1.5 to fit HCN 3-2. As seen in fig. 4.9 a1, the modeled absorption dip will shift to blue side of the real absorption. One solution is that if the outer envelope is not static, but has a constant inward velocity, then the modeled absorption center will "move" to the real absorption dip. So in the following test, we assigned the outer envelope a constant infall velocity V_r=-2.0 km/s. The HCN 3-2 line can then be fitted by the same LSR velocity as optically thin tracers. We applied the same assumption to CS 5-4, CS 7-6; the fit is not perfect, but OK (fig. 4.9 c). This assumption seems to have no effect on the modeled lines of the optically thin lines $H^{13}CN$ 3-2 and $C^{34}S$ 5-4 (fig. 4.9 d).

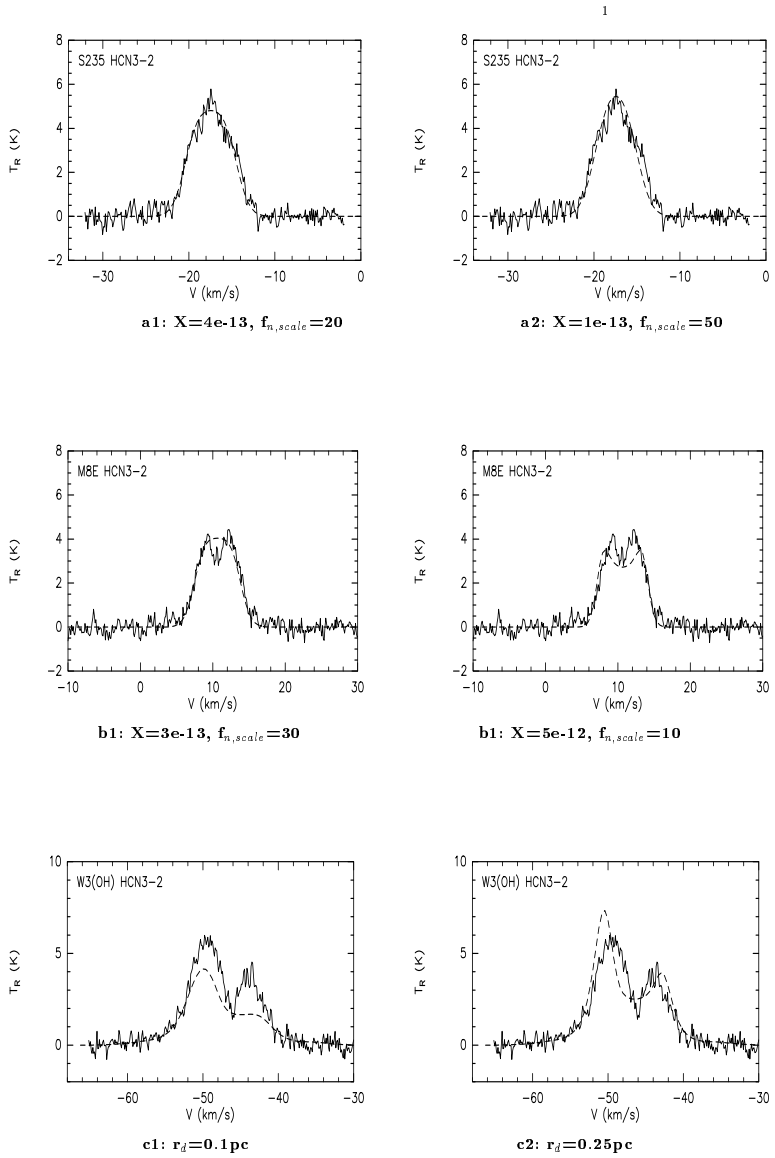

Figure 4.1 Examples to model a spectral line. The dashed lines are profiles from our models, and the solid lines are from observations. a: Decreasing X can be compensated by increasing $f_{n,scale}$; b: A constraint to X is that very high X leads to self-absorption feature that changes line profile with the changing of X; c: r_d can change the line shape by changing the amount of absorption.

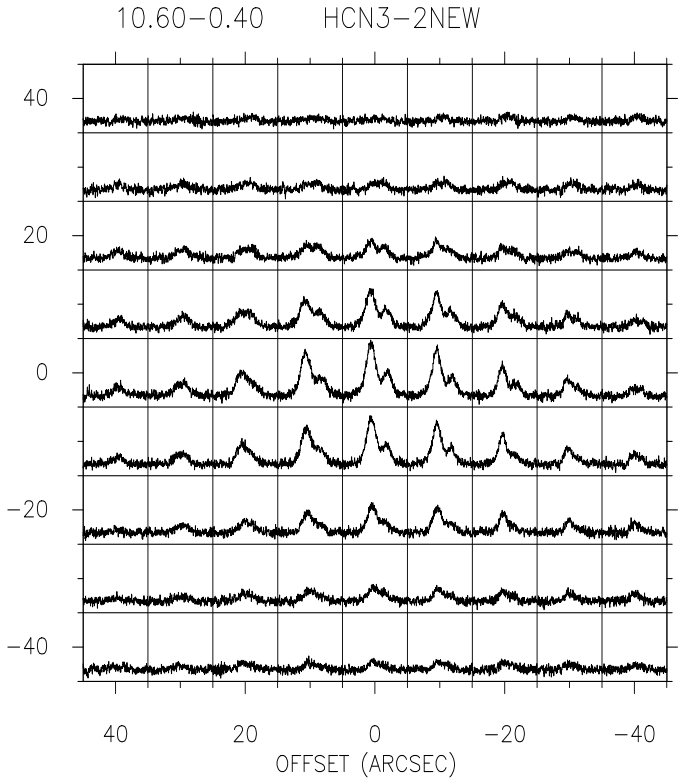

Figure 4.2 HCN 3-2 grid map of G10.60-0.40

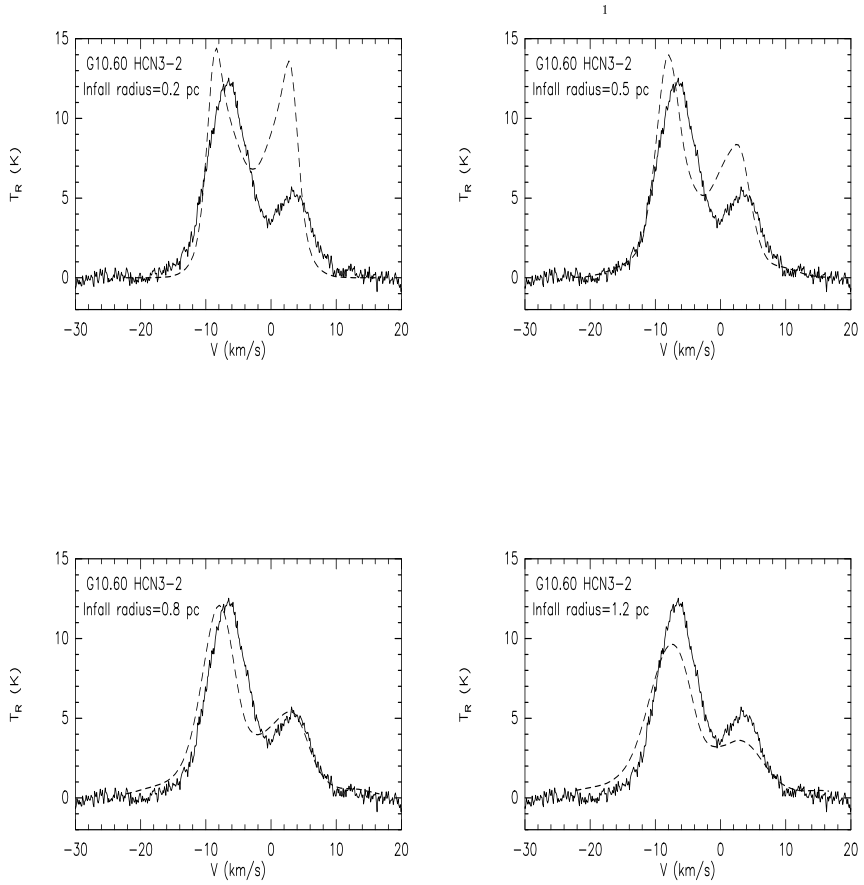

Figure 4.3 The intensity ratio of the two peaks of HCN 3-2 spectral line can be used to constrain the infall radius of the cloud

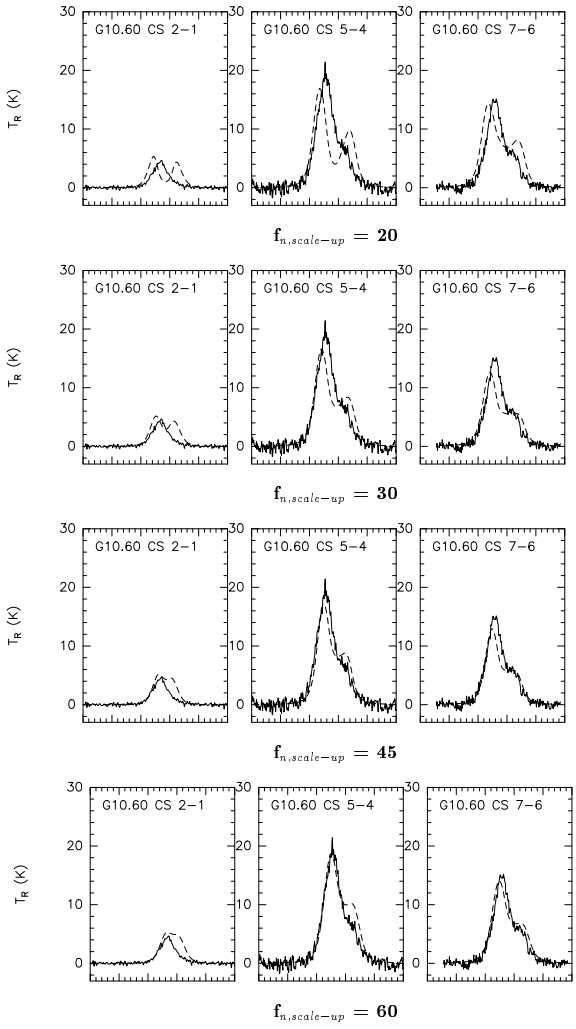

Figure 4.4 The intensity ratio of CS 7-6 to CS 5-4, together with the absorption feature, can be used to constrain the density scale-up factor

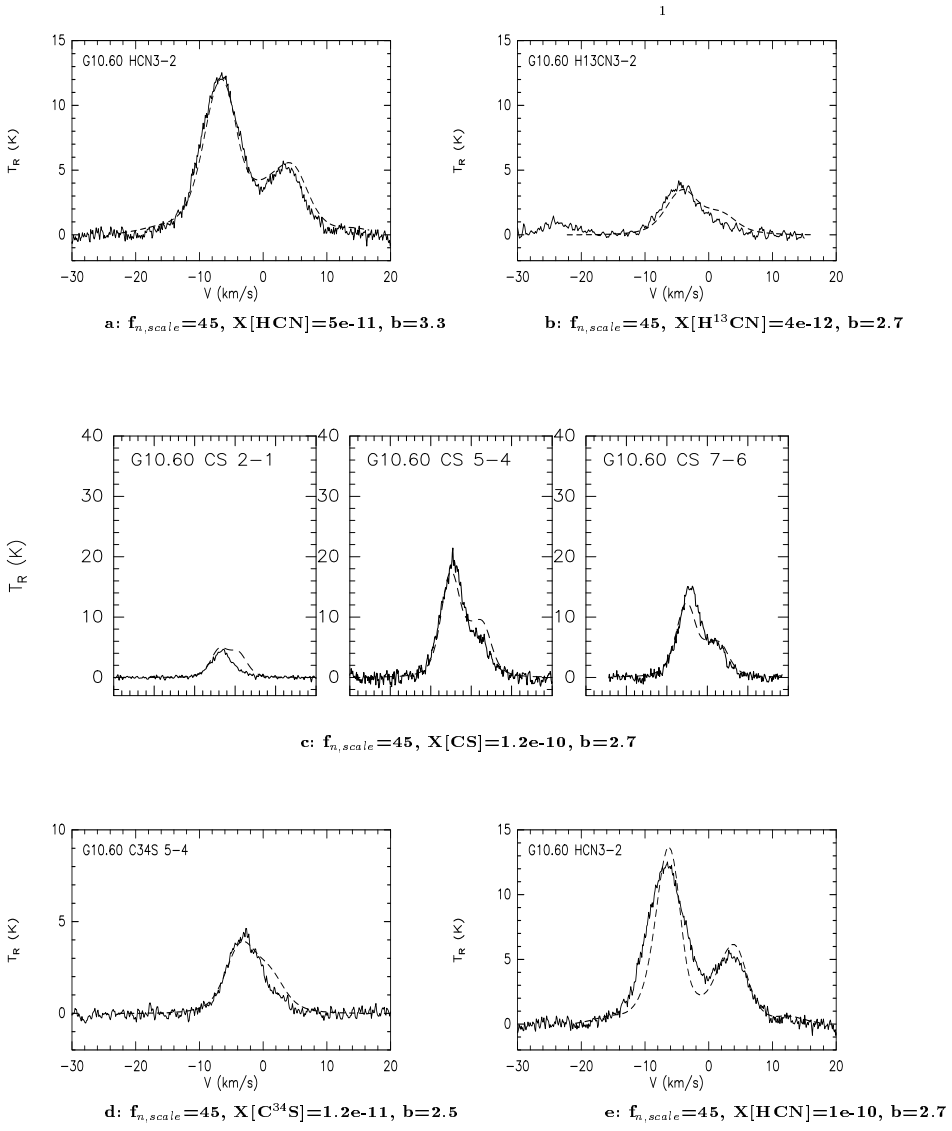

a: $f_{n,scale}$=45, X[HCN]=5e-11, b=3.3

b: $f_{n,scale}$=45, X[$H^{13}CN$]=4e-12, b=2.7

c: $f_{n,scale}$=45, X[CS]=1.2e-10, b=2.7

d: $f_{n,scale}$=45, X[$C^{34}S$]=1.2e-11, b=2.5

e: $f_{n,scale}$=45, X[HCN]=1e-10, b=2.7

Figure 4.5 The best-fit model for G10.6-0.4. Fig. 4.5e shows that the micro-turbulence b that fit in other lines can not match HCN 3-2 line, which needs a large turbulence.

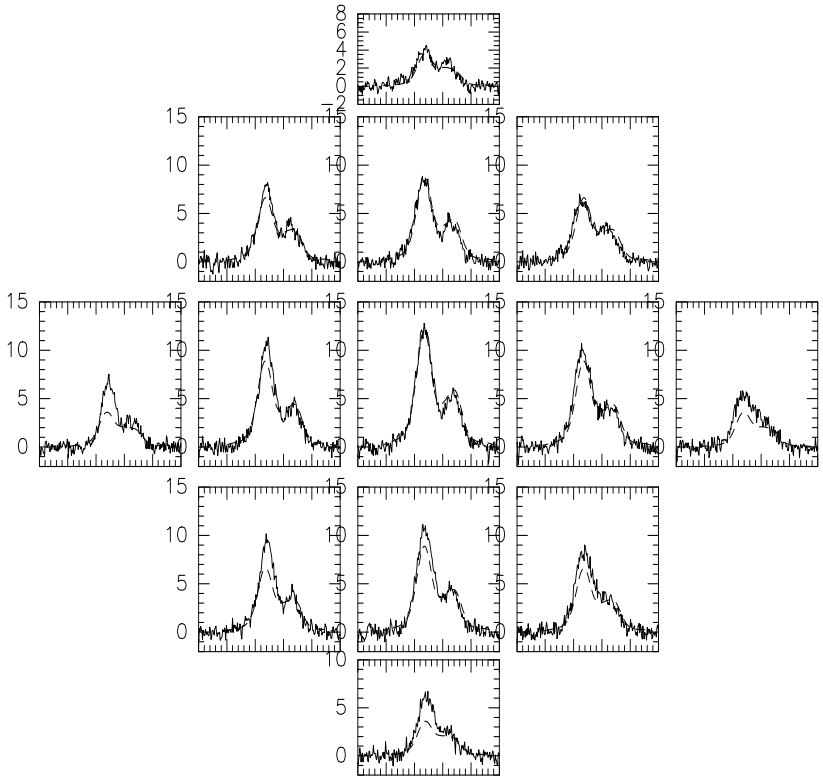

Figure 4.6 The best-fit Shu model of HCN 3-2 grid map for G10.60-0.40. Solid line is observed spectra, and the dashed line are modeled lines. The Shu model fit the observed HCN 3-2 map well.

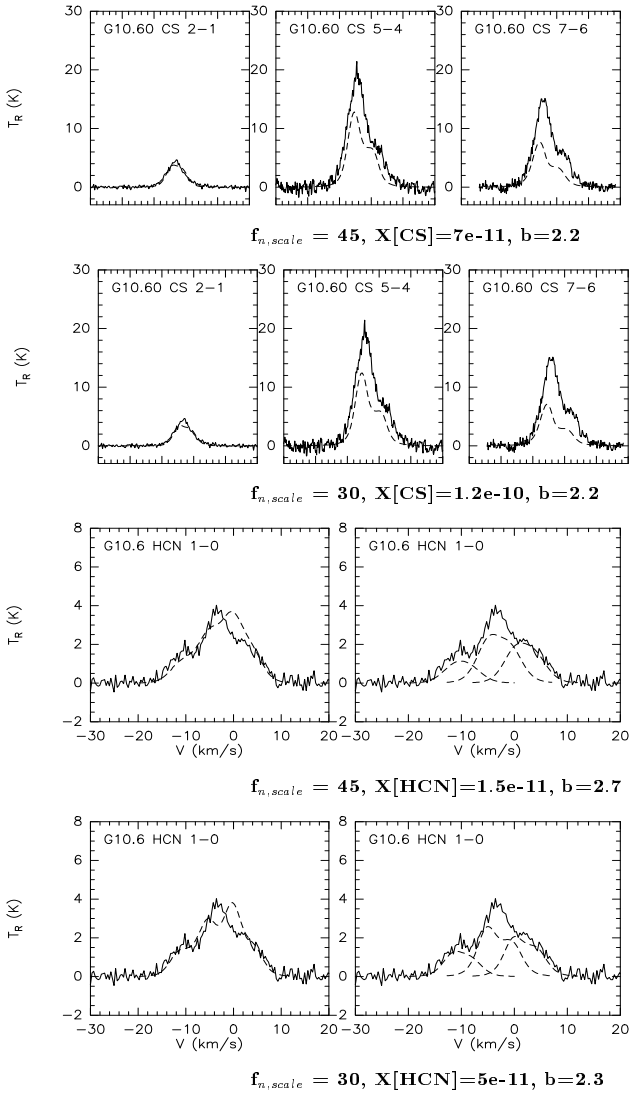

Figure 4.7 Low J transitions (CS 2-1 and HCN 1-0) need a lower abundance (1st and 3rd plot) or lower density (2nd and 4th plot) compared to the best-fit of high J tansitions, to fit their observations. The dashed line in the left panels of HCN 1-0 models are modeled line that are combined from individual models of each hyperfine component, shown in right panels.

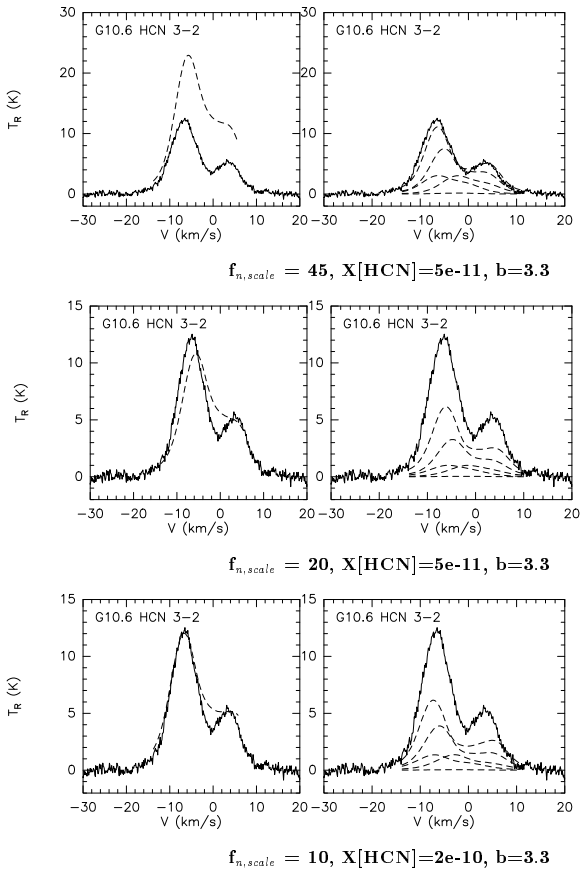

Figure 4.8 Test the contribution of hyperfine components to the unusual larger linewidth in HCN 3-2. The tests show that hyperfine components is not the answer to the large linewidth. The dashed line in the left panels are modeled line that are combined from individual models of each hyperfine component, which are shown in right panels.

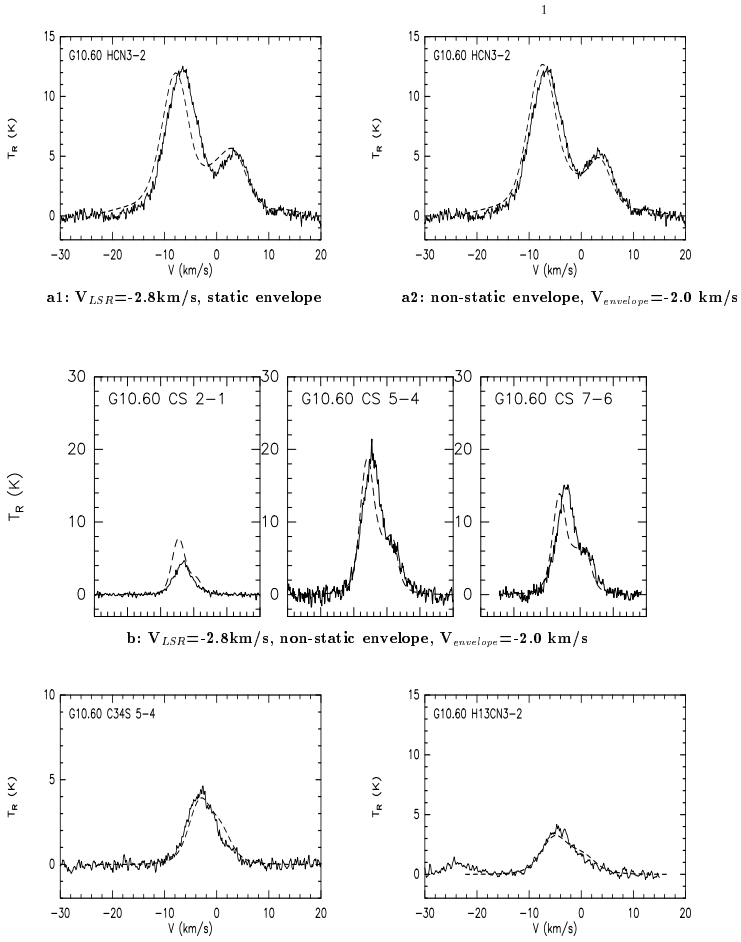

a1: V_{LSR}=-2.8km/s, static envelope **a2: non-static envelope, $V_{envelope}$=-2.0 km/s**

b: V_{LSR}=-2.8km/s, non-static envelope, $V_{envelope}$=-2.0 km/s

c: V_{LSR}=-2.8km/s, non-static envelope, $V_{envelope}$=-2.0 km/s

Figure 4.9 A non-static infalling envelope (a2 to c) instead of a static one (a1) can solve the problem of different V_{LSR} between optically thick and optically thin lines for G10.6-0.4.

4.4.1.3 Model with power-law dynamical model

When modeling G10.6-0.4 with a Shu model, we have introduced a constant infall velocity for the outer envelope to solve the problem of the absorption feature shift between the modeled line and the observed line. If we don't keep the outer envelope static, but let the infall velocity field extend from inner to outer envelope, this in fact assigns a power-law density and velocity distribution in the outer envelope. Starting with this idea, we have tested the simulation on G10.6-0.4 with power-law models using various values of p and q.

We set the inner and outer radius of the gas and dust grids for the power-law model of G10.6-0.4 to be the same as we set for Shu model. The density profile of the continuum model for G10.6-0.4 gives a power index of p=2.5 (Mueller et al. 2002), which is larger than 2. But q can't be negative, so we need to test a flatter density profile with smaller p. We first chose the velocity profile to be a natural extension of Shu model, which means q=0.5, and p=1.5. This model supposes that there is not a distinct break of infall in the whole cloud. Then we run models to constrain other parameters.

The first step is to constrain the density (n_0). Based on the relative intensity of high J CS transitions (CS 7-6 and CS 5-4) and the modeled line profile, we concluded that n_0 is about 7×10^4 (at $r = 1pc$) for this model (see fig. 4.10). Fig. 4.10 b shows that adjusting V_0 and b together can not only change the line width, but also adjust the line shape, such as the absorption feature. The fit of the HCN 3-2 line based on this density is shown in fig.

Table 4.2 Best-fit parameters for the power-law ($p = 1.5$) model of G10.6-0.4

Transition	n_0	v_0	abundance (X_0)	Microturbulence(b)
HCN (3-2)	7×10^4	-2.0 km/s	6×10^{-11}	3.3 km/s
CS (5-4, 7-6)	7×10^4	-2.0 km/s	3×10^{-10}	2.0 km/s
H^{13}CN (3-2)	7×10^4	-2.0 km/s	3×10^{-12}	2.7 km/s
C^{34}S (5-4)	7×10^4	-2.0 km/s	8×10^{-12}	2.0 km/s

4.11 a, and the best-fit models for $H^{13}CN$ 3-2 and $C^{34}S$ 5-4 are presented in fig. 4.11d and 11e. The fitting of HCN and CS lines for the power-law model is as good as that in Shu model. The best-fit parameters for the power-law ($p = 1.5$) model of G10.6-0.4 are listed in Table 4.2.

In modeling G10.6-0.4 with Shu model, we have found that high J HCN (3-2) and CS (7-6, 5-4) transitions need a shifted V_{LSR} from the central velocity of optically thin lines to best fit their lines. This problem also exists in the power-law model. As seen in fig. 4.10c and fig. 4.11b, if we set the V_{LSR} of HCN 3-2 and CS 7-6, CS 5-4 to be -1.5, different by 1.3km/s from the V_{LSR} of optically thin lines (-2.8km/s), then the modeled line and the observations fit best. To solve the puzzle, we introduce a constant infall velocity for the outer part of envelope (r> 0.35 pc) as we did in Shu model. The resulting models are shown in fig. 4.10d and fig. 4.11c; it doesn't help a lot this time.

The density distribution of the power-law model with $p = 1.5$ is shown in fig. 4.12 to compare with that of Shu model. The grid map of HCN 3-2 spectra created by this power-law model is shown in fig 4.13. It shows that

Table 4.3 Best-fit parameters for the power-law ($p = 1.25$) model of G10.6-0.4

Transition	n_0	v_0	abundance (X_0)	Microturbulence(b)
HCN (3-2)	1×10^5	-1.6 km/s	6×10^{-11}	2.5 km/s
CS (5-4, 7-6)	1×10^5	-1.6 km/s	2×10^{-10}	1.8 km/s
H^{13}CN (3-2)	1×10^5	-1.6 km/s	3×10^{-12}	2.0 km/s
C^{34}S (5-4)	1×10^5	-1.6 km/s	8×10^{-12}	1.8 km/s

despite the difference in the density profiles, the modeled HCN 3-2 spectra show little difference and both fit the grid map.

Then we varied the density profile, to set p to be flatter and steeper, ($p = 1.25$ and $p = 1.75$, then $q = 0.75$ and $q = 0.25$, respectively) and tested the power-law model. The density profiles of these two models are shown in fig. 4.14. We followed the same routine to constrain the free parameters, and got their best-fit models, as shown in fig. 4.15 and fig. 4.16. The best-fit parameters for the power-law ($p = 1.25$) model of G10.6-0.4 are given in Table 4.3.

These parameters are not very different from the fitting of $p = 1.5$ power-law model. The model with the flatter density profile ($p = 1.25$) has a better model fit for the HCN 3-2 line, while the model with steeper p (1.75) can not fit the absorption feature well. Their fitted grid maps of HCN 3-2 are shown in fig. 4.17.

We can see that in these power-law models, the fitting to the observations are still good, although the absorption features of HCN 3-2 spectra are

not so perfectly fitted as in Shu model. The turbulence in the cores is less than predicted by the Shu model. Another interesting result is that the HCN isotope ratio is larger ($\sim$20 in the power-law models than in Shu model ($\sim$13), and the CS isotope ratio is also double its value from that in Shu model. These ratios are closer to the predicted ratio in ISM.

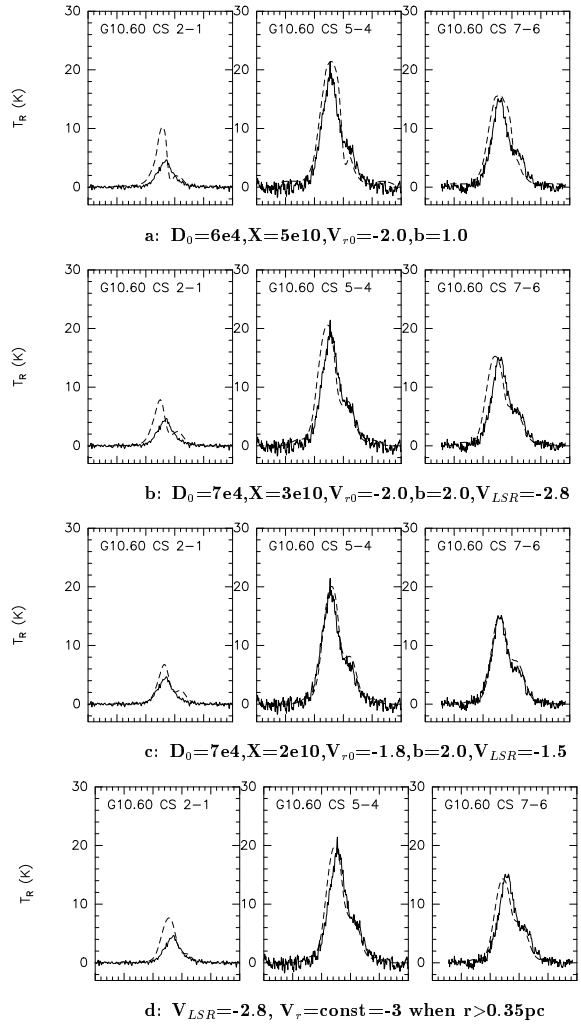

Figure 4.10 Using the intensity ratio and the absorption feature of high J CS transitions to constrain density, and turbulence for power-law model of G10.6-0.4. a and b: changing b will affect the absorption in high J CS lines. b and c: high J CS seems to prefer a different V_{LSR} than optically thin line. d: Give the outer envelope an constant infall velocity doesn't help a lot on this problem.

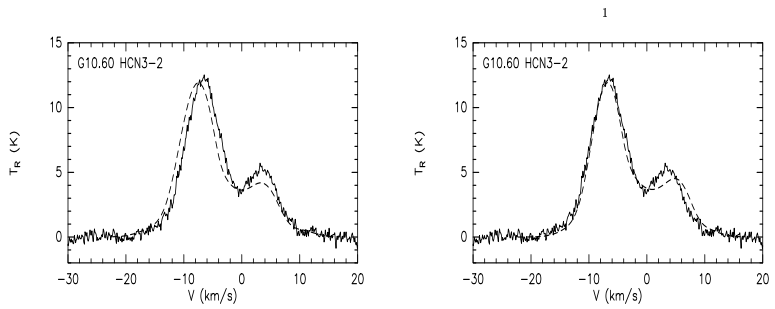

a: n_0=7e4,X=6e11,b=3.3,V_{r0}=-2.0,V_{LSR}=-2.8 **b: n_0=7e11,b=3.5,V_{r0}=-1.7,V_{LSR}=-1.5**

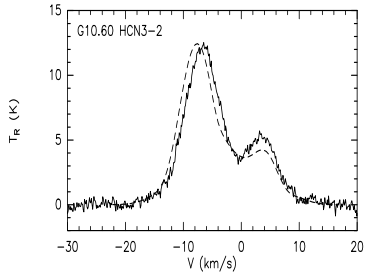

c: V_{r0}=-1.7,V_{LSR}=-2.8, V_r=const=-3.0 when r> 0.35 pc

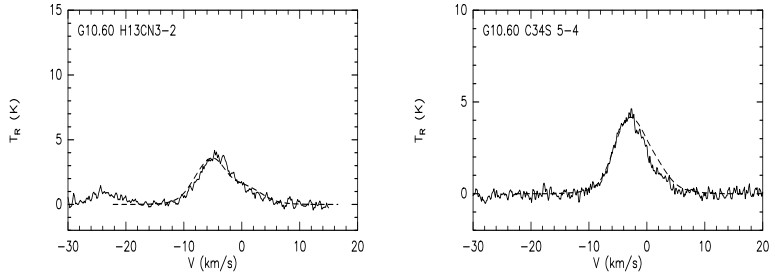

d: n_0=3e12,b=2.7,V_{r0}=-1.7,$\frac{X[HCN]}{X[H^{13}CN}$=23 **e: n_0=8e12,b=2.0,V_{r0}=-1.7,$\frac{X[CS]}{X[C^{34}S}$=25**

Figure 4.11 Best-fit power-law model of G10.6-0.4 for HCN 3-2, $H^{13}CN$ 3-2 and $C^{34}S$ 5-4, with $p = 1.5$

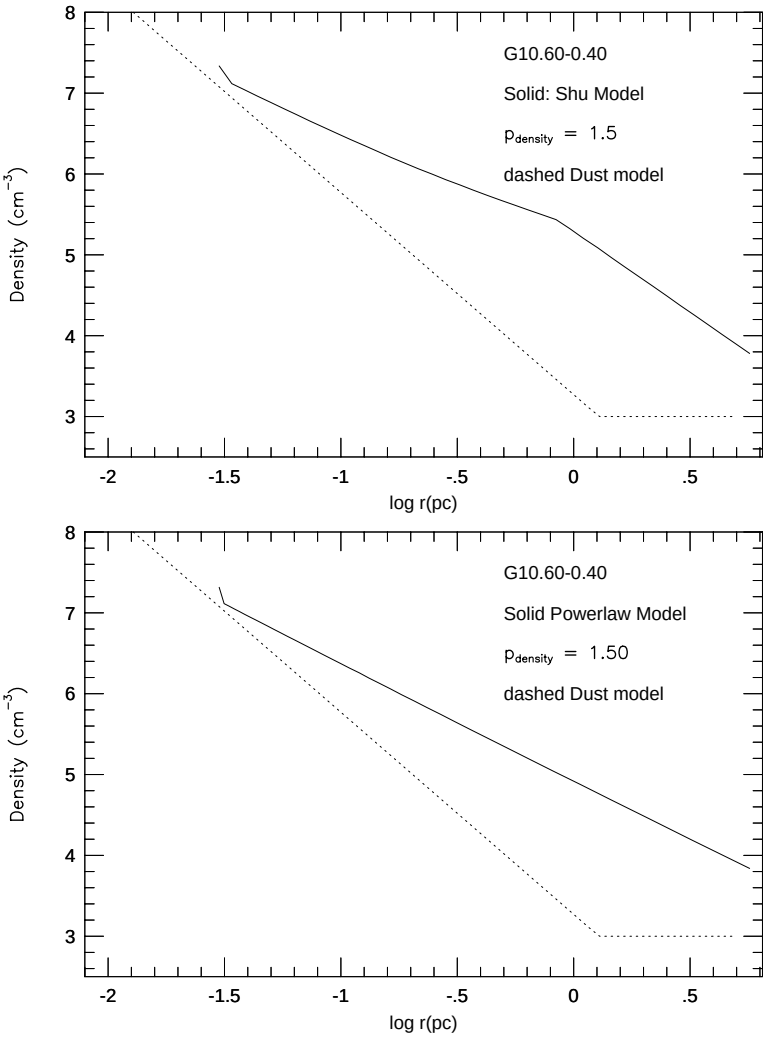

Figure 4.12 The density profile of Shu model and power-law model with $p = 1.5$ for G10.6-0.4

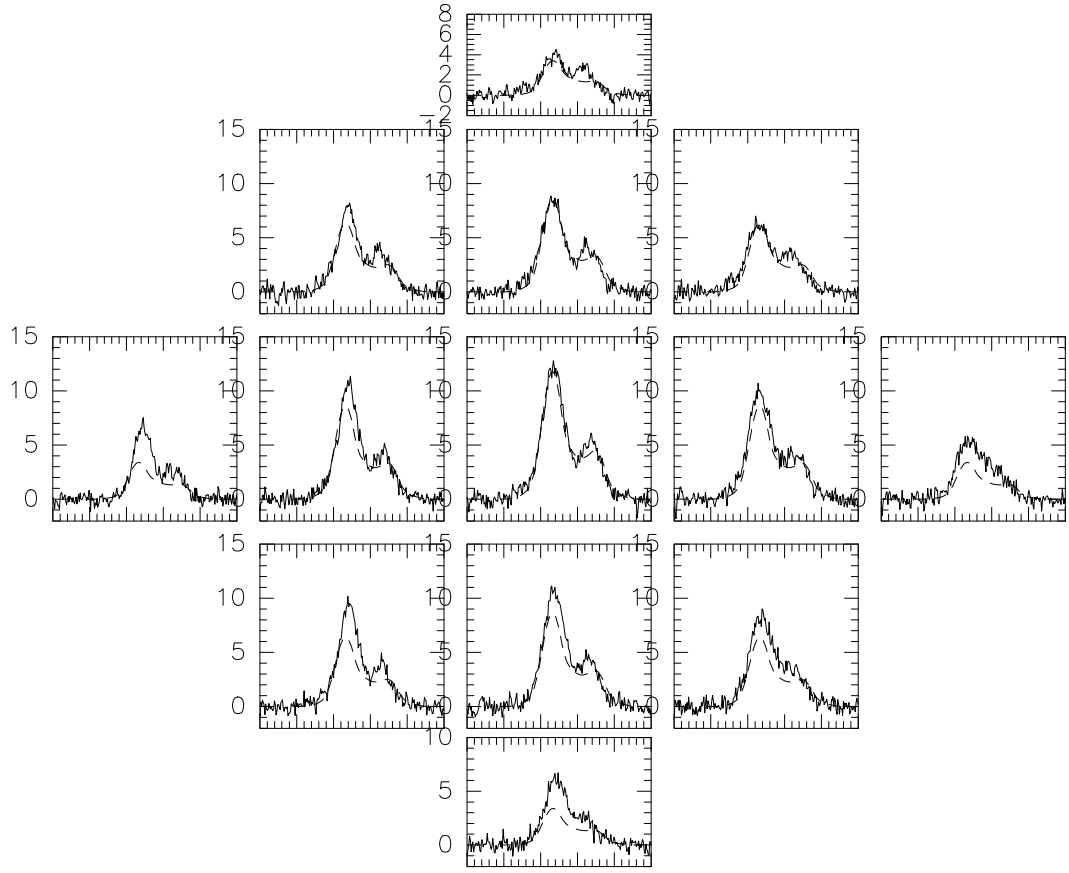

Figure 4.13 HCN 3-2 grid map of G10.60-0.40, with power-law model p=1.5

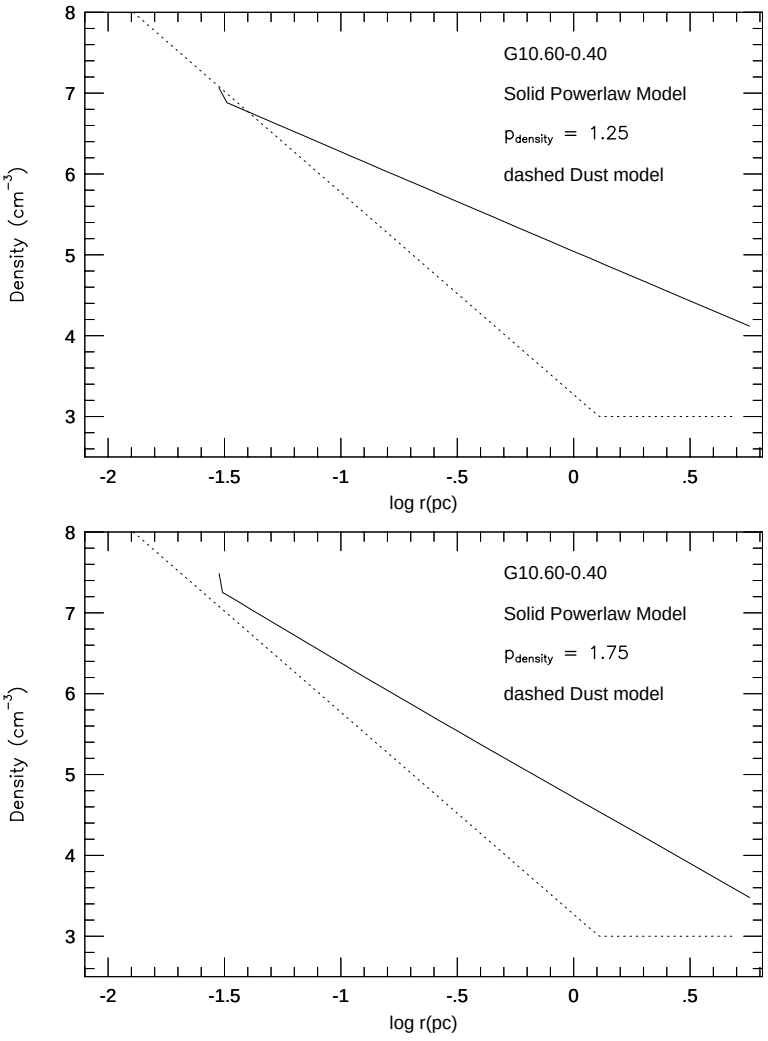

Figure 4.14 The density profile of power-law model with $p = 1.25$ and $p = 1.75$ for G10.6-0.4

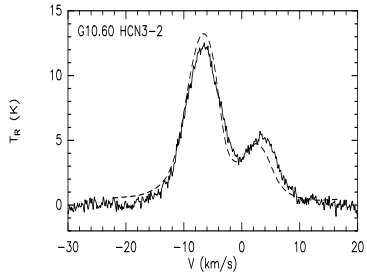

a: n_0=1e5,X=6e-11,b=2.5,V_{r0}=-1.6,p=1.25, q=0.75

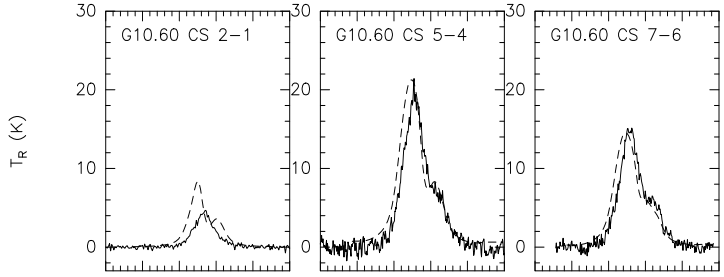

b: n_0=1e5,X=2e-10,b=1.8,V_{r0}=-1.6,p=1.25, q=0.75

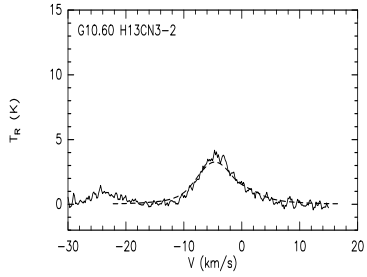

c: n_0=3e-12,b=2.0,V_{r0}=-1.6,$\frac{X[HCN]}{X[H^{13}CN}$=20

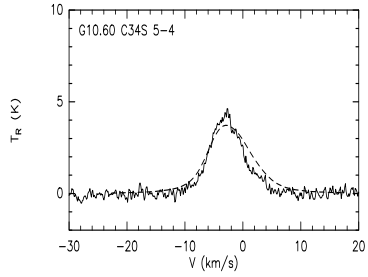

d: n_0=8e-12,b=1.8,V_{r0}=-1.6,$\frac{X[CS]}{X[C^{34}S}$=25

Figure 4.15 Best-fit power-law model of G10.6-0.4 for HCN 3-2, $H^{13}CN$ 3-2 and $C^{34}S$ 5-4, with $p = 1.25$

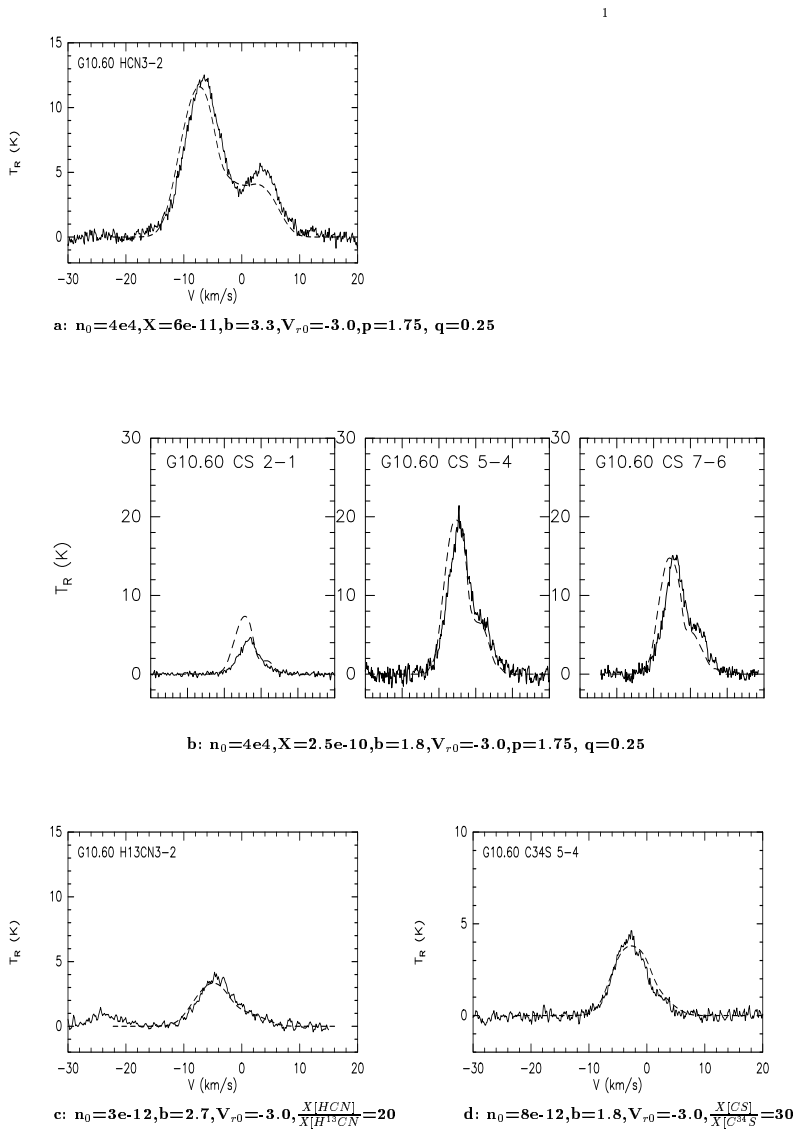

Figure 4.16 Best-fit power-law model of G10.6-0.4 for HCN 3-2, $H^{13}CN$ 3-2 and $C^{34}S$ 5-4, with $p = 1.75$

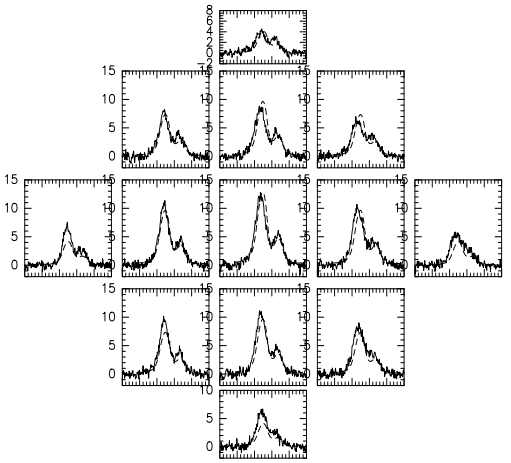

a: p=1.25, q=0.75

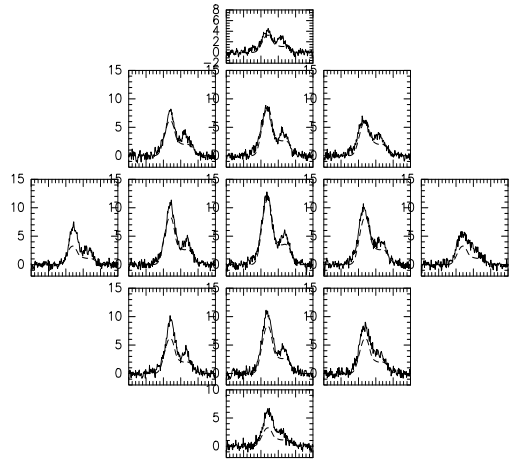

b: p=1.75, q=0.25

Figure 4.17 HCN 3-2 grid maps for G10.6-0.4 fitted by power-law model with $p = 1.25$ and $p = 1.75$

4.4.2 S235, A Case of a Static Massive Core

S235 is a massive core located 1.6 kpc away (Blitz et al. 1982). There is no self-absorption feature in the HCN 3-2 spectra for S235, so we treat the source as a static case.

From the dust model, Mueller et al. (2002) derived that the central luminosity of S235 is $1.1\times10^4 L_\odot$, and the outer cloud radius is 1.86 pc. Technically, we set the infall radius of S235 to be 0.001 pc to simulate a case with a negligible infall region. Following the same way as we did in G10.6-0.4, we set the inner radius of gas grid and for dust grid of cloud to be 0.008 pc and 0.0016 pc, respectively, and set the outer radius of dust grid to be 2.4 pc.

4.4.2.1 Model with inside-out collapse model

To start the model, we still need to find the density scale-up factor from the ratio of high J CS transitions first. The example was shown in fig. 18. We concluded that $f_{n,scale}$=50 best fit the CS 7-6 and CS 5-4 observations. So we took $f_{n,scale}$=50 for the modeling of other lines.

Fig. 19 demonstrates the fittings of the best fit model for other lines for S235, with the method to constrain the model as introduced in previous sections. The best-fit parameters for the inside-out model of S235 are given in Table 4.4.

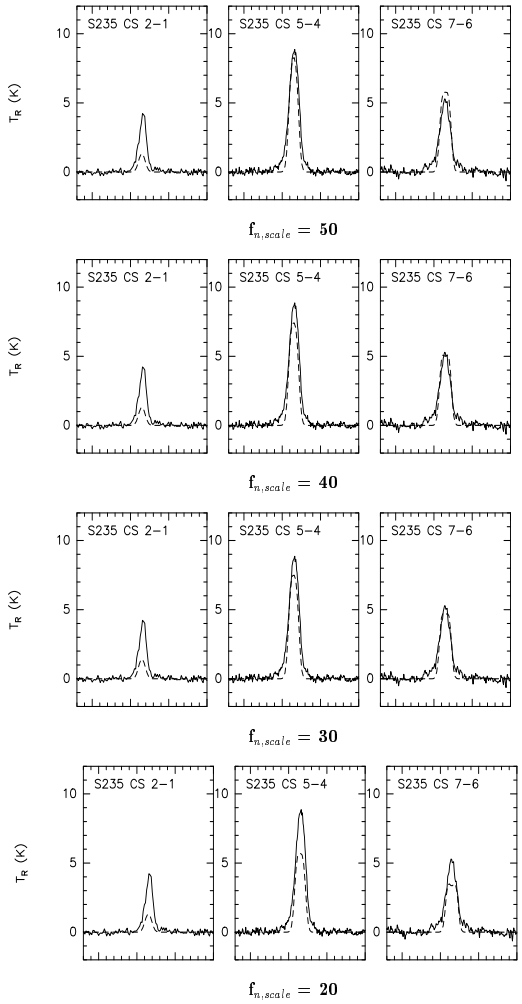

Figure 4.18 S235 with Shu model: Use the intensity ratio of CS 7-6 to CS 5-4 and the line shape to constrain the density scale-up factor.

Table 4.4 Best-fit parameters for the inside-out model of S235

Transition	r_{inf}	$f_{n,scale}$	abundance (X_0)	Microturbulence(b)
HCN (3-2)	0.001 pc	50	1×10^{-13}	2.5 km/s
CS (5-4, 7-6)	0.001 pc	50	1×10^{-12}	1.1 km/s
H^{13}CN (3-2)	0.001 pc	50	3×10^{-14}	1.2 km/s
C^{34}S (5-4)	0.001 pc	50	7×10^{-14}	1.1 km/s

The derived abundance ratios are: X[CS]/X[$C^{34}S$] $\sim$ 14, and X[HCN]/X[$H^{13}CN$] $\sim$ 3.5. This ratio is much lower than predicted in ISM. Again, the turbulence required to fit the HCN 3-2 spectra is larger than other lines.

4.4.2.2 Model with power-law model

The Shu model for S235 is actually a power-law model with the power index $p = 2.0$, because we treat S235 as a static core. Now we change p and q to test S235 with a different power-law model. We set p to be much flatter, $p = 1.25$. Since the core does not have infall velocity, the V_0 is set to 0, so q doesn't matter in this case. The density profiles for the Shu model and for the power-law model with $p = 1.25$ is shown in fig. 4.20.

We used the intensity ratio of CS7-6 and CS 5-4 to constrain the density of S235, as shown in fig. 4.21. We take the density of the core to be n_0=3.5$\times$ 10^5. Using this density, we fit the HCN 3-2, $H^{13}CN$ 3-2 and $C^{34}S$ 5-4. The best-fit model is presented in fig. 4.22. The best-fit parameters for the power-law ($p = 1.25$) model of S235 are listed in Table 4.5.

Table 4.5 Best-fit parameters for the power-law ($p = 1.25$) model of S235

Transition	n_0	v_0	abundance (X_0)	Microturbulence(b)
HCN (3-2)	3.5×10^5	0 km/s	4×10^{-13}	2.7 km/s
CS (5-4, 7-6)	3.5×10^5	0 km/s	1.2×10^{-12}	1.1 km/s
H^{13}CN (3-2)	3.5×10^5	0 km/s	2.5×10^{-14}	1.2 km/s
C^{34}S (5-4)	3.5×10^5	0 km/s	7×10^{-14}	1.1 km/s

We found that the observations can be well fitted in this power-law model. The line width is almost the same as in the Shu model ($p = 2.0$) since no infall velocity has been involved in this core. But the the isotope ratio for this model is different from the Shu model. The X[HCN]/X[H^{13}CN] ratio is about 16, larger than that calculated from Shu model, but still lower than that predicted for ISM. The CS isotope ratio is closer to that of Shu model.

4.5 Discussion

There are some problems that commonly appear in both Shu model and power-law model. Some of them have been discussed in the previous sections. I will discuss the rest in this section.

One of the most impressive problems in the model result is the very low ratio of X[HCN]/X[H^{13}CN], especially in the result of Shu model (about 5-10), which is an order of magnitude lower than the normal HCN to H^{13}CN ratio in the interstellar medium (about 70, Wilson & Rood 1994). How can we explain this low X[HCN]/X[H^{13}CN] ratio?

The first guess is that the abundance of HCN has been underestimated by accepting a very high density ($f_{n,scale}$). If we take a lower $f_{n,scale}$ but larger

X[HCN], how will this ratio change? Take S235 for example, fig. 4.23 and fig. 4.24 show the fits to $H^{13}CN$ 3-2 and HCN 3-2 lines for a range of $f_{n,scale}$ from 1 to 50. Although a lower density leads to higher X[HCN], the ratio of X[HCN]/X[$H^{13}CN$] doesn't change a lot. On the other side, a large $f_{n,scale}$ is required by the modeling of high J CS transitions. So the low HCN isotope ratio can not be improved by a changed density scale-up factor, at least in our simple model.

Then we tried other possibilities that may change the abundance. Since HCN 3-2 line has a larger turbulence b than other lines, is it possible that this broad linewidth is actually caused by a much higher abundance that leads to the saturation of the line? To test this situation, we use the b from $H^{13}CN$ 3-2 to fit HCN 3-2 with a very high X[HCN]. We test two cases for S235: X[HCN]=1e-12 and X[HCN]=2e-12, corresponding to a X[HCN] to X[$H^{13}CN$] ratio of 35 and 70 for Shu model, respectively. As seen in Fig. 4.25 a1 and a2, this model can not fit the observation, since the modeled line doesn't get much wider, but a big absorption feature shows up at the center. The other possibility is that $H^{13}CN$ 3-2 should has the same turbulence b as HCN 3-2, but lower X. So we use the b from HCN 3-2 (2.5km/s) to fit $H^{13}CN$ 3-2 at a lower X[$H^{13}CN$], but this also doesn't fit (fig. 4.25 b1, b2).

We know that changing the abundance of the outer part of cloud will change the absorption feature. Can we keep the low b, high X[HCN] for HCN 3-2 as shown in fig.4.25 a, but change the fraction of evaporation (for now it is always 0.01) to remove the big absorption caused by large X? Fig. 4.25 c1, c2

show the change of modeled line profiles as f_d varies. It seems that increasing f_d (which means a large evaporation ratio for $r < r_d$) will help to decrease the self-absorption.

Then we test how we can fit the HCN 3-2 line at higher abundance by adjusting f_d to remove self-absorption. Fig. 4.26 a1 and a2 gives the sample of such a fit, with X[HCN]=1e-12 and X[HCN]=2e-12, they are fit well, actually with the larger b. But we need to see how this change of f_d affects the fit of $H^{13}CN$ 3-2. Unfortunately, as seen in fig. 4.26 b1, b2, this new f_d also change the $H^{13}CN$ 3-2, so that we have to increase the abundance of $H^{13}CN$ equally to fit the observation. The resulting HCN isotope ratio is the same as that before the change of f_d (fig. 4.26 c). So all these tests didn't give the solutions to the low HCN isotope ratio problem.

There may be some hints for the solution to this problem, however, that we noticed when we fit the HCN 1-0 hyperfine lines for S235. The 3 hyperfine components of S235 are quite separated, so there is no worry about trapping problem in the fitting and we can fit them individually and combine them later. But as seen from the fig. 4.27, it is obvious that the theoretical abundance ratio of optically thin lines under LTE conditions between the three hyperfine components (1:5:3) doesn't agree with the observation. We can make an estimation of the abundance based on the mostly optically thin transition, the F=1-0 components. If based on the fit on F=1-0 component (Fig 4.27. the middle plot), the X[HCN] is about 100 times higher than $X[H^{13}CN]$, suggesting that the X[HCN] derived from HCN 3-2 is different from derived from HCN

1-0, which is closer to the normal value in ISM. Since the HCN 3-2 has a larger b than other tracers, while HCN 1-0 has the same b as others, the unusually low HCN isotope ratio may have something to do with the more turbulent region that HCN 3-2 probes. In other words, HCN 3-2 may be not a good tracer to probe the abundance of HCN in massive star forming cores, but it does trace the turbulent infall region.

We still have a big problem for the model results, which is the big difference of the density profile derived from continuum model and those can fit gas model (e.g. fig. 4.12, fig. 4.20). The model that can fit the molecular lines always requires a much larger density than required by the continuum model, which requests the mass that is traced by molecular gas is about 10-30 times larger than predicted by the continuum model. There are two possible solutions to this problem. One uses small changes to the basic model. The high density may reflect an abundance that is too low. In the current model frame work, the change of abundance is hard, since a much larger X will cause greater absorptions, and the resulting low density can not satisfy the intensity ratio of high J CS transitions. But a big change of chemical model, that allows the big changes of f_d or r_d may help to reach this requirement. These changes need more study of the chemical model in these massive regions.

The other solution lies in the physics of the cloud. The cloud may be clumpy (e.g. Zhou et al. 1994b). The excitation of molecular gas depends on the collision rate of gas, which is roughly proportional to the second power of the density, while the emission of dust is proportional to the first power of

density. Therefore you need higher density in these clumpy regions to excite the observed molecular lines, but the average density to generate dust emission can be lower. The clumpy cloud needs a more complex radiative transfer model (e.g. Juvela 1998).

4.6 Summary

We have attempted to use a 1D Monte Carlo simulation code to model the molecular lines in massive star forming cores. A simple chemical model of a step function was adapted, and different dynamical models, the inside-out collapse model, and the power-law model, have been tested. We tested these models on one massive infall candidates G10.6-0.4, and one massive core S235 that may have a static envelope. The results show that both dynamical models can fit most observations, although some problems remain for further consideration. We found the inside-out model with a scaled-up density may fit better for the massive infall candidate for the details of absorption feature of optically thick lines. The derived infall scale, turbulent velocity, and accretion rate are much larger than those in low-mass cores.

The current model is only a simple start to this work. A more detailed chemical model is needed to improve the model, and more sources need to be included to get statistical result for the modeling.

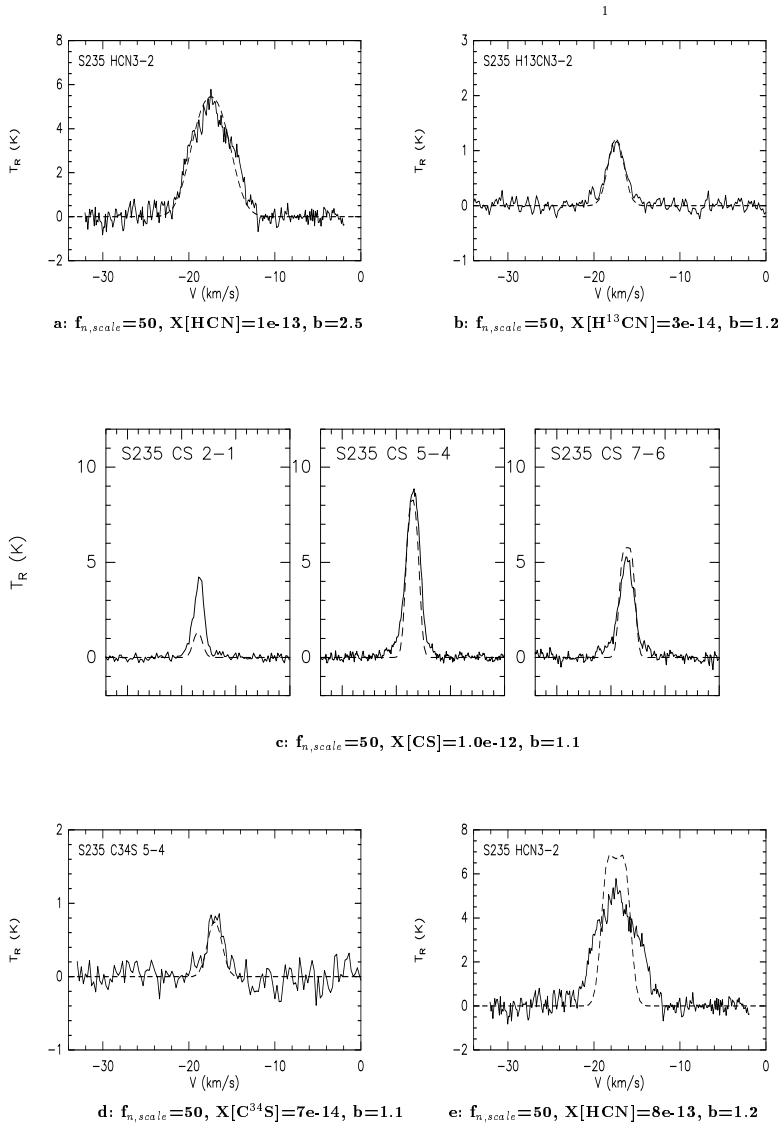

a: $\mathbf{f_{n,scale}}$**=50, X[HCN]=1e-13, b=2.5**

b: $\mathbf{f_{n,scale}}$**=50, X[**$\mathbf{H^{13}CN}$**]=3e-14, b=1.2**

c: $\mathbf{f_{n,scale}}$**=50, X[CS]=1.0e-12, b=1.1**

d: $\mathbf{f_{n,scale}}$**=50, X[**$\mathbf{C^{34}S}$**]=7e-14, b=1.1**

e: $\mathbf{f_{n,scale}}$**=50, X[HCN]=8e-13, b=1.2**

Figure 4.19 The best-fit model for S235 with Shu model. Fig. 4.19e shows that the microturbulence b that being well fitted in other lines can not match HCN 3-2 line, which need a large turbulence.

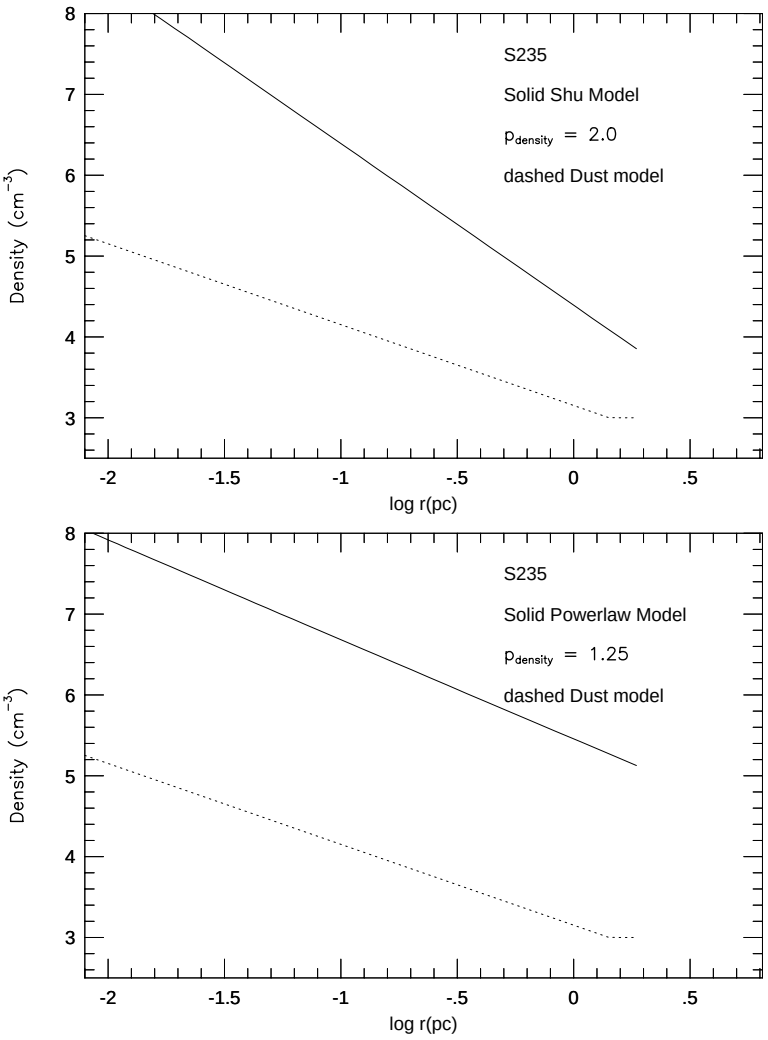

Figure 4.20 The density profile of Shu model with $p = 2$ and power-law model with $p = 1.25$ for S235. The dashed line shows the dust continuum model by Mueller et al. (2002). But this dust model was not well converged in Mueller's test, so it may be not accurate. The difference of density between gas model and dust model may be not so large.

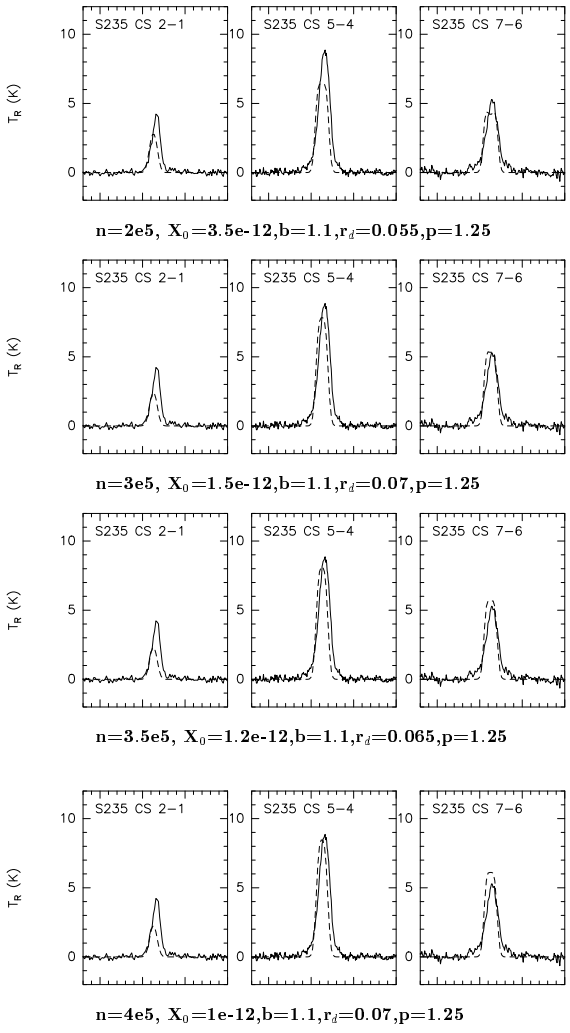

Figure 4.21 S235: Use the intensity ratio of CS 7-6 to CS 5-4 to constrain the density, with power-law model $p = 1.25$

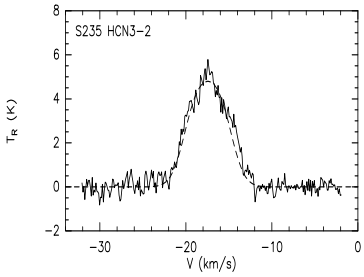

a: n_0=3.5e5,X_0=4e-13,b=2.7,V_{r0}=0,p=1.25, q=0.75

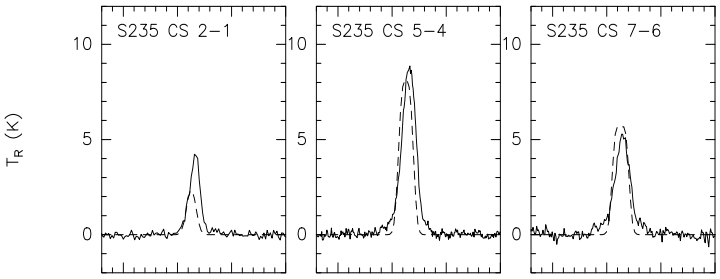

b: n_0=3.5e5,X_0=1.2e-12,b=1.2,p=1.25, q=0.75

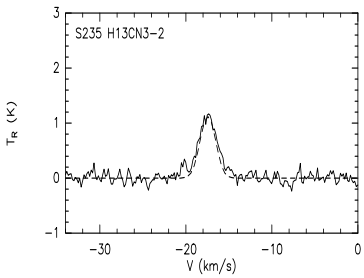

c: n_0=2.5e-14,b=1.2,$\frac{X[HCN]}{X[H^{13}CN}$=16

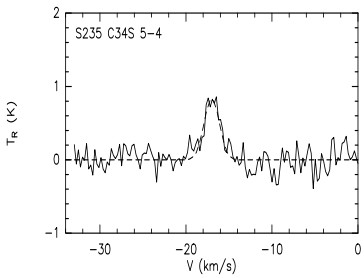

d: n_0=7e-14,b=1.1,$\frac{X[CS]}{X[C^{34}S}$=17

Figure 4.22 Best-fit power-law model of S235 for HCN 3-2, $H^{13}CN$ 3-2 and $C^{34}S$ 5-4, with $p = 1.25$

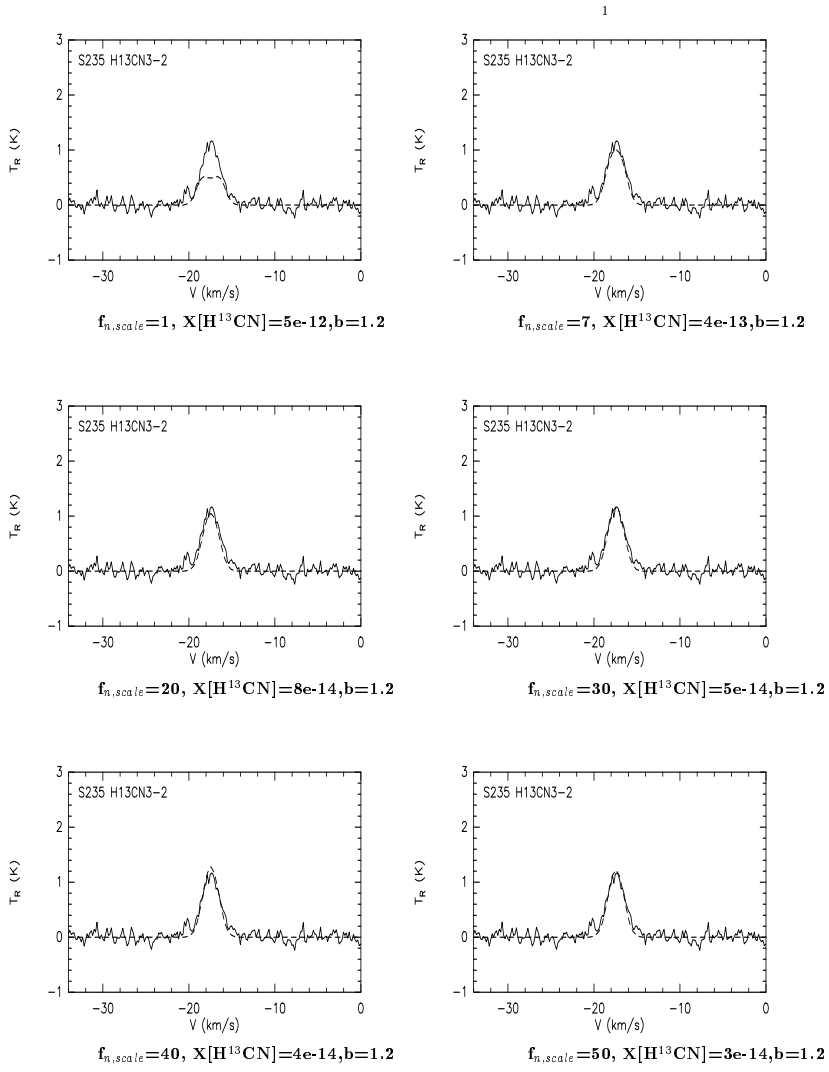

Figure 4.23 Modeled $H^{13}CN$ 3-2 line of S235 with $f_{n,scale}$ changing from 7 to 50.

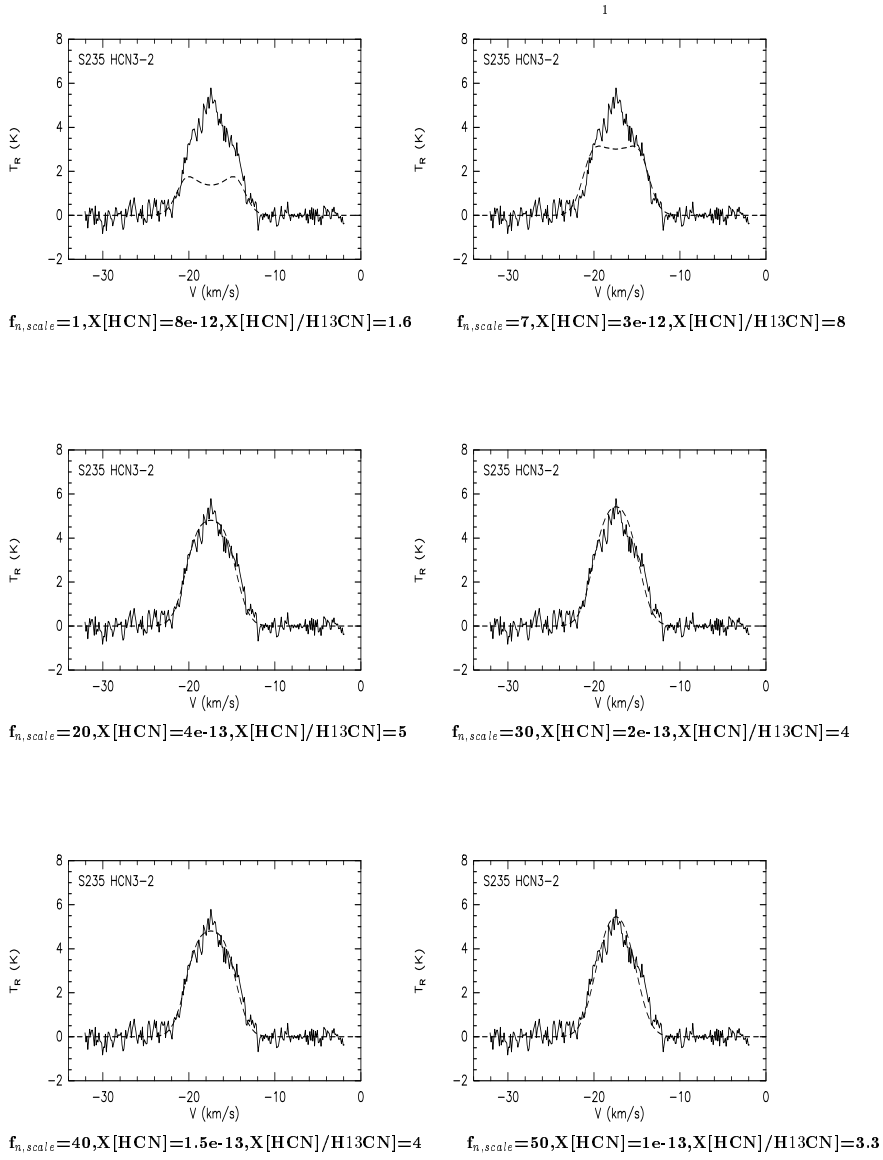

Figure 4.24 Modeled HCN 3-2 line of S235 and the HCN isotope ratios with $f_{n,scale}$ change from 7 to 50. The HCN isotope doesn't change with the change of $f_{n,scale}$.

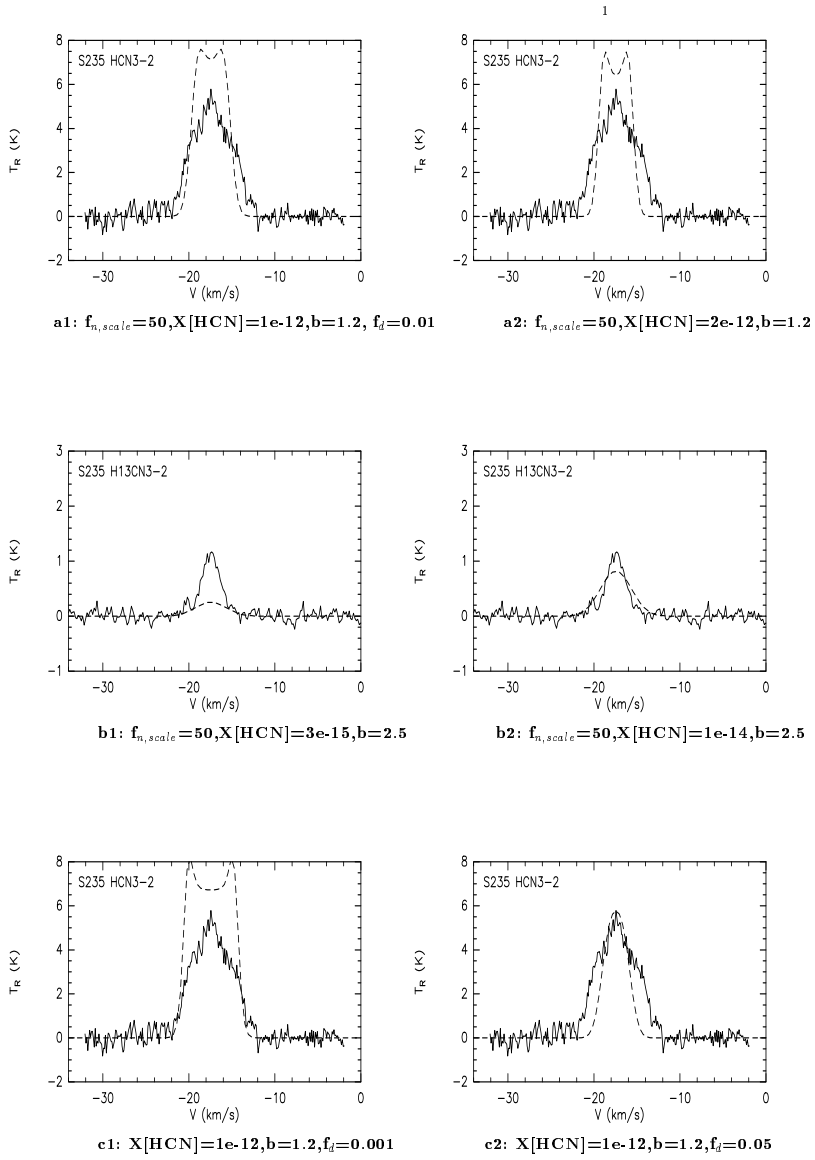

Figure 4.25 Vary b, X and f_d to test their influence on the HCN isotope ratio. a: keep a smaller constant b for HCN 3-2 but increase abundance; b: Keep a larger b for $H^{13}CN$ 3-2 but decrease abundance; c: change f_d to release the self-absorption.

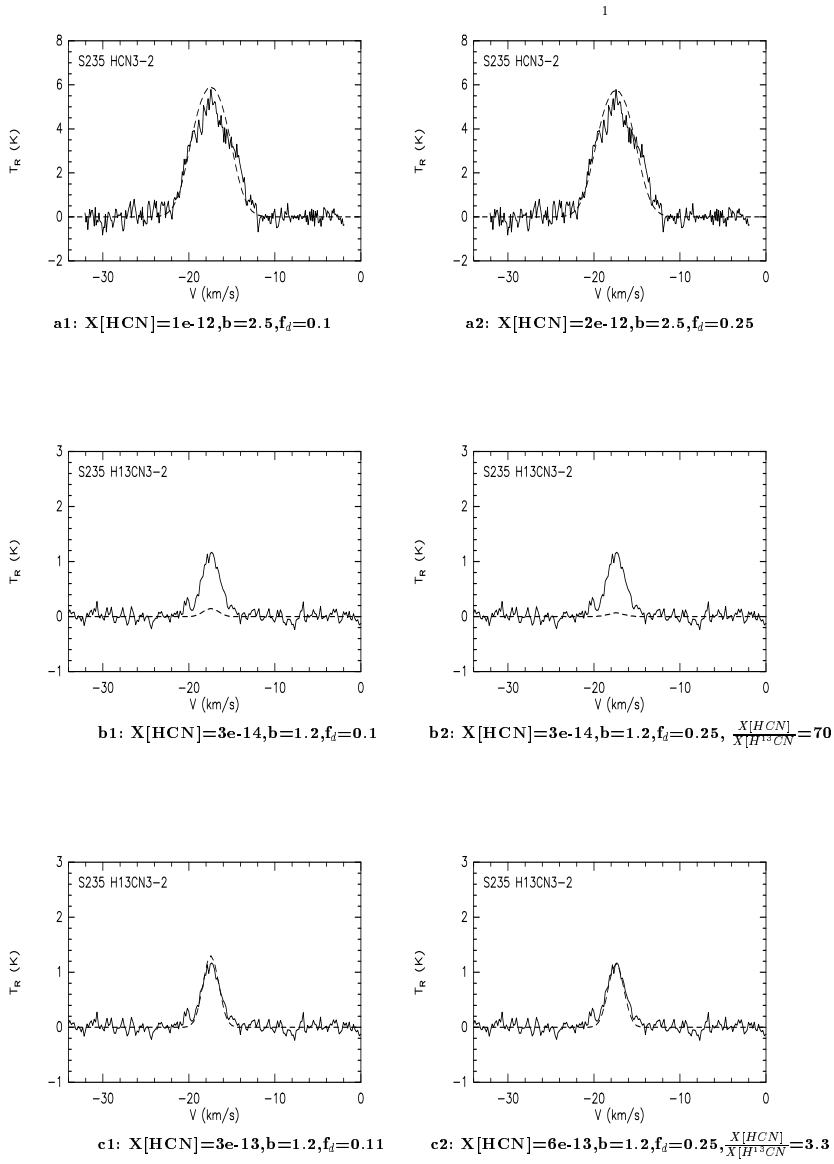

a1: X[HCN]=1e-12,b=2.5,f$_d$=0.1 **a2: X[HCN]=2e-12,b=2.5,f$_d$=0.25**

b1: X[HCN]=3e-14,b=1.2,f$_d$=0.1 **b2: X[HCN]=3e-14,b=1.2,f$_d$=0.25, $\frac{X[HCN]}{X[H^{13}CN]}$=70**

c1: X[HCN]=3e-13,b=1.2,f$_d$=0.11 **c2: X[HCN]=6e-13,b=1.2,f$_d$=0.25,$\frac{X[HCN]}{X[H^{13}CN]}$=3.3**

Figure 4.26 Changing f_d will change the abundance of HCN and $H^{13}CN$ together. It can't solve the low HCN isotope ratio problem in the current model.

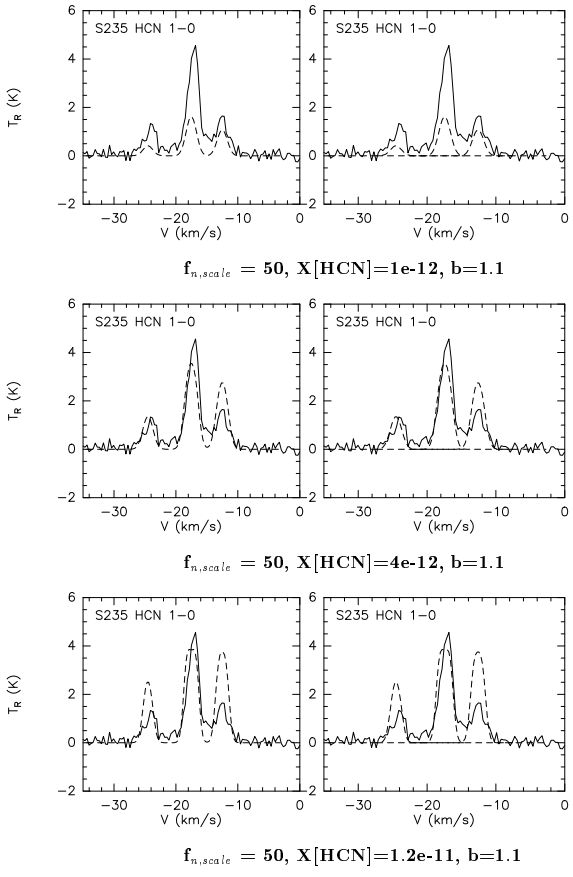

Figure 4.27 Modeling HCN 1-0 lines of S235 with Shu model. a: The abundance from best-fit of HCN 3-2 can't fit HCN 1-0. b: higher abundance is needed to fit the F=1-0 hyperfine component. c: The F=2-1 component can't be fitted by increase X[CS].

Chapter 5

SHARC-II mapping of Spitzer c2d Small Clouds and Cores

5.1 Abstract

We present the results of a submillimeter survey of 53 low-mass dense cores with the Submillimeter High Angular Resolution Camera II (SHARC-II). The survey is a follow-up project to the *Spitzer* Legacy Program "From Molecular Cores to Planet-Forming Disks", with the purpose being to create a complete data set of nearby low-mass dense cores from the infrared to the submillimeter. We present maps of 52 cores at 350 μm and three cores at 450 μm, two of which were observed at both wavelengths. 41 of these cores were detected by SHARC-II: 32 contained one submillimeter source while 9 contained multiple sources. For each submillimeter source detected we report various source properties including source position, fluxes in various apertures, size, aspect ratio, and position angle. For the 12 cores that were not detected we present upper limits.

5.2 Introduction

Many questions remain in the study of low-mass star formation despite several decades of study. One of the primary reasons is that stars form in extremely dense regions of dust and gas, obscuring nearly all the light emitted in the optical portion of the spectrum. In the near- and mid-infrared the opacities of the dust grains are low enough such that light can begin to escape. Thus, images at these wavelengths can reveal the central object (a protostar and possibly a circumstellar disk), and it is only through the development of imaging technology at longer wavelengths that these regions can be studied. The *Spitzer Space Telescope* Legacy project "From Molecular Cores to Planet-Forming Disks" (c2d; Evans et al. 2003) has carried out a survey of low-mass dense cores with the Infrared Array Camera (IRAC; Fazio et al. 2004) and the Multiband Imaging Photometer (MIPS; Rieke et al. 2004), providing images ranging from 3.6 to 70 μm. *Spitzer* is much more sensitive than previous space infrared missions, providing an ability to detect fainter, less-luminous sources than possible with previous infrared surveys. In fact, *Spitzer* c2d observations have shown that several cores believed to be starless (containing no protostars) actually harbor Very Low Luminosity Objects (VeLLOs) with internal luminosities[1] $L_{int} \leq 0.1$ $L_{\odot}$ (e.g. Young et al. 2004, Di Francesco et al. 2006). Infrared images can reveal a wealth of information about the

[1]The internal luminosity of an object, L_{int}, is defined to be the luminosity of the central object (star and disk, if present), and excludes luminosity arising from heating by the Interstellar Radiation Field (ISRF) (Di Francesco et al. 2006).

internal sources embedded in dense cores, but the infrared alone does not tell the whole story.

To fully understand the process of low-mass star formation and the nature of embedded protostars, one must understand the details of the dusty envelopes in which they are embedded. Even though these envelopes are usually quite cold ($\sim$ 10 K; e.g. Di Francesco et al. 2006), except for the inner regions where they are heated by the internal source, their thermal emission can easily be detected at submillimeter and millimeter wavelengths. Observations with the bolometer arrays SCUBA (Young et al. 2006, in preparation), MAMBO (Kauffmann et al. 2006, in preparation), and SIMBA (Brede et al. 2006, in preparation) provide data at 850 μm, 1.2 mm, and 1.2 mm, respectively. SCUBA also provides observations at 450 μm. However, Young et al. (2006) obtained SCUBA data whenever the weather was good enough for 850 μm observations, and since better weather is required for observations at 450 than 850 μm, the 450 μm data is not always of high enough quality to produce reliable results. Since the peak of a 15 K blackbody occurs at 340 μm, a reliable measurement that is close to this wavelength and fills the gap between 70 μm (*Spitzer*) and 850 μm (SCUBA) is essential to constrain the peak of the Spectral Energy Distributions (SEDs) of these objects. The MIPS instrument aboard *Spitzer* can also provide images at 160 μm, but most low-mass dense cores would saturate the detector. Thus, SHARC-II, with its capability to provide high-quality data at 350 μm, is ideally suited to fill this gap.

SHARC-II is a background-limited 350 and 450 μm facility camera

mounted on the Caltech Submillimeter Observatory (CSO) at Mauna Kea, Hawaii (Dowell et al. 2002). It adopts the advanced "CCD-style" bolometer array with 12 × 32 pixels, resulting in a $2.59' \times 0.97'$ field of view. SHARC-II features relatively high angular resolution: it has a beam size of $8.5''$ at 350 μm and $\sim 11''$ at 450 μm with good focus and pointing. Since the atmospheric transmission is very sensitive to the weather at the higher frequencies at which SHARC-II operates, it only works well in very dry weather. Under optimal weather conditions ($\tau_{225GHz} < 0.05$), SHARC-II can reach a RMS noise of 25 mJy beam^{-1} in one hour of integration at 350 μm.

Because SHARC-II achieves optimum performance at 350 μm, and many of our sources have been observed at 450 μm with SCUBA, we mapped our sources at 350 μm. We also present three sources that were mapped at 450 μm due to an observing mistake, but turned out to have smaller uncertainties than typical 450 μm SCUBA maps. In this paper, we present the basic data of this survey, including images and source properties, in a manner that is consistent with other papers presenting submillimeter and millimeter continuum data on the c2d cores and clouds. We leave a detailed analysis combining all available data on these objects to later papers. § 5.3 discusses the observations, § 5.4 details the data reduction, § 5.5 discusses the preliminary results of this survey, § 5.6 discusses the differences between SHARC-II maps of cores with and without protostars embedded within them, and § 5.7 presents our conclusions.

5.3 Observations

5.3.1 Target Selection

This survey is designed to provide a complementary dataset to the c2d observations of low-mass dense cores, thus most of our targets are selected from the list of low-mass cores observed by that project. For the earlier observation runs that occured before the *Spitzer* data was available, we chose what we believed to be the most scientifically interesting cores from the Molecular Cloud Cores Database[2] created by members of the c2d team at the Harvard-Smithsonian Center of Astrophysics (CfA). However, not all of these cores made the final *Spitzer* target list, so some of the cores in our sample do not have corresponding *Spitzer* data. Once the *Spitzer* data became available, we focused on cores found to be interesting and worthy of follow-up submillimeter observations. In addition to the observations of dense cores, c2d also obtained maps of five large molecular clouds and IRS data on a number of sources, and some of our targets are drawn from these two projects. Finally, some targets are chosen from cores observed in both a number of follow-up *Spitzer* General Observer (GO) programs and by other observers with Guaranteed Time Observations (GTO) data.

The primary criteria for selecting sources for this survey from the various projects were as follows: (1) provide complementary data to the *Spitzer* c2d data, (2) create as much overlap as possible between the various programs

[2]http://cfa-www.harvard.edu/sirtf-c2d-cfa/CORES-DB/

providing complementary data at submillimeter and millimeter wavelengths, and (3) obtain submillimeter observations of the most scientifically interesting cores. As of November 2005, we have mapped 52 cores at 350 μm and three at 450 μm, two of which were observed at both wavelengths. The first column of Table 5.1 lists each core observed, in order of Right Ascension.

Table 5.1. Observing Information of low-mass cores

CORE[a]	Map center RA (2000.0)	Map center Dec (2000.0)	Dist (pc)	Ref[b]	Project[c]	Obs.Date (mm/yyyy)	1σ noise (mJy beam^{-1})
L1455	03:27:41.0	+30:12:45.0	250	1	Per	11/2005	140
IRAS 03282+3035	03:31:20.4	+30:45:24.7	250	1	Per	11/2005	150
IRAS 03292+3039	03:32:18.0	+30:49:47.0	250	1	Per	11/2005	190
BOLO68	03:32:28.1	+31:02:17.5	250	1	Per	11/2005	55
IRAS 03301+3111	03:33:12.9	+31:21:24.2	250	1	Per/IRS	09/2004	160
LKH-alpha327	03:33:30.4	+31:10:50.4	250	1	Per/IRS	09/2004	90
HH211-MM	03:43:56.8	+32:00:50.2	250	1	Per	11/2005	290
IRAS 03439+3233	03:47:05.5	+32:43:08.5	250	1	Per/IRS	09/2004	270
IRAS 03445+3242	03:47:41.6	+32:51:43.8	250	1	Per/IRS	09/2004	220
IRAM 04191+1522	04:21:56.9	+15:29:45.0	140	2	c2d	11/2005	100
L1521B	04:24:14.9	+26:36:53.0	140	2	Oth	11/2005	35
L1521F	04:28:38.9	+26:51:35.0	140	2	c2d	11/2005	70
L1521E	04:29:13.6	+26:14:05.0	140	2	c2d+	11/2005	70
B18-1 (TMC-2A)	04:31:57.7	+24:32:30.0	140	2	c2d	11/2005	75
TMC2 (L1529)	04:32:44.8	+24:23:58.0	140	2	c2d	11/2005	45
B18-4 (TMC3)	04:35:37.5	+24:09:20.0	140	2	GTO	11/2005	150
TMC1-A	04:41:18.9	+25:48:45.0	140	2	c2d	11/2005	35
L1544	05:04:16.6	+25:10:48.0	140	2	GTO	11/2005	30
L1582B (RNO43)	05:32:19.4	+12:49:43.0	400	3	exc	10/2003	130
B35A (L1594)	05:44:29.2	+09:08:52.0	400	3	c2d	11/2005	220
DC255.4-3.9 (BHR16)	08:05:34.0	-39:09:12.0	440	4	c2d	11/2005	200
CG30 (DC253.3-1.6, BHR12)	08:09:32.7	-36:04:58.0	450	5	c2d	11/2005	380
L134A	15:53:36.3	-04:35:25.9	110	6	c2d	03/2005	55
L43 (RNO91)	16:34:33.0	-15:47:08.0	125	7	c2d	06/2005	130
						03/2005	
L146 (CB68)	16:57:20.5	-16:09:02.0	125	7	c2d	06/2004	360
B59 (L1746)	17:11:22.7	-27:24:28.0	125	7	c2d	06/2005	400
L492 (CB128)	18:15:48.4	-03:45:47.0	270	8	c2d	06/2005	60
L507 (CB130)	18:16:16.4	-02:32:38.0	270	8	c2d	06/2005	35
L328 (CB131)	18:16:59.5	-18:02:30.0	270	8	c2d	06/2005	80
L483	18:17:29.9	-04:39:40.0	270	8	c2d	06/2005	280
EC74	18:29:55.7	+01:14:31.6	260	9	IRS	06/2004	510
EC88	18:29:57.6	+01:13:00.6	260	9	IRS	06/2004	700

5.3.2 Observations

Observations were conducted in May and September of 2003, June and September of 2004, and March, June and November of 2005 at the CSO. We used the sweep mode of SHARC-II without chopping to observe all our sources. In this mode the telescope moves in a Lissajous pattern that keeps the central regions of the maps fully sampled. It works best for sources whose sizes are less than or comparable to the size of the array. During most of our observations, the Dish Surface Optimization System (DSOS[3]) was used to correct the dish surface figure for imperfections and gravitational deformations as the dish moves in elevation during observations.

Table 5.1 lists, for each core observed in this survey, the coordinates of the center of the map, the adopted distance to the core, the project from which the core was selected, the date(s) the core was observed, and the 1σ RMS noise of the map. The coordinates of the map centers were taken from either the positions of interesting objects in the *Spitzer* observations, if available, the location of molecular emission peaks from literature (e.g., Lee et al. 2001; Caselli et al. 2002), or positions suggested by collaborators to optimize the mapping coverage. The B59 core consists of a cluster of low mass sources, and in this survey we only observed the one that is most likely associated with B59-MMS1 (Reipurth et al. 1996; Brooke et al. in preparation). Integrations on each source were separated into blocks of ten minutes in stable weather

[3]See http://www.cso.caltech.edu/dsos/DSOS_MLeong.html

Table 5.1 (cont'd)

CORE[a]	Map center RA (2000.0)	Map center Dec (2000.0)	Dist (pc)	Ref[b]	Project[c]	Obs.Date (mm/yyyy)	1σ noise (mJy beam^{-1})
L723	19:17:53.8	+19:12:18.5	300	10	c2d	05/2003	80
CB188 (L673-1)	19:20:15.0	+11:36:08.0	300	11	c2d	06/2004	60
B335	19:37:01.1	+07:34:10.8	230	12	GTO	05/2003	340
L694-2 (B143, CB200)	19:41:04.3	+10:57:09.0	230	12	c2d	11/2005	90
L1152-1	20:35:46.4	+67:53:02.0	325	13	c2d	11/2005	80
L1152-2	20:36:20.2	+67:56:33.0	325	13	c2d	11/2005	75
L1041-2	20:37:20.7	+57:44:13.0	400	14	exc	06/2004	300
L1157	20:39:06.2	+68:02:16.0	325	13	exc	11/2005	510
L1148B	20:40:56.8	+67:23:05.5	325	13	c2d	06/2005	80
L1228	20:57:11.8	+77:35:47.9	200	15	c2d	09/2004	960
Bern48 (RNO129)	20:59:15.0	+78:22:59.9	200	15	c2d	05/2003	350
L1177 (CB230)	21:17:40.0	+68:17:31.9	288	13	exc	05/2003	230
L1021	21:21:47.0	+50:58:16.0	250	16	c2d	09/2004	110
L1014	21:24:07.0	+49:59:09.0	250	16	c2d	09/2004	100
L1165	22:06:50.4	+59:02:46.0	300	14	c2d	06/2005	90
L1221	22:28:04.7	+69:00:57.0	250	17	c2d	09/2004	190
L1251A-1	22:30:32.2	+75:14:09.4	300	18	c2d	11/2005	170
L1251A-2	22:31:03.3	+75:13:39.0	300	18	c2d	11/2005	180
L1251C (L1251N)	22:35:24.1	+75:17:07.9	300	18	c2d	09/2003	140
L1251B (L1251E)	22:38:47.1	+75:11:28.8	300	18	c2d	05/2003	220
L507 (CB130)^{450}	18:16:16.4	-02:32:38.0	270	8	c2d	06/2005	55
L483^{450}	18:17:29.9	-04:39:40.0	270	8	c2d	06/2005	150
L673-7^{450}	19:21:34.8	+11:21:24.0	300	11	c2d	06/2005	30

[a]A core with superscript "450" indicate that the map of that core was observed at 450 μm.

[b]References: (1) Enoch et al. (2006); (2) Kenyon, Dobrzycka, & Hartmann (1994); (3) Murdin & Penston (1977); (4) Herbst (1975); (5) Woermann, Gaylard, & Otrupcek (2001); (6) Franco (1989); (7) de Geus et al. (1989); (8) Straižys et al. (2003); (9) Straižys et al. (1996); (10) Goldsmith et al. (1984); (11) Herbig & Jones (1983); (12) Kawamura et al. (2001); (13) Straižys et al. (1992); (14) Dobashi et al. (1994); (15) Kun (1998); (16) Pagani & Breart de Boisanger (1996); (17) Yonekura et al. (1997); (18) Kun & Prusti (1993)

[c]The project from which the core was selected:
Per: Observed in Perseus c2d cloud map; IRS: Observed in c2d IRS program; c2d: Observed in cores c2d program; Oth: Selected for SHARC-II observations for other reasons; c2d+: Observed in c2d-related GO program; GTO: Observed in GTO observations; exc: Originally part of c2d cores program but cut from final target list;

or five minutes in unstable (variable) weather. The pointing was checked every 1-2 hours each night, primarily with planets such as Mars, Uranus, and Neptune. If no planets were available we used secondary objects such as CRL618, IRC+10216, and IRAS 16293-2422. After averaging over all the runs, the blind pointing uncertainty is 2.1″ for azimuth and 3.1″ for zenith angle. But since we corrected the pointing after each check, these actually represent upper limits. For any given observation, the pointing uncertainty should be smaller than this. The pointing sources were also used as flux calibrators (see Section 5.4.2). The RMS noise of each map was calculated based on the statistics of the off-source regions of the maps.

5.4 Data Reduction and Calibration

5.4.1 Data Reduction

All of the raw scans were reduced with the Comprehensive Reduction Utility for SHARC-II (CRUSH), a publicly available[4], Java-based software package. Observations obtained through the end of 2004 were reduced with version 1.35 of CRUSH, while observations taken in 2005 were reduced with version 1.40a9-2. We found that data reduced with versions of CRUSH older than 1.35 often give results that depend on the version used. For versions 1.35 or newer, however, the results do not vary with the software version. Because all of our reduction was performed with version 1.35 or newer, there is no inconsistency in our results introducted by not using the same version of

[4]http://www.submm.caltech.edu/ sharc/crush/index.htm

CRUSH for all of the data in our sample.

As mentioned above, the Lissajous scan pattern results in a map that is better sampled in the center than at the edges. This causes the edges to be much noisier than the central regions, and can often result in noise at the edges that looks like real emission. To compensate for this, we used "imagetool," a tool that is part of the CRUSH package, to eliminate the regions of each map that had a total exposure time less than 25% of the maximum. This eliminates most, but not all, of the spurious edge emission.

After removing the poorly sampled map edges, we used Starlink's "stats" package to assess the 1σ RMS noise of the map, calculated using all of the pixels in the off-source regions. We then used the derived RMS of each map to create contour maps overlaid on greyscale images for each core, and we present these in Figures B.1 to B.9 in Appendix B for the cores observed at 350 μm and in Figure B.10 in Appendix B. for the three cores observed at 450 μm. Contours start at 2σ and increase by 2σ unless otherwise indicated. We arrange the images in alphabetical order rather than by Right Ascension to make a specific map easier to find.

5.4.2 Calibration

To measure the flux densities of the sources in a given aperture in units of Jy (as opposed to the units of nV given by the instrument), we have calculated Flux Conversion Factors (FCF) for each aperture. A brief description of the calibration method, explained in greater detail in Shirley et al. (2000), is

as follows. The FCF for an aperture of diameter θ, C_θ, is defined to be the total flux density of a calibrator source (a source with a known flux density at the wavelength of the observations) in Jy divided by the flux density in the same aperture of that calibrator in the instrument units. Since CRUSH includes an atmospheric correction, the flux density of a source in a given aperture is then obtained by simply multiplying the flux of the source in that aperture, in the instrument units, by the FCF for that aperture. A set of standard apertures were adopted for all of the papers presenting ancillary millimeter and submillimeter data to the c2d project (SHARC-II, this work; SCUBA, Young et al. 2006, in preparation; MAMBO, Kauffmann et al. 2006, in preparation; SIMBA, Brede et al. 2006, in preparation): $20''$, $40''$, $80''$, and $120''$. Only the two smallest apertures, $20''$ and $40''$, are used in this work as the maps are not sensitive to emission on scales larger than this (see § 5.5.1). We used Starlink's "aperadd" package to measure the flux densities in instrument units in these apertures for both the sources and the calibrators.

In addition to the aperture FCFs, C_{20} and C_{40}, we also calculate C_{beam}, the FCF for one beam (necessary for expressing both the peak flux of each source and the 1σ RMS of the maps in units of Jy beam^{-1}). Similar to the aperture FCFs, we calculated C_{beam} by dividing the flux density of a calibrator in one beam by the value of the peak pixel of the map in the instrument units. The flux density of the calibrator in one beam, S_{beam}, was calculated by assuming a gaussian beam.

Over the various observing runs, we used Mars, Uranus, and Neptune

as calibrators. As described above, we also used several secondary calibrators to check the pointing when none of the planets were available. While they are adequate for checking the pointing, we did not use them as calibrators both because their flux densities are not as well known as for the planets and because they are not as bright as the planets and thus produce larger measurement uncertainties. Table 5.2 presents C_{beam}, C_{20}, C_{40} for each observing scan of one of the three planets listed above. Table 5.3 lists the average and standard deviation of the FCFs for each run. It is clear from these tables that the FCFs are consistent both within and between each run. We were unable to observe any of these three planets in March 2005, but since the FCFs are seen to be consistent between the various observing runs, we used the average FCFs over all of the runs (listed in Table 5.3) to calibrate data taken during this run. Based on the variation in FCF values from one observation to the next, we assign a 15% calibration uncertainty to all of our data.

5.5 Results

5.5.1 Fluxes, Sizes, and Shapes

The SHARC-II maps are oversampled, with pixel sizes three times smaller than those of a Nyquist sampled map. We have used these oversampled maps to derive the properties listed in Table 5.4: the barycenter position, flux densities in 20″ and 40″ diameter apertures (S_{20} and S_{40}, respectively), peak position, distance between barycenter and peak positions (δ_{pk}), and peak flux for each submillimeter source detected by SHARC-II. For cores with no

sources detected, we list the 3σ upper limit in each aperture. The barycenter position is derived by extracting sources using Starlink's Extractor, which is based on SExtractor (Bertin 2003), at the 2σ contours. The flux densities and peak flux are derived as described in § 5.4.2, and the peak position is located by determining the position of the peak pixel. The flux uncertainties include components from both the measurement uncertainty and a 15% calibration uncertainty, added in quadrature. The last column of Table 5.4 lists whether or not each submillimeter source is associated with a *Spitzer* source (see § 5.5.3). The peak fluxes (as well as the RMS noise of each map listed in Table 5.1) are given in units of Jy beam^{-1}. To obtain these quantities in MJy sr^{-1}, a unit that can be used to compare between different instruments with different beams, the relevant conversions are: 1 Jy beam^{-1} = 519.7 MJy sr^{-1} at 350 μm; and 1 Jy beam^{-1} = 310.3 MJy sr^{-1} at 450 μm.

Table 5.2 Calibrators for SHARCII

Date	Calibrator	scan	filter (μm)	Tau (225GHz)	C_{beam}	C_{20}	C_{40}
05/17/03	Mars	11949	350	0.07	5.82	0.22	0.19
05/18/03	Uranus	12029	350	0.085	6.83	0.22	0.21
09/29/03	Uranus	12802	350	0.054	5.75	0.20	0.19
09/30/03	Uranus	12868	350	0.09	9.43	0.26	0.25
10/01/03	Uranus	12954	350	0.063	6.23	0.21	0.21
06/19/04	Neptune	16797	350	0.08	6.71	0.21	0.19
	Uranus	16807	350	0.09	8.45	0.24	0.22
09/24/04	Uranus	18890	350	0.065	7.55	0.23	0.21
09/25/04	Uranus	18951	350	0.081	7.14	0.22	0.21
	Neptune	18946	350	0.071	6.43	0.19	0.18
	Uranus	18964	350	0.061	5.57	0.16	0.17
09/28/04	Neptune	19067	350	0.065	10.38	0.24	0.19
06/16/05	Neptune	24334	350	0.045	6.94	0.22	0.17
	Uranus	24341	350	0.045	6.86	0.23	0.18
	Uranus	24349	350	0.039	6.42	0.32	0.17
06/17/05	Neptune	24402	350	0.048	6.29	0.22	0.19
	Uranus	24408	350	0.049	6.36	0.23	0.19
11/03/05	Uranus	26737	350	0.061	6.42	0.20	0.16
	Uranus	26749	350	0.055	5.98	0.18	0.15
	Uranus	26762	350	0.070	5.35	0.16	0.14
11/04/05	Uranus	26803	350	0.071	5.72	0.18	0.14
	Uranus	26817	350	0.082	7.05	0.22	0.20
	Uranus	26824	350	0.062	7.54	0.21	0.18
11/05/05	Uranus	26880	350	0.059	6.38	0.22	0.19
	Uranus	26888	350	0.065	8.29	0.26	0.22
	Uranus	26898	350	0.056	5.43	0.18	0.17
11/12/05	Uranus	26942	350	0.077	7.09	0.21	0.16
	Uranus	26951	350	0.087	7.45	0.22	0.17
	Uranus	26957	350	0.076	6.62	0.20	0.15
06/15/05	Neptune	24277	450	0.058	10.75	0.23	0.20
	Neptune	24278	450	0.058	10.93	0.24	0.19
	Neptune	24279	450	0.058	11.86	0.37	0.24
	Uranus	24286	450	0.063	9.71	0.22	0.18

Table 5.3 Calibration factors for each run

Date	Filter (μm)	Average C_{beam} (Jy / beam / unit)	Average C_{20} (Jy / unit)	Average C_{40} (Jy / unit)
05/2003	350	6.33 ± 0.51	0.22 ± 0.00	0.20 ± 0.01
09/2003	350	7.14 ± 1.63	0.22 ± 0.03	0.22 ± 0.02
06/2004	350	7.58 ± 0.87	0.23 ± 0.02	0.21 ± 0.02
09/2004	350	7.41 ± 1.63	0.21 ± 0.03	0.19 ± 0.02
06/2005	350	6.57 ± 0.27	0.24 ± 0.04	0.18 ± 0.01
11/2005	350	6.61 ± 0.87	0.20 ± 0.03	0.17 ± 0.02
06/2005	450	10.81 ± 0.76	0.27 ± 0.06	0.20 ± 0.02
All Runs*	350	6.88 ± 1.16	0.22 ± 0.04	0.19 ± 0.03

* The average flux conversion factor over all the runs is only presented for 350 μm as the June 2005 run was the only run in which 450 μm data was taken.

Table 5.4. Source Properties for low-mass cores

SOURCE[a]	Barycenter RA (J2000)	Barycenter Dec (J2000)	S_{20}[b] (Jy)	S_{40}[b] (Jy)	Peak RA (J2000)	Peak Dec (J2000)	δ_{pk}[c] ($''$)	Peak Flux (Jy beam^{-1})	SST[d]
L1455-IRS5	03:27:38.39	+30:14:01.5	4.3 (0.6)	9.8 (1.5)	03:27:38.32	+30:13:58.6	3.0	1.6	Y
L1455-IRS1	03:27:39.21	+30:13:03.8	11.6 (1.9)	13.0 (2.1)	03:27:39.19	+30:13:03.6	0.3	7.6	Y
L1455-IRS4	03:27:43.26	+30:12:29.4	5.3 (0.8)	6.0 (1.0)	03:27:43.31	+30:12:29.6	0.7	3.1	Y
L1455-IRS2	03:27:48.44	+30:12:09.6	3.0 (0.5)	5.1 (0.8)	03:27:48.49	+30:12:10.2	0.9	1.2	Y
IRAS 03282+3035	03:31:21.10	+30:45:30.2	11.1 (1.8)	12.3 (2.1)	03:31:21.12	+30:45:30.4	0.3	8.2	Y
IRAS 03292+3039	03:32:18.03	+30:49:46.5	14.1 (2.3)	17.5 (2.8)	03:32:18.06	+30:49:46.2	0.5	10.4	Y
BOLO68	03:32:29.32	+31:02:39.6	1.7 (0.3)	2.9 (0.4)	03:32:29.30	+31:02:41.0	1.4	0.8	Y
IRAS 03301+3111	-	-	0.19 (0.06)	-	-	-	-	0.6	Y
LKH-alpha327	-	-	($<$ 0.09)	($<$ 0.19)	-	-	-	-	Y
HH211-MM	03:43:56.93	+32:00:48.9	16.4 (2.6)	25.2 (4.1)	03:43:56.94	+32:00:49.4	0.5	10.4	Y[f]
IRAS 03439+3233	-	-	1.1 (0.2)	-	-	-	-	0.6	Y
IRAS 03445+3242	03:47:41.77	+32:51:47.8	6.4 (1.0)	11.5 (1.7)	03:47:41.83	+32:51:48.3	0.9	3.6	Y
IRAM 04191+1522[g]	04:21:57.04	+15:29:49.1	3.6 (0.5)	5.0 (0.8)	04:21:57.07	+15:29:47.4	1.8	1.6	Y
IRAS 04191+1523[h]	04:22:00.60	+15:30:23.4	3.7 (0.6)	-	04:22:00.43	+15:30:24.7	2.8	2.0	Y
L1521B	-	-	($<$ 0.03)	($<$ 0.06)	-	-	-	-	U
L1521F[g]	04:28:39.11	+26:51:36.4	2.8 (0.4)	4.5 (0.7)	04:28:38.96	+26:51:35.8	2.1	1.3	Y
L1521E	-	-	($<$ 0.02)	($<$ 0.08)	-	-	-	-	U
B18-1	-	-	($<$ 0.05)	($<$ 0.13)	-	-	-	-	N
TMC2	-	-	($<$ 0.03)	($<$ 0.07)	-	-	-	-	N
B18-4	04:35:37.23	+24:09:15.8	1.9 (0.3)	4.7 (0.7)	04:35:37.68	+24:09:19.2	7.0	1.6	U
IRAS 04325+2402[i]	04:35:35.27	+24:08:20.3	3.8 (0.6)	7.1 (1.1)	04:35:35.31	+24:08:22.6	2.4	0.6	U
TMC1-A	-	-	($<$ 0.03)	($<$ 0.07)	-	-	-	-	N
L1544	-	-	($<$ 0.03)	($<$ 0.05)	-	-	-	-	U
L1582B	05:32:19.34	+12:49:41.1	12.2 (2.0)	14.2 (2.4)	05:32:19.30	+12:49:40.5	0.8	9.1	U
B35A-SMM1	05:44:29.49	+09:08:54.7	11.8 (1.8)	17.3 (2.6)	05:44:29.42	+09:08:54.4	1.1	6.3	Y
B35A-SMM2	05:44:30.41	+09:09:15.7	5.0 (0.8)	-	05:44:30.29	+09:09:16.3	1.9	2.0	N
B35A-SMM3	05:44:31.68	+09:09:01.1	3.6 (0.5)	-	05:44:31.63	+09:09:00.9	0.8	1.5	Y
DC255.4-3.9[j]	-	-	($<$ 0.08)	($<$ 0.21)	-	-	-	-	Y
CG30-SMM1[j]	08:09:32.55	-36:05:16.6	16.3 (2.6)	24.7 (4.0)	08:09:32.50	-36:05:16.6	0.6	10.2	Y
CG30-SMM2	08:09:32.87	-36:04:56.3	15.6 (2.5)	25.9 (4.1)	08:09:32.90	-36:04:55.6	0.8	9.4	Y
L134A	-	-	($<$ 0.05)	($<$ 0.09)	-	-	-	-	N
L43-RNO91	16:34:29.42	-15:47:01.3	6.9 (1.0)	9.9 (1.6)	16:34:29.29	-15:47:01.4	1.9	3.0	Y

Table 5.4 (cont'd)

SOURCE[a]	Barycenter RA (J2000)	Barycenter Dec (J2000)	S_{20}[b] (Jy)	S_{40}[b] (Jy)	Peak RA (J2000)	Peak Dec (J2000)	δ_{pk}[c] ($''$)	Peak Flux (Jy beam^{-1})	SST[d]
L43-SMM1	16:34:32.61	-15:46:32.9	0.9 (0.1)	1.0 (0.2)	16:34:32.68	-15:46:32.7	1.0	0.4	N
L43-SMM2	16:34:35.08	-15:47:03.2	3.0 (0.5)	6.5 (1.0)	16:34:35.06	-15:47:03.5	0.4	1.0	N
L43-SMM3	16:34:37.15	-15:47:37.4	2.2 (0.3)	4.6 (0.7)	16:34:37.11	-15:47:34.2	3.2	0.8	Y
L146	16:57:19.73	-16:09:20.9	9.9 (1.5)	19.1 (2.9)	16:57:19.77	-16:09:22.2	1.4	4.8	Y
B59[m]	17:11:23.16	-27:24:32.8	40.2 (6.8)	45.2 (7.7)	17:11:23.18	-27:24:32.9	0.3	30.3	Y
L492	18:15:47.65	-03:45:48.6	0.8 (0.1)	2.2 (0.4)	18:15:48.23	-03:45:49.4	8.7	0.3	N
L507[j]	18:16:16.56	-02:32:40.7	1.6 (0.2)	2.8 (0.4)	18:16:16.57	-02:32:40.4	0.3	0.7	Y
L328-SMM1	18:16:59.50	-18:02:09.5	3.1 (0.5)	6.2 (0.9)	18:16:59.55	-18:02:06.5	3.1	1.1	N
L328-SMM2[j]	-	-	-	-	18:16:59.69	-18:02:31.6	-	0.9	Y
L328-SMM3	18:17:00.86	-18:02:08.8	2.0 (0.3)	-	18:17:00.88	-18:02:09.0	0.4	0.7	N
L483	18:17:29.90	-04:39:40.8	30.3 (4.5)	50.1 (7.5)	18:17:30.07	-04:39:42.4	3.1	11.8	Y
EC74	-	-	3.0 (0.5)	-	-	-	-	1.8	Y
EC88	-	-	2.2 (0.4)	-	-	-	-	1.6	Y
L723	19:17:53.41	+19:12:12.8	8.5 (1.4)	11.3 (1.8)	19:17:53.37	+19:12:12.9	0.5	4.7	Y
CB188	19:20:15.27	+11:35:48.7	1.0 (0.2)	1.0 (0.2)	19:20:15.31	+11:35:47.8	1.0	0.6	Y
B335	19:37:01.20	+07:34:10.2	20.7 (3.3)	25.9 (4.1)	19:37:01.20	+07:34:10.0	0.2	11.4	Y
L694-2	-	-	($<$ 0.11)	($<$ 0.20)	-	-	-	-	N
L1152-1	20:35:46.75	+67:53:02.1	4.1 (0.7)	7.3 (1.1)	20:35:46.83	+67:53:02.8	0.8	2.5	Y
L1152-2	20:36:20.20	+67:56:31.8	0.6 (0.1)	-	20:36:20.27	+67:56:32.1	0.5	0.7	Y
L1041-2	20:37:21.34	+57:44:15.4	8.2 (1.2)	15.8 (2.4)	20:37:21.21	+57:44:15.0	1.1	4.0	U
L1157	20:39:06.82	+68:02:22.2	23.5 (3.5)	36.4 (5.8)	20:39:06.95	+68:02:21.7	0.9	12.6	U
L1148B[j]	-	-	($<$ 0.04)	($<$ 0.11)	-	-	-	-	Y
L1228	20:57:16.52	+77:35:42.2	15.5 (2.5)	21.7 (3.5)	20:57:16.08	+77:35:43.9	2.2	11.9	Y
Bern48	20:59:16.57	+78:23:07.8	21.7 (3.5)	21.4 (3.4)	20:59:16.50	+78:23:08.2	0.5	13.2	Y
L1177	21:17:39.78	+68:17:33.1	12.8 (2.0)	18.0 (2.9)	21:17:39.76	+68:17:32.8	0.3	7.0	U
L1021	-	-	($<$ 0.12)	($<$ 0.23)	-	-	-	-	N
L1014[g]	21:24:08.16	+49:59:09.3	1.5 (0.2)	3.2 (0.5)	21:24:08.27	+49:59:08.7	1.2	0.8	Y
L1165	22:06:51.03	+59:02:40.3	14.3 (2.3)	17.0 (2.6)	22:06:51.13	+59:02:40.3	0.8	8.5	Y
L1221-SMM1	22:28:03.48	+69:01:21.9	4.6 (0.7)	9.3 (1.4)	22:28:03.35	+69:01:22.9	1.2	2.5	Y
L1221-SMM2[j]	22:28:07.99	+69:00:42.8	4.9 (0.8)	6.4 (1.0)	22:28:07.86	+69:00:43.2	0.8	3.6	Y
L1251A-1	22:30:32.88	+75:14:12.9	5.6 (0.8)	9.4 (1.4)	22:30:32.83	+75:14:13.5	0.6	3.0	Y[n]
L1251A-2	22:31:06.06	+75:13:40.9	3.8 (0.6)	7.5 (1.1)	22:31:06.05	+75:13:41.4	0.5	1.9	Y[n]

For properties relating to the sizes and shapes of the cores, the oversampled maps may not always give reliable results. Thus, we used the IDL procedure "hrebin," available as part of the online IDL Astronomy User's Library[5], to rebin the data into Nyquist sampled maps. These maps were used to derive the properties listed in Table 5.5: the major and minor axes, aspect ratio, and position angle of each submillimeter source. These properties are extracted, again using Starlink's Extractor, at both the FWHM and 2σ contours contours.

The distributions of the angular diameter (defined to be $\sqrt{ab}$, where a and b are the major and minor axes, respectively), linear diameter, δ_{pk}, and aspect ratio of each source are shown in Figure 5.1. The distribution of linear diameters has a mean and median of 8.1 and 7.2 $\times 10^3$ AU, respectively, while the distribution of angular diameters has both a mean and median of $31.9''$ and a maximum of $57.3''$. Comparing the results of this work and those from SCUBA by Young et al. (2006) show that sources included in both surveys have sizes derived from SHARC-II that are generally $2-4$ times smaller than those derived from the SCUBA data.

One possible explanation for this is that observations at 350 μm are much more sensitive to the combination of temperature and density than those at longer submillimeter/millimeter wavelengths, which primarily only trace the dust column density. Submillimeter sources heated internally by embedded

[5]http://idlastro.gsfc.nasa.gov/

Table 5.4 (cont'd)

SOURCE[a]	Barycenter RA (J2000)	Barycenter Dec (J2000)	S_{20}[b] (Jy)	S_{40}[b] (Jy)	Peak RA (J2000)	Peak Dec (J2000)	δ_{pk}[c] ($''$)	Peak Flux (Jy beam^{-1})	SST[d]
L1251C	22:35:25.02	+75:17:06.2	10.4 (1.6)	20.8 (3.2)	22:35:24.22	+75:17:08.9	4.1	5.4	Y
L1251B-SMM1	-	-	-	-	22:38:46.84	+75:11:39.5	-	6.2	Y
L1251B-SMM2	22:38:48.64	+75:11:36.5	20.0 (3.0)	36.9 (5.5)	22:38:49.58	+75:11:35.4	3.8	6.5	N
L507^{450}	18:16:16.58	-02:32:39.9	0.8 (0.1)	1.1 (0.2)	18:16:16.68	-02:32:38.8	1.8	0.5	Y
L483^{450}	18:17:29.97	-04:39:37.2	11.4 (1.7)	20.0 (3.0)	18:17:30.20	-04:39:37.6	3.4	6.5	Y
L673-7^{450}[j]	19:21:34.92	+11:21:20.1	0.8 (0.1)	1.1 (0.2)	19:21:34.88	+11:21:20.0	0.7	0.5	Y

[a]Submillimeter sources detected with SHARCII. We also include cores with no sources detected and give upper limits for those nondetections. A "450" superscript indicates that the source is located in a core mapped at 450 μm, otherwise the source is located in a core mapped at 350 μm.

[b]For detected sources, the value in parentheses indicates the 1σ flux uncertainty. For cores with no sources detected, the value in parentheses indicates the 3σ upper limit.

[c]Distance between peak and barycenter positions

[d]A Y indicates that *Spitzer* detects a candidate Young Stellar Object within $10''$ of the submillimeter source, while a N indicates that there is no such *Spitzer* source (see § 5.5.3). A U indicates that *Spitzer* data is unavailable for that source.

[f]HH211-MM is classified as a candidate YSO as defined in § 5.5.3.

[g]Confirmed VeLLO

[h]Covered in the map of IRAM 04191+1522

[i]Covered in the map of B18-4

[j]Candidate VeLLO

[m]The SHARCII map does not cover the entire B59 core; the observed 350 μm peak is most likely associated with B59-MMS1 (Reipurth et al. 1996; Brooke et al. in preparation)

[n]There are *Spitzer* sources within $10''$ of each source that appear to be embedded protostars.

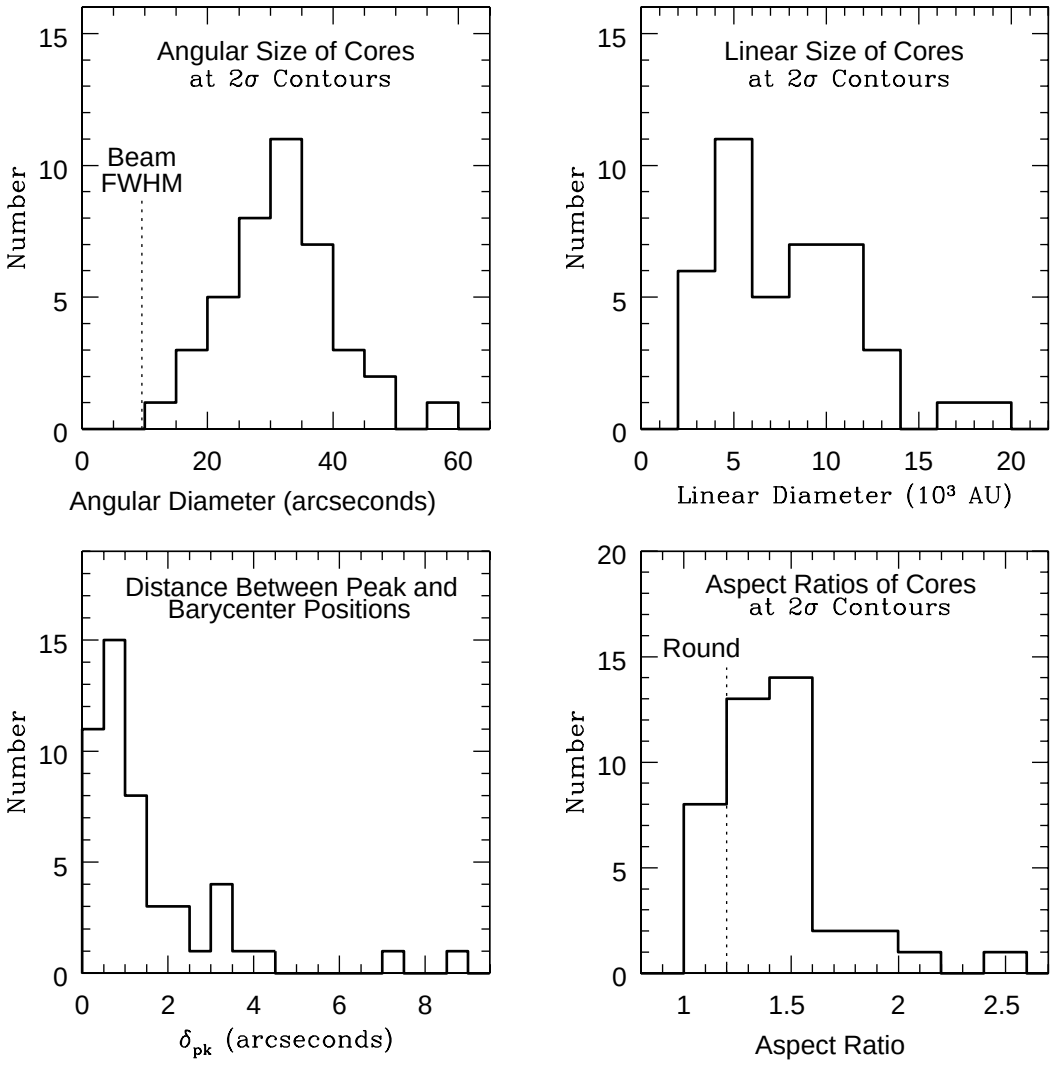

Figure 5.1 Histograms of core angular sizes at the 2σ contours (upper left), linear sizes at the 2σ contours (upper right), distances between barycenter and peak positions (lower left), and aspect ratios at the 2σ contours (lower right)

protostars should thus appear much more centrally condensed at 350 μm than at longer wavelengths. If the small sizes of the 350 μm sources were due to our observations only going deep enough to detect the emission from the warm dust in the central regions, integrating longer on a specific source should result in the detection of the more extended emission from cooler dust farther away from the source of internal heating. The net effect of this would be that the source size would increase with integration time. However, this is inconsistent with our actual observations. We found that the detected submillimeter sources were primarily detected in very short integration times (usually within the first five or ten minute integration), and that continued integration improved the signal-to-noise ratio and sharpened the boundary between the source and the background, but left the size basically unchanged.

An alternate explanation for the smaller source sizes is thus required. Considering that the mean and median of the distribution of angular diameters is 31.9$''$ and that the SHARC-II field of view is $2.59' \times 0.97'$, another possibility is that the observations presented in this work begin to lose sensitivity to extended emission on scales larger than about half the size of the array. This is in agreement with the statement from § 5.3.2 that the Lissajous observing method used for this survey works best for sources with sizes less than or comparable to the size of the array. This size scale on which our SHARC-II observations begin to lose sensitivity to extended emission is not currently well characterized, but if it truly is as small as $\sim 30''$ this has important implications for the flux densities in $40''$ apertures presented in Table 5.4.

Thus, future work is necessary and will be dedicated to better understanding and characterizing the type of emission that these observations are and are not sensitive to. The preliminary conclusion is that the sizes presented in Table 5.5 should be used with the caveat that they most likely do not capture the full extent of the cores.

Table 5.5. Source Properties derived from Nyquist binned maps

SOURCE[a]	FWHM				2σ level			
	Major axis (″)	Minor axis (″)	Aspect ratio	Position angle	Major axis (″)	Minor axis (″)	Aspect ratio	Position angle
L1455-IRS5	25	18	1.35	-45.5	53	41	1.27	71.1
L1455-IRS1	10	10	1.01	-46.3	32	26	1.24	71.8
L1455-IRS4	15	11	1.35	-42.8	28	19	1.49	-43.9
L1455-IRS2	22	14	1.60	-21.0	28	20	1.37	-36.8
IRAM 03282+3035	11	10	1.02	-47.0	31	24	1.29	-69.8
IRAS 03292+3039	11	10	1.01	-58.5	34	29	1.15	-18.6
BOLO68	19	14	1.36	-72.5	45	25	1.80	-71.1
HH211-MM	11	10	1.03	-47.9	47	33	1.41	-47.6
IRAS 03445+3242	15	13	1.11	79.1	39	29	1.37	83.2
IRAM 04191+1522	19	14	1.36	67.0	32	24	1.31	45.7
IRAS 04191+1523	-	-	-	-	30	19	1.56	48.9
L1521F	16	16	1.05	33.5	42	28	1.48	52.0
B18-4	27	19	1.40	-28.5	31	21	1.46	-14.1
IRAS 04325+2402	19	13	1.38	-67.6	35	33	1.06	2.2
L1582B	11	10	1.05	61.3	28	26	1.10	-53.1
B35A-SMM1	17	14	1.22	39.3	59	29	2.06	-13.5
CG30-SMM1	10	10	1.00	40.8	-	-	-	-
CG30-SMM2	11	10	1.01	54.7	-	-	-	-
L43-RNO91	21	18	1.20	-48.7	45	31	1.42	-20.6
L43-SMM1	10	10	1.01	46.3	-	-	-	-
L43-SMM2	35	19	1.80	44.6	52	30	1.74	42.7
L146	17	11	1.49	29.3	35	32	1.10	-27.8
B59	11	7	1.50	-48.1	33	27	1.22	87.2
L507	19	9	2.17	-71.1	47	32	1.45	-66.5
L328-SMM1	32	12	2.56	-70.1	50	39	1.27	-65.2
L483	24	14	1.68	-14.4	67	33	1.98	-12.4
L723	15	9	1.58	-76.4	35	30	1.19	-89.0
CB188	17	8	1.95	45.5	22	16	1.36	62.1
B335	11	10	1.02	-41.1	29	27	1.09	-76.0
L1152-1	12	11	1.07	-87.8	80	41	1.94	-34.4
L1152-2	10	5	1.95	0.0	14	10	1.47	69.6
L1041-2	21	9	2.11	-9.7	39	31	1.27	-35.4

The distance between the peak and barycenter positions, δ_{pk}, is a measure of the degree of axial symmetry of each source, while the aspect ratio is a measure of the roundness of the source. Following Enoch et al. (2006), we consider any source with an aspect ratio less than 1.2 to be round. The distribution of aspect ratios in Figure 5.1 shows that, while most sources do have aspect ratios at the 2σ contours greater than 1.2, very few show significant flattening (only two sources have aspect ratios greater than 2.0). Figure 5.2, which plots the aspect ratio of each source as a function of its value of δ_{pk}, shows no significant correlation between roundness and axial symmetry. While there is no obvious reason why these two quantities should be correlated, revisiting this plot in future work that combines the various millimeter and submillimeter datasets currently being assembled into a more complete sample is necessary in order to confirm this conclusion.

5.5.2 Multiplicity

Nine of the 41 cores detected by SHARC-II (approximately 20%) contain multiple submillimeter sources: L1455, IRAM 04191+1522, B18-4, B35A, CG30, L43, L328, L1221, and L1251B. The multiple sources in L1455, IRAM 04191+1522, B18-4, L43, L1221, and L1251B all correspond to previously known sources, although the eastern, starless core in L43 is resolved into several submillimeter peaks that were not previously known. The multiplicity in B35A, CG30, and L328, however, is a new result. As 350 μm observations are more sensitive to temperature than longer-wavelength bolometer obser-

Table 5.5 (cont'd)

SOURCE[a]	FWHM				2σ level			
	Major axis ($''$)	Minor axis ($''$)	Aspect ratio	Position angle	Major axis ($''$)	Minor axis ($''$)	Aspect ratio	Position angle
L1157	16	10	1.54	1.2	47	29	1.60	6.6
L1228	11	10	1.12	46.3	22	17	1.30	-66.5
Bern48	11	10	1.02	-73.5	25	21	1.18	-76.4
L1177	15	9	1.53	70.7	34	29	1.17	8.1
L1014	18	16	1.11	62.8	32	23	1.38	-66.4
L1165	16	10	1.50	86.0	46	32	1.42	-86.8
L1221-SMM1	10	5	2.00	90.0	46	33	1.41	89.6
L1221-SMM2	11	10	1.02	-51.4	28	19	1.46	-24.6
L1251A-1	12	12	1.01	-84.8	42	28	1.50	-23.9
L1251A-2	18	11	1.68	44.2	51	20	2.50	39.4
L1251C	6	5	1.14	-83.0	20	14	1.39	21.5
L1251B-SMM1	24	19	1.29	24.8	55	35	1.59	19.7
$L507^{450}$	19	11	1.73	-56.9	31	18	1.67	-70.4
$L483^{450}$	24	14	1.68	-14.4	67	33	1.98	-12.4
$L673\text{-}7^{450}$	15	13	1.08	76.2	32	22	1.45	-7.5

[a] A source with superscript "450" indicate that the source is located in a core mapped at 450 μm.

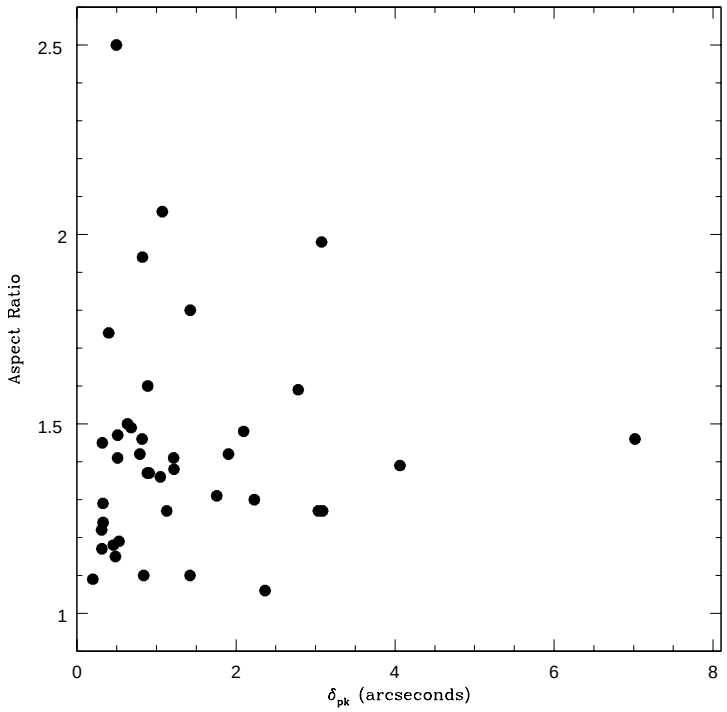

Figure 5.2 Aspect ratio of each core plotted as a function of δ_{pk}, the distance between the barycenter and peak positions of the core.

vations, multiple protostellar sources contained in one core could result in localized heating of the dust surrounding each protostar and thus the detection of multiple sources at 350 μm, but the detection of only one source at the longer wavelengths that are more sensitive to density than temperature. However, one of the three sources in B35A and two of the three sources in L328 are not associated with embedded sources (see § 5.5.3), and, furthermore, the starless core in L43 is resolved into multiple sources despite having no embedded sources. Thus, the observed multiplicity in these cores is not simply

due to the sensitivity of these observations to dust temperature, but instead suggests that multiple density peaks are in fact present.

5.5.3 Association with Embedded Young Stellar Objects

The last column of Table 5.4 indicates whether or not each submillimeter source is associated with an embedded Young Stellar Object (YSO) based on a search of *Spitzer* c2d data. The c2d team has identified candidate YSOs based on their positions in two different *Spitzer* color-magnitude diagrams: [8.0] vs. [4.5] − [8.0] and [24] vs. [8.0] − [24] (e.g., Harvey et al. 2006; Jørgensen, J.K. et al. 2006; Evans et al. 2006). To be classified as a candidate YSO, a source must meet at least one of the two following sets of criteria:

- $[4.6] - [8.0] > 0.5$ and $[8.0] < 14 - ([4.6] - [8.0])$
- $[8] - [24] > 0.7$ and $[24] < 12 - ([8] - [24])$

These criteria were selected both to pick out red objects with excess infrared emission over that of stars and to eliminate galaxies, which can appear similar to Young Stellar Objects in *Spitzer* data. It is important to note that the criteria are selected to eliminate galaxies in a statistical sense; a complete separation of these two types of objects is not yet possible with *Spitzer* data alone. Thus, a small fraction of the objects identified as candidate YSOs from the *Spitzer* data will in fact be galaxies, just as a small fraction of candidate YSOs will fall outside these criteria and thus be rejected as galaxies. We searched for objects classified as candidate YSOs, based on the above criteria,

within 10″ of the peak position of each submillimeter source. For cores with no detections, we searched for candidate YSOs within the full region covered by the SHARC-II map. We note in the table whether or not such an object was found for each submillimeter source, and we also indicate the cores for which *Spitzer* data is unavailable. There are four exceptions where the presence or absence of an embedded YSO as indicated in Table 5.4 was not determined as described above. We note these exceptions in the table and describe them below.

The first exception is L1455-IRS2. There is no candidate YSO detected by *Spitzer* within 10″ of the peak position of L1455-IRS2, but there is one 11.9″ away. The 350 μm map suggests L1455-IRS2 may in fact be comprised of two separate submillimeter sources, and although they are not well-resolved enough to present them as two separate sources, the *Spitzer* source is coincident with the western sub-structure. Thus, we consider L1455-IRS2 to be associated with an embedded YSO despite not meeting the above criterion of being located less than 10″ from the peak of the emission.

Another exception is found in HH211-MM. This source is associated with an object detected by *Spitzer* at both 70 and 160 μm, but not at shorter wavelengths. It is not classified as a candidate YSO since the shorter wavelengths are necessary for such a classification, but the detections at 70 and 160 μm lead us to conclude that it is associated with an embedded source.

L43-SMM3 is the third exception. There is an object detected by *Spitzer*, located $\sim$ 9″ from the peak position of L43-SMM3, that has 4.5 and

8.0 μm fluxes consistent with being a candidate YSO. However, it is not detected by *Spitzer* at 24 or 70 μm. The combination of the fact that the sample of candidate YSOs identified with *Spitzer* data are expected to contain a small amount of contamination from galaxies, as described above, and the nondetections at 24 and 70 μm, lead us to conclude that this object is unlikely to actually be a protostar. Thus, we do not consider L43-SMM3 to be associated with an embedded YSO.

The final exceptions are the two L1251A sources. There are *Spitzer* sources within 10″ of both L1251A-1 and L1251A-2 that fail to meet the criteria for classification as a candidate YSO but still appear to be protostars. The source associated with L1251A-1 was not detected at 8.0 μm, and since a detection at this wavelength is required according to the above criteria, it is not classified as a candidate YSO. The source associated with L1251A-2 falls just beyond the $[24] < 12 - ([8] - [24])$ criterion, but since these criteria provide a statistical sample of candidate YSOs that do not separate protostars and galaxies with complete reliability, the failure to meet this criterion does not rule out the possibility that this source is in fact a YSO. Additionally, both sources are detected by *Spitzer* at 70 μm; thus we consider L1251A-1 and L1251A-2 to be associated with embedded YSOs.

5.6 Starless vs. Starred Cores

Of the 53 cores observed and listed in Table 5.1, 12 are classified as starless based upon no detection of an embedded protostar by either *IRAS*

or *Spitzer*: L1521B, L1521E, B18-1, TMC2, B18-4, TMC1-A, L1544, L134A, L43[6], L492, L694-2, and L1021. Only three of these 12 starless cores are detected by SHARC-II: B18-4, L43, and L492. Both B18-4 and L43 are located close to potential strong sources of external heating; IRAS 04325+2402 in the case of B18-4 and L43-RNO91 in the case of L43. The same can not be said for L492, but the detection of L492 is quite weak ($\sim 5\sigma$). Furthermore, none of these three show very centrally peaked emission.

In addition to the nine starless cores not detected, the other three cores not detected by SHARC-II are LKH-alpha327, DC255.4-3.9, and L1148B. Four other cores, IRAS 03301+3111, IRAS 03439+3233, EC74, and EC88, show very weak detections (between 3σ and 6σ). All of these seven, except for DC255.4-3.9 and L1148B, which are discussed below, were selected from IRS targets of interest that were not restricted to objects known to still be heavily embedded in dense cores. The lack of a submillimeter detection for these cores can thus be used to infer that they are in later stages of evolution where most of the dense, circumstellar envelope has dissipated, and because of their likely status as more evolved objects, they are not included in the discussion below.

The detection statistics quoted above suggest that the SHARC-II observations presented in this paper distinguish quite well between starless cores and cores with protostars. This is not unexpected because, as already mentioned, 350 μm is much more sensitive to the dust temperature than longer

[6]L43 contains both a starless core and a protostar

wavelengths. Thus, the presence or absence of central heating from an embedded protostar should be more noticeable at this wavelength, and, indeed, starless cores are generally not detected while cores with embedded protostars generally are detected. Two of the three exceptions to this appear to occur when there is a strong souce of external heating, as in the case of B18-4 and L43, and all three of the exceptions show much less centrally peaked emission than cores with protostars. This comes with the important caveat, however, that only 12 starless cores have been observed, and seven of them are located in Taurus. L492, the only starless core detected that is not close to an obvious source of strong external heating, is also the only starless core observed that is located in the Serpens molecular cloud. Future work will be devoted to expanding the sample of starless cores with SHARC-II to include cores located in a variety of star-forming regions with different properties and expected amounts of external heating. The preliminary results from this survey suggest that a clear distinction between starless cores and those with protostars is present in SHARC-II observations, but more conclusive results require a larger sample.

Perhaps the most interesting result from this survey concerns the VeLLOs. As discussed in § 5.2, *Spitzer* c2d observations have shown that several cores believed to be starless (containing no protostars) actually harbor Very Low Luminosity Objects (VeLLOs) with internal luminosities $L_{int} \leq 0.1$ $L_{\odot}$ (e.g. Young et al. 2004, Di Francesco et al. 2006). Three confirmed VeLLOs (IRAM 04191+1522, Dunham et al. 2006; L1521F, Bourke et al. 2006; L1014, Young et al. 2004) and seven candidate VeLLOs (DC255.4-3.9, CG30, L507,

L328, L1148B, L1221, and L673-7) were included in the survey[7]. Except for DC255.4-3.9 and L1148B, which are not detected, VeLLOs show reasonably strong detections and centrally peaked emission reminiscent of cores with protostars. In other words, VeLLOs look much more like cores with protostars than starless cores in SHARC-II data, indicating that observations of VeLLO candidates with SHARC-II can be an essential part of confirming their status as very low luminosity, embedded objects. The nondetections of DC255.4-3.9 and L1148B cast doubt on their status as embedded objects, since embedded objects appear to be essentially always detected. Future study will be devoted to these and other VeLLOs (Kauffmann et al. in preparation; Dunham et al. in preparation).

5.7 Conclusions

We present maps of 53 low-mass dense cores with SHARC-II at the CSO, 52 at 350 μm and 3 at 450 μm, with two observed at both wavelengths. 41 of these cores are detected while 12 are not, and 9 of the 41 detected cores show multiple submillimeter sources. We derive and tabulate the basic properties for each detected submillimeter source: position, fluxes in 20$''$ and 40$''$ apertures, peak flux, size, aspect ratio, and position angle. We also use data from the *Spitzer Space Telescope* to indicate whether or not each core is

[7]Confirmed VeLLOs have had their very low internal luminosities confirmed with radiative transfer models, while candidate VeLLOs have simply been identified as potential Very Low Luminosity Objects based on their *Spitzer* fluxes (Huard et al. 2006; Dunham et al. in preparation)

associated with an embedded Young Stellar Object.

The results of this survey suggest that SHARC-II observations of dense cores are capable of distinguishing between starless cores and cores with protostars much better than observations with other bolometer arrays at longer wavelengths. VeLLOs, Very Low luminosity Objects discovered by *Spitzer* in cores previously believed to be starless, look very similar to other cores with protostars, indicating that 350 μm observations of these objects may be a key component in confirming their status as very low luminosity, embedded objects. Future work will concentrate on expanding the sample of cores observed with SHARC-II and combining this dataset with others being assembed at other submillimeter and millimeter wavelengths in order to assemble a more complete picture of the processes involved in low-mass star formation.

Chapter 6

Connecting Dense Gas Tracers of Star Formation in our Galaxy to High-z Star Formation

6.1 Abstract

Observations have revealed prodigious amounts of star formation in starburst galaxies as traced by dust and molecular emission, even at large redshifts. Recent work shows that for both nearby spiral galaxies and distant starbursts, the global star formation rate, as indicated by the infrared luminosity, has a tight and almost linear correlation with the amount of dense gas as traced by the luminosity of HCN. Our surveys of Galactic dense cores in HCN $1-0$ emission show that this correlation continues to a much smaller scale, with nearly the same ratio of infrared luminosity to HCN luminosity found over 7-8 orders of magnitude in L_{IR}, with a lower cutoff around $10^{4.5}$ $L_{\odot}$ of infrared luminosity. The linear correlation suggests that we may understand distant star formation in terms of the known properties of local star-forming regions. Both the correlation and the luminosity cutoff can be explained if the basic unit of star formation in galaxies is a dense core, similar to those studied in our Galaxy.

6.2 Introduction

Recent work has revealed large amounts of dust and molecules in starburst galaxies, even at large redshifts (e.g. Isaak et al. 2002; Reuland et al. 2003; Greve et al. 2005; Solomon & Vanden Bout 2005). Understanding star formation in galaxies at high redshift is a critical step in understanding the formation of galaxies in the early Universe.

The simplest and most widely used relations between the star formation rate and a property of the interstellar medium (ISM) are the so-called "Schmidt laws". Schmidt (1959) proposed that the star formation rate was proportional to ρ^2, where ρ is the gas volume density. In their modern form, these "laws" relate the *surface density* of star formation to the *surface density* of gas:

$$\Sigma_{SFR} = A\Sigma_{gas}^{N} \tag{6.1}$$

(e.g., Kennicutt 1998). The index N has been inferred by various authors to be in the range of 1 to 2 (Kennicutt 1997). Measurements of HI, CO, and Hα on a large sample of normal spiral galaxies and starburst galaxies (Kennicutt 1998) could be fitted with $N = 1.4$. It should be noted that for many of these galaxies, particularly the starburst galaxies, in the Kennicutt sample the surface density or surface brightness was not measured but obtained only by dividing the luminosity by a characteristic size often obtained from another parameter.

On a global scale, including luminous and ultraluminous starburst galaxies, there is a correlation between the total luminosity of far-infrared

emission, which traces the star formation rate (e.g. Sanders and Mirabel 1996; Kewley et al. 2002), and the total luminosity of CO, tracing the molecular gas mass. However, this relation is not linear; the ratio of L_{IR} to L_{CO} increases with increasing L_{IR} (Sanders and Mirabel 1996; Solomon et al. 1997; Gao & Solomon 2004a, 2004b; Solomon & Vanden Bout 2005). Does this variation reflect an increase in "efficiency" of star formation, or an increasing failure of CO to trace the gas that is relevant to star formation?

The latter possibility is suggested by data on HCN $J = 1 - 0$ in galaxies. A recent survey of HCN $J = 1 - 0$ emission in 65 normal spiral and starburst galaxies found that the star formation rate, as traced by the infrared luminosity, has a tight and linear correlation with the luminosity of HCN (Gao & Solomon 2004a, 2004b). Those authors argued that CO is not linearly correlated with star formation because it traces only the low density GMC envelopes, not the really active star-forming part, the dense cores. The critical molecular parameter that measures star formation rates in galaxies is the amount of dense molecular gas, measured by the HCN luminosity. Because HCN traces the dense gas better than CO, L_{HCN} has a tighter correlation with L_{IR} than does L_{CO}. The correlation remains linear over a factor of 10^3 in luminosity for both normal galaxies and extreme starbursts, like luminous and ultraluminous infrared galaxies (LIRGs and ULIRGs, see Sanders and Mirabel, 1996). Gao and Solomon (2004a) therefore argue that both normal galaxies and starbursts should have the same star formation rate per amount of *dense* gas.

At lower luminosities, the relation for galaxies between L_{IR} and L_{CO} is linear, but the ratio between L_{IR} and L_{CO} has a dispersion of an order of magnitude. An even larger variation in L_{IR}/L_{CO} (several orders of magnitude) is seen in Galactic clouds (Mooney & Solomon 1988; Evans 1991; Mead et al. 1990). The dispersion in the relation for galaxies is less if L_{HCN} is used instead of CO; the same is true for other tracers of dense gas in Galactic cores (e.g. Mueller et al. 2002, Shirley et al. 2003), suggesting that studies of Galactic star formation can shed light on the trends in other galaxies.

In the Milky Way, star formation is dominated by clustered star formation (Carpenter 2000; Lada & Lada 2003). Clustered star formation produces stars with a range of masses, but massive stars form nearly exclusively in clusters within massive dense cores. Since massive stars dominate the luminosity, they are the stars directly probed in studying star formation in other galaxies. Thus, understanding the relation between star formation and massive, dense cores in our Galaxy may shed light on the starburst phenomenon.

These cores are dense, turbulent, and dusty. They are well identified by the continuum emission from dust (e.g., Mueller et al. 2002) and line emission from molecular dense gas tracers like CS (Plume et al. 1992, 1997; Shirley et al. 2003) and HCN (Wu & Evans 2003). In our previous work on a large sample of massive cores, we found that the bolometric (almost all far-infrared) luminosity of the cores is roughly proportional to the mass inferred from the dust emission (Mueller et al. 2002) and the virial mass determined from CS (Shirley et al. 2003). This result suggests that a relation between L_{IR} and

L_{HCN} may exist in Galactic dense cores, possibly similar to that in starburst galaxies.

One difficulty is that systematic studies of the Galactic dense cores have used dust continuum emission and CS, while HCN has been more commonly used for studies of galaxies. To facilitate comparison with the HCN $J = 1 - 0$ galaxy survey, we have mapped the HCN $J = 1 - 0$ transition in a sample of 47 Galactic star forming cores (Wu et al. 2005, in preparation). In this paper we will summarize the results from this survey in connection with the HCN surveys of other galaxies.

The sample mapped in HCN $J = 1 - 0$ is mostly a subset of a larger sample of Galactic massive dense cores that have been mapped in CS and dust emission (Shirley et al. 2003; Mueller et al. 2002). The sources in this category have infrared luminosities ranging from 10^3 - 10^7 $L_\odot$ and most contain compact or ultracompact H II (UCHII) regions. To extend the sample towards lower luminosities, we selected 14 IRAS sources from outflow surveys (Zhang et al. 2005; Wu et al. 2004) and a few from other publications.

6.3 Observation & Data Analysis

Observations of HCN $J = 1 \rightarrow 0$ (88.6318473 GHz) on Galactic dense cores were made with the 14-m telescope of the Five College Radio Astronomy Observatory (FCRAO) in 2004 April, December and 2005 February. The FWHM of the beam for this frequency is $58''$. The 16-element focal plane array (SEQUOIA) was used, with typical system temperatures 100-200K. A

velocity resolution of 0.1 km s^{-1} was achieved with the 25 MHz bandwidth on the dual channel correlator (DCC). We convert the measured T_A^* to $T_R$via $T_R = T_A^*/(\eta_{FSS}\eta_c)$, with $\eta_{FSS} = 0.7$. The value of η_c depends on source size; for the typical map in this study ($\sim 10'$), $\eta_C = 0.7$. The map size was extended until the edge of the HCN $J = 1 \rightarrow 0$ emission was reached, typically at the 2σ level (mean $\sigma \sim 0.3$ K km/s), so we could get the total HCN luminosity.

Maps of HCN 1-0 emission were obtained for 47 Galactic star-forming cores. Detailed results will be presented elsewhere (Wu et al. 2005, in preparation), but we give a few properties of the sample here, which are relevant to this paper. More than 90% of the cores were well resolved by the maps. We focus on these resolved sources in this paper.

The size of the core is characterized by the nominal core radius after beam deconvolution, R_{HCN}, the radius of a circle that has the same area as the half peak intensity contour:

$$R_{HCN} = D(\frac{A_{1/2}}{\pi} - \frac{\theta_{beam}^2}{4})^{1/2},$$

where $A_{1/2}$ is the area within the contour of half peak intensity. The median R_{HCN1-0} of the sample is 0.48 pc.

The HCN line luminosity of each core, assuming a gaussian brightness distribution for the source and a gaussian beam, is:

$$L_{HCN} = 23.5 \times 10^{-6} \times D^2 \times (\frac{\pi \times \theta_s^2}{4ln2}) \times (\frac{\theta_s^2 + \theta_{beam}^2}{\theta_s^2}) \times \int T_R dv \qquad (6.2)$$

Here D is the distance in the unit of kpc, θ_s and θ_{beam} are the angular size of the source and beam in arcsecond. This method is parallel to that of Gao

& Solomon (2004b), but adapted to Galactic cores. L_{HCN} ranges from 0.4 to 8000 K km s^{-1} pc^2, with the median value of 80 K km s^{-1} pc^2 .

The total infrared luminosity (8-1000 μm) was calculated based on the 4 IRAS bands (Sanders and Mirabel 1996), as was done for the galaxy sample of Gao & Solomon (2004a):

$$L_{IR} = 0.56 \times D^2 \times (13.48 \times f_{12} + 5.16 \times f_{25} + 2.58 \times f_{60} + f_{100}), \qquad (6.3)$$

where f_x is the flux in band x from the four IRAS bands in the units of Jy, D in kpc, and L_{IR} in $L_\odot$.

6.4 Comparison of Milky Way and galactic Relations

The derived L_{IR} and L_{HCN} are plotted in a log-log diagram in Fig. 6.1 to compare with data on galaxies from Gao & Solomon (2004a). The correlation of L_{IR}–L_{HCN} extends from galaxy scales to the much smaller scales of Galactic molecular cores. The fit for Gao & Solomon's galaxy sample is $\log(L_{IR}) = 1.00 \times \log(L_{HCN}) + 2.9$, without a few galaxies that only have upper limits to HCN emission. This linear correlation continues to the Galactic massive cores, but a decline in L_{IR} occurs at $10^{4.5}$ $L_\odot$, below which the slope of the correlation becomes much steeper. When fit to Galactic cores with $L_{IR} > 10^{4.5}$ $L_\odot$, the linear least squares fit gives $\log(L_{IR}) = 1.02(\pm0.06) \times \log(L_{HCN}) + 2.79(\pm0.16)$. This relation agrees remarkably well with the relation for galaxies, as seen in fig. 6.1a. In fig. 6.1b, we fit simultaneously the data of galaxies from Gao & Solomon (2004a) and Galac-

tic cores with $L_{IR} > 10^{4.5}$ $L_\odot$. The result is $\log(L_{IR}) = 1.01 \times \log(L_{HCN}) + 2.83$, with a correlation coefficient of 0.99. Understanding the physics behind this linear correlation will lead to a better understanding of star formation on galactic scales.

The linear $\log(L_{IR}) - \log(L_{HCN})$ correlation and the turnoff can be seen more clearly from fig. 6.2, where the distance independent ratio L_{IR}/L_{HCN} has been plotted versus L_{IR} (top) and against L_{mol} (bottom). A constant mean value of L_{IR}/L_{HCN} is seen over 8 orders of magnitude in L_{IR}, from galaxies to Galactic cores, as long as $L_{IR} > L(min)$, with $L(min)$ being around $10^{4.5}$ $L_\odot$. The corresponding cut-off value for L_{HCN} is $L_{unit} = 10^{1.5}$ K km s^{-1} pc^2. For Galactic cores, $\langle L_{IR}/L_{HCN} \rangle = 911 \pm 227$, with median 380. For galaxies, $\langle L_{IR}/L_{HCN} \rangle = 950 \pm 76$, with median 855. The uncertainties are the standard deviation of the means, which are remarkably similar, though the dispersion is much higher for Galactic cores. The median for dense cores is significantly smaller than its mean, which indicates that the mean is dominated by a few quite large values. The logarithmic mean and median are 2.64±0.53 and 2.54±0.56 for dense cores with $L_{HCN} > L_{unit}$, and 2.91±0.24 and 2.93±0.25 for galaxies.

For comparison, we added CO data on Galactic cores (Mooney & Solomon 1988), galaxies (Gao & Solomon 2004a) and high-z molecular emission line galaxies (Solomon & Vanden Bout 2005) in fig. 6.2. The ratio, L_{IR}/L_{CO}, changes by two orders of magnitude as L_{CO} increases from Galactic cores to distant galaxies, confirming Gao & Solomon's conclusion that CO is

not as good a tracer of star-forming gas as is HCN, especially for very luminous starburst galaxies.

6.5 Discussion

The fact that L_{IR}/L_{HCN} is similar, on average, for star-forming cores in the Galaxy, normal spirals, starbursts, and ULIRGs suggests the possibility of interpreting intense high-z star formation in terms of nearby high mass star forming regions. Before we can exploit this possibility, we must understand some key points. Why does L_{IR}/L_{HCN} rise steeply with L_{HCN} and then remain constant for $L_{HCN} > L_{unit}$? And why is the ratio, L_{IR}/L_{CO}, NOT constant for starbursts?

As a first step, we seek a more physical basis for the relations. We have so far discussed L_{HCN} as a measure of the mass of dense gas, but can we quantify this assumption? A roughly linear correlation between the mass of dense gas and bolometric luminosity has been found by our work on CS and dust emission (Shirley et al. 2003; Mueller et al. 2002). To see whether this applies also to HCN $J = 1 \rightarrow 0$, we have calculated the virial mass of the dense gas ($M(dense)$) using the most optically thin line ($C^{34}S$ $J = 5 \rightarrow 4$) to measure the linewidth and compared $M(dense)$ to L_{HCN}. Based on the 31 cores with available $C^{34}S$ $J = 5 \rightarrow 4$ data, we obtained the correlation: $\log(M_{vir}(R_{HCN1-0}))=(0.81\pm0.03)\times \log(L_{HCN1-0}) +1.29(\pm0.09)$. The correlation is roughly linear. The M_{vir}-L_{HCN1-0} plot and details of the observations of $C^{34}S$ $J = 5 \rightarrow 4$ will be presented by Wu et al. (2005, in preparation).

Leaving out one peculiar source (G35.58-0.03), we get $\langle M(dense)/L_{HCN} \rangle = 11 \pm 2$ $M_\odot$/K km s^{-1} pc^2, where the uncertainty is the standard deviation of the mean; the median value is 6 $M_\odot$/K km s^{-1} pc^2, indicating that the mean is affected by some quite large values. The logarithmic mean is 7±2 $M_\odot$/K km s^{-1} pc^2. Some of the scatter in the ratio may be caused by distance uncertainties because the virial mass depends linearly on distance, while $L_{HCN} \propto D^2$.

Even after establishing that L_{HCN} traces the mass of dense gas, it is not at all clear why L_{IR}/L_{HCN} should be constant, since the luminosity of a cluster is typically dominated by its most massive members, and $L_\star \propto {M_\star}^\alpha$, with $\alpha \approx 3$ to 4. Indeed, below the cutoff of $10^{4.5}$ $L_\odot$, L_{IR} does rise rapidly with $M(dense)$. What causes the transition to a constant value?

To solve this puzzle, we propose the existence of a basic unit of cluster formation. For $M(dense)$ less than the mass of this unit, $L_{IR}/M(dense)$ rises rapidly with $M(dense)$, as higher mass stars can form. For $M(dense)$ greater than the mass of this unit, the IMF is reasonably sampled and further increases in mass produce more units, but no further change in $L_{IR}/M(dense)$. If we suppose that larger scale cluster formation is built up by adding more and more such units, then the linear correlation between the total L_{IR} and $M(dense)$ is a natural result. In that case, the only difference between star formation on different scales and in different environments–big clusters, normal galaxies, massive ULIRGs–is just how *many* such cores they contain. This is of course somewhat of a simplification because the cores have a range of properties.

The fact that the mean is roughly twice the median for both L_{IR}/L_{HCN} and $M(dense)/L_{HCN}$ for Galactic cores suggests that the most extreme cases may dominate when averaged over a whole galaxy. Since most of our cores contain compact H II or UCH II regions, which trace the most massive stars, it is interesting to compare to the luminosity function of these regions. A study of Galactic UCH II regions did find a peak luminosity ($\sim 10^5 L_\odot$) that is close to that of a basic unit (Cassassus et al. 2000). The detailed discussion of this model will be presented in a separate paper (Wu et al. 2005, in preparation).

Another question is why does L_{IR}/L_{CO} increase as we move from Galactic Cores or normal spiral galaxies to starburst galaxies. In Galactic clouds, CO can be used as a tracer of the overall mass of molecular clouds, even though it is optically thick and thermalized. However, CO does not specifically trace the mass of dense cores. For that, dust continuum emission, or molecules, like HCN, that are only excited at higher densities are required. In the Galaxy, these dense cores occupy a small fraction of the mass of a cloud (typically a few percent). If the fraction of dense gas in the overall cloud stays roughly constant, the relation between L_{IR} and L_{CO} can stay linear, but this relation is secondary to that between L_{IR} and $M(dense)$. For starburst galaxies, the fraction of the molecular gas concentrated in dense cores increases, causing (Gao & Solomon 2004a) the secondary relation between L_{IR} and L_{CO} to become non-linear.

These considerations lead us to offer some new versions of "Schmidt

Laws":

$$\dot{M}_\star(\mathrm{M}_\odot yr^{-1}) \sim 1.4 \times 10^{-7} L_{HCN}(K\mathrm{km\ s^{-1}}\ pc^2) \tag{6.4}$$

$$\dot{M}_\star(\mathrm{M}_\odot yr^{-1}) \sim 1.2 \times 10^{-8} M(dense)(\mathrm{M}_\odot) \tag{6.5}$$

where $\dot{M}_\star$ is the star formation rate, and we have assumed that $\dot{M}_\star(\mathrm{M}_\odot yr^{-1}) = 2.0 \times 10^{-10} L_{IR}(\mathrm{L}_\odot)$ (see Gao & Solomon (2004b)) and we use the fit to both dense cores and galaxies. The coefficients (1.4×10^{-7} and 1.2×10^{-8}) are very similar to, but slightly less than, those values (1.8×10^{-7} and 1.8×10^{-8}) given by Gao & Solomon (2004b), based only on the galaxies.

Given these simpler, linear relations, how do we understand the usual star formation law (Kennicutt 1998) relations, with a steeper dependence ($\Sigma_{SFR} \propto \Sigma_{gas}^{1.4}$) of $\dot{M}_\star$ on gas mass? We suggest that the steeper dependence reflects the dependence of $M(dense)$ on the surface density, or total mass, of gas. All the tracers of gas used by Kennicutt trace lower density components, not the actual gas that is directly involved in star formation. Once it is clear that it is the dense gas mass that indicates the star formation rate, it becomes clear why the total surface density of gas may not be a clean star formation indicator. For example, there is no evidence that HI emission in galaxies correlates at all with the star formation rate deduced form the far-infrared luminosity, so its contribution to the surface density may have no effect on the star formation rate. Attempts to provide a theoretical framework (e.g., Li et al. 2005, Krumholz & McKee 2005) for the Kennicutt relations should also be able to explain the new relations.

It will be interesting to see how far these ideas can be extended. One future project is to look at HCN in more nearby galaxies, especially in individual regions forming super-star clusters, which may be the building blocks of star formation in starburst regions like ULIRGs and LIRGs (Ho 1997). ALMA will allow detailed study of HCN in other galaxies, including the $J = 3 \rightarrow 2$ transition. Another is to explore how far toward higher z these relations can be pushed, and to understand how the relations depend on metallicity and chemistry. Theoretical work by Lintott et al. (2005) suggest that HCN may trace very early star formation, depending on the nucleosynthetic yield of the earliest stars.

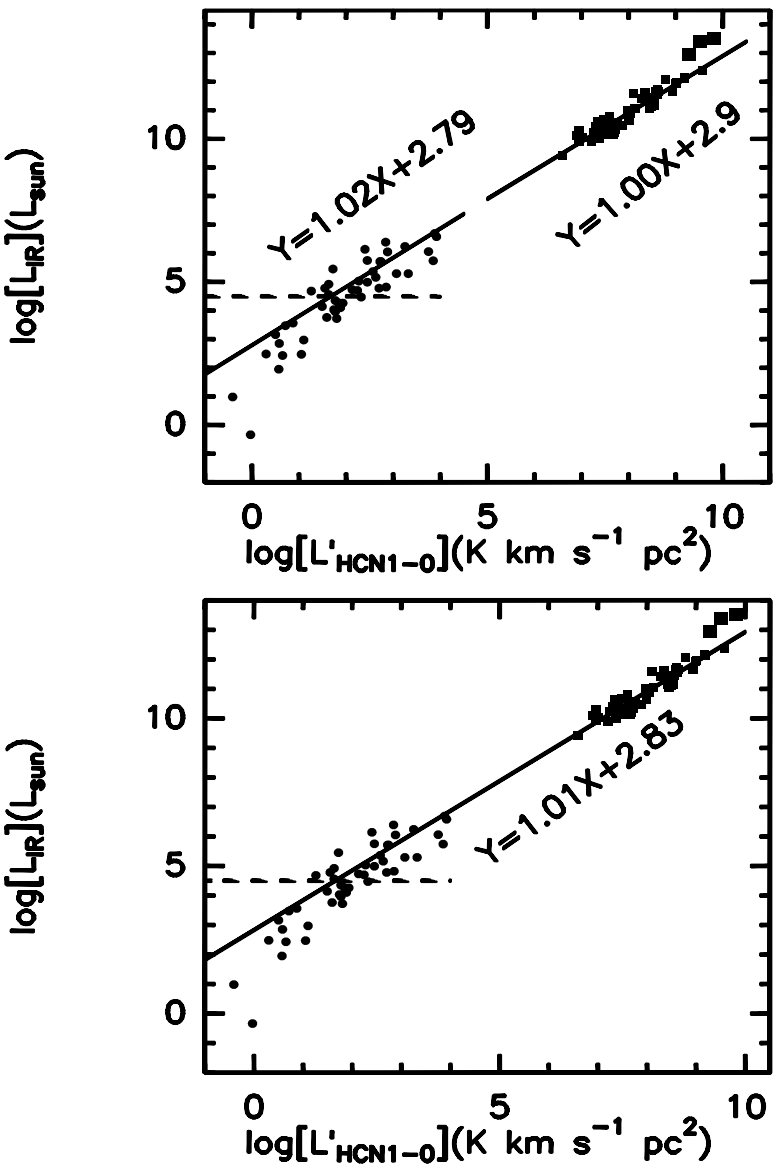

Figure 6.1 logL_{IR} - logL'_{HCN1-0} correlation for Galactic and extragalactic sources. Fig.6.1a (above) indicates the linear least squares fit for Galactic cores (with $L_{IR} > 10^{4.5}$ $L_\odot$, points above the dashed line) and for galaxies, separately. Fig. 6.1b (down) shows a overall fit for both parts. The three isolated solid squares are high z HCN 1-0 points from Solomon et al. (2003), Vanden Bout et al. (2004) and Carilli et al. (2005); they are not included in the fit because the sources are QSOs and the contribution from the AGN to L_{IR} is not yet clear.

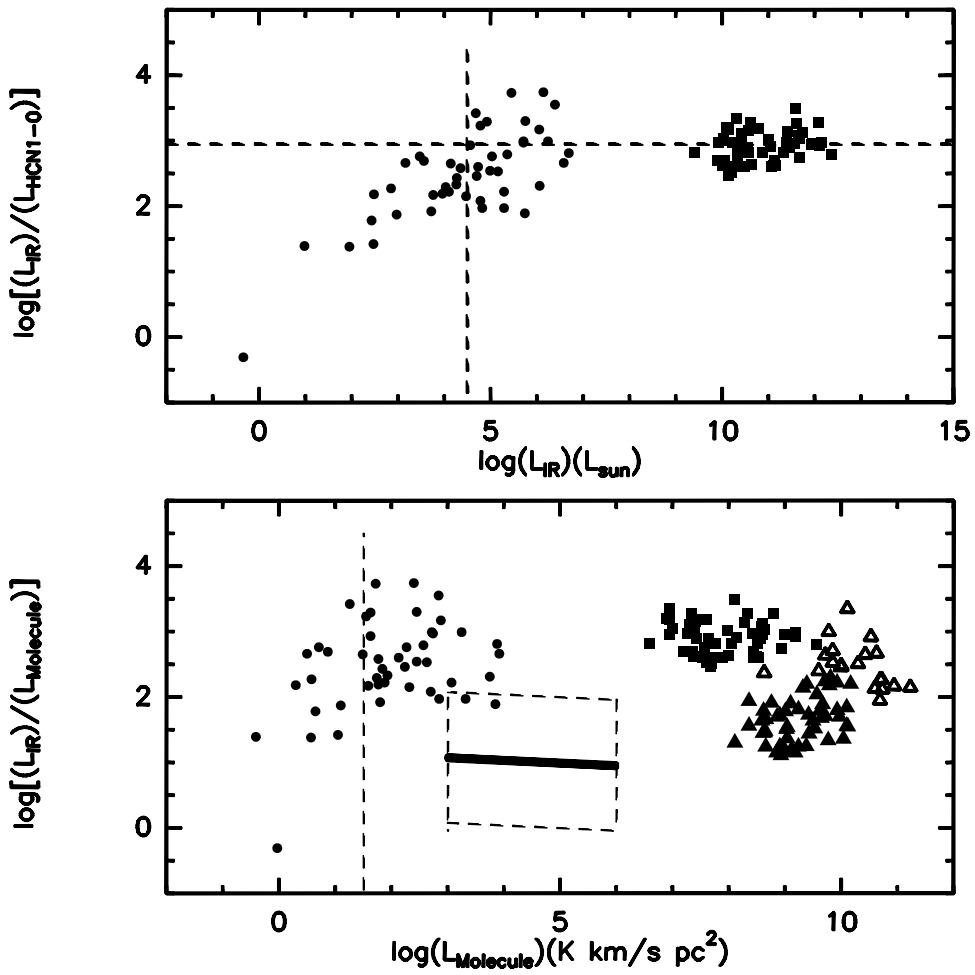

Figure 6.2 Above: Correlation between L_{IR} and L_{IR}/L_{HCN1-0} for galaxies (solid squares) and Galactic star forming cores (filled circles). L_{IR}/L_{HCN1-0} is constant for a large range of L_{IR} utill a turn off around $L_{IR}=10^{4.5}$ $L_{\odot}$. Below: L_{IR} per unit of molecular gas vs. molecular line luminosity. The star formation rate per amount of CO gas changes a lot from Galactic GMCs (the heavy line, with a dashed line boundary to indicate the variation), to galaxies (filled triangles) and high-z CO galaxies (hollow triangles).

Chapter 7

Summary of Thesis

Unlike the field of low-mass star formation, the study of which has gone as fast as the details of evolutionary stages, the theoretical framework of high-mass star formation has not been well established. Some of the most basic questions concerning the formation and early evolution of massive star formation are unresolved. This thesis has contributed to the study of massive star formation, not by providing a solution to any key problems, but by giving some observational supports, constraints, and some important hints to the understanding of how massive star formation proceeds.

Gravitational collapse is widely accepted as the basic mechanism leading to star formation, but the observational evidence for collapse in massive star forming regions is extremely rare. Our spectral line survey of a sample of 28 massive star forming cores with HCN 3-2 transition revealed a large fraction of the cores had asymmetric line skewed to the blue, an indication of infall (Chap.2). This is the first systematic survey to provide evidence of global collapse in massive star forming regions. The characteristic blue profile will appear only if the molecular tracer has a suitable optical depth and critical density. Our work found that HCN 3-2 is a better indicator of infall in massive

star forming regions than other molecular tracers (like CS, HCO^+). Although the blue excess E (an index to quantify the significance of infall) dropped from 0.25 to 0.15 when more massive cores were included in the statistics (Chap. 3), the indication that global collapse exists in massive star forming cores is still strong.

The other major observational component of this study is a set of molecular mapping surveys using different dense gas tracers (HCN, CS), different excitation levels (from $J = 7 \rightarrow 6$, to $J = 1 \rightarrow 0$), and line surveys with different isotopes, of a large sample of over 50 massive star-forming cores (Chap. 3). Combined with previous spectral line surveys and a dust continuum survey, these surveys give a complete dataset to study the embedded dense cores of high-mass star forming regions. The data can be used to derive the general properties of high-mass star forming cores, to study the difference between massive dense cores, to test and constrain theoretical models, and to provide a good base for other surveys of massive star forming regions.

Besides observational contributions, this thesis also help to improve our understanding of the mechanism of massive star formation. We have modeled the molecular lines (Chap. 4) of some massive cores with a 1D Monte Carlo simulation, using the continuum information from a dust model (Mueller et al. 2003) combined with a simple chemical model, and tested different dynamical models (the inside-out infall model, and the power-law density distribution model). We found that at least for some high-mass sources, the inside-out collapse model can fit the observations, indicating the inflow motion found in

these source can be gravitational, and these cores can be treated as a scaled-up version of low-mass star formation system, but with much larger density and turbulent motion. The infall radius is as large as 1 parsec, with the infall time scale of the order of 10^5 years, and an accretion rate of about 10^{-3} $M_\odot$.

We also showed the connection between star formation in the Milky Way and other galaxies. Recent work (Gao & Solomon 2004a,b) shows that a tight and almost linear correlation exists between the global star formation rate, as indicated by the infrared luminosity, and the amount of dense gas, as traced by the luminosity of HCN 1-0, for both normal and starburst galaxies, suggesting the star formation efficiency is constant in these different systems. Our HCN 1-0 and HCN 3-2 surveys shows that this correlation extends to Galactic scales. The ratio of L_{IR}/L_{HCN1-0} is constant over almost 8 orders of magnitude, from distant Ultraluminous Infrared Galaxies (ULIRGs), possibly even high z galaxies, to Galactic cores, until a lower cut-off is reached around $L_{IR} \sim 10^{4.5}$ $L_\odot$ (Chap. 6). This suggests that star formation may follow a very simple relationship, when the appropriate tracers are used, in both nearby and distant galaxies.

Why does L_{IR} increase linearly with L_{HCN}? This question arises because L_{IR} nearly traces the stellar luminosity and L_{HCN} traces the mass of dense star forming gas, leading one to expect $L \sim M_{dense}$. Normally, L increases sharply with M_* for a given IMF. To solve this puzzle, we propose that there is a threshold of clustered star formation, a basic unit. For M_{dense} less than the mass of this unit, L_{IR}/M_{dense} rises rapidly with M_{dense}, as higher

mass stars can form. For M_{dense} greater than the mass of this unit, the IMF is reasonably sampled and further increases in mass produce more basic units, but no further change in L_{IR}/M_{dense}. If we suppose that larger scale cluster formation is built up by adding more and more such units, then the linear correlation between the total L_{IR} and M_{dense} is a natural result. In that case, the only difference between star formation on different scales and in different environments–GMCs, normal galaxies, distant starbursts including ULIRGs– is simply how many such cores they contain. From the L_{IR}-L_{HCN} correlation and its cut-off, we estimate the typical properties of basic units are: $L_{IR} \sim 10^5$ $L_\odot$, size $R_{dense} \sim 0.5$ pc, and $M_{dense} \sim$ 300-1000 $M_\odot$.

The work of this thesis is only a beginning, and there is much more to be done for the future study of massive star formation. For example, the model we are using to simulate molecular lines has very simple assumptions, such as a 1D spherical symmetry, a simple step-function for the abundance variation, and the restriction of motion to infall and turbulence. Some improvements can be made in the near future. We can improve the chemical model to better match the physical conditions of high-mass dense cores. We have only modeled a few cores at this time; more sources will be tested with different dynamical models to get statistical properties. The details of the inner region of the core can not be resolved by the current observations of single-dish telescope; interferometer data will be obtained to improve the model.

For the study of connecting nearby and distant massive star formation, more observational tests, especially high-resolution observations, are needed

to explore the existence of the basic units for clustered star formation. The relation between massive star formation in the Galactic GMC cores, in the super star clusters of other galaxies, and even extreme star formation in the high-z galaxies, is a natural extension of the linear L_{IR}-L_{HCN} correlation study. These studies may reveal the general mechanism that controls clustered star formation in galaxies.

Massive star-forming cores have been mapped and studied in 350 μm dust continuum (Mueller et al. 2002), and we have started modeling them with molecular lines in this thesis. For low-mass cores, some cores have been modeled with molecular tracers (e.g. Lee et al. 2003, Evans et al. 2005), but little have been mapped in 350 μm. I have carried out a survey of submillimeter continuum emission with SHARC II at the CSO, on a sample of low-mass star-forming cores (Chap. 5). Fifty-two low-mass dense cores were mapped at 350 μm and three at 450 μm, with two observed at both wavelengths. Torty-one of these cores were detected. Properties of the detected sources were obtained. We found that SHARC-II observations of dense cores are capable of distinguishing between starless cores and cores with protostars, much better than observations with other bolometer arrays at longer wavelengths, and it is also possible to detect Very Low luminosity Objects (VeLLOs) that have been discovered by the Spitzer telescope.

Appendices

Appendix A

Contour Maps of HCN and CS Emission towards Massive Cores

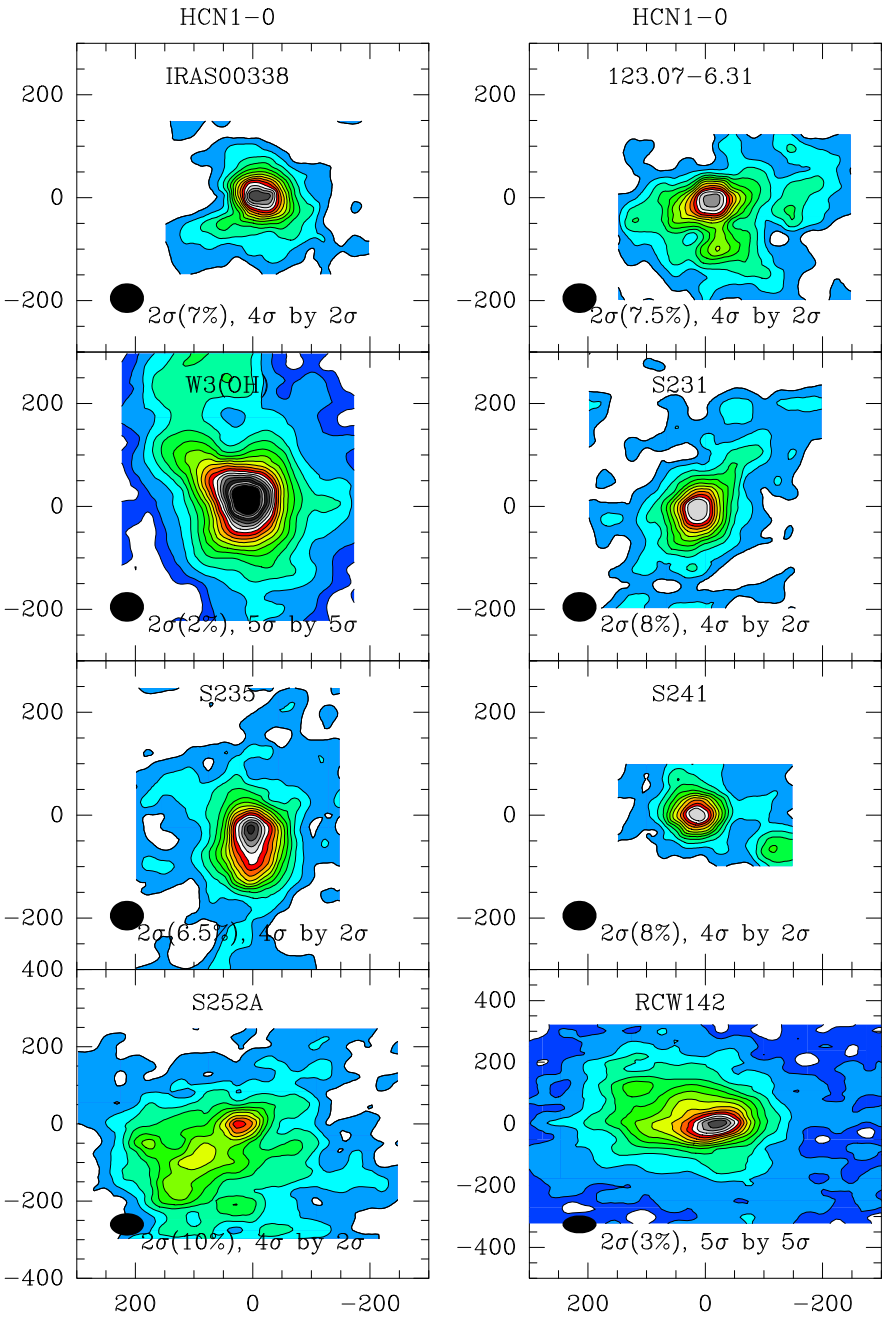

Figure A.1 HCN 1-0 contour maps of massive cores. The lowest contour level and increasing step of contours are indicated in the plot. The beam size is shown at the lower left of each map.

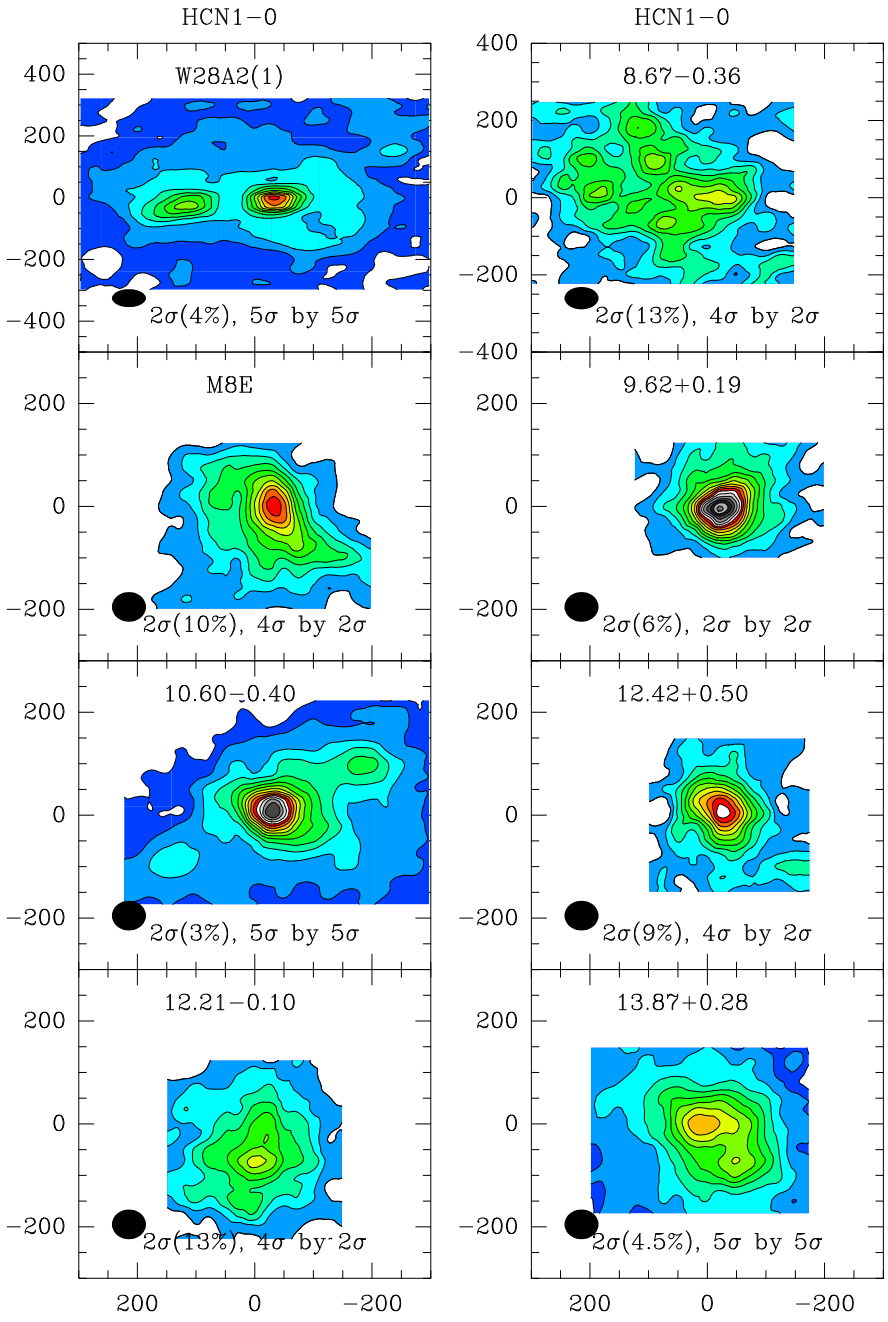

Figure A.2 HCN 1-0 contour maps continue...

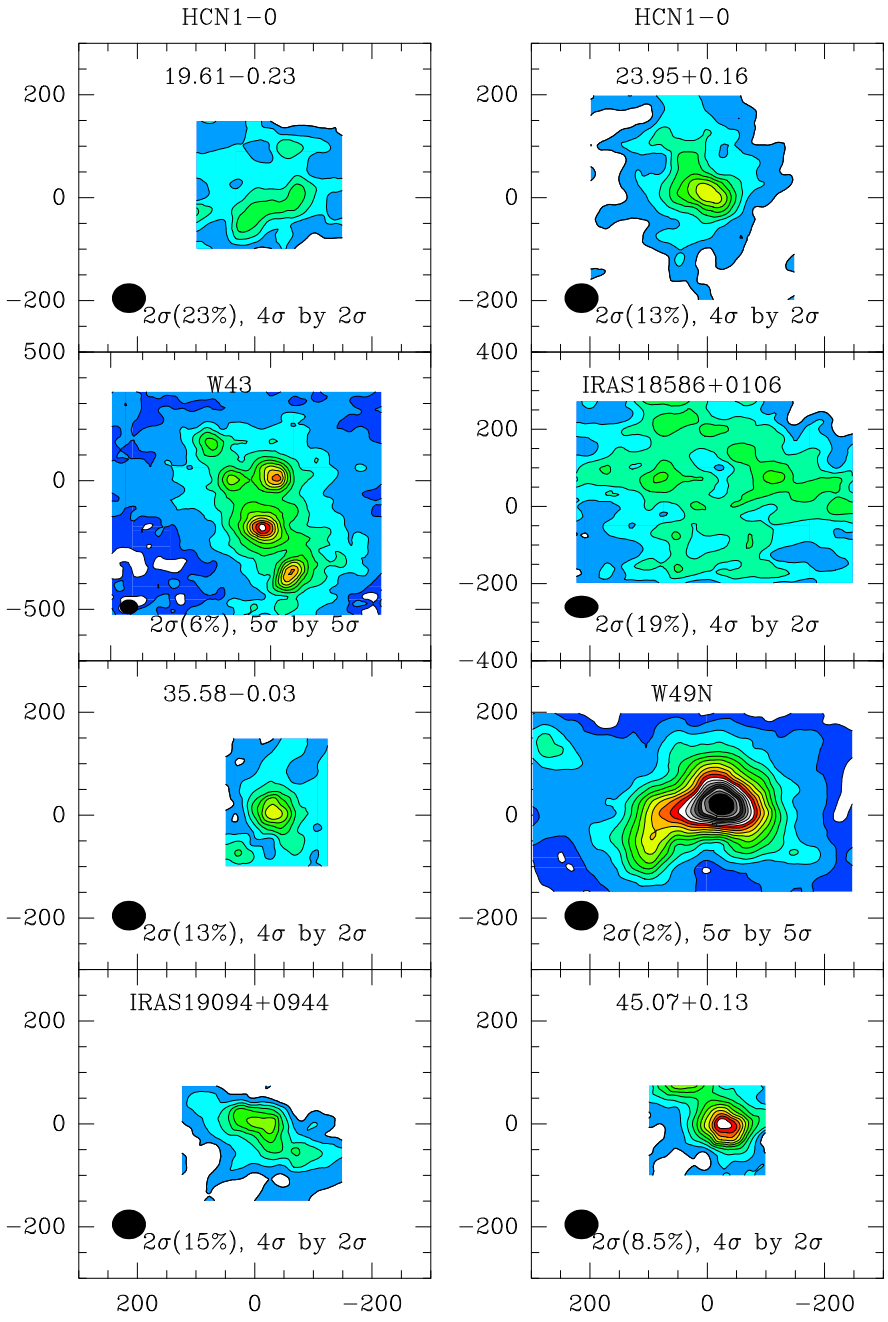

Figure A.3 HCN 1-0 contour maps continue...

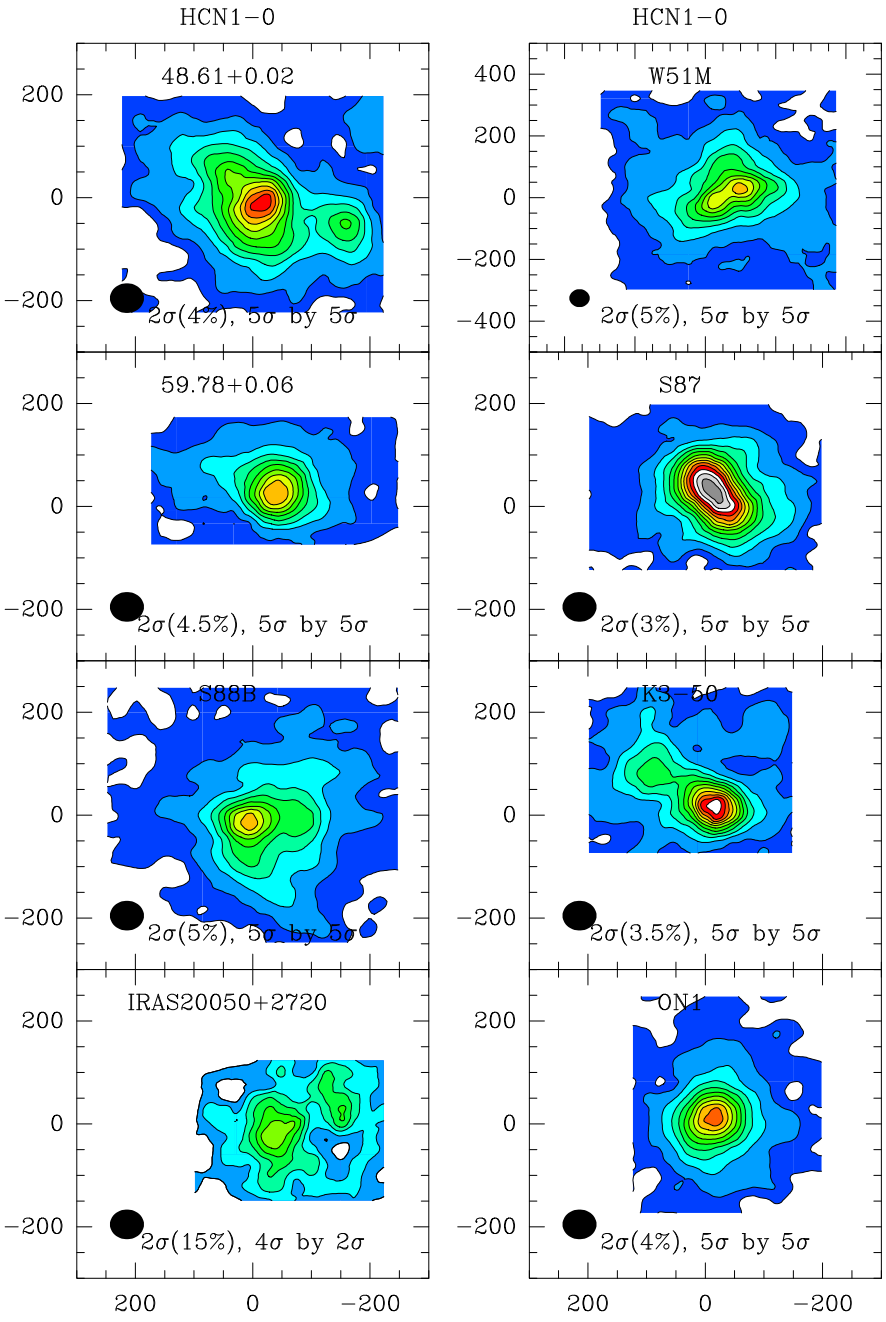

Figure A.4 HCN 1-0 contour maps continue...

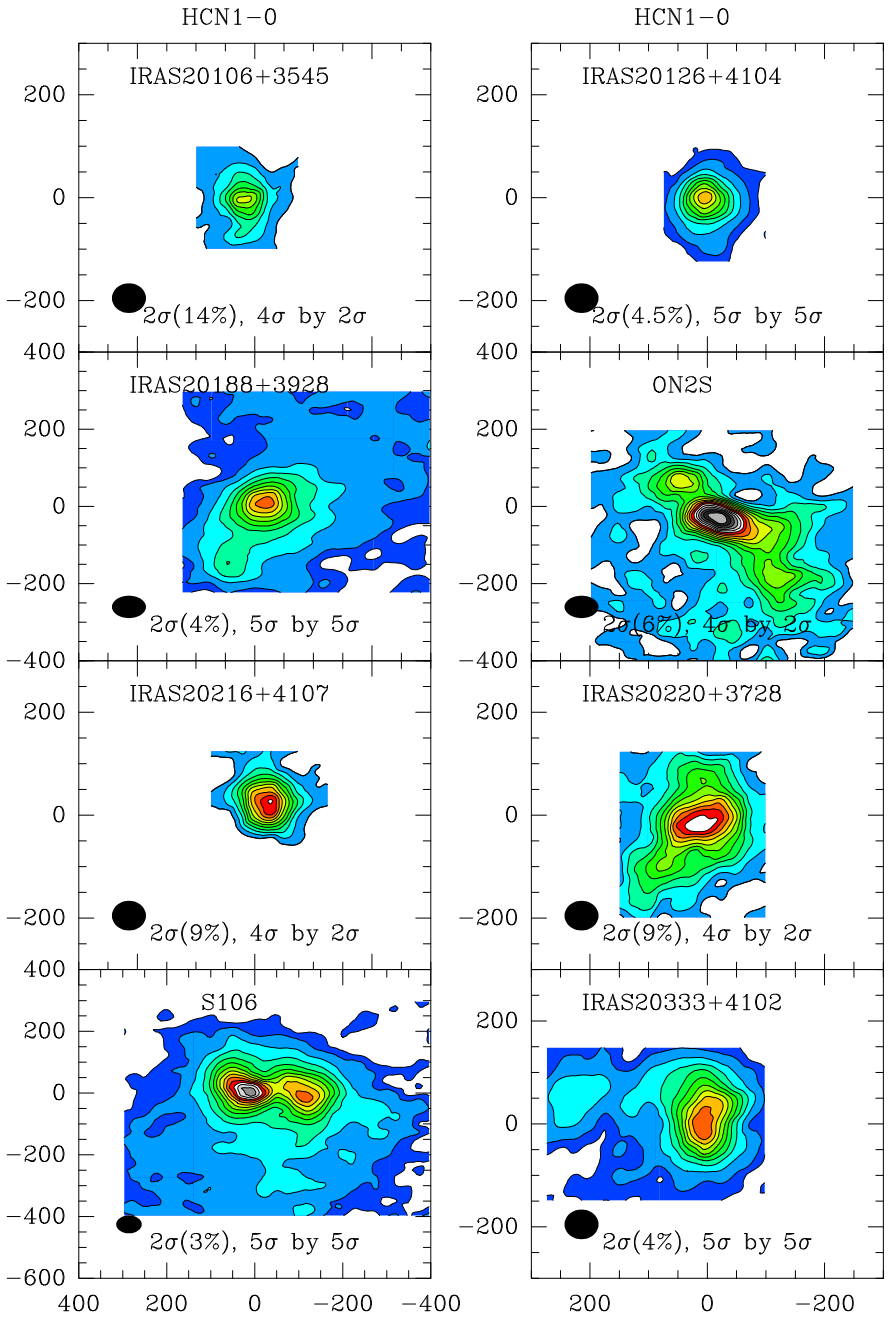

Figure A.5 HCN 1-0 contour maps continue...

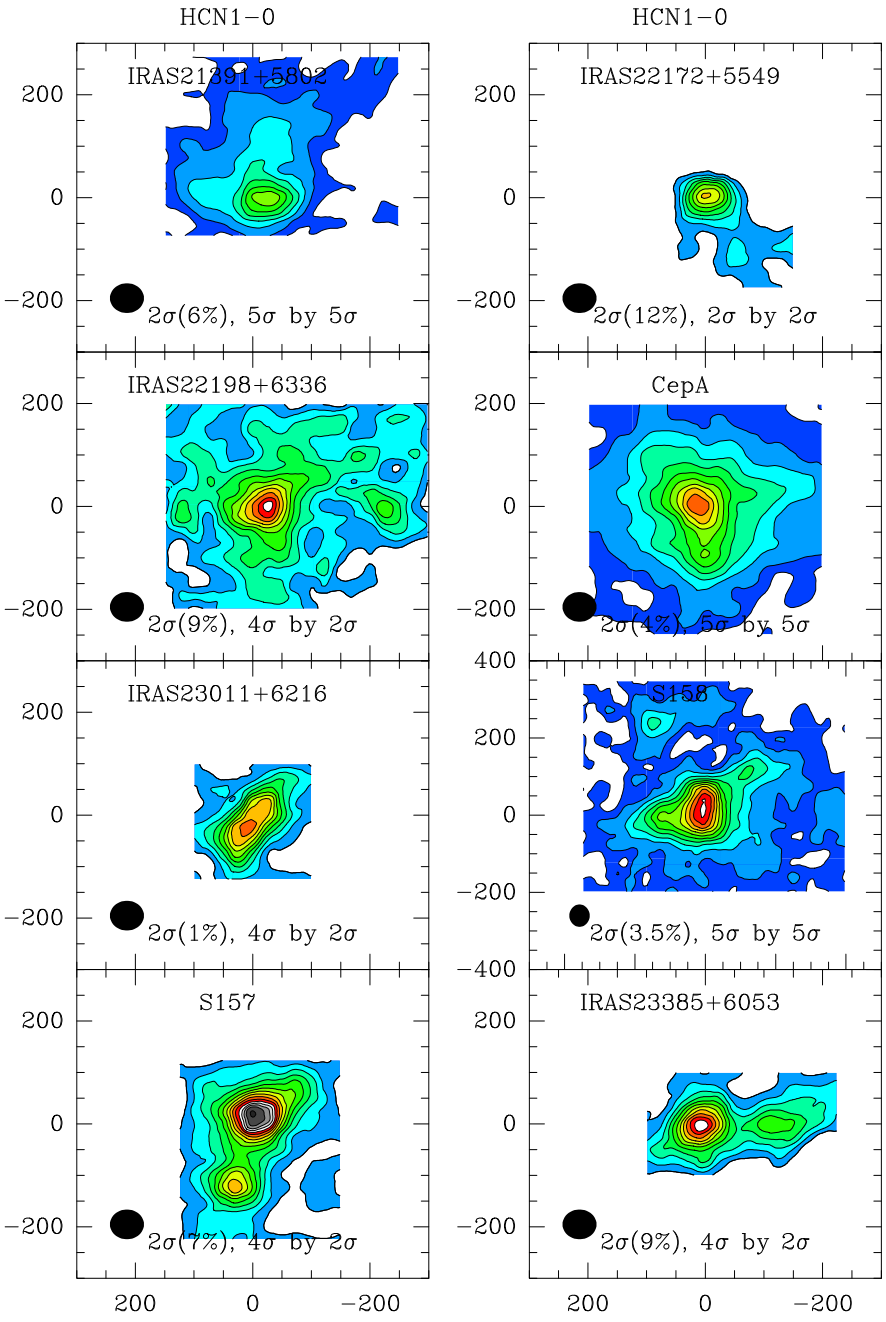

Figure A.6 HCN 1-0 contour maps continue...

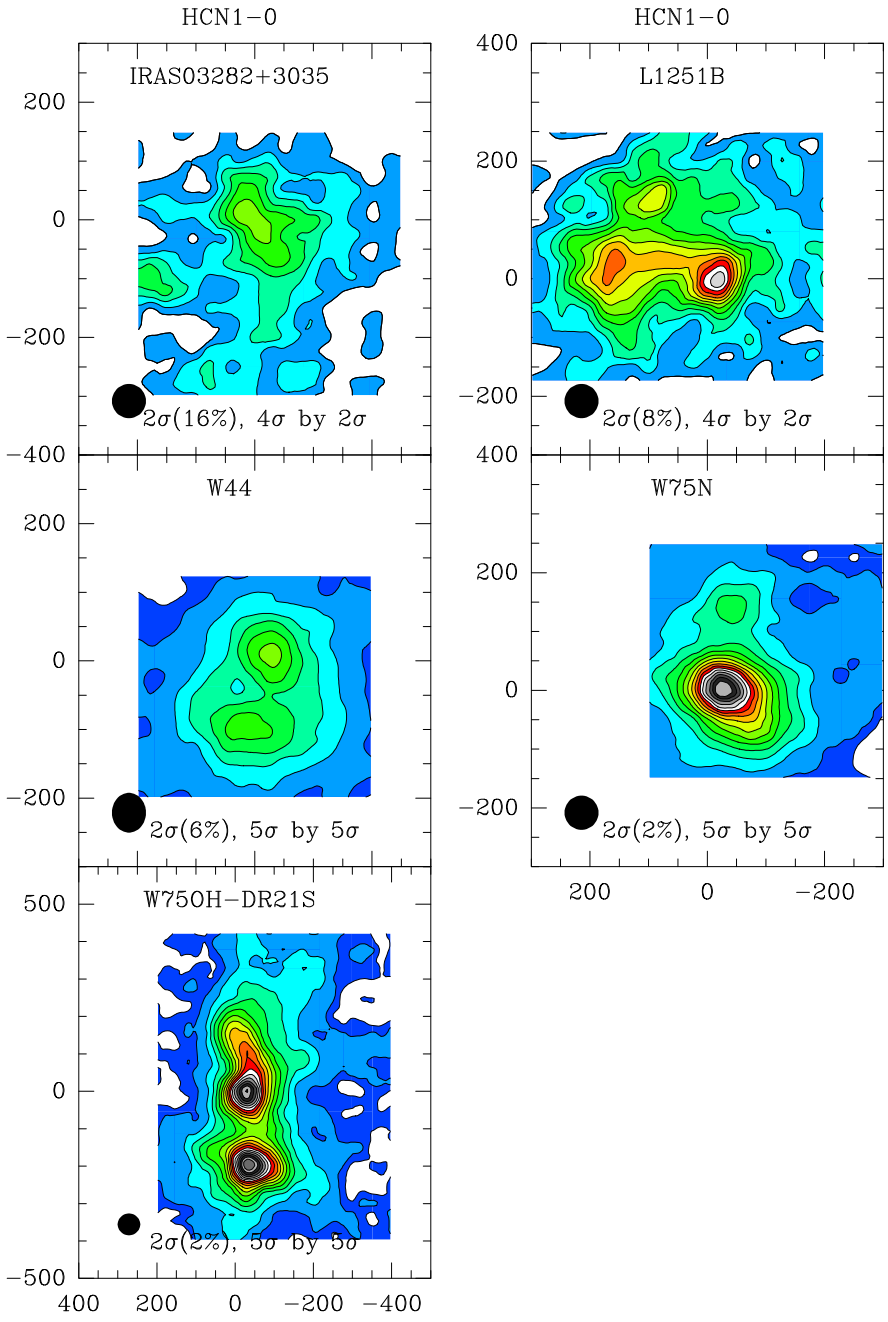

Figure A.7 HCN 1-0 contour maps continue...

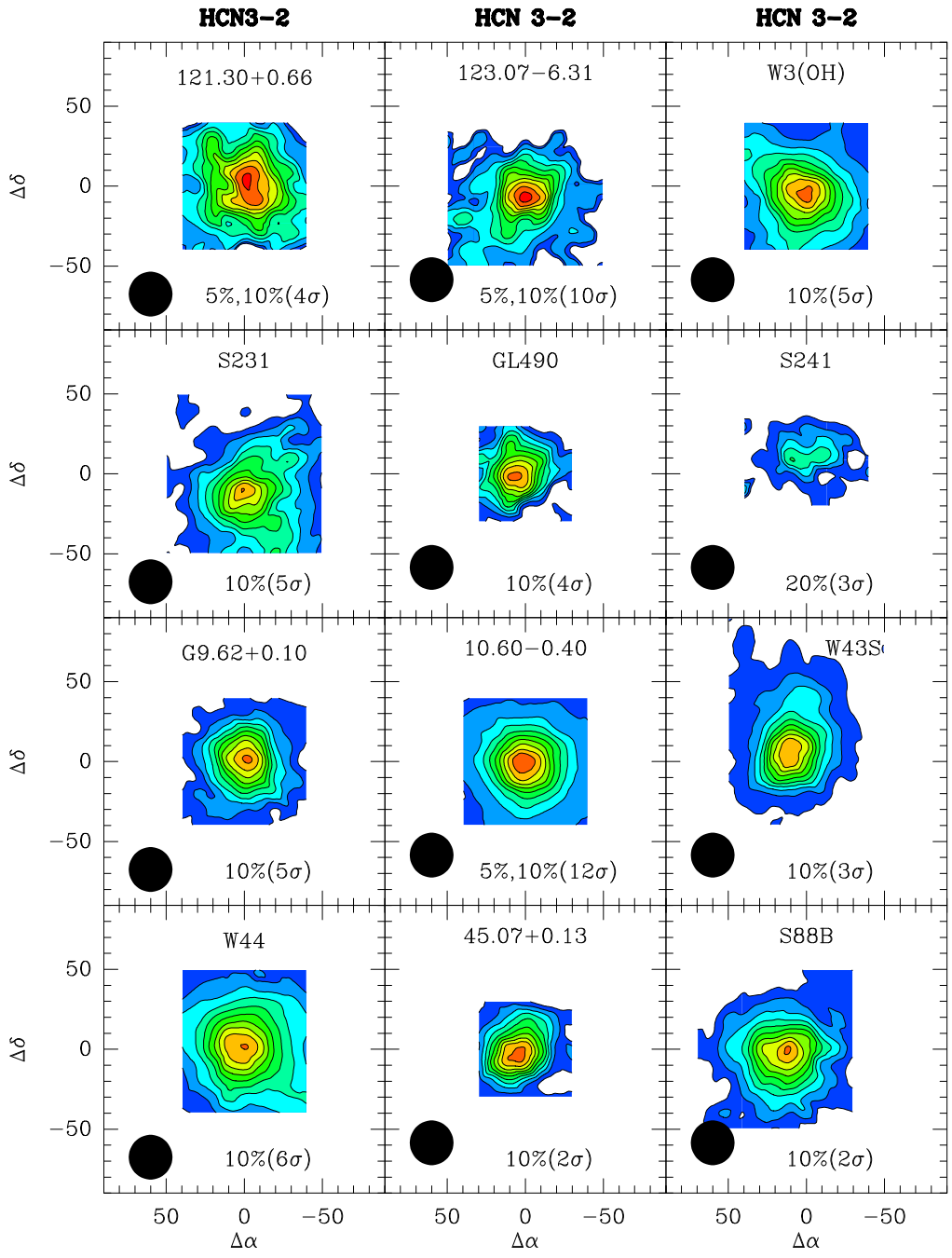

Figure A.8 HCN 3-2 contour maps of massive cores. The lowest contour level and increasing step of contours are indicated in the plot. The beam size is shown at the lower left of each map.

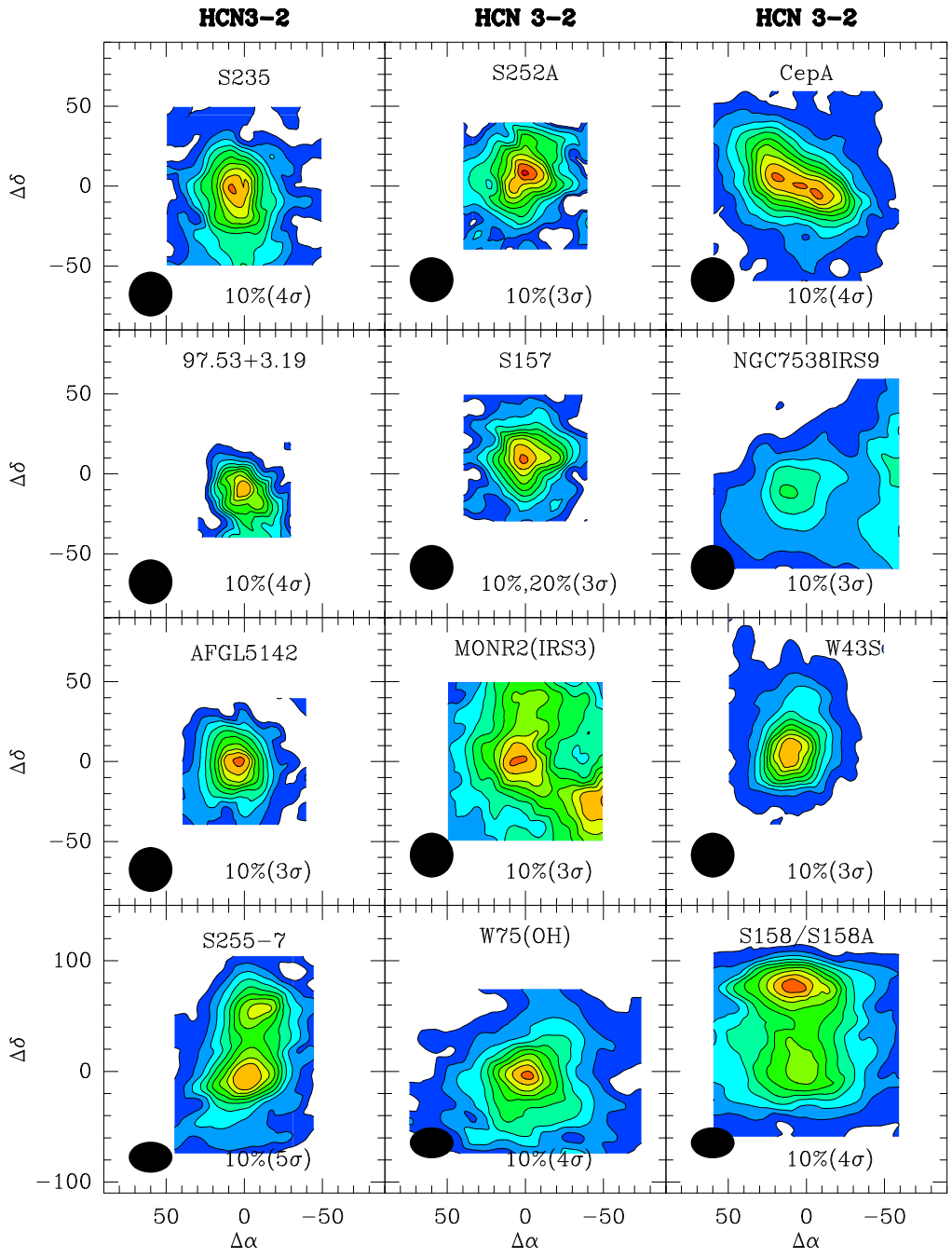

Figure A.9 HCN 3-2 contour maps continue...

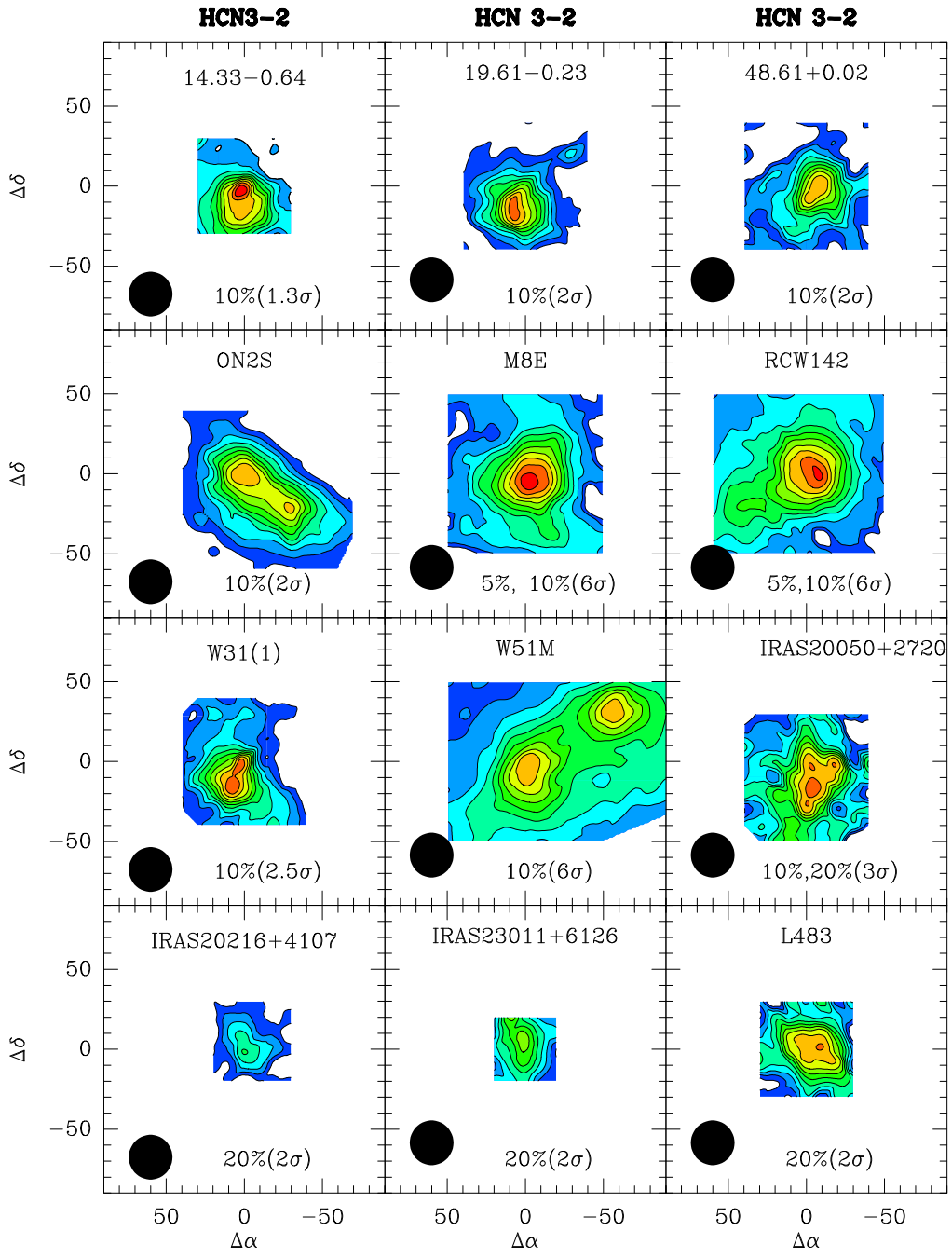

Figure A.10 HCN 3-2 contour maps continue...

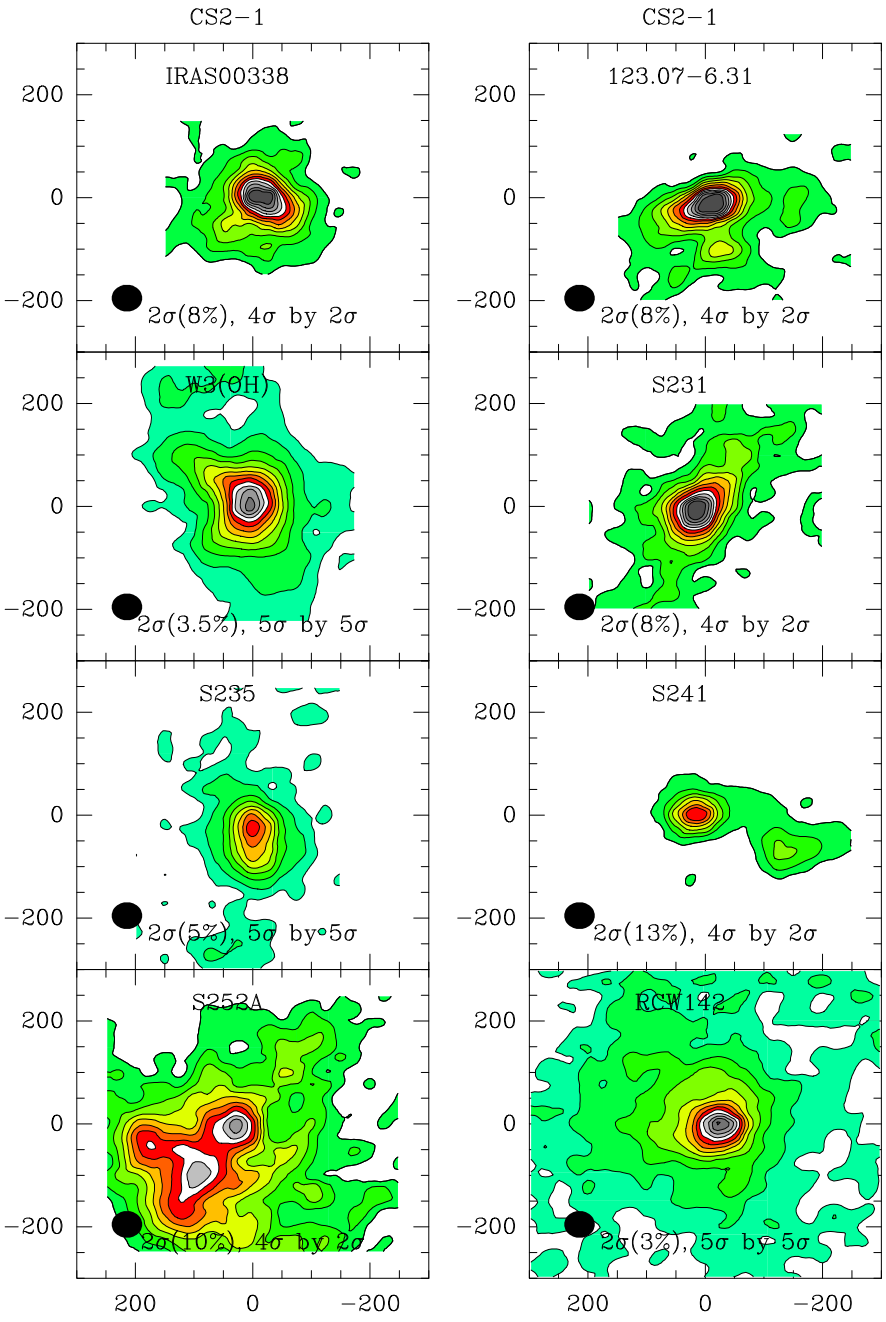

Figure A.11 CS 2-1 contour maps of massive cores. The lowest contour level and increasing step of contours are indicated in the plot. The beam size is shown at the lower left of each map.

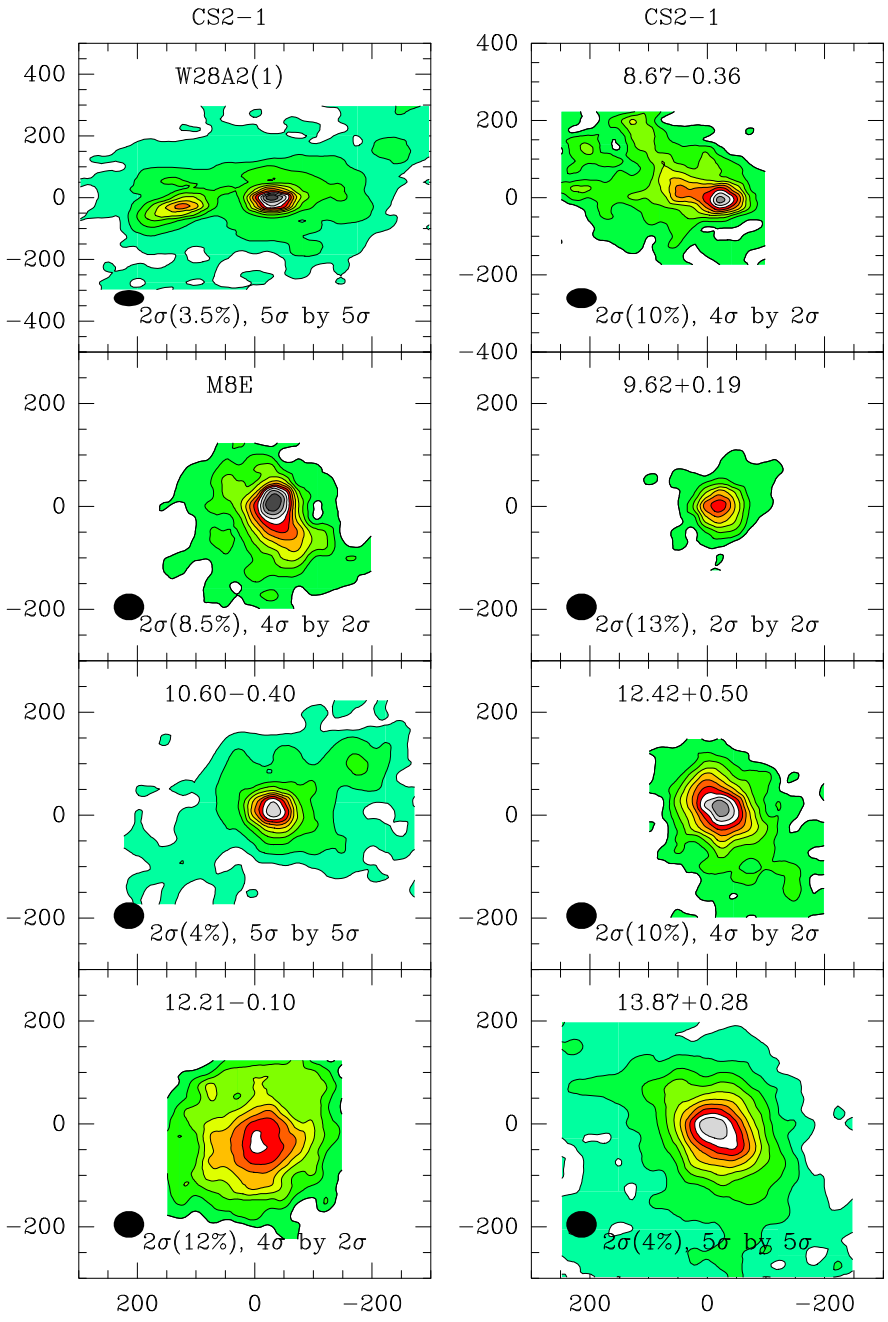

Figure A.12 CS 2-1 contour maps continue...

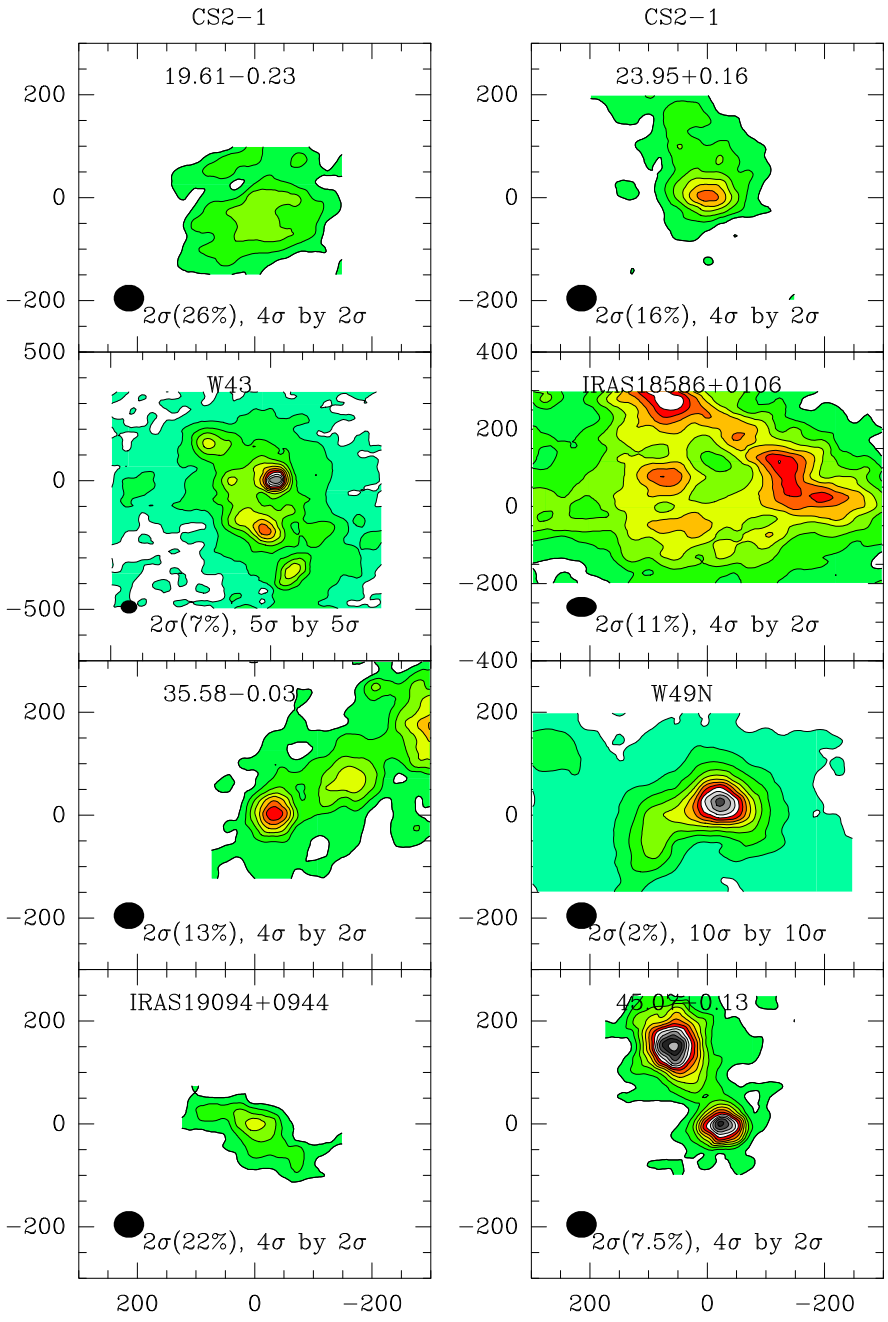

Figure A.13 CS 2-1 contour maps continue...

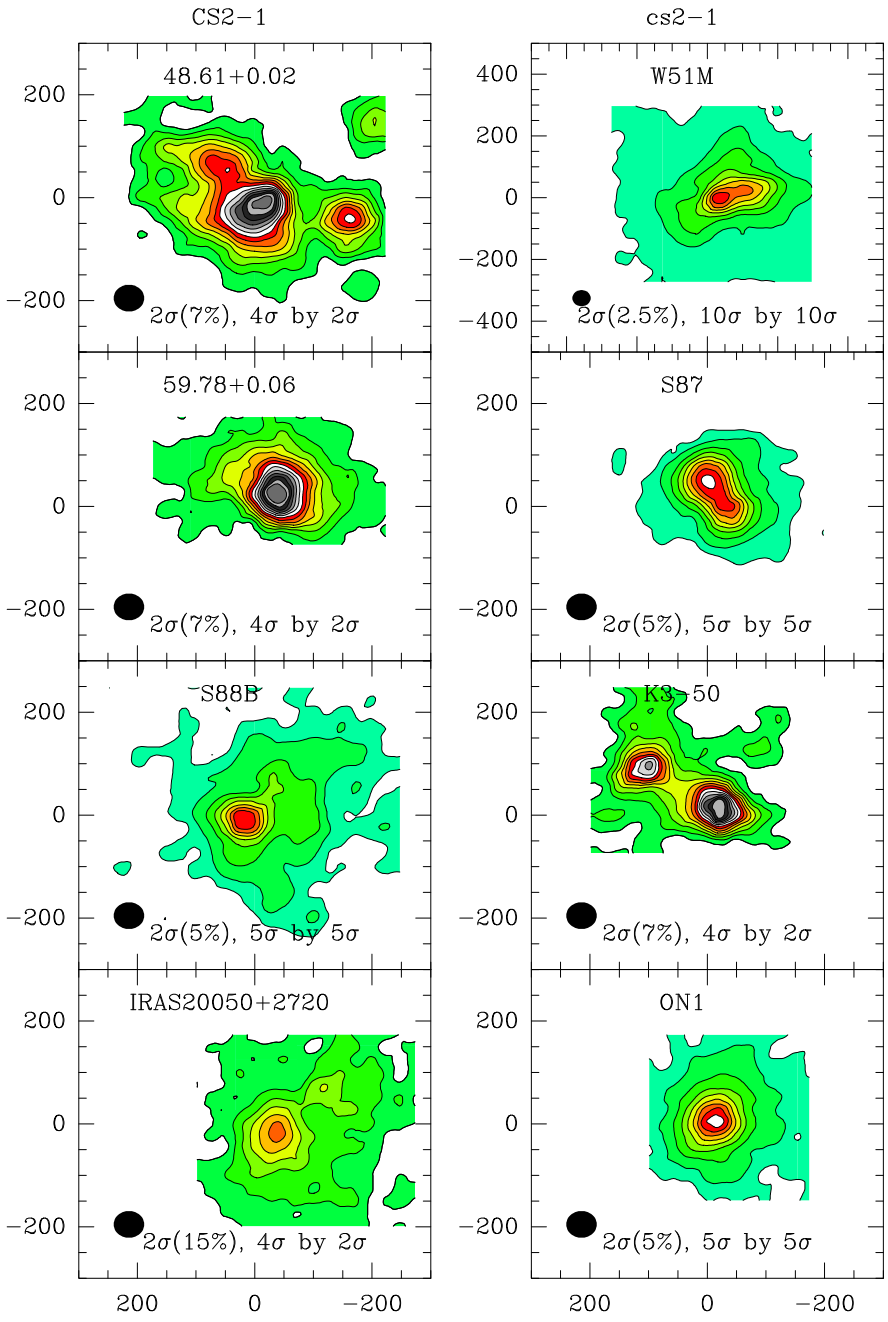

Figure A.14 CS 2-1 contour maps continue...

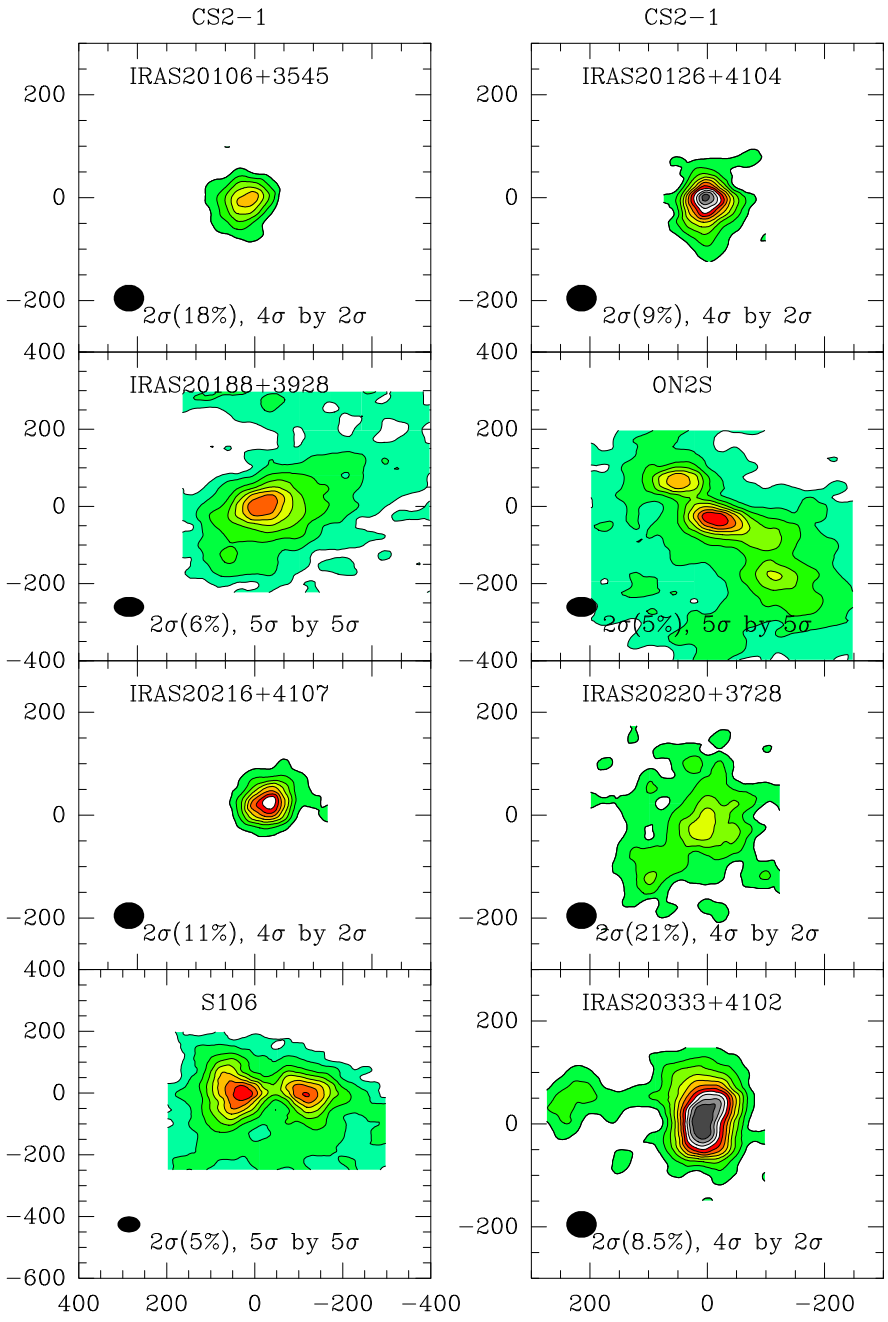

Figure A.15 CS 2-1 contour maps continue...

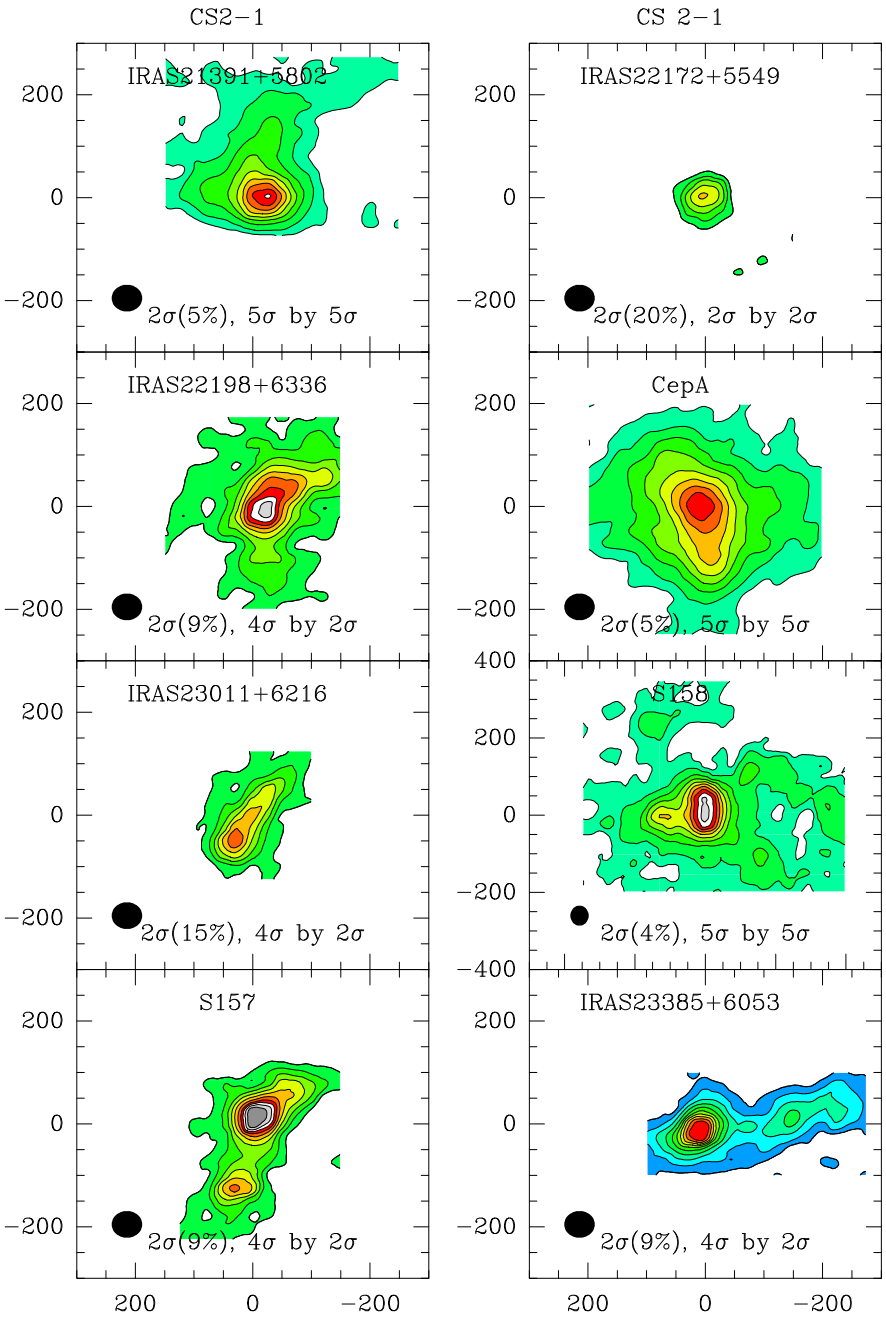

Figure A.16 CS 2-1 contour maps continue...

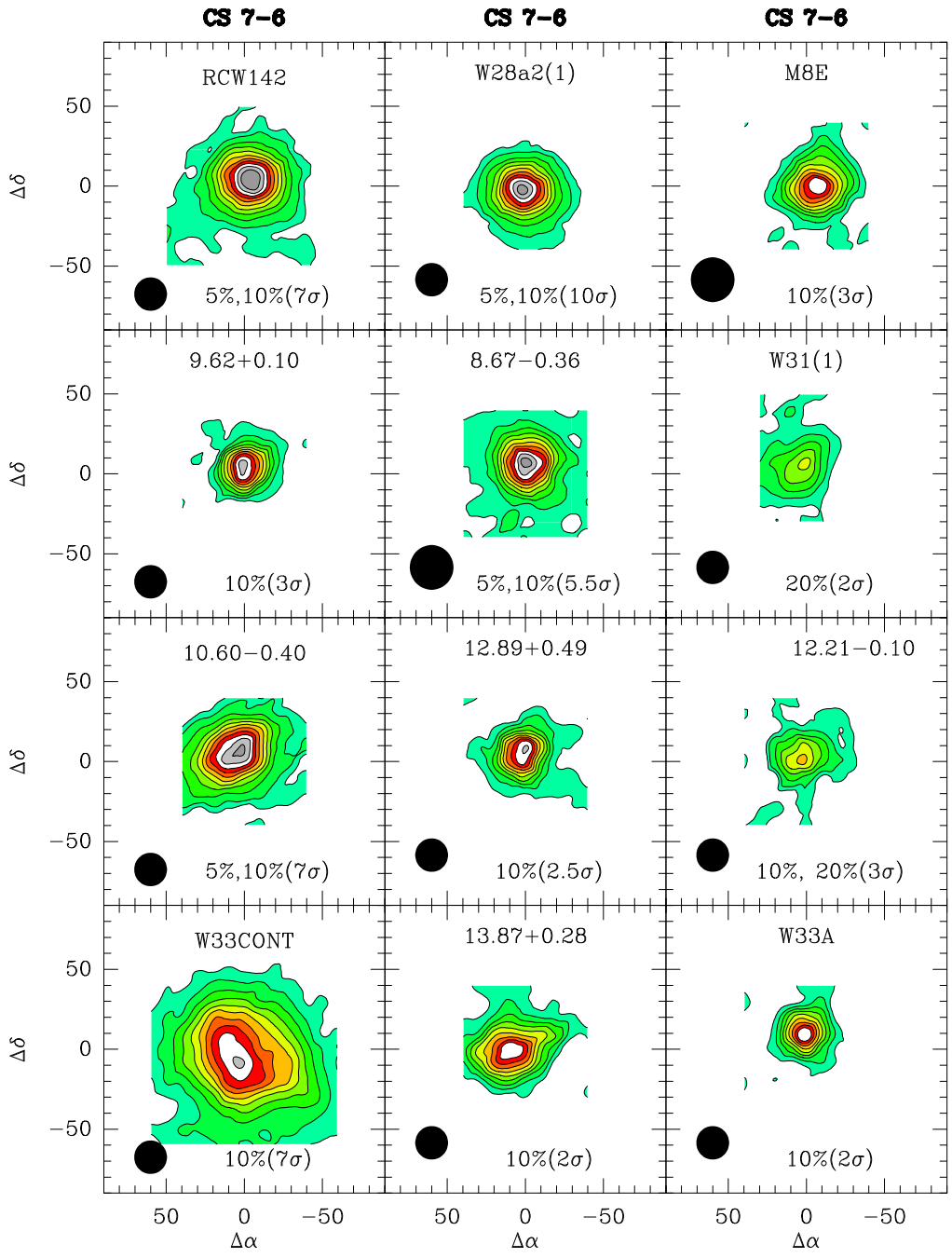

Figure A.17 CS 7-6 contour maps of massive cores. The lowest contour level and increasing step of contours are indicated in the plot. The beam size is shown at the lower left of each map.

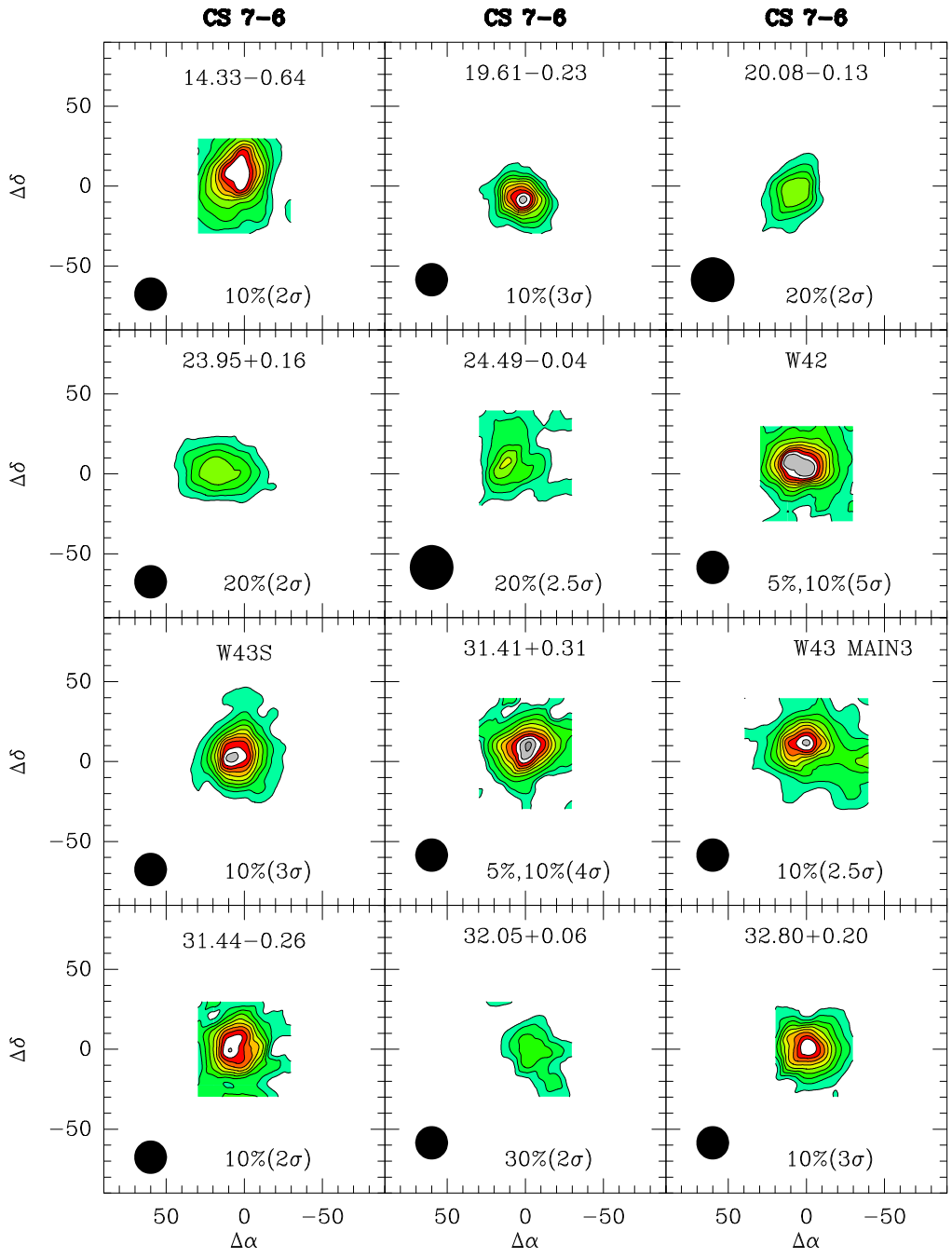

Figure A.18 CS 7-6 contour maps continue...

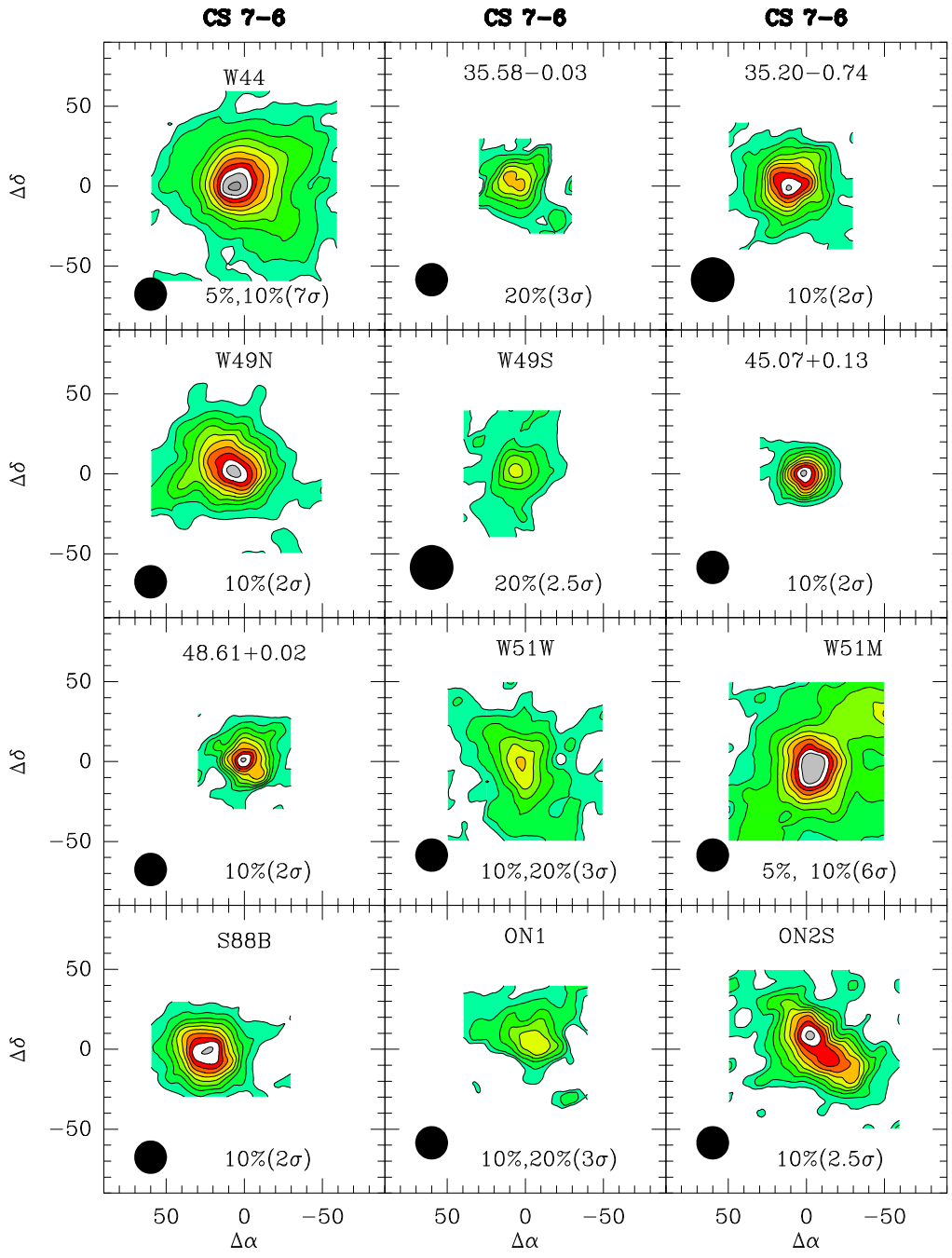

Figure A.19 CS 7-6 contour maps continue...

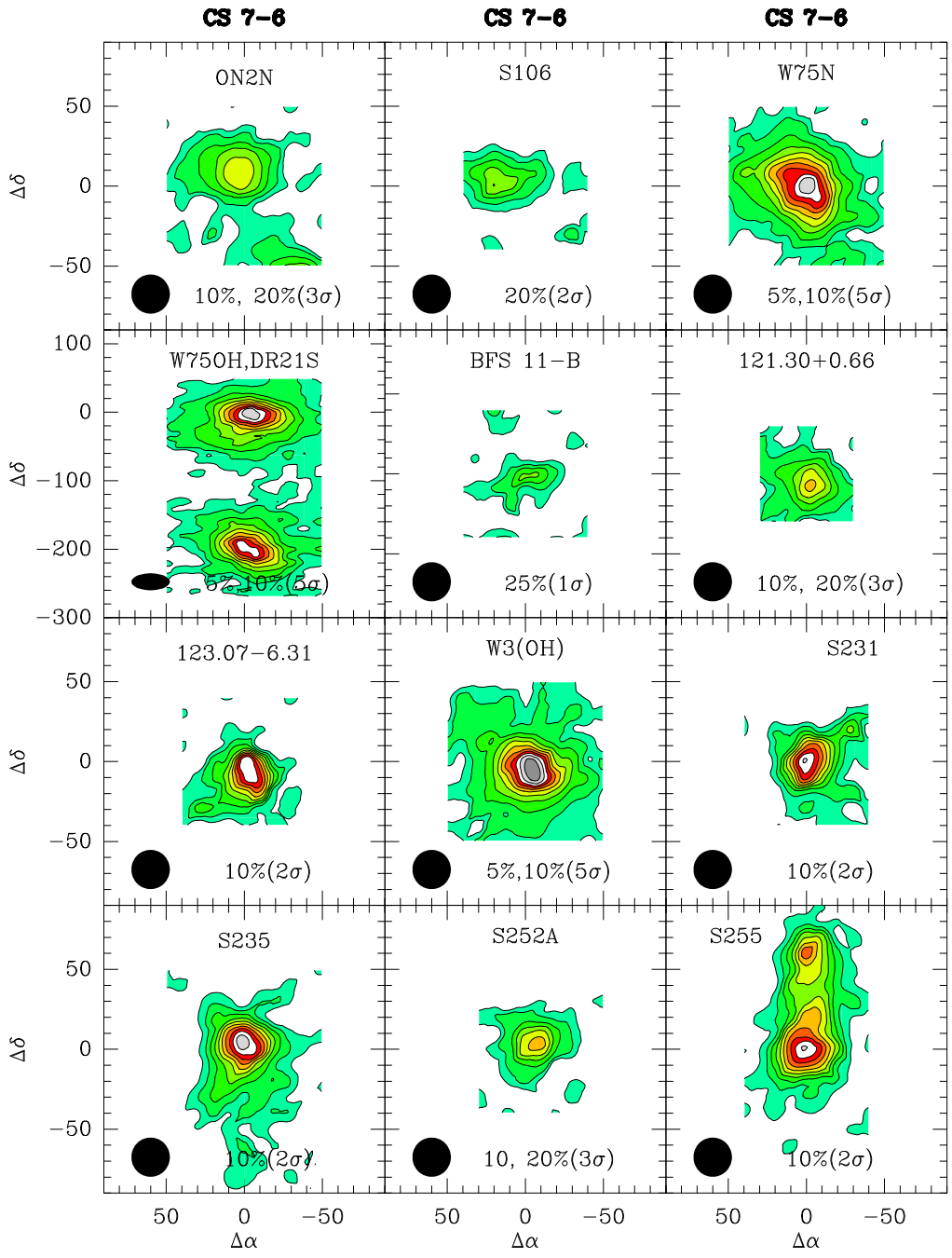

Figure A.20 CS 7-6 contour maps continue...

Appendix B

SHARCII Maps of Low-Mass Nearby Dense Cores

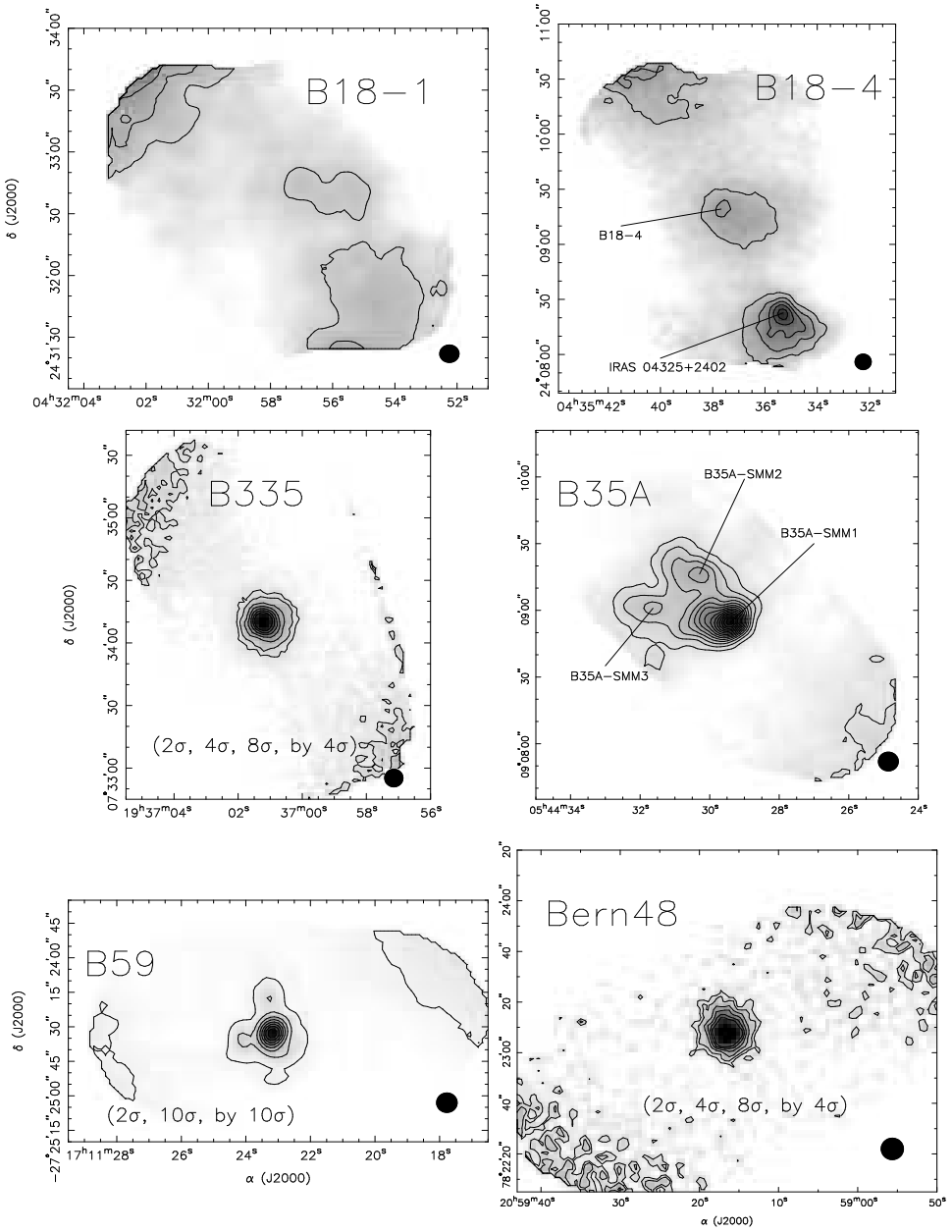

Figure B.1 SHARCII 350 μm maps of the low-mass cores listed in in Table 5.1. Contours begin at 2σ and increase by 2σ, unless otherwise indicated. The beam size is shown at the lower right of each map, and cores with multiple sources have each source labeled. Emission seen towards the edges of some maps is not reliable and should be ignored.

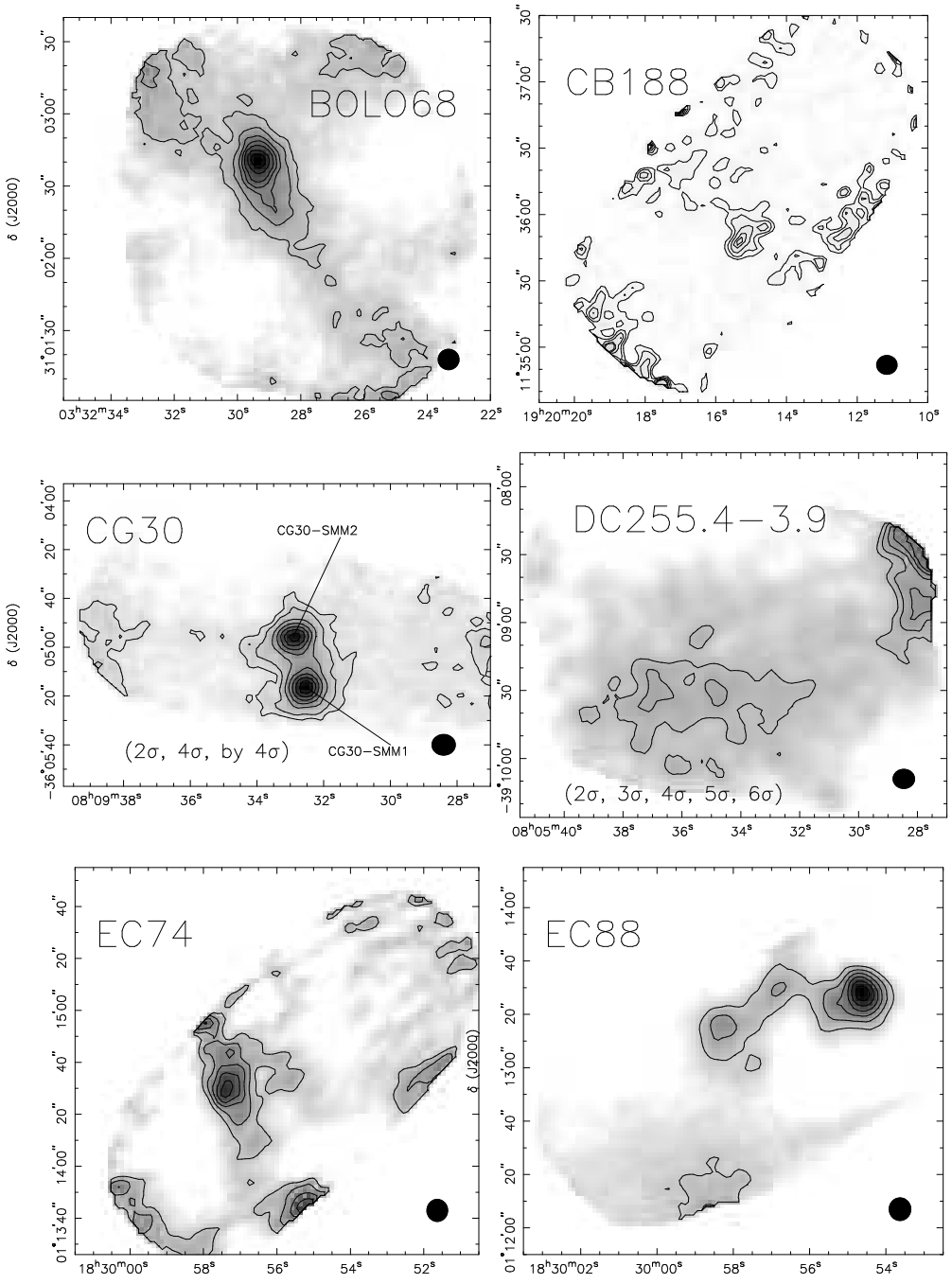

Figure B.2 SHARCII 350 μm maps, continued...

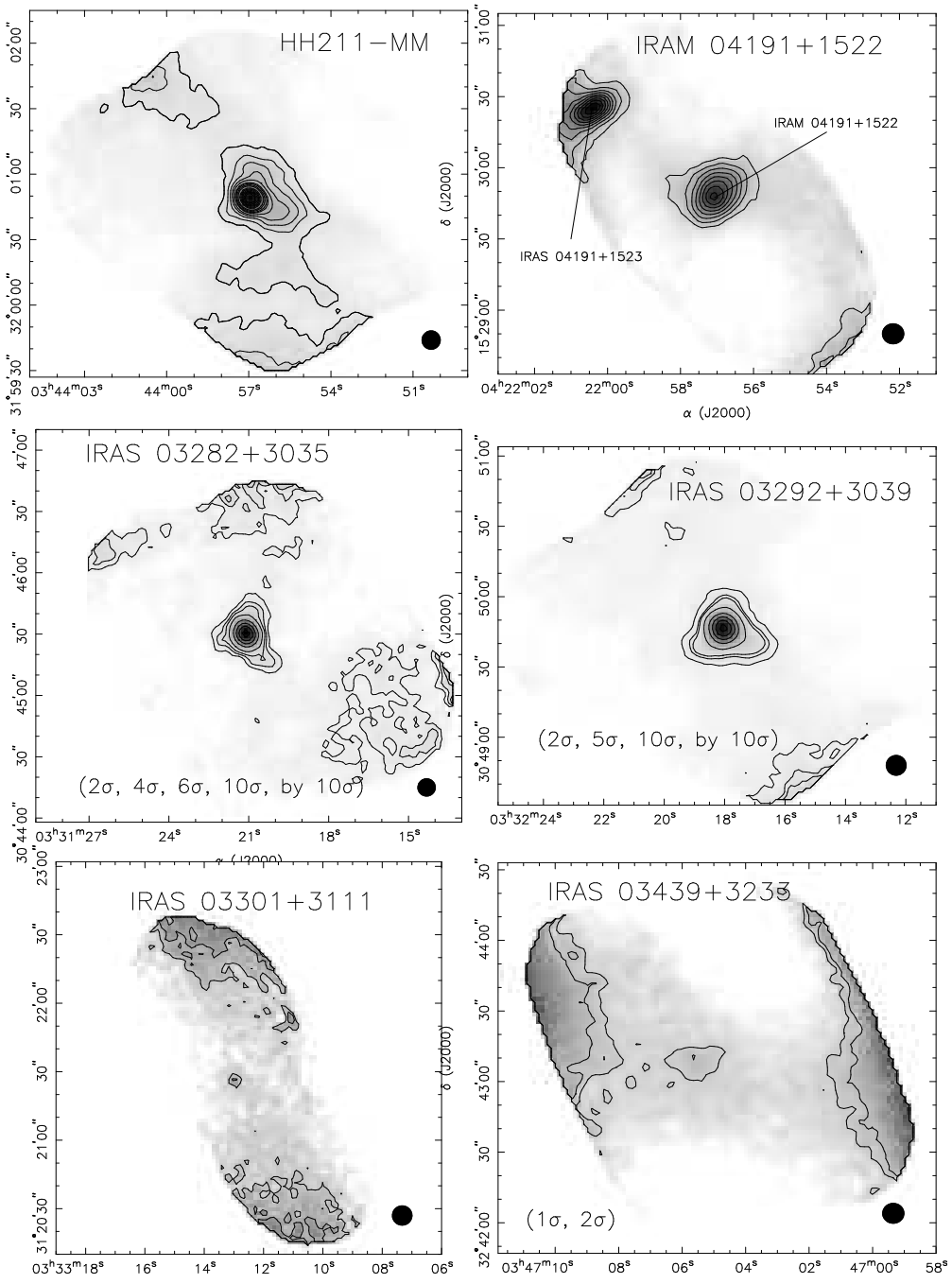

Figure B.3 SHARCII 350 μm maps, continued...

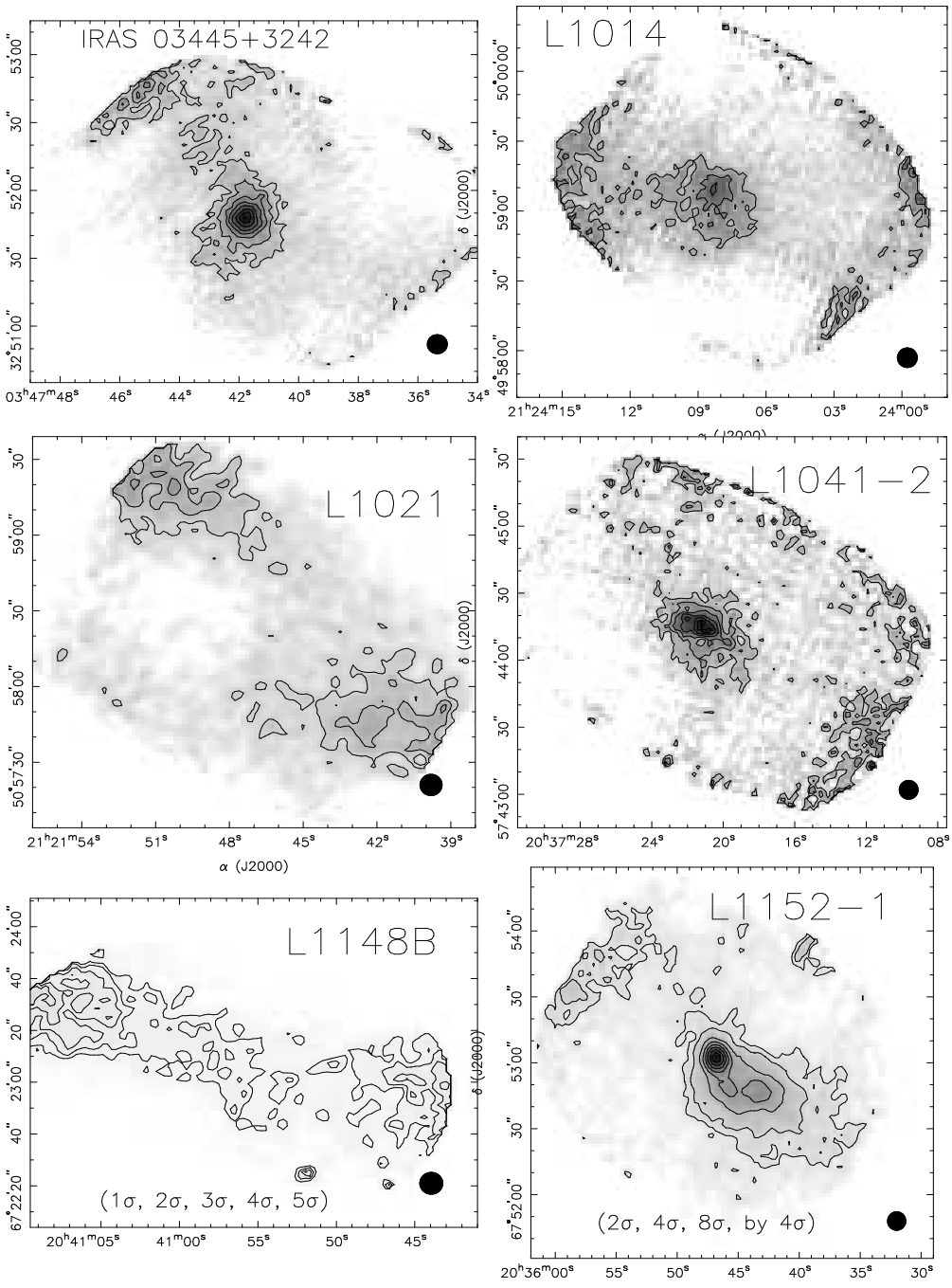

Figure B.4 SHARCII 350 μm maps, continued...

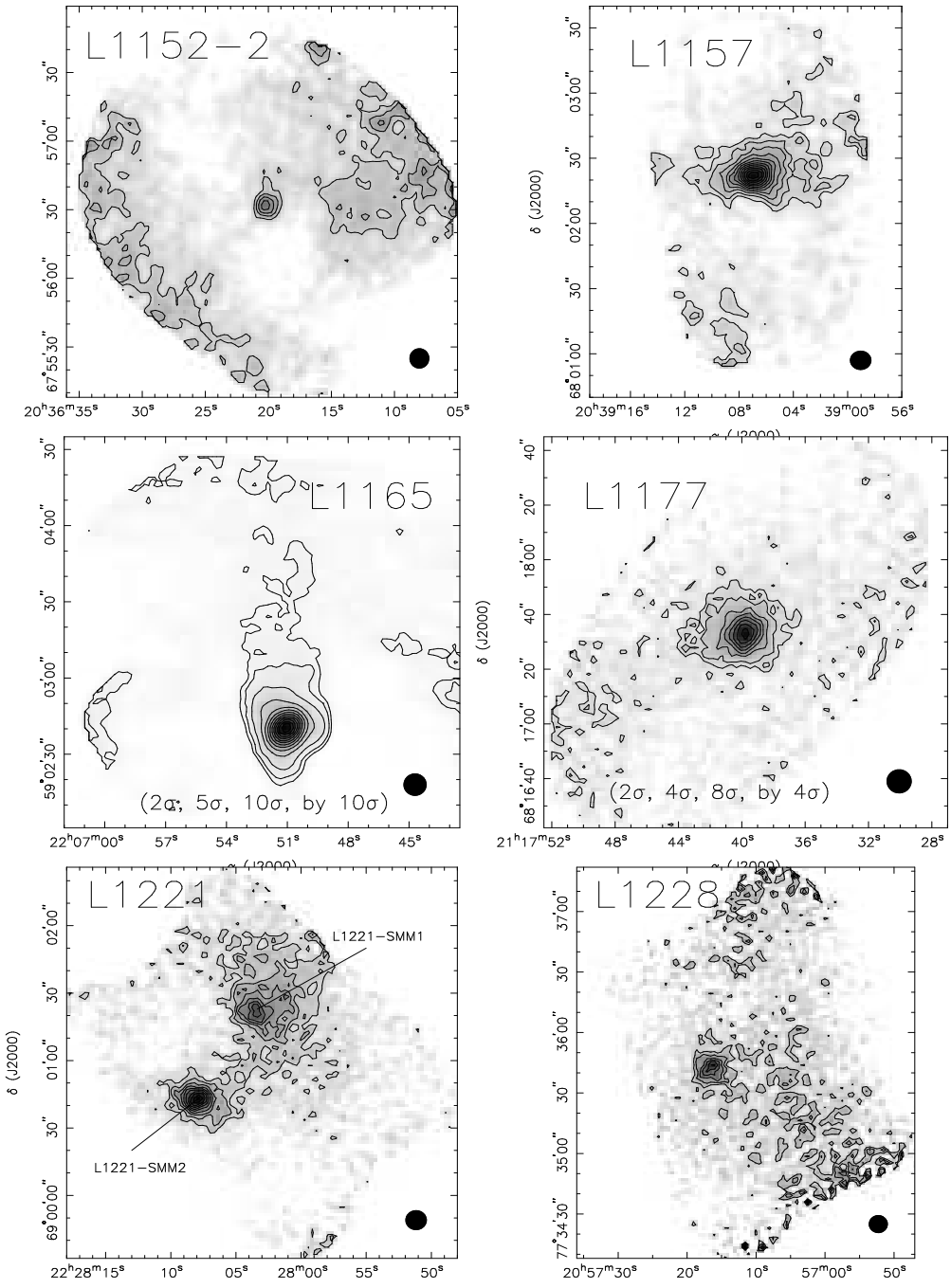

Figure B.5 SHARCII 350 μm maps, continued...

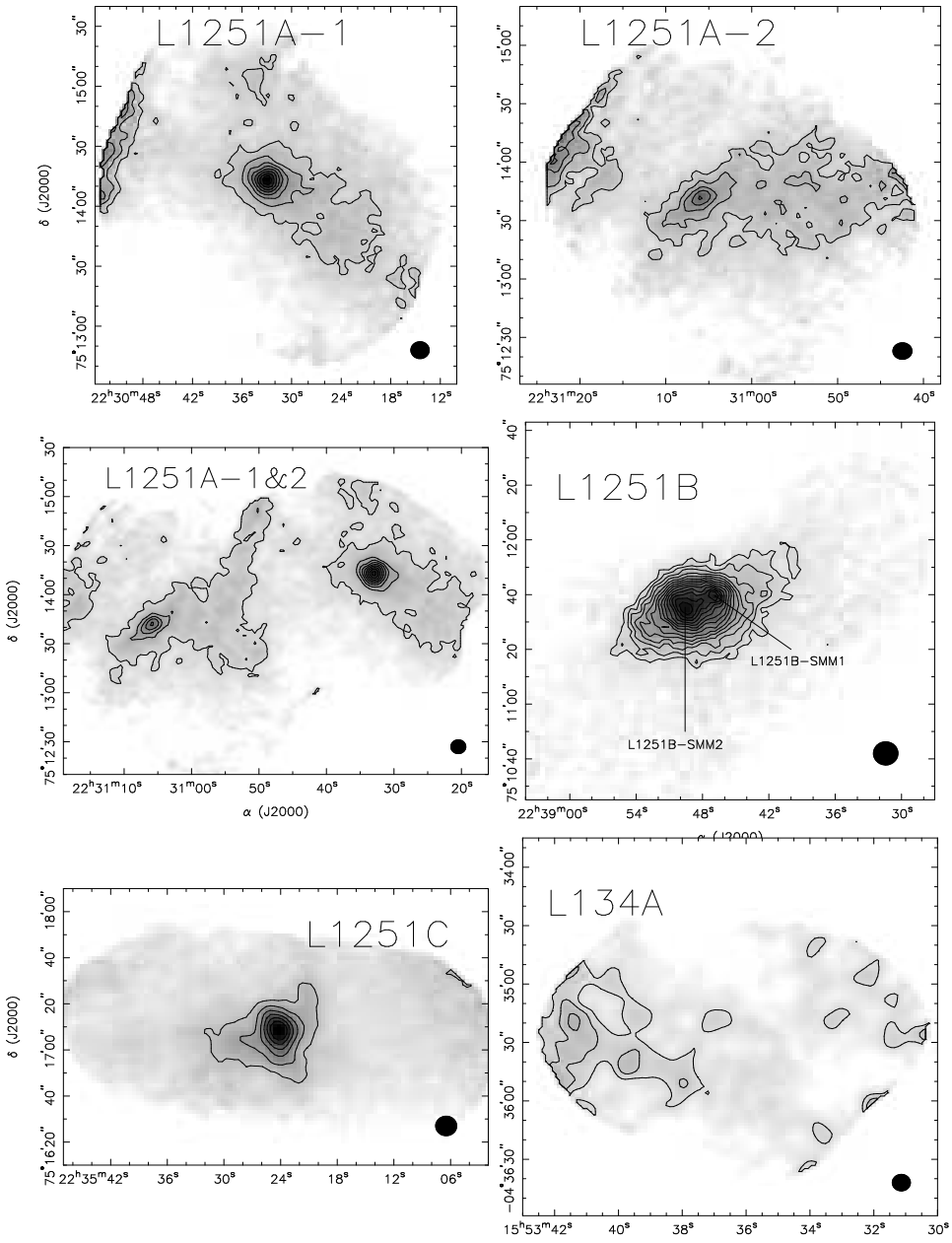

Figure B.6 SHARCII 350 μm maps, continued. The combined map of L1251A-1 and L1251A-2 includes a filament between the two sources extending south from the northern edge of the map. This results from spurious edge emission at the edges of the individual maps of L1251A-1 and L1251A-2 and should not be considered as real emission.

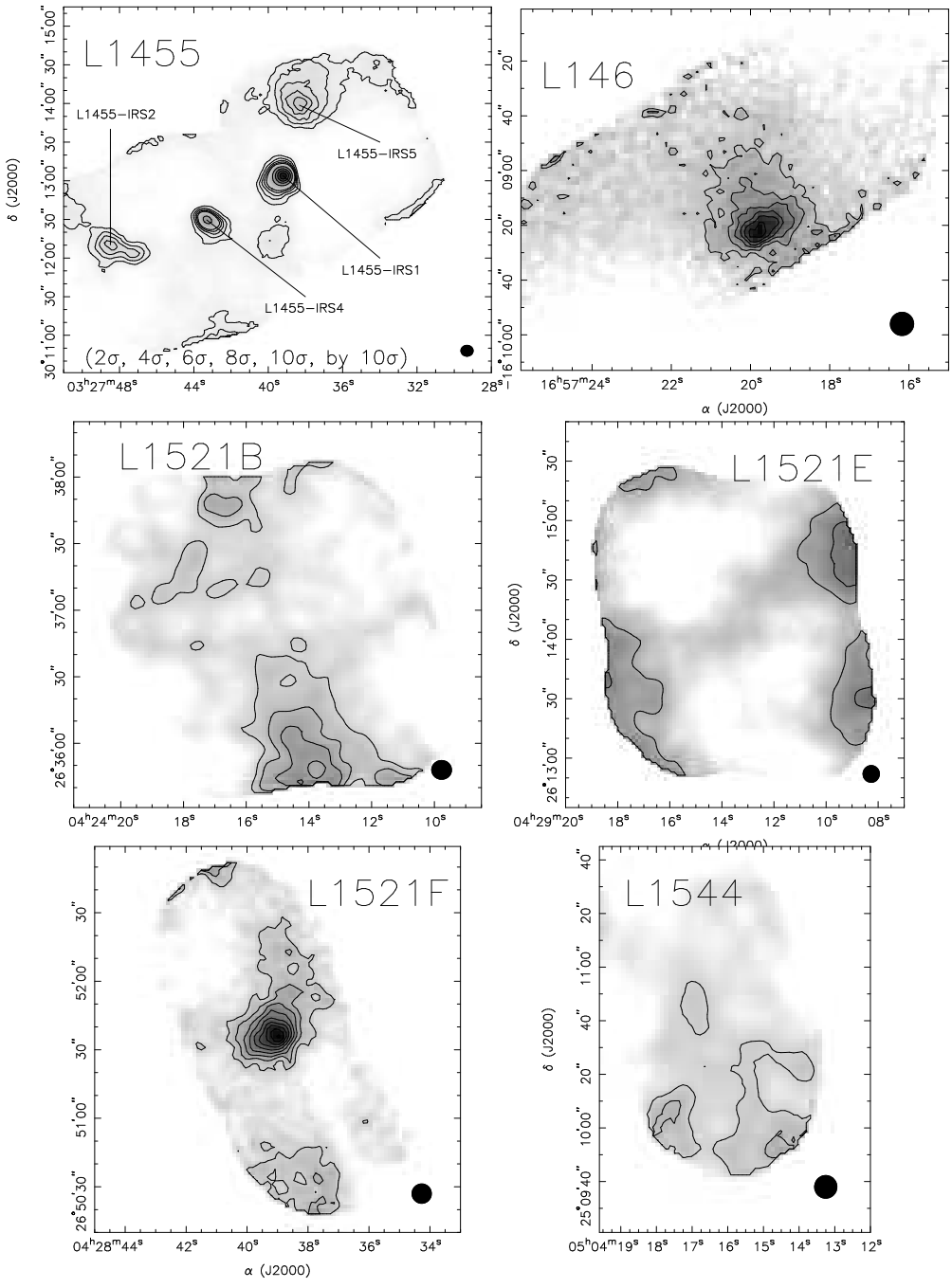

Figure B.7 SHARCII 350 μm maps, continued...

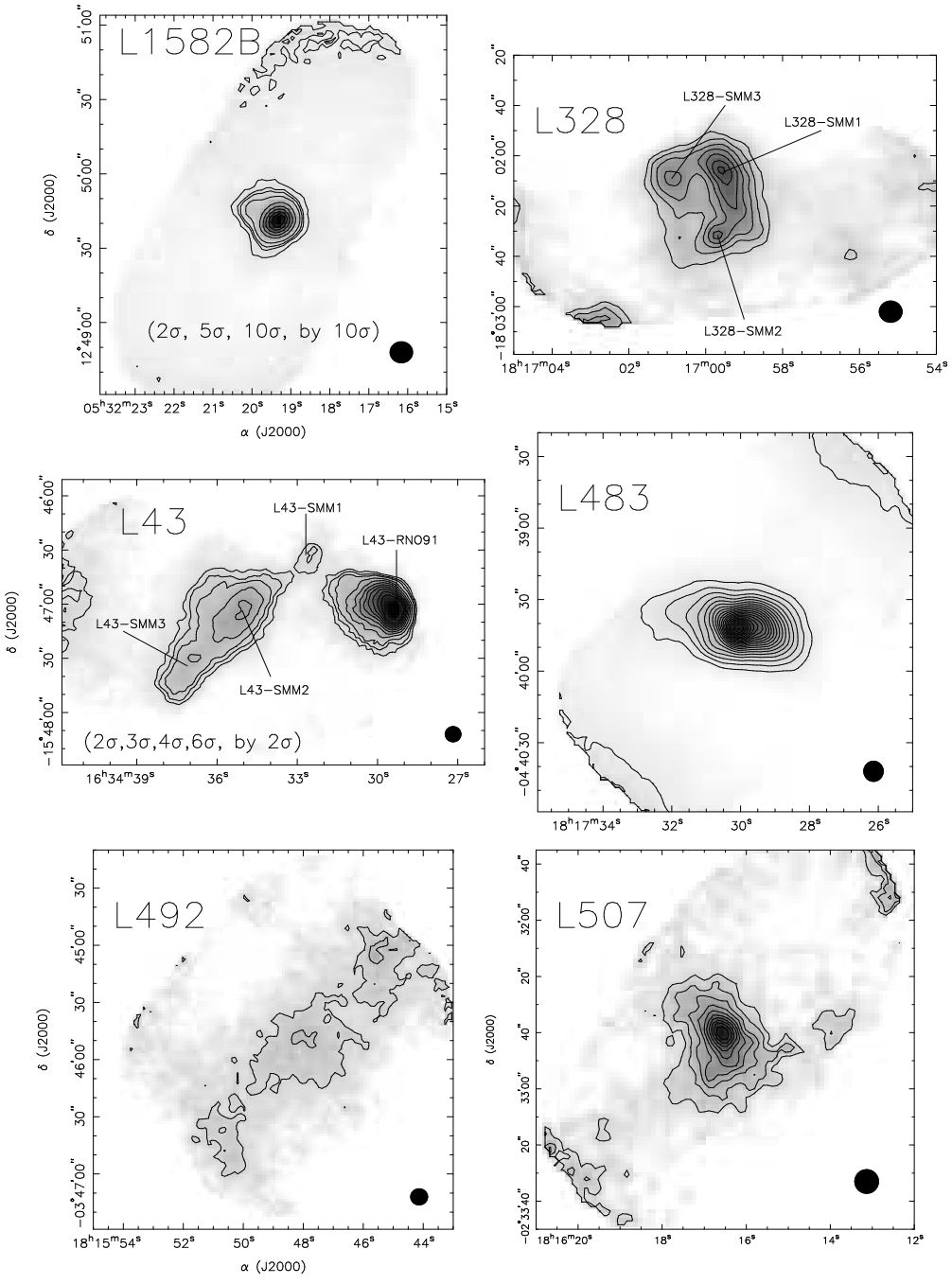

Figure B.8 SHARCII 350 μm maps, continued...

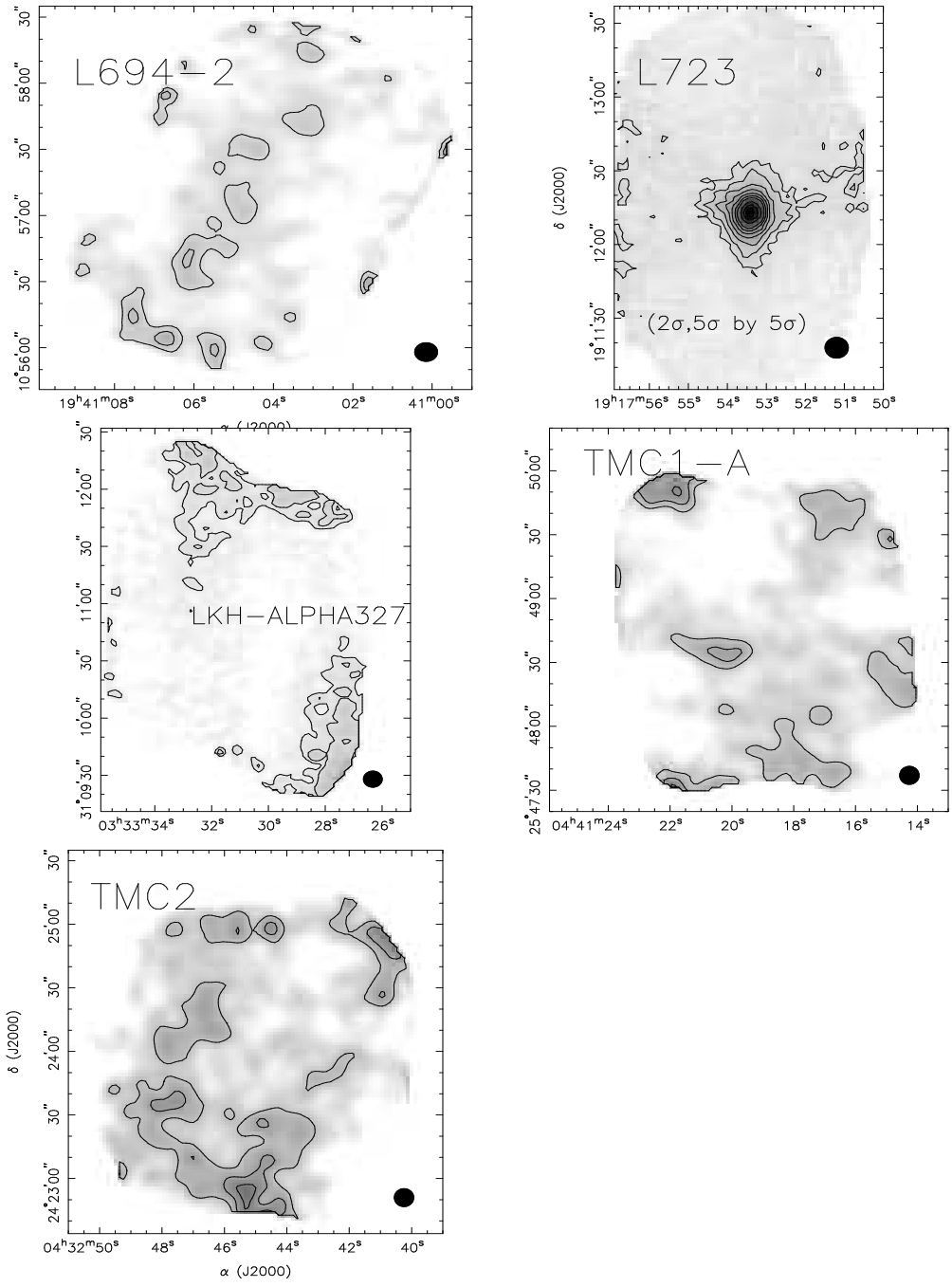

Figure B.9 SHARCII 350 μm maps, continued...

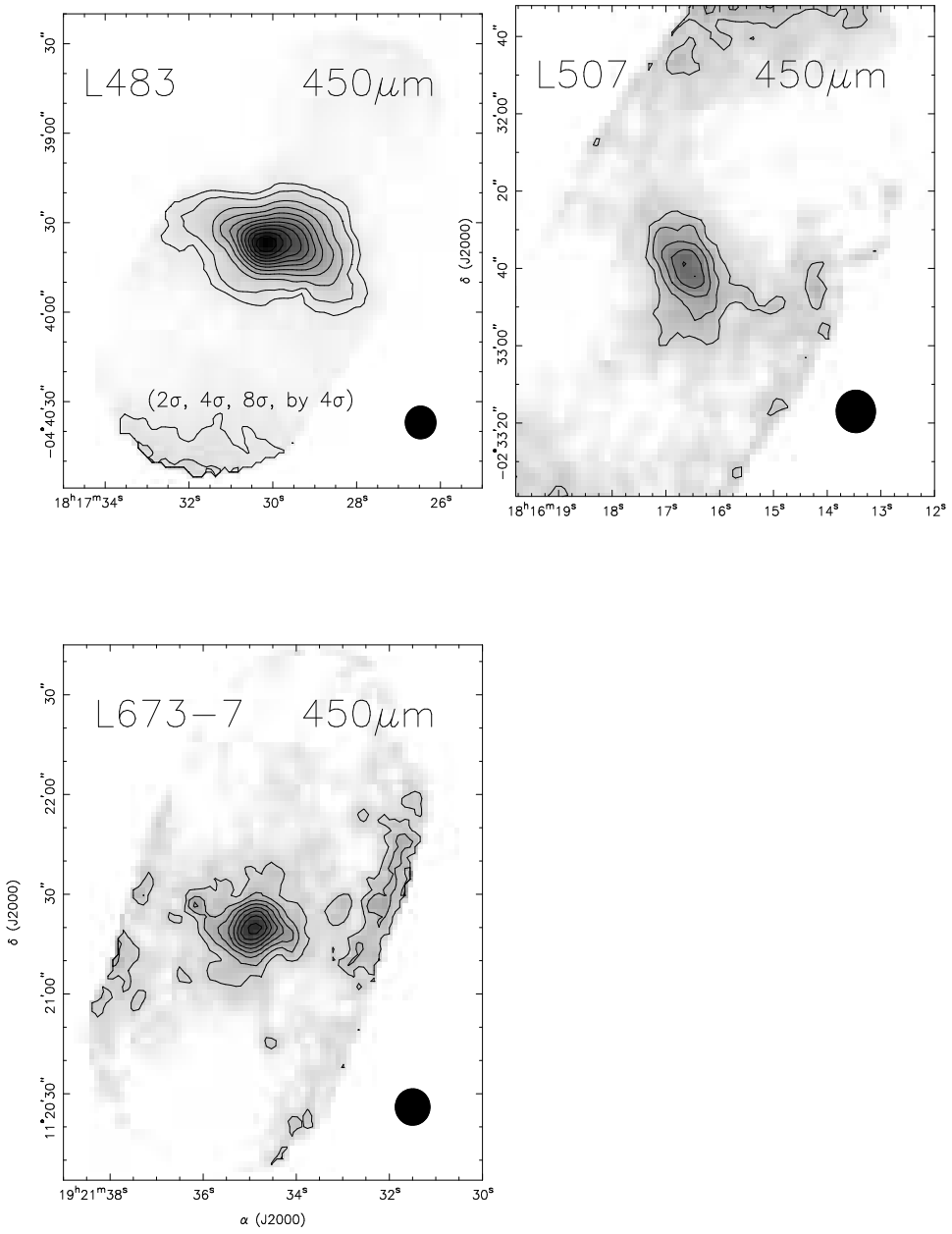

Figure B.10 SHARCII 450 μm maps of the three cores listed in Table 5.1 observed at this wavelength. Contours begin at 2σ and increase by 2σ, unless otherwise indicated. The beam size is shown at the lower right of each map. Emission seen towards the edges of some maps is not reliable and should be ignored.

Bibliography

[1] Ahrens, V., Lewen, F., Takano, S., Winnewisser, G., Urban, S., Negirev, A. A., & Koroliev, A. N. 2002, Z. Naturforsch., 57a, 669.

[2] Bertin, E., SExtractor v2.3 User's Manual (Paris: Insitut d'Astrophysique)

[3] Blitz, L., Fich, M., & Stark, A.A. 1982, ApJS, 49 183

[4] Brand, J., Blitz, L. 1993, A&A, 275, 67

[5] Braz, M.A., & Epchtein, N. 1983, A& A, 54, 167

[6] Brede, K., et al. 2006, in preparation

[7] Bourke, T.L., et al. 2006, ApJ submitted

[8] Carilli, C. L., Solomon., P. M., Vanden Bout, P. A., Walter, F., Beelen, A., and Cox, P., Bertoldi, F., Menten, K. M., Isaak, K. G., Chandler, C. J., & Omont, A. 2005, ApJ, 618, 586

[9] Carpenter, J. M. 2000, AJ, 120, 3139

[10] Casassus, S., Bronfman, L., May, J., & Nyman, L. -A. 2000, A&A, 358, 514

[11] Caselli, P., Benson, P. J., Myers, P. C., & Tafalla, M. 2002, ApJ, 572, 238

[12] Cernis, K. 1990, Ap&SS, 166, 315

[13] Chen, H., Myers, P. C., Ladd, E. F., & Wood, D. O. S. 1995, ApJ, 445, 377

[14] Chini, R., Kreysa, E., Mezger, P. G., & Gemuend, H. -P. 1986, A&A, 154, L8

[15] Choi, M., Evans, N. J. II, Gregersen, E. M, & Wang, Y. 1995, ApJ, 448, 742

[16] Churchwell, E., Wolfire, M. G., & Wood, D. O. S. 1990, ApJ, 354, 247

[17] Dame, T. M., & Thaddeus, P. 1985, ApJ, 297, 751

[18] de Geus, E. J., de Zeeuw, P. T., & Lub, J. 1989, A&A, 216, 44

[19] Di Francesco, J. D., Evans N. J .II, Caselli, P., Myers, P. C., Shirley, Y. L., Aikawa, A., and Tafalla, M. 2006, to appear in "Protostars and Planets V".

[20] Dickel, H. R., & Auer, L. H. 1994, ApJ, 437, 222

[21] Dobashi, K., Bernard, J.-P., Yonekura, Y., & Fukui, Y. 1994, ApJS, 95, 419

[22] Dowell, C.D., et al. 2002, SPIE, 4855

[23] Downes, D., Wilson, T.L., Bieging, J., & Wink, J. 1980, A& A, 91, 186

[24] Dunham, M.M., et al. 2006, ApJ submitted

[25] Egan, M. P., Leung, C. M., & Spagna, G. F., 1988, Comput. Physics Comm., 48, 271

[26] Elmegreen, B.G. 1985, in Protostar and Planets II, ed. D.C. Black & M.S.Matthews(Tucson:Univ.Arizona Press), 33

[27] Enoch, M.L., et al. 2006, ApJ, 638, 293

[28] Evans, N. J. II, 1991, ASP Conf. Ser. 20: Frontiers of Stellar Evolution, 45

[29] Evans, N. J. II, 1999, ARAA, 37, 311

[30] Evans, N. J. II, 2003, Proceedings of the conference "Chemistry as a Diagnostic of Star Formation", University of Waterloo, Canada, 21-23 August 2002 (C.L. Curry & M. Fich eds.).

[31] Evans, N.J. II et al. 2003, PASP, 115, 965

[32] Evans, N. J., II, Lee, J.-E., Rawlings, J. M. C., & Choi, M. 2005, ApJ, 626, 919

[33] Evans, N. J., II et al. 2006, Delivery of Data from the c2d Legacy Project: IRAC and MIPS (Pasadena, SSC), http://ssc.spitzer.caltech.edu/legacy/original.html

[34] Fazio, G.G., et al. 2004, ApJS, 154, 10

[35] Franco, G. A. P. 1989, A&A, 223, 313

[36] Gao, Y., & Solomon, P. M., 2004a, ApJ, 606, 271

[37] Gao, Y., & Solomon, P. M., 2004b, ApJS, 152, 63

[38] Genzel, R. & Downes, D. 1977, A& AS, 30 145

[39] Goldsmith, P. F., Snell, R. L., Hemeon-Heyer, M., & Langer, W. D. 1984, ApJ, 286, 599

[40] Gottlieb, C. A., Myers, P. C., and Thaddeus, P. 2003, ApJ, 588, 655

[41] Gregersen, E. M. & Evans, N. J. 2000, ApJ, 538, 260

[42] Gregersen, E. M., Evans, N. J. II, Mardones, D., & Myers, P. C. 2000, ApJ, 533, 440

[43] Gregersen, E. M., Evans, N. J. II, Zhou, S., & Choi, M. 1997, ApJ, 484, 256

[44] Greve, T. R., Bertoldi, F., Smail, Ian, Neri, R., Chapman, S. C., Blain, A. W., Ivison, R. J., Genzel, R., Omont, A., Cox, P., Tacconi, L., Kneib, J. -P. 2005, MNRAS, 359, 1165.

[45] Harris, S., & Wynn-Williams, C. G. 1976, MNRAS, 174, 649

[Harvey et al. 2006] Harvey, P.M. et al. 2006, ApJ in press

[46] Herbig, G. H., & Jones, B. F. 1983, AJ, 88, 1040

[47] Herbst, W. 1975, AJ, 80, 212

[48] Ho, L. C. 1997, in Rev. Mexicana Astron. Astrofis. Conf., Vol. 6, 1st Guillermo Haro Conference on Astrophysics: Starburst Activity in Galaxies, 5

[49] Hofner, P., Kurtz, S., Churchwell, E., Walmsley, C. M., & Cesaroni , R. 1996, ApJ, 460, 359

[50] Huard, T.L., et al. 2006, in preparation

[51] Hunter, T. R., Churchwell, E., Watson, C., Cox, P., Benford, D. J., & Roelfsema, P. R. 2000, AJ, 119, 2711

[52] Isaak, K. G., Priddey, R. S., Mcmahon, R. G., Omont, A., Peroux, C., Sharp, R. G., and Withington, S. 2002, MNRAS, 329, 149

[53] Jorgensen, J. K.; Schoier, F. L.; van Dishoeck, E. F. 2004, A&A, 416, 603

[54] 2006ApJ...inpress2]Jorgensen, J.K. et al. 2006, in press

[55] Juvela, M. 1998, A&A, 329, 659

[56] Kauffmann, J., et al. 2006, in preparation

[57] Kawamura, A., Kun, M., Onishi, T., Vavrek, R., Domsa, I., Mizuno, A., & Fukui, Y. 2001, PASJ, 53, 1097

[58] Kennicutt,R. C. 1997, in The Interstellar Medium in Galaxies, ed. J. M. van der Hulst (Dordrecht: Kluwer), 171

[59] Kennicutt,R. C. 1998, ApJ, 498, 541

[60] Kenyon, S. J., Dobrzycka, D., & Hartmann, L. 1994, AJ, 108, 1872

[61] Keto, E. R., Ho, P. T. P., Haschick, A. D. 1988, ApJ, 324, 920

[62] Kewley, L. J., Geller, M. J., Jansen R. A. & Dopita, M. A. 2002, AJ, 124, 3135

[63] Kun, M., & Prusti, T. 1993, A&A, 272, 235

[64] Kun, M. 1998, ApJS, 115, 59

[65] Krumholz, M. R. & McKee, C. F. 2005, ApJ, 630, 250

[66] Lada, C. J. & Lada, E. A. 2003, Ann. Rev. Ast. & Astrophys., 41, 57

[67] Lee, C. W., Myers, P. C., & Tafalla, M. 1999, ApJ, 526, 788

[68] Lee, C. W., Myers, P. C., & Tafalla, M. 2001, ApJS, 136, 703

[69] Lee, J.-E., Evans, N.J.II, Shirley, Y.L., & Tatematsu, K. 2003, ApJ, 583, 789

[70] Lee, J.-E., Bergin, E. A., Evans, N.J.II, 2004, ApJ, 617, 360

[71] Li, Y., Mac Low, M.-M., & Klessen, R. S. 2005, ApJ, 626, 823

[72] Lintott, C. J., Viti, S., Williams, D. A., Rawlings, J. M. C., Ferreras, I. 2005, MNRAS, 360, 1527

[73] Mardones, D., Myers, P. C., Tafalla, M., Wilner, D. J., Bachiller, R., & Garay, G. 1997, ApJ, 489, 719

[74] McKee, C. F., Tan, J. C. 2002, Nature, 416, 59

[75] McKee, C. F., Tan, J. C. 2003, ApJ, 585, 850

[76] Mead, K. N., Kutner, M. L. and Evans, N. J. II. 1990, ApJ, 354, 492

[77] Mooney, T. J., & Solomon, P. M. 1988, ApJ, 334, 51

[78] Motte, F., & Andre, P. 2001, A&A, 365, 440

[79] Mueller, K. E., Shirley, Y. L., Evans, N. J. II, & Jacobson, H. R. 2002, ApJS, 143, 469

[80] Murdin, P. & Penston, M.V. 1977, MNRAS, 181, 657

[81] Myers, P. C., Evans, N. J. II, & Ohashi, N. 2000, Protostars and Planets IV, 217

[82] Myers, P. C., Mardones, D., Tafalla, M., Williams, J. P., & Wilner, D. J. 1996, ApJ, 465, 133

[83] Ossenkopf, V., & Henning, Th. 1994, A & A, 291, 943

[84] Pagani, L., & Breart de Boisanger, C. 1996, A&A, 312, 989

[85] Paglione, T. A. D., Jackson, J. M., & Ishizuki, S. 1997, ApJ, 484, 656

[87] Plume, R., Jaffe, D. T., Evans, N. J. II. 1992, ApJS, 78, 505

[87] Plume, R., Jaffe, D. T., Evans, N. J. II. 1992, ApJS, 78, 505

[88] Plume, R., Jaffe, D. T., Evans, N. J. II, Martin-Pintado, J., & Gomez-Gonzalez, J. 1997, ApJ, 476, 730

[89] Reuland, M., Röttgering, H., and van Breugel, W. 2003, New Astronomy Reviews, 47, 303

[90] Rieke, G.H., et al. 2004, ApJS, 154, 25

[91] Sanders, D. B., & Mirabel, I. F. 1996, Ann. Rev. Ast. & Astrophys., 34, 749

[92] Schmidt, M. 1959, ApJ, 129, 243

[93] Shirley, Y. L., Evans N. J .II, Rawling, J. M. C., and Gregersen, E. M. 2000, ApJS, 131, 249

[94] Shirley, Y. L., Evans, N. J. II, Mueller, K. E., Knez, C., Jaffe, D. T. 2003, ApJS, 149, 375.

[95] Shu, F. H. 1977, ApJ, 214, 488

[96] Shu, F. H., Adams, F. C., and Lizano, S. 1987, ApJ1987, Ann. Rev. Ast. & Astrophys., 25, 23

[97] Sollins, P. K.; Zhang, Q., Keto, E., Ho, P.T. P. 2005, ApJ, 624, 49.

[98] Solomon, P.M., Rivolo, A.R., Barret, J., & Yahil, A. 1987, ApJ, 319,370

[99] Solomon, P. M., Downes, D., Radford, S. J. E., Barrett, J. W. 1997, ApJ, 478, 144

[100] Solomon., P. M., Vanden Bout, P. A.,Carilli, C. L., & Guelin, M. 2003, Nature, 426, 636

[101] Solomon., P. M. & Vanden Bout, P. A. 2005, Ann. Rev. Ast. & Astrophys, 43, 677

[102] Straižys, V., Černis, K., & Bartašiūtė, S. 2003, A&A, 405, 585

[103] Straižys, V., Černis, K., & Bartašiūtė, S. 1996, Baltic Astronomy, 5, 125

[104] Straižys, V., Černis, K., Kazlauskas, A., & Meištas, E. 1992, Baltic Astronomy, 1, 149

[105] Val'tts, I. E., Ellingsen, S. P., Slysh, V. I., Kalenskii, S. V., O trupcek, R., & Larionov, G. M. 2000, MNRAS, 317, 315

[106] Vanden Bout, P. A., Solomon., P. M., & Maddalena, R. J. 2004, ApJ, 614, 97

[107] Welch, W. J., Dreher, J. W., Jackson, J. M., Terebey, S., Vogel, S. N. 1988, Science, 238, 1550

[108] Williams, J. P. & Myers, P. C. 1999, ApJ, 511, 208

[109] Wilson, T. L., & Rood, R. 1994, ARA&A, 32, 191

[110] Wink, J.E., Altenhoff, W.J., & Mezger, P.G. 1982, A& A, 108, 227

[111] Woermann, B., Gaylard, M. J., & Otrupcek, R. 2001, MNRAS, 325, 1213

[112] Wolf-Chase, G. A.,& Gregersen E. 1997, ApJ, 479, 67

[113] Wood, D. O. S, & Churchwell, E. 1989, ApJ, 340, 265

[114] Wu, J., & Evans, N. J. II, 2003, ApJ, 592, L79

[115] Wu, Y., Wei, Y., Zhao, M., Shi, Y., Yu, W., Qin, S., and Huang, M. 2004, A&A, 426, 503

[116] Wu, J., Evans, N.J.II, Gao, Y., Solomon, P., Shirley, Y., Vanden Bout, P. A. 2005, ApJ, 635, L173

[117] Yonekura, Y., Dobashi, K., Mizuno, A., Ogawa, H., & Fukui, Y. 1997, ApJS, 110, 21

[118] Young, C.H., et al. 2004, ApJS, 154, 396

[119] Young, C.H., et al. 2006, in preparation

[120] Zhang, Q. & Ho, P. T. P. 1997, ApJ, 488, 241

[121] Zhang, Q., Ho, P. T. P., & Ohashi, N. 1998, ApJ, 494, 636

[122] Zhou, S. & Evans, N. J. II. 1994, ASP Conf. Ser. 65: Clouds, Cores, and Low Mass Stars, 183

[123] Zhou, S., Evans, N. J. II, Koempe, C., & Walmsley, C. M. 1993, ApJ, 404, 232

[124] Zhou, S., Evans, N. J. II, Koempe, C., & Walmsley, C. M. 1994, ApJ, 421, 854

[125] Zhou, S., Butner H.M., Evans, N. J. II, Gusten R., Kutner M.L., Mundy L.G., 1994, ApJ, 428, 219

[126] Zhou, S., Evans, N. J., Wang, Y. 1996, ApJ, 406, 296

[127] Zhang, Q., Hunter, T. R., Brand, J., Sridharan, T. K., Cesaroni, R., Molinari, S., Wang, J., and Kramer, M. 2005. AJ, 625, 864

[128] Zinchenko, I., Forsstroem, V., Lapinov, A., & Mattila, K. 1994, A&A, 288, 601

Vita

Jingwen Wu was born in Beijing, China, on 23 June 1975. He grew up there until he went to graduate school. He was a boy with lots of curiosity. He has many interests since young; he likes Chinese ancient literatures; he loves sports; he had even been trained as a high jumper in the middle school. But eventually, he chose Astronomy as his major of career, since he thought it is a major that can greatly satisfy his curiosity, a field of real science that needs both diligence and imagination.

Jingwen received his Bachelor of Science degree in the department of Geophysics in Peking University, China, in 1998, and a Master of Science degree in department of Astronomy in the same university in 2001. Although he had studied in the vicinity of his hometown for such a long time (all his schools, from elementary school to graduate school, are within 10 miles of his hometown), he decided to go across half the world to study at the University of Texas at Austin. He entered the department of Astronomy in UT as a graduate student in 2001, and became a PhD candidate in 2003.

Permanent address: 1919 Burton Dr. Apt.260B, Austin, TX, 78741

This dissertation was typeset with LaTeX[†] by the author.

[†]LaTeX is a document preparation system developed by Leslie Lamport as a special version of Donald Knuth's TeX Program.